



National Library  
of Canada

Bibliothèque nationale  
du Canada

Acquisitions and  
Bibliographic Services Branch

Direction des acquisitions et  
des services bibliographiques

395 Wellington Street  
Ottawa, Ontario  
K1A 0N4

395, rue Wellington  
Ottawa (Ontario)  
K1A 0N4

*Your file* *Voire référence*

*Our file* *Notre référence*

## NOTICE

The quality of this microform is heavily dependent upon the quality of the original thesis submitted for microfilming. Every effort has been made to ensure the highest quality of reproduction possible.

If pages are missing, contact the university which granted the degree.

Some pages may have indistinct print especially if the original pages were typed with a poor typewriter ribbon or if the university sent us an inferior photocopy.

Reproduction in full or in part of this microform is governed by the Canadian Copyright Act, R.S.C. 1970, c. C-30, and subsequent amendments.

## AVIS

La qualité de cette microforme dépend grandement de la qualité de la thèse soumise au microfilmage. Nous avons tout fait pour assurer une qualité supérieure de reproduction.

S'il manque des pages, veuillez communiquer avec l'université qui a conféré le grade.

La qualité d'impression de certaines pages peut laisser à désirer, surtout si les pages originales ont été dactylographiées à l'aide d'un ruban usé ou si l'université nous a fait parvenir une photocopie de qualité inférieure.

La reproduction, même partielle, de cette microforme est soumise à la Loi canadienne sur le droit d'auteur, SRC 1970, c. C-30, et ses amendements subséquents.

THE UNIVERSITY OF ALBERTA

HIGH TEMPERATURE MICROWAVE DIELECTROMETER  
USING A RE-ENTRANT CAVITY

BY



WEIGUO XI

A THESIS  
SUBMITTED TO THE FACULTY OF GRADUATE STUDIES AND RESEARCH  
IN PARTIAL FULFILLMENT OF THE REQUIREMENTS FOR THE DEGREE OF  
DOCTOR OF PHILOSOPHY

DEPARTMENT OF ELECTRICAL ENGINEERING

EDMONTON ALBERTA

FALL 1992



National Libra-  
of Canada

Bibliothèque nationale  
du Canada

Canadian Theses Service    Service des thèses canadiennes

Ottawa, Canada  
K1A 0N4

The author has granted an irrevocable non-exclusive licence allowing the National Library of Canada to reproduce, loan, distribute or sell copies of his/her thesis by any means and in any form or format, making this thesis available to interested persons.

The author retains ownership of the copyright in his/her thesis. Neither the thesis nor substantial extracts from it may be printed or otherwise reproduced without his/her permission.

L'auteur a accordé une licence irrévocable et non exclusive permettant à la Bibliothèque nationale du Canada de reproduire, prêter, distribuer ou vendre des copies de sa thèse de quelque manière et sous quelque forme que ce soit pour mettre des exemplaires de cette thèse à la disposition des personnes intéressées.

L'auteur conserve la propriété du droit d'auteur qui protège sa thèse. Ni la thèse ni des extraits substantiels de celle-ci ne doivent être imprimés ou autrement reproduits sans son autorisation.

ISBN 0-315-77233-6

Canada

THE UNIVERSITY OF ALBERTA

RELEASE FORM

NAME OF AUTHOR: Weiguo Xi

TITLE OF THESIS: High Temperature Microwave Dielectrometer  
Using A Re-Entrant Cavity

DEGREE: Doctor of Philosophy

YEAR THIS DEGREE GRANTED: 1992

Permission is hereby granted to the University of Alberta Library to reproduce single copies of this thesis and to lend or sell such copies for private, scholarly or scientific research purpose only.

The author reserves all other publication and other rights in association with the copyright in the thesis, and except as hereinbefore provided neither the thesis nor any substantial portion thereof may be printed or otherwise reproduced in any material form whatever without the author's prior written permission.

X:   
\_\_\_\_\_

Apt Blk 522  
Hougang Ave 6, #12-31  
Singapore (1953)

Date: September 30, 1992

THE UNIVERSITY OF ALBERTA

FACULTY OF GRADUATE STUDIES AND RESEARCH

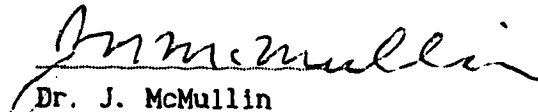
The undersigned certify that they have read, and recommend to the Faculty of Graduate Studies and Research for acceptance, a thesis titled **High Temperature Microwave Dielectrometer Using A Re-Entrant Cavity** submitted by Weiguo Xi in partial fulfillment of the requirements for the degree of Doctor of Philosophy in Electrical Engineering.

  
\_\_\_\_\_

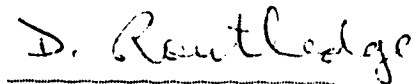
Dr. W.R. Tinga, Supervisor

  
\_\_\_\_\_

Dr. Z. Koles

  
\_\_\_\_\_

Dr. J. McMullin

  
\_\_\_\_\_

Dr. D. Routledge

  
\_\_\_\_\_

Dr. F. Vermeulen

  
\_\_\_\_\_

Dr. R.H. Johnston, External Examiner

Date: September 11, 1992

**To my dear grandma, Yu Jia**

## ABSTRACT

Current techniques for high temperature microwave dielectric measurements utilize an external heater to raise the sample's temperature. The temperature range in such a conventional sample heating scheme is limited by overheating and expansion of the test chamber. To overcome this limitation, a dielectrometer system using microwave power for sample heating is developed. By virtue of the selectivity of microwave heating, a sample can be rapidly heated up to its melting point whereas the test chamber remains at room temperature.

A modified coaxial re-entrant cavity is designed as the test chamber using a hollow center conductor for ease and repeatability of sample insertion. Two quasi TEM modes, at about 3GHz and 915MHz respectively, are used for sample measuring and heating. The electromagnetic fields in this sample loaded cavity are analyzed using a four-subarea mode-matching formulation. The calculated resonant frequency and Q-factor directly provide two theoretical calibration curves for the dielectric determinations.

An automatic measuring and heating system is implemented which has three channels connected to the cavity, each for testing, heating and temperature measuring and controlling. The sample's temperature is controlled so that the heating rate is almost a constant. An analog circuit is designed to electronically tune the heating source frequency to that of the sample loaded resonator. A small cylindrical sample can readily be inserted into the cavity to be heated and tested simultaneously. Via the computer data acquisition program, one dielectric measurement takes one second and a complete curve of complex dielectric constant versus temperature needs about one minute.

All possible error sources in the dielectric determination are examined in detail and the worst-case errors in the determined dielectric data are evaluated. The room temperature permittivity results obtained from a number of well characterized materials are compared with the published data, showing a good agreement between the two.

Various ceramic samples are measured from room temperature up to 1600°C and based on the results, the polarization and loss mechanisms are discussed.

## ACKNOWLEDGEMENT

I feel deeply indebted to my supervisor, Dr. W.R.Tinga, for his patience, constant encouragement, expert technical advice and unfailing personal help throughout the course of this project. I am very grateful to my fellow graduate student, Mr. Bai Qiang Tian, for stimulating discussions.

I acknowledge gratefully the financial support provided by the Natural Science and Engineering Research Council of Canada and the Electrical Engineering Department of the University of Alberta. I also wish to express my gratitude to Canada as a whole for having given me the opportunity to study here.

I wish to convey my thanks to our machine shop, in particular, Mr. Herb Gans, for their skillful assistance. Technical support received from Mr. Don Presakarchuk is also acknowledged.

My special thanks must go to Dr. Eric Valk, Mr. Henrik Johansen and Mr. Gavin Millier. Their generous help with my experimental work as well as my English is most unforgettable.

I also wish to thank my former supervisor, Prof. Linsu Tong in Southeast University, Nanjing, China, who introduced me into the area of numerical analysis of electromagnetic fields. The knowledge and skill I acquired with him have been proved to be invaluable for the development of this project.

Furthermore, I am grateful to Dr. J.McMullin, Dr. D.Routledge and Dr. F.Vermeulen for their serving on the doctoral committee and reviewing my thesis manuscript. I wish to thank Dr. A.Mackay for his help in editing part of this thesis. I am also appreciative of the advice and help given by the departmental administration, especially by Dr.R.Lawson and Ms. C.Brennan.

Finally, I thank my wife, Angela K.L. Yeo for her love and understanding. Owing to her companionship in countless difficult moments, I made progress. I thank my family and my relatives for their support, especially, my grandmother to whom I owe the most. I dedicate this thesis to her, aware that by no means can this pay off the hardship she endured to bring me up and for the suffering of our separation since I left China.



## TABLE OF CONTENTS

CHAPTER 1	Introduction	1
1.1	Thesis Objective	1
1.2	Evaluation of Dielectric Measurement Techniques	3
1.3	Solution to High Temperature Measurement Problems	6
1.4	Thesis Content Overview	8
CHAPTER 2	Dielectric Determination Using Resonant Cavity Method	10
2.1	Experimental Calibration	10
2.2	Perturbation Formula	11
2.3	Direct Field Analysis	15
CHAPTER 3	Cavity Field Analysis Using Mode-Matching Method	20
3.1	Mode-Matching Method	20
3.2	Mode-Matching Formulations	22
3.2.1	Case 1: Gap Completely Filled with Sample	22
	A. Step One: Expressing Subarea Fields	22
	B. Step Two: Matching Fields between Subareas	25
	C. Step Three: Solving System Equations	28
3.2.2	Case 2: Gap Partially Filled with Sample	29
3.2.3	Case 3: Arbitrary Gap Position	31
3.2.4	Case 4: Gap with Sample Insertion Holes	33
3.2.5	Case 5: Sample with Holder	37
3.3	Numerical Algorithm and Computer Program	41
3.4	Calculation Errors	43
3.5	Verification for Calculations	45
CHAPTER 4	Theoretical Cavity Resonance Characteristics	49
4.1	Field Distribution	49
4.2	Quasi-TEM Resonant Modes	54
4.3	Equivalent Gap Capacitance	56

4.4	Resonant Frequency	58
4.5	Cavity Q-factor	60
4.5.1	Normalized $Q_c$	61
4.5.2	Normalized $Q_D$ and Sample Energy Density	63
4.6	Effects of Insertion Hole	64
4.6.1	Hole Field Attenuation	66
4.6.2	Gap Field Distribution	66
4.6.3	Resonant Frequency Shift	66
4.6.4	Energy Stored and Dissipated in Sample	70
4.6.5	Hole Effects and Wavelength	71
4.7	Calibration Curves for Dielectric Determination	73
CHAPTER 5 Measurement and Control System		77
5.1	Cavity Design	78
5.1.1	Design Considerations	78
5.1.2	Determination of Cavity Dimensions	79
	A. Cavity Radius	79
	B. Cavity Length	80
	C. Insertion Hole Radius and Gap Width	80
5.1.3	Non-contact Short Circuit Design	82
5.1.4	Mechanical Tolerance of Cavity Dimensions	83
5.2	Testing Channel Operation	85
5.3	Heating Channel Operation	88
5.4	Temperature Measuring Channel Operation	91
5.5	Dynamic Measurement Range	93
5.5.1	Dielectric Constant	93
5.5.2	Loss Factor and Loss Tangent	93
CHAPTER 6 Experimental Results and Error Analysis		99
6.1	Calibration Curves	99
6.2	Error Analysis	100

6.3	Room Temperature Measurement	114
6.4	High Temperature Measurement Procedure	114
6.4.1	Sample Preparation	114
6.4.2	System Setup Check	116
6.4.3	Heating and Testing	117
6.5	Experimental Results and Discussion	117
CHAPTER 7 Conclusion		130
REFERENCES		133
APPENDIX 1	Integration Function of $e_{ij}(a,b)$	139
APPENDIX 2	Approximate Calculation of Cavity Q-factor	142
APPENDIX 3	Evaluation of Return Loss and Q-Measurement Uncertainty	146
APPENDIX 4	Automatic Tuning Circuit	154
APPENDIX 5	Analysis of Sample Temperature Non-uniformity	159

## LIST OF TABLES

TABLE 3.1	Convergence of modal coefficients	45
TABLE 3.2	Calculated resonant frequencies compared with Karpova's data	46
TABLE 3.3	Calculated resonant frequency of an empty cavity for varying gap widths, compared with experimental data	46
TABLE 3.4	Calculated resonant frequency shift by Teflon samples compared with experimental data	46
TABLE 3.5	Calculated resonant frequency shift by distilled water for varying cavity lengths, compared with the measured data	47
TABLE 4.1	Calculated normalized $Q_c$ : approximate analytical results versus numerical results	63
TABLE 5.1	Evaluation of mechanical tolerance of a cavity	84
TABLE 5.2	Lower and upper limits of loss factor and loss tangent	98
TABLE 6.1	Polynomial fitting coefficients for the calibration curves in Figure 6.1	107
TABLE 6.2	Polynomial fitting coefficients for the calibration curves in Figure 6.2	107
TABLE 6.3	Polynomial fitting coefficients for the calibration curves in Figure 6.3	108
TABLE 6.4	Evaluation of error limits in the determined dielectric constant and loss tangent	113
TABLE 6.5	Experimental results of dielectric constants and loss tangents at $T=23^{\circ}\text{C}$ as compared with published data	115
TABLE 6.6	High temperature dielectric properties of ceramics measured at 3GHz while the sample is being heated by a 120W, 915MHz solid state power source	118
TABLE A5.1	The parameter $\alpha$ and $p$ for evaluating the error of the sample temperature non-uniformity	164

## LIST OF FIGURES

FIGURE 1.1	Cross section of the coaxial re-entrant cavity designed for the high temperature dielectric measurement	8
FIGURE 2.1	A sample loaded cylindrical cavity and its $TM_{010}$ mode field configuration	16
FIGURE 3.1	Subarea division for mode-matching formulation of Case 1 - gap completely filled with sample	23
FIGURE 3.2	Subarea division for mode-matching formulation of Case 2 - gap partially filled with sample	30
FIGURE 3.3	Subarea division for mode-matching formulation of Case 3 - arbitrary gap position	32
FIGURE 3.4	Subarea division for mode-matching formulation of Case 4 - gap with sample insertion holes	34
FIGURE 3.5	Subarea division for mode-matching formulation of Case 5 - sample with sample holder	38
FIGURE 3.6	Truncation error in $f_0$ and $\Delta f_0$ and required computation time on an Amdahl(5870) computer	44
FIGURE 3.7	The determinant of matrix $\underline{G}$ as a function of wavelength	48
FIGURE 4.1	Coaxial re-entrant cavity with a gap partially filled with a dielectric sample	51
FIGURE 4.2	E and H fields for a capacitive mode	52
FIGURE 4.3	E and H fields for an inductive mode	53
FIGURE 4.4	Graphic solution for resonant frequencies	55
FIGURE 4.5	Equivalent gap capacitance	57
FIGURE 4.6	Resonant frequency versus (a) gap width, (b) dielectric constant and (c) sample radius	59
FIGURE 4.7	Resonant wavelength as a function of the dielectric constant	60

FIGURE 4.8	Inverse normalized cavity Q-factor versus (a) gap width, (b) dielectric constant and (c) sample radius	62
FIGURE 4.9	Sample energy density ratio versus (a) gap width (b) dielectric constant and (c) sample radius	65
FIGURE 4.10	Axial distribution of the normalized $E_z$ in the gap and adjacent hole region at $r=0$	67
FIGURE 4.11	The effective hole depth of cavity (3) as a function of dielectric constant	67
FIGURE 4.12	Radial distribution of the normalized $E_z$ at the gap midplane in three cavity structures	68
FIGURE 4.13	Resonant frequency shift produced by a sample for in three cavity structures	69
FIGURE 4.14	Normalized electric energy stored in a sample as a function of the sample's dielectric constant	70
FIGURE 4.15	(a) The axial distribution ( $r=0$ ) of normalized $E_z$ and (b) the resonant frequency shift, as a function of sample's dielectric constant in two frequency bands	72
FIGURE 4.16	The sample loading factor as a function of sample's dielectric constant; perturbation results compared with mode-matching results	74
FIGURE 4.17	Calibration curve for determining dielectric constant by the length variation method	75
FIGURE 4.18	Calibration curve for determining dielectric constant by the gap variation method	76
FIGURE 5.1	Experimental system for high temperature dielectric measurements	77
FIGURE 5.2	Cavity structure of dielectrometer	78
FIGURE 5.3	Resonant frequency plotted as a function of cavity length in both the testing and heating band	81
FIGURE 5.4	Cross section of the coaxial shorting bucket	82

FIGURE 5.5	Normalized input impedance of the shorting bucket	84
FIGURE 5.6	The square of the reflection coefficient as a function of the normalized frequency increment	86
FIGURE 5.7	(a) Block diagram of the external tuning system and (b) Timing cycle of the automatic tuner	89
FIGURE 5.8	Typical waveform of the reflection voltage and the tuning voltage in the automatic tuning circuit	90
FIGURE 5.9	Sample's temperature control (a) Block diagram of the control loop and (b) Temperature response of a properly tuned PID controller	91
FIGURE 5.10	Controlled and uncontrolled microwave heating curve of Macor	92
FIGURE 5.11	Maximum measurable dielectric constant as function of the gap width	94
FIGURE 5.12	The parameter of $(\epsilon'_r / Q_0 F_\ell)$ used for estimating the maximum and minimum loss factor which can be covered by the testing and heating system	97
FIGURE 6.1a	Calibration curves for determining the dielectric constant for three types of sample holders	101
FIGURE 6.1b	Calibration curves for determining the loss factor for three types of sample holders	102
FIGURE 6.2a	Calibration curves for determining the dielectric for different gap widths	103
FIGURE 6.2b	Calibration curves for determining the loss factor for different gap widths	104
FIGURE 6.3a	Calibration curves for determining the dielectric for different sample radii	105
FIGURE 6.3b	Calibration curves for determining the loss factor for different sample radii	106

<b>FIGURE 6.4</b>	The relative error in the dielectric constant due to variation in sample radius	109
<b>FIGURE 6.5</b>	The error transfer function for three types of sample holders	112
<b>FIGURE 6.6</b>	Measured dielectric constants and loss tangents of various ceramics, at 3GHz, as functions of temperature	122
<b>FIGURE A2.1</b>	Schematic diagram of a coaxial re-entrant cavity with a partially dielectric loaded gap	142
<b>FIGURE A3.1</b>	Return loss uncertainty in a reflectometer	148
<b>FIGURE A3.2</b>	Relative error in measured Q-factor caused by a one dB return loss uncertainty as a function of the normalized frequency increment	151
<b>FIGURE A3.3</b>	Relative error in measured Q-factor versus the reflection coefficient	152
<b>FIGURE A4.1</b>	Block diagram of the automatic tuning circuit	155
<b>FIGURE A4.2</b>	Automatic tuning circuit	156
<b>FIGURE A5.1</b>	Dielectric non-uniformity due to the E-fields and the sample temperature distribution	160
<b>FIGURE A5.2</b>	The measured axial temperature distribution of a glass sample compared with calculated testing and heating field distributions	165
<b>FIGURE A5.3</b>	The dielectric data measured at a fixed temperature	165



## LIST OF SYMBOLS AND ABBREVIATIONS

$a_1, a_2, \dots$	polynomial coefficients of the calibration curve for determining the dielectric constant (ch.6)
$a, b, c, d$	modal coefficients in subarea A, B, C and D
A, B, C, D	subarea
AMV	astable multivibrator (App.4)
$b_0, b_1, \dots$	polynomial coefficients of the calibration curve for determining the loss factor (ch.6)
BRG	bootstrap ramp generator (App.4)
$c$	light velocity in vacuum ( $3 \times 10^8$ m/s); a constant
$C_0$	equivalent gap capacitance
CRT	cathode ray tube
CW	continuous wave
D	gap width; directivity of a directional coupler
det	determinant value of a square matrix
DUT	device under test
E	electric field intensity
$e_{ij}$	a Fourier expansion coefficient evaluated in Appendix 1
$f$	frequency; a function
F	generalized filling factor which is the ratio of the stored electric energy in the volume occupied by a sample to that in the whole cavity before the sample is loaded (ch.2); constant associated with a combinational Bessel function (ch.3)
$f_0$	resonant frequency
$F_0$	filling factor, the volume ratio of a sample to the cavity
$f_\ell$	$\approx F_\ell / F_0$ , the ratio of the energy density in the sample to that in the cavity (ch.4)
$F_\ell$	sample loading factor, the ratio of the stored electric energy in the sample to that in the whole cavity
FDM	finite difference method
FEM	finite element method
$g$	geometry factor, the ratio of internal to external E-field of a dielectric (ch.2); gap between the shorting bucket and the center conductor (ch.5)

$H, H_1, H_2$	length of the hole
H	magnetic field intensity; a function of $r_2/r_1$ in the Q expression for a coaxial cavity (App.3)
I	unity matrix
$I_0$	TEM current in a coaxial cavity
$I_0, I_1$	modified Bessel function of the first kind
ID	inner diameter
ISM	industrial, scientific and medical
$J_0, J_1$	the first and the second order Bessel function of the first kind
k	radial wave number
$k_0$	wave number in free space
$K_0, K_1$	modified Bessel function of the second kind
$l$	length of a center conductor, or length of a standard coaxial cavity; mode integer in subarea C and D (ch.3)
$l_b$	length of the shorting bucket
L	cavity length; the highest mode number in subarea C and D after the truncation (ch.3)
$L_0$	equivalent gap inductance
$L_R$	loss of the short circuit in decibel
m	mode integer in subarea B
M	the highest mode in subarea B after the truncation (ch.3)
MMV	mono-multi-vibrator
n	mode integer in subarea A
N	the highest mode in subarea A after the truncation (ch.3)
Ob	objective function of minimization (ch.3)
OD	outer diameter
OFT	optical fiber thermometer
p	power density; a parameter signifying the sample temperature non-uniformity error (App.5)
$P_D$	electric power dissipated in a dielectric
$P_I$	incident power
$P_{refl}$	reflected power
$P_w$	electric power dissipated on the cavity wall
PD	peak detector (App.4)

PID	proportional, integral and derivative
Q	quality factor (of empty or loaded cavity)
$Q_0$	Q-factor of an empty cavity
$Q_c$	cavity Q-factor due to the wall loss
$Q_L$	Q-factor of a sample loaded cavity
$Q_E$	external Q-factor
$Q_D$	cavity Q-factor due to the sample loss
$Q_m$	measured Q-factor
r	radial distance in a cylindrical coordinate
$\bar{R}$	normalized input resistance
$r_0$	radius of the sample insertion hole; sample radius when the sample holder is not used
$r_{oc}$	critical hole radius
$r_1$	radius of center conductor; sample radius (ch.2)
$r_2$	radius of outer conductor
$r_s$	sample radius
$R_s$	surface resistance
r.m.s.e.	root-mean-square-error in the least square fitting (ch.6)
RL	return loss in dB
RTR	re-trace remover (App.4)
s	second
S	surface area
ST	Schmitt trigger (App.4)
SWR	(voltage) standing wave ratio
S/H	sample/hold (App.4)
t	time
$t_h$	holding period of the tuning circuit
$t_s$	searching period of the tuning circuit
T	temperature; a superscript which denotes matrix transposition
$\tan\delta$	loss tangent, i.e., $\epsilon'_r/\epsilon''_r$
TE	transverse electric field mode
TEM	transverse electric and magnetic field mode
TM	transverse magnetic field mode
$V_c$	cavity volume
$V_D$	sample volume

$V_f$	frequency tuning voltage
$V_{IN}$	analog voltage of incident power (App.4)
$V_R$	analog voltage of the reflected power
VCO	voltage controlled oscillator
$W_1, W_2, W_3$	weight factor in a summation
$W_n$	electric energy stored in a dielectric
$W_E$	total electric energy stored in a cavity
WC	window comparator (App.4)
x	modal coefficient (ch.3); normalized frequency increment (ch.5)
$y(x)$	normal distribution (App.5)
$Y_0$	equivalent gap admittance
$Y_0, Y_1$	the first and the second order Bessel function of the second kind
$Y_c$	characteristic admittance of a coaxial line or cavity
z	axial position in a cylindrical coordinate
$Z_c$	characteristic impedance of a coaxial line or cavity
$Z_0, Z_1$	the first and the second order combinational Bessel function
$z_h$	effective hole depth
$Z_s$	input impedance of the shorting bucket
$\alpha$	a parameter in a normal distribution which is one third of the effective hole depth when it approximates the E-field distribution in the insertion hole (App.5)
$\alpha_i$	a function with a value of 1 when $i=0$ and of 2 otherwise
$\beta$	axial wave number; coupling factor (ch.5)
$\Gamma$	(amplitude of) reflection coefficient
$\delta_{ij}$	Kronecher Delta function with value 1 if $i=j$ and 0 otherwise
$\delta f_0$	frequency increment (ch.5)
$\Delta f_0$	cavity resonant frequency shift due to sample insertion
$\Delta(1/Q)$	variation in the inverse of the cavity Q-factor due to sample insertion
$\epsilon$	$=\epsilon_0 \epsilon_r = \epsilon_0 (\epsilon'_r - j\epsilon''_r)$ , complex dielectric constant or permittivity
$\epsilon_0$	permittivity of free space ( $8.854 \times 10^{-12}$ farads/m)
$\epsilon_r$	complex relative dielectric constant or permittivity (of a sample); dielectric constant (ch.3)

$\epsilon_{rh}$	sample holder's dielectric constant
$\epsilon_{rs}$	sample's dielectric constant
$\epsilon'_r$	dielectric constant (of sample)
$\epsilon''_r$	loss factor (of sample)
$\zeta$	error transfer function (ch.6)
$\eta_0$	free space impedance ( $120\pi\Omega$ )
$\theta_b$	electrical length of the shorting bucket
$\lambda$	wavelength
$\lambda_0$	resonant wavelength
$\lambda_c$	cutoff wavelength
$\mu$	permeability
$\mu_0$	permeability of free space ( $4\pi \times 10^{-7}$ henry/m)
$\sigma$	electrical conductivity
$\phi$	angle in a cylindrical coordinate
$\chi$	dielectric susceptibility
$\Omega$	$=\omega + j\omega/(2Q)$ , complex resonant frequency; unit of resistance
$\omega$	angular frequency

# CHAPTER 1

## INTRODUCTION

### 1.1 Thesis Objective

In order to use microwave energy to advantage in high temperature material processing, this thesis is devoted to the investigation of and improvement on the technique of high temperature dielectric measurements. This improved technique will allow the measurement of materials with a wider range of dielectric properties at a higher temperature than existing techniques. It has an acceptable accuracy and is also very fast, versatile and convenient to use so that it is not only suitable for lab research but also applicable to quality control in industrial production.

In conventional heating, heat is first transferred to the material surface by either conduction, convection or radiation, and then to the interior by thermal conduction. In comparison, microwave heating is fundamentally different. First, in microwave heating, microwave energy-to-heat conversion takes place directly inside the material. This volumetric heating leads to a reduced thermal gradient, a higher heating rate and a better temperature uniformity. Second, microwave heating is nearly instantaneous since the heat source can be turned on or off without the thermal inertia that exists in conventional heating sources. The highly ordered microwave energy eases the heating process control. Finally, microwave heating is also material dependent. This selectivity is one of the essential features which make microwave heating effective and unique.

The field of microwave heating has become firmly established after millions of microwave ovens entered homes in Northern America, Europe, Japan and other countries [1,2]. The popularity of domestic microwave ovens increases the awareness of the advantages of microwave heating in society, which in turn, encourages the development of microwave processing of materials in various industries, such as in the ceramic industry which requires an enormous amount of energy input [3]. The use of microwave energy may benefit these industries in many ways. Less energy consumption and processing time reduces processing cost. The other benefits include improved or unique microstructure and physical properties

and opportunity for new material synthesis [4].

In recent years, considerable progress has been made in applying microwave energy to various ceramic processes, including drying, calcining, sintering and joining [4]. However, many of the possible benefits of microwave heating have yet to be realized because some problems remain unsolved. These problems range from a lack of theoretical understanding of microwave-material interaction to a need for optimum processing and equipment design. Their solution depends heavily on making available a broad data base of dielectric properties from room temperature to very high temperatures for a wide range of ceramic materials.

The need for dielectric data is evident from the principles of microwave heating. The heat generated by a microwave field is proportional to the power absorbed per unit volume which is given as

$$p = \frac{1}{2} \omega \epsilon_0 \epsilon_r'' E^2 \quad (1.1)$$

It shows the absorbed power density,  $p$ , is proportional to the loss factor,  $\epsilon_r''$ , of the material and the square of the electric field inside the material. It should be noted that the internal E-field is a function of many factors; among them is the dielectric constant,  $\epsilon_r'$ , of the material. In the simplest case of a plane wave striking the material interface, the field inside the material can be readily shown to be [5]

$$E = \frac{2}{1 + \sqrt{\epsilon_r'}} E_0 \quad (1.2)$$

if the E-field is parallel to the interface, or

$$E = \frac{1}{\sqrt{\epsilon_r'}} E_0 \quad (1.3)$$

if the E-field is perpendicular to the interface, where  $E_0$  is the E-field of the incident wave. In general, the solution of the E-field inside the material has to be found directly or indirectly from the Helmholtz equation [6]

$$\nabla^2 E + \omega \mu \epsilon E = 0 \quad (1.4)$$

under specific boundary conditions. In this equation, the complex dielectric constant,

$$\epsilon = \epsilon_0 (\epsilon'_r - j\epsilon''_r) \quad (1.5)$$

appears as the only parameter describing the electric behavior of the material.

We have seen that energy conversion via microwave heating depends on the dielectric properties of a material, with the internal field, power absorption, heating rate and temperature profile all depending on them. What complicates the microwave heating analysis more is that the dielectric properties are generally functions of temperature. In order to predict the internal field and the heating pattern, one must know the dielectric properties of the material and their temperature dependence. The predictability of heating response is essential for developing optimum processing parameters to meet given product requirements.

Unfortunately, dielectric property data are lacking at high temperatures (over 500<sup>0</sup>C) and present techniques of dielectric measurements are far from satisfactory at these temperatures. The lack of development of high temperature techniques is mainly attributed to the fact that most processes for which dielectric data are required remain at or near room temperature. Only with the increasing application of microwave heating in high temperature material processing such as sintering and joining does the demand for high temperature data and their measurement techniques rise. Another factor is the technical difficulty associated with high temperatures, mainly due to the conflicting requirements between efficient sample heating and accurate measurement as we will see later in this chapter.

## 1.2 Evaluation of Dielectric Measurement Techniques

Dielectric measurements at room and at high temperatures differ in technique rather than in principle; however, the methods for high temperatures are far less developed than those for room temperature [7] partly due to technical difficulties involved in sample heating. The earliest and the most extensive dielectric measurements were primarily carried out at room temperature by von Hippel and his co-workers, though some elevated temperature data up to 500<sup>0</sup>C were also obtained [8]. Since then, progress has been made towards accurate, fast, flexible, automatic tests and the dielectric data obtained have covered a wide



variety of materials and different frequency bands [8-11]. However, only a few papers have been published on the high temperature techniques [84]. Though being subject to certain limitations, it is necessary to review and evaluate previous work which may serve as a starting point for this thesis work.

Brydon et al. [12] used the short-circuit-line method to conduct dielectric measurements at 9375MHz over the temperature range of 20-700<sup>o</sup>C. In this method, a section of silver cylindrical waveguide is heated and the temperature is measured by a thermocouple external to the shorted end of the waveguide. The maximum measurement temperature is limited to 750<sup>o</sup>C due to distortion and melting of the silver guide.

Tinga and Wong [13,14] measured dielectric constants of metal oxides using a rectangular waveguide impedance bridge at 2450MHz. The sample was contained in a quartz holder centered in a section of stainless steel waveguide and was heated by an external electric strip heater. A modified commercial infrared detector was employed to monitor the actual sample surface temperature through a hole in the guide wall. The upper temperature limit of 1000<sup>o</sup>C was set by insufficient heating ability and significant thermal loss.

Rockwell International Science Center [15] has developed two separate facilities for measuring millimeter wave dielectric constant at temperatures up to 1600<sup>o</sup>C. One of them is the free-wave transmission and reflection method. A plate of the sample is placed between a set of transmitter and receiver horns. In such a scheme, only the sample needs to be heated but it must be much larger than the wavelength. Therefore, this scheme is impractical at decimeter wavelengths. The other Rockwell scheme is a cavity perturbation measurement system consisting of a rectangular cavity operating in the TE<sub>107</sub> mode. A very small cylindrical sample (<0.04" diameter by 0.75" length) is inserted into the cavity through holes in the wall and aligned parallel to the maximum electric field. A small tungsten heating coil wound around the sample is used to generate high sample temperatures. Cooling water coils are attached to the cavity body to maintain the cavity wall at or near room temperature. It is also difficult to adapt this method for decimeter waves and yet achieve the same upper temperature limit and good thermal insulation.

We have shown schemes using conventional sample heating suffering from an upper temperature limit. Since the test chamber (a waveguide or

a cavity) is unavoidably heated along with the sample, it is eventually overheated, resulting in an expansion and distortion which severely degrades the accuracy of dielectric determinations. Moreover, the sample temperature in such a scheme is hardly uniform as it takes time to transfer heat from an external heater to the sample via thermal conduction. This thermal inertia also leads to a low heating rate, which in turn increases the heat loss, in particular at a high temperature.

Some investigators have pursued other schemes to avoid overheating the test chamber. Hutcheon et al. [16] have recently developed an ingenious system for studying the temperature dependence of the dielectric constant at 2450MHz. After being heated in a separate furnace, a sample is quickly inserted into a copper cavity. Dielectric tests are made as the sample cools. A computer-controlled network analyzer is employed for rapid testing and data recording. In this cooling curve approach, the cavity's temperature will not be raised significantly. The other advantage is that the sample temperature does not need to be measured, instead, it can be inferred from the cooling curve of the cavity. However, the practical upper temperature is limited to 800°C due to heat loss. Another recent paper [17] reported a technique using an open-ended air-filled coaxial probe to measure mineral samples. The probe is brought in contact with the surface of the sample which is heated by an electric heater, and then the reflection coefficient is measured to determine the dielectric data. The temperature range of 25°C to 325°C cannot be extended easily because the problems of probe-sample contact and probe expansion become more intractable at higher temperatures. Furthermore, the open-ended coaxial line method, by its very nature [18-19], is not accurate for low permittivity and low loss materials.

Significant progress is achieved when microwave energy is used to heat the sample under test. Couderc et al [20] used a cylindrical cavity operating in two different resonant modes, one for measuring and the other for heating. Since the power levels required for heating and testing are different by several orders of magnitude, two microwave sources were employed. Ollivon et al. [21] did use a single generator (6W) for both heating and testing a sample in a rectangular waveguide. Jaw et al. [22] also employed this one-generator method for on-line monitoring of epoxy curing in a cylindrical cavity, but the heating and

dielectric measuring were conducted at a power level of 12-14W and 3-6W respectively. In both cases, the low power generator used for both heating and testing was not sufficient to raise the sample temperature over 200<sup>o</sup>C. It should be noted that all these microwave sample heating techniques use a resonant cavity as a test chamber in which a sample is positioned in the area of maximum E-field so that it can be heated effectively. What should also be mentioned is that the sample volume is very limited because the first-order perturbation method is always used to determine the dielectric properties.

In summary, we can say that the method using conventional sample heating is handicapped by an upper limit to its attainable temperature range. One of the promising solutions is to use microwave energy for sample heating as well as dielectric testing as the selectivity of microwave heating makes it possible to heat the sample only and maintain the test chamber at or near room temperature. Theoretically speaking, a higher practical measurement temperature should be obtainable when using microwave sample heating. Moreover, microwave heating promises a higher heating rate, better temperature uniformity and easier control.

### 1.3 Solution to High Temperature Measurement Problems

Based on the above evaluation, the microwave sample heating scheme is chosen in this thesis. However, as a relatively new technique, this scheme is presently faced with the following difficulties.

(a) The testing signal must be isolated from the heating power because the heating power needs to be higher than the testing signal by several orders of magnitude. The heating capability is very limited if only one microwave source is used for both heating and testing due to the cross-coupling and the conflicting requirements between them.

(b) Though a resonant field was exploited for sample heating by other researchers, sample temperatures obtained were hardly higher than those using conventional heating. This suggests that either a more focused field or a higher power should be chosen. A focused field allows us to use a lower heating power level to achieve a higher sample temperature. However, a standard cavity structure seems to be incapable of providing a sufficiently focused field.

(c) Heating capability is also affected by the detuning and mis-

matching which arise from changing dielectric properties of the sample with temperature. Even if the detuning and mismatching are eliminated, one should not expect that a very low loss sample can be heated easily.

(d) Sample volume or the practical dielectric measurement range has to be restricted due to the use of the first order perturbation formulation, otherwise the accuracy of dielectric determination will decrease quickly. This limitation is common to all cavity perturbation methods. Besides, in microwave power sample heating, the sample volume and the measurement range are also limited by the heating ability mentioned in (b) and (c).

The solutions to these problems are the following:

(a) Two separate microwave sources of different frequencies are utilized, one for testing in the band around 2450MHz; the other for heating at another ISM (Industrial, Scientific and Medical) frequency - 915MHz. Consequently, the testing signal can be easily separated from the heating power by using a high-pass filter. If interested in dielectric properties at 915MHz, one can interchange the testing and the heating source and use a low-pass filter instead.

(b) A coaxial re-entrant structure is selected because it presents an intense E-field in its gap center due to its  $1/r$  dependence. The cavity designed for the test chamber is shown in Figure 1.1. It has a hollow center conductor and a hole in its endplate, so that a sample can be easily loaded into the cavity without disassembling the cavity. Tinga et al. developed this cavity into a microwave applicator and achieved a heating rate up to  $700^{\circ}\text{C/s}$  [23].

(c) An external tuning approach is chosen rather than an internal tuning method. This approach can avoid internal adjustments which will complicate the procedure of dielectric determinations. A controller is to be designed for performing the tuning automatically.

(d) The cavity fields are analyzed in terms of a sample's volume and dielectric properties, commonly referred to as sample loading [24], to construct theoretical calibration curves for determining dielectric constants and loss factors. This can overcome the limitation of perturbation methods and ensure a better accuracy. To analyze the field in the coaxial re-entrant cavity, a numerical method is needed since the analytical solution is not available. In addition, the presence of the sample insertion holes alters the gap fields and thus complicates the

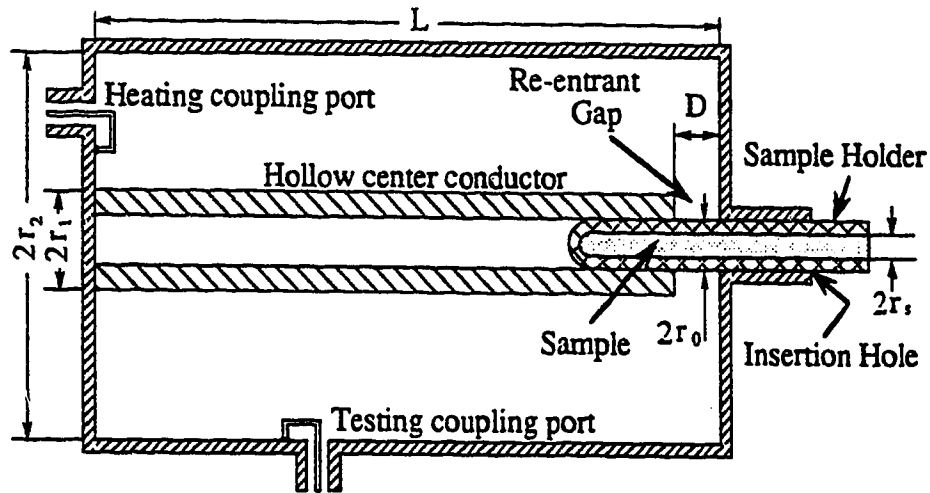


Figure 1.1 Cross section of the coaxial re-entrant cavity designed for the high temperature dielectric measurement.

analysis further, making the numerical approach the only choice.

To sum up, the proposed scheme for high temperature dielectric measurements in this thesis is a cavity method where a modified coaxial re-entrant cavity serves both as a test chamber and as a microwave heater. Microwave sources at different ISM bands – 2450MHz and 915MHz will be used for testing and heating respectively. Dielectric determination is based on the results of a numerical analysis of the loaded cavity, surpassing the limitation of perturbation methods on the sample volume and the measurement range. An external control system will be implemented to tune the heating source dynamically.

#### 1.4 Thesis Content Overview

Chapters in this thesis are arranged almost in accordance with the on-going process of the thesis research. Although the contents of each chapter are closely related, they are organized in such a manner that each chapter stands independently from the others.

In Chapter 2, resonant cavity methods for dielectric determinations are reviewed. Three approaches: experimental calibration, perturbation formula and direct field analysis are inspected and compared. It follows that the direct field analysis is most suitable for this thesis.

Chapter 3 is devoted to the mode-matching formulation for field analysis of a dielectric loaded coaxial re-entrant cavity. The formula-

tion is developed from the simplest to the most complex case in which a sample insertion hole and a sample holder are included. The numerical algorithm and computer program for the computation are then briefly described. The calculation error is also examined. Finally, calculation results and corresponding measurement results are presented and compared with each other, showing the reliability of the formulation and the high accuracy of the numerical results.

Cavity characteristics are covered in Chapter 4. With the aid of the mode-matching program, field distributions, energy depositions, resonant frequencies and Q-factors are calculated and presented in graphical form. The results are discussed with emphasis on the effects of sample loading on the cavity characteristics. The effects of a sample insertion hole and a holder are also closely examined. Most importantly, calibration curves are obtained from the mode-matching analysis and used for determining the dielectric constant and loss factor of a sample from the measured frequency shift and Q-factor change produced by the sample.

The actual measurement and control system and its performance are described in Chapter 5. This system has three channels connected to the cavity for testing, heating and temperature measuring. The cavity design is addressed first. Then, the errors in the frequency shift and Q-factor measured by the testing channel are analyzed. This is followed by a description of apparatus and techniques used for sample heating and temperature measuring. In particular, the techniques involved in automatic tuning and sample temperature controlling are covered. At the end of this chapter, the upper and lower limits of measurable dielectric constant and loss factor are evaluated. This evaluation shows that these limits are mainly determined by heating ability of the heating channel and measurement accuracy of the testing channel.

In Chapter 6, the experimental results are presented. First, calibration curves for dielectric determinations are given in both graphical and polynomial form. Then, the errors in the determined dielectric constant and loss factor are analyzed and their limits are evaluated. The data found for a number of well-characterized samples, measured at room temperature, are then listed together with the published data as a verification of the experimental system. Finally, results for various ceramics and oxides from 300<sup>o</sup>C to 1500<sup>o</sup>C are presented and discussed.

Chapter 7 is the conclusion which completes the thesis.

## CHAPTER 2

### DIELECTRIC DETERMINATION USING RESONANT CAVITY METHOD

A material's complex relative dielectric constant,  $\epsilon_r$ , or dielectric constant,  $\epsilon'_r$ , and loss factor,  $\epsilon''_r$ , can be determined by any measurable effect the material may have on an electromagnetic field since it is the only constitutive parameter present in Maxwell's equations that completely specifies the electric behavior of the material. The dielectric constant of a material determines its ability to store the electric energy, while the loss factor determines its ability to convert the stored energy into heat. In a resonant cavity method, the dielectric constant and the loss factor are obtained from the measured resonant frequency shift,  $\Delta f_0$ , and Q-factor change,  $\Delta(1/Q)$ . Compared with the other methods, this method is narrowband due to the filtering nature of a resonant cavity. However, it is this very nature that makes a resonant cavity method very sensitive even to a sample with a small volume or a low permittivity and loss. In fact, broad band methods often have reduced sensitivity. On the other hand, many engineering applications need only a relatively narrow band or a single frequency. For instance, an industrial or medical application mainly uses the ISM frequencies of 2450 and 915MHz. In such a case, the resonant cavity method, though being narrowband, is sufficient.

As in any dielectric measurement method, a resonant cavity method starts with model developing, in which a relationship is built up between measurable parameters, that is,  $\Delta f_0$  and  $\Delta(1/Q)$ , and  $\epsilon'_r$  and  $\epsilon''_r$ . To do this, one of the three approaches can be chosen: experimental calibration, perturbation formula and direct field analysis. Each approach will be reviewed and discussed in this chapter but the focus will be on the cavity perturbation theory: its approximation, limitation and application in dielectric measurements.

#### 2.1 Experimental Calibration

This is an experimental approach in which a cavity's frequency response is calibrated against some known materials. In calibrating the cavity,  $\Delta f_0$  and  $\Delta(1/Q)$  or transmission attenuation produced by a series of materials with known dielectric values are measured and the obtained

data are used to construct calibration curves by regression or fitting methods. Such a calibration procedure has to be repeated if the cavity or sample geometry changes, therefore, it is time consuming. Even neglecting the experimental errors from sample preparations and measurements, the calibration curves obtained may not be reliable unless the reference values of the calibrating materials are accurate. Unfortunately, this is not always the case since, oftentimes, the dielectric values for the same material from different sources show a large variation.

Nevertheless, this approach is less restricted in the sense that a detailed knowledge of the cavity field is not necessary and a larger sample volume or a more complex sample shape can be used. As a result, it is an effective engineering approach, especially, in dealing with a complex cavity structure. Several authors have adopted this approach in their use of a cylindrical cavity in  $TM_{012}$  mode for measuring food and liquid samples [25-27].

## 2.2 Perturbation Formula

The well-known equation for the shift of complex resonant frequency

$$\Omega = \omega + j\frac{\omega}{2Q} \quad (2.1)$$

produced by the insertion of a non-magnetic sample into a resonant cavity with lossless walls is given by [9,28,29]

$$\frac{\Omega_2 - \Omega_1}{\Omega_2} = \frac{-\int_{V_D} (\epsilon_2 - \epsilon_1) E_1^* \cdot E_2 dv}{\int_{V_C} (\epsilon E_1^* \cdot E_2 + \mu H_1^* \cdot H_2) dv} \quad (2.2)$$

where  $V_C$  and  $V_D$  are the cavity and sample volume, subscript 1 and 2 designate values before and after the sample insertion, and an asterisk denotes the complex conjugate. It should be noted that this equation is not an approximation at all. Thus, calling it a perturbation equation is a misnomer. However, this equation is of little use in practice unless the following simplifications are made.

(1) **Complex frequency shift.** In order to relate Eq. (2.2) to resonant frequency and Q-factor change, the complex frequency shift needs to



be simplified as follows.

$$\begin{aligned}
\Delta\Omega_1/\Omega_2 &= \frac{\Omega_2 - \Omega_1}{\Omega_2} = \frac{\omega_2 - \omega_1 + j\left(\frac{\omega_2}{2Q_2} - \frac{\omega_1}{2Q_1}\right)}{\omega_2(1 + j\frac{1}{2Q_2})} \\
&= \left[\frac{\omega_2 - \omega_1}{\omega_2} + j\left(\frac{1}{2Q_2} - \frac{\omega_1}{\omega_2} \cdot \frac{1}{2Q_1}\right)\right] \cdot \left[1 - j\frac{1}{2Q_2} - \left(\frac{1}{2Q_2}\right)^2 - \dots\right] \\
&\approx \frac{\omega_2 - \omega_1}{\omega_2} + j\left(\frac{1}{2Q_2} - \frac{\omega_1}{\omega_2} \cdot \frac{1}{2Q_1}\right) \tag{2.3}
\end{aligned}$$

for  $1/(2Q_2) \ll 1$ . Furthermore, if the frequency shift,  $|\omega_2 - \omega_1|/\omega_2 \ll 1$ , we have  $\omega_2 \approx \omega_1$  and then

$$\frac{\Omega_2 - \Omega_1}{\Omega_2} \approx \frac{f_2 - f_1}{f_1} + j\left(\frac{1}{2Q_2} - \frac{1}{2Q_1}\right) = \frac{\Delta f_1}{f_1} + j\Delta\left(\frac{1}{2Q_1}\right) \tag{2.4}$$

Thus, Eq. (2.2) becomes

$$\frac{\Delta f_1}{f_1} + j\Delta\left(\frac{1}{2Q_1}\right) \approx \frac{-\int_{V_D} (\epsilon_2 - \epsilon_1) \mathbf{E}_1^* \cdot \mathbf{E}_2 \, dv}{\int_{V_C} (\epsilon \mathbf{E}_1^* \cdot \mathbf{E}_2 + \mu \mathbf{H}_1^* \cdot \mathbf{H}_2) \, dv} \tag{2.5}$$

This equation holds to better than 1% if  $Q_2 > 50$  and  $\Delta f_1/f_1 < 1\%$ .

(2) Denominator. If the energy variation caused by sample insertion can be neglected compared with the total energy in the cavity,  $W_E$ , the denominator of the right side of Eq. (2.5) can be simply reduced to four times the electric energy stored in the cavity before sample insertion, i.e.,

$$\frac{\Delta f_1}{f_1} + j\Delta\left(\frac{1}{2Q_1}\right) \approx \frac{-\int_{V_D} (\epsilon_2 - \epsilon_1) \mathbf{E}_1^* \cdot \mathbf{E}_2 \, dv}{4W_E} \tag{2.6}$$

$$W_E = \frac{1}{2} \int_{V_C} \epsilon_0 |\mathbf{E}_1|^2 \, dv \tag{2.7}$$

It is important to note that this condition is what the name "perturbation" implies. Eq. (2.6) is the so called perturbation formula. It should also be understood that the condition of small energy

perturbation is equivalent to a small  $\Delta\Omega_1/\Omega_2$  or small  $\Delta f_1/f_1$  and  $\Delta(1/Q)$  and  $1/(2Q_2) \ll 1$ . A justifiable perturbation condition can be either a small dielectric sample with a large  $\epsilon_r$  or a large sample with a low  $\epsilon_r$ .

(3) Field  $E_1$  and  $E_2$ . In order to use the perturbation formula of Eq. (2.6) in practice, we must know  $E_1$  and  $E_2$ . There is no difficulty in obtaining  $E_1$  if a standard cavity such as a rectangular or cylindrical cavity is used since the field expressions for such a cavity are given in most text books [30-32]. For a known  $E_1$ ,  $E_2$  can be evaluated approximately by first assuming that the electric field just outside the sample,  $E_{2out}$ , is the same as the known empty cavity value,  $E_1$ ,

$$E_{2out} \approx E_1 \quad (2.8)$$

and then finding the link between  $E_{2out}$  and the field inside the sample,  $E_{2in}$ . If a sample with a proper shape is positioned in a particular location, usually a region with a relatively uniform or maximum electric field, inside the cavity, the relation of  $E_{2in}$  and  $E_{2out}$  can be of the simple form,

$$E_{2in} = gE_{2out} \approx gE_1 \quad (2.9)$$

where  $g$  is the geometry factor. It is actually a function of the sample's dielectric constant and has values from 0 to 1. The form of this function depends on the sample's shape and location. It is usually derived from a static field solution. Following are some examples [9].

A. When a sample is positioned in such a way that the electric field in the cavity is parallel to its surface everywhere,  $g$  is simply unity,

$$g = 1 \quad (2.10)$$

B. If a sample has all of its surface perpendicular to the E-field, again using the boundary condition, one can write,

$$g = 1/\epsilon'_r \quad (2.11)$$

C. When a spherical or an ellipsoidal sample is placed in a uniform E-field region and far from the cavity walls,  $g$  is closely approximated by

$$g = \frac{3}{\epsilon'_r + 2} \quad (2.12)$$

D. If an infinite cylindrical sample is placed perpendicular to a uniform E-field,  $g$  can be expressed by

$$g = \frac{2}{\epsilon'_r + 1} \quad (2.13)$$

We can now simplify the perturbation formula of Eq. (2.6) further by expressing  $E_2$  inside the sample using the function  $g(\epsilon'_r)$ . Substituting the complex form of  $\epsilon_r$  into Eq. (2.6) and separating its real and imaginary part, we have,

$$\frac{\Delta f_1}{f_1} = \frac{F}{4} g(\epsilon'_r) (\epsilon'_r - 1) \quad (2.14)$$

$$\Delta\left(\frac{1}{Q_1}\right) = \frac{F}{2} g(\epsilon'_r) \epsilon''_r \quad (2.15)$$

$$F = \frac{\int_{V_D} |E_1|^2 dv}{\int_{V_C} |E_1|^2 dv} \quad (2.16)$$

where  $F$  is called the generalized filling factor and is defined as the ratio of the stored electric energy in the volume occupied by a sample to that in the whole cavity before the sample is introduced. In the special case of a uniform E-field throughout the cavity,  $F$  turns out to be the sample-to-cavity volume ratio. It is interesting to note that  $\Delta(1/Q_1)$  can be related to  $\Delta f_1$  without knowing the details of  $g$  and  $F$ . Substituting Eq. (2.14) into Eq. (2.15), we can express  $\Delta(1/Q_1)$  in terms of  $\Delta f_1$  as

$$\Delta\left(\frac{1}{Q_1}\right) = - \frac{2\Delta f_1}{(\epsilon'_r - 1)f_1} \cdot \epsilon''_r \quad (2.17)$$

Using this relation, one needs only one calibration curve, i.e.,

$$\epsilon'_r = \epsilon'_r(\Delta f_1) \quad (2.18)$$

for experimental determinations of  $\epsilon''_r$  as well as  $\epsilon'_r$ . However, one should not take this advantage for granted because Eq. (2.17) is valid only when the real-imaginary separation is possible in Eq. (2.6). If the

field integration result of Eq. (2.6) is not a real value, due to either the filling factor or the geometry factor being complex, the separation would be very difficult or even impossible.

If the perturbation condition is satisfied, the error due to the above approximations can be negligible, making the accuracy of the perturbation formulas higher than what one might expect. This condition can be fulfilled whenever the electric energy perturbed by a sample is much less than the total energy stored in the cavity. A small resonant frequency shift and a small Q-factor change are a good indication of a valid perturbation condition. To use the perturbation formula for dielectric determinations, one needs to know the field distribution inside as well as outside the sample. This will impose little difficulty if a standard cavity is chosen and the sample is properly shaped and positioned. However, it is a problem for our coaxial re-entrant cavity, for its electric field is as yet unknown.

### 2.3 Direct Field Analysis

In situations where the cavity field is unknown or a more rigorous treatment is desired for a more accurate dielectric determination, an alternative to the perturbation formula is to directly analyze the cavity field in terms of the sample loading. To illustrate this method, we use the simple example of a  $TM_{010}$  cylindrical cavity loaded with a cylindrical sample along its axis as shown in Figure 2.1. This is also an example of the simplest mode-matching formulation where only one mode and two subareas are involved. The treatment given below mainly follows Horner's [34].

The presence of the sample does not affect the circular symmetry of the electromagnetic field, but modifies the radial distribution. Different field expressions are needed for the interior of the sample (denoted as subarea B) and for the air space between the sample and the cavity cylindrical wall (denoted as subarea A). The field expressions are given for subarea B by

$$\begin{cases} H_{\phi}^B = bJ_1(k_0\sqrt{\epsilon_r}r) \\ E_z^B = \frac{j\omega\mu_0}{k_0\sqrt{\epsilon_r}} \cdot bJ_0(k_0\sqrt{\epsilon_r}r) \end{cases} \quad (2.19)$$

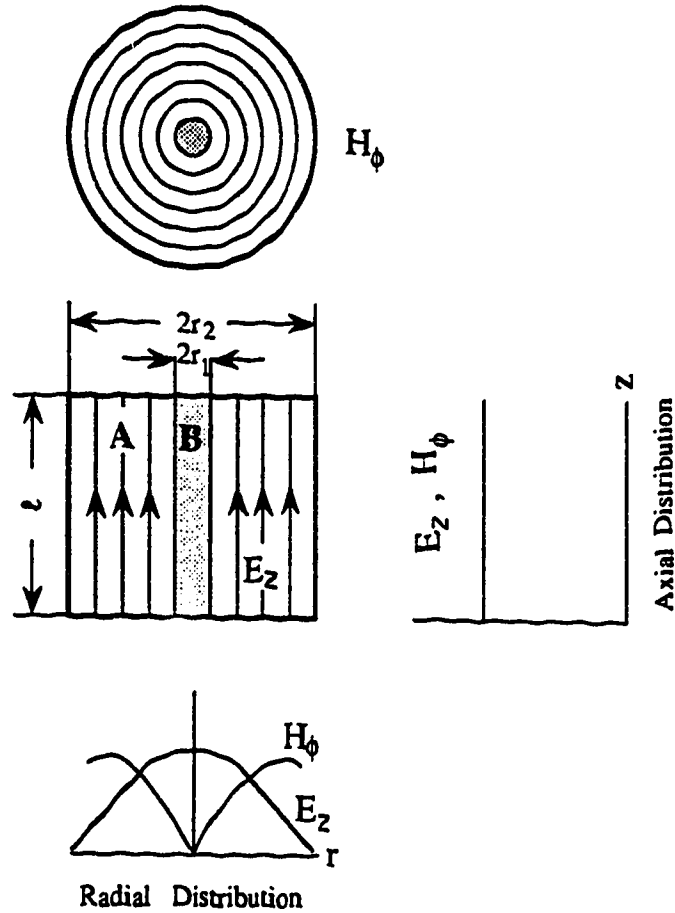


Figure 2.1 A sample loaded cylindrical cavity and its  $TM_{010}$  mode field configuration.

and for subarea A by

$$\begin{cases} H_{\phi}^A = a_1 J_1(k_0 r) + a_2 Y_1(k_0 r) \\ E_z^A = \frac{j\omega\mu_0}{k_0} \cdot [a_1 J_0(k_0 r) + a_2 Y_0(k_0 r)] \end{cases} \quad (2.20)$$

where  $k_0 = 2\pi/\lambda_0$  is the free-space wave number,  $a_1$ ,  $a_2$  and  $b$  are the amplitude constants and  $J_0$ ,  $J_1$  and  $Y_0$ ,  $Y_1$  are the Bessel functions of the first and the second kind. The boundary conditions that must be met are

$$E_z(r=r_2) = 0 \quad (2.21)$$

$$E_2^A(r=r_1) = E_2^B(r=r_1) \quad (2.22)$$

$$H_\phi^A(r=r_1) = H_\phi^B(r=r_1) \quad (2.23)$$

Applying these conditions to Eqs. (2.19) and (2.20), we have

$$a_1 J_0(k_0 r_2) + a_2 Y_0(k_0 r_2) = 0 \quad (2.24)$$

$$\sqrt{\epsilon_r} [a_1 J_0(k_0 r_1) + a_2 Y_0(k_0 r_1)] = b J_0(k_0 \sqrt{\epsilon_r} r_1) \quad (2.25)$$

$$a_1 J_1(k_0 r_1) + a_2 Y_1(k_0 r_1) = b J_1(k_0 \sqrt{\epsilon_r} r_1) \quad (2.26)$$

Eliminating  $a_1$ ,  $a_2$  and  $b$  from these equations leads to a relation which gives the resonant wavelength,  $\lambda_0$  or  $2\pi/k_0$  of the loaded cavity in terms of the dielectric constant and radius of the sample as follows

$$\sqrt{\epsilon_r} = \frac{J_0(k_0 \sqrt{\epsilon_r} r_1)}{J_1(k_0 \sqrt{\epsilon_r} r_1)} \cdot \left[ \frac{Y_0(k_0 r_2)/J_0(k_0 r_2) - Y_1(k_0 r_1)/J_1(k_0 r_1)}{Y_0(k_0 r_2)/J_0(k_0 r_2) - Y_0(k_0 r_1)/J_0(k_0 r_1)} \right] \cdot \frac{J_1(k_0 r_1)}{J_0(k_0 r_1)} \quad (2.27)$$

This transcendental equation can be simplified and can also be reduced to the same result as that from the perturbation formula when the sample radius is very small [34,35].

Eq. (2.27) gives not only the relation of the resonant frequency with the dielectric constant but also that of the Q-factor with the loss factor if  $k_0$  and  $\epsilon_r$  are replaced by their complex values. However, to avoid solving such a complex transcendental equation, the Q-factor is normally expressed directly in terms of the field integration. By definition, the loaded cavity Q-factor is

$$Q_L = \frac{\omega W_E}{P_W + P_D} \quad (2.28)$$

where  $W_E$  is the energy stored in the cavity,

$$W_E = \iiint_V \frac{1}{2} \epsilon_0 |\mathbf{E}|^2 dv \quad (2.29)$$

$P_W$  is the power dissipated on the cavity wall,

$$P_W = \sqrt{\omega \mu_0 / (2\sigma)} \iint_S \frac{1}{2} \epsilon_0 |\mathbf{H}|^2 ds \quad (2.30)$$

and  $P_D$  is the power loss in the sample,

$$P_D = \omega \tan \delta W_D \quad (2.31)$$

$$W_D = \iiint_{V_D} \frac{1}{2} \epsilon_0 |E|^2 dv \quad (2.32)$$

Therefore,  $\tan \delta$  can be expressed by

$$\tan \delta = \frac{W_E}{W_D} \left( \frac{1}{Q_L} - \frac{P_W}{\omega W_E} \right) \quad (2.33)$$

If  $P_W/\omega W_E$  is approximated by its empty cavity value, namely, the inverse of the empty cavity Q-factor,  $1/Q_0$ ,

$$\frac{1}{Q_0} \approx \frac{P_W}{\omega W_E} \quad (2.34)$$

we finally have

$$\tan \delta = \frac{W_E}{W_D} \left( \frac{1}{Q_L} - \frac{1}{Q_0} \right) = \frac{1}{F_l} \Delta(1/Q_0) \quad (2.35)$$

$$F_l = \frac{W_D}{W_E} \quad (2.36)$$

where  $F_l$  is the loading factor which is defined as the ratio of the stored energy in the sample to that in the whole cavity. Recalling the definition of the generalized filling factor,  $F$ , in Eq.(2.16), we can find the relation between  $F_l$  and  $F$  as

$$F_l = \frac{\epsilon_r' \iiint_{V_D} \frac{1}{2} \epsilon_0 |E|^2 dv}{W_E} = \frac{\epsilon_r' g^2 \iiint_{V_D} \frac{1}{2} \epsilon_0 |E_0|^2 dv}{W_E} = \epsilon_r' g^2 F \quad (2.37)$$

We see that a small loading factor means a sample with a small volume or a low  $\epsilon_r'$ , or a sample placed in a weak E-field region or its surface perpendicular to the E-field. When the loading factor becomes very small, we should obtain the identical loss tangent whether from Eq.(2.15) of the perturbation approximation, which is rewritten as

$$\tan\delta = \frac{2}{\epsilon_r' g F} \cdot \Delta(1/Q_0) \quad (2.38)$$

or from Eq.(2.35) of the direct field analysis. Equating Eq.(2.38) with Eq.(2.35) gives

$$g = 1/2 \quad (2.39)$$

which is simply the average value of geometry factors for all possible sample shapes and orientations to the E-field.

This approach of direct field analysis was also called the exact resonance method in [33]. A number of authors adopted this approach in their resonant field analyses of non-standard cavities [33,36-38], or cavities having a modified structure due to, for instance, a sample insertion hole and a sample holder [39-41], or cavities with a less restricted sample, such as a sample with a relatively large radius or a length less than the cavity height [34,42]. For a complex structure, an analytical method such as the method used in the above example may not be feasible; instead, a numerical technique must be chosen. As we will see in the next chapter, a mode-matching technique is chosen for the field analysis of the dielectric loaded coaxial cavity with a hollow center conductor which is to be used for the high temperature dielectric determinations in this thesis.



## CHAPTER 3

### CAVITY ANALYSIS USING MODE-MATCHING METHOD

The focus of this chapter is the formulation of the mode-matching analysis for our dielectric loaded coaxial re-entrant cavity. A sample insertion hole and a sample holder are considered in this formulation. The numerical algorithm and computation program are then briefly described with a look at the calculation error. Eventually, a comparison of the calculation results and the corresponding measurement data is made, reflecting the formulation reliability and the calculation accuracy.

#### 3.1 Mode-Matching Method

Numerical methods are chosen on the basis of trade-offs among accuracy, speed, storage requirement, versatility and so forth. A more important factor is that every method is more or less problem dependent, in particular, structure dependent. The problem of the cavity analysis in this thesis has two peculiarities. First, the structure depicted in Figure 1.1 is circularly symmetrical, hence; its field analysis is reduced to a two-dimensional problem. Moreover, the shape of the structure is quite regular, though several media - the air space, the sample and the sample holder - are involved. Second, the principal parameter to be derived is the resonant frequency; its accuracy is a decisive factor which affects the accuracy of evaluation of the sample's dielectric constant. In addition, the field distribution is also required for calculating the energy deposition or the Q-factor to determine the sample's loss factor.

Some well-known methods, such as the finite difference method (FDM) and the finite element method (FEM), are least analytical [43,44]. The mathematical preprocessing is limited. They can be applied to a wide range of structures. However, they are not the best choice for simple structures because of their numerical inefficiency, program complexity and large memory capacity requirement. In contrast, the mode-matching method is very efficient when the structure can be identified as a junction of two or more regions, each having a set of well-defined field solutions that satisfies all the boundary conditions except those at the junction [44-47]. Unlike discrete results from the FDM or FEM tech-

niques, this method gives the final field solution in a series form, thus avoiding the discretization procedure and requiring little computer storage. This series form result shows directly the mode composition of the fields under analysis and also offers great convenience for integration and differentiation. However, it is mathematically very involved. As a result, a large portion of this chapter is devoted to the formulation of the method. Once the formulation is obtained, the programming is straightforward.

Electromagnetic field analysis through mode-matching involves three steps. In the first step, the unknown fields in the individual regions, or the so called subareas, are expressed in the expansion of their respective normal modes. The functional form of the normal modes is known. For example, the radial function is Bessel and the axial function is sinusoidal and cosinusoidal in a cylindrical region with metallic ends. Thus, the problem is reduced to the determination of modal coefficients associated with the field expansions in each region. The second step is to match the fields of neighboring regions along the common surface by applying the field continuity properties. By virtue of the orthogonality property of the normal modes, this procedure eventually leads to an infinite system of equations. Finally, these equations are solved with numerical approximation techniques such as truncation and iteration. The condition for a non-trivial solution of the equation set gives the resonant frequency if the analyzed structure is a cavity.

Several authors employed the mode-matching method to analyze re-entrant cavities for dielectric measurements. Karpova [36] formulated a single-post cavity loaded with a dielectric which has the same diameter as that of the center conductor. The restricted sample diameter does not allow measurements beyond values of  $\epsilon_r = 30$  because of a large degree of detuning. Milewski [37] analyzed a double-post structure, in which the sample is positioned a distance away from the endplate. Being present in the region of a weaker E-field, the sample produces less detuning, resulting in a wider measurement range [48]. Recently, Kaczkowski and Milewski [38] extended the formulation to allow the sample diameter to be smaller than the center conductor. The lower filling factor of the sample further widens the practical measurement range and samples with  $\epsilon_r$  up to 240 were measured. However, this double-post structure makes sample loading difficult.

The cavity structure under analysis in this thesis is shown in Figure 1.1. It is a single-post structure having a hollow center conductor and a sample insertion hole in the endplate. A cylindrical sample can thus be easily inserted into the cavity and further into the hollow center conductor. To accommodate liquid or powder samples, a sample holder must be used. Such a composite sample insertion hole greatly complicates the analysis. For this reason, the formulation given in the next section will be gradually developed from the initial structure to the final version used in practice.

### 3.2 Mode-Matching Formulations

The emphasis of this section will be on the method and results of mode-matching formulations. The following derivation is intended to be as concise as possible yet showing each step. A consistent system of notation will be used throughout this section. Superscripts A, B, C and D denote the subareas, subscripts n, m and  $\ell$  designate each mode integer and a, b, c and d are the expansion constants, i.e., modal coefficients, of subareas A, B, C and D. The symbols for matrices are underlined upper case letters; matrix elements are expressed by their lower case letters.

#### 3.2.1 Case 1: Gap completely filled with sample

When a sample fills the re-entrant gap completely, the whole cavity is composed of only two subareas A and B as shown in Figure 3.1. This is the simplest and also the best case for illustrating the procedure of mode-matching formulations.

##### A. Step one: Expressing subarea fields

According to the structure symmetry, an infinite number of circularly symmetric normal modes,  $TM_{01}$ , can be assumed for the field expansions in each subarea. Using a generalized notation, the field expansions for subarea X, say, A or B, are expressed by [31]

$$E_z^X = \sum_{i=0}^{\infty} x_i Z_{01}^X (k_1^X r) \cos \beta_1^X (z+z_0^X) \quad (3.1)$$

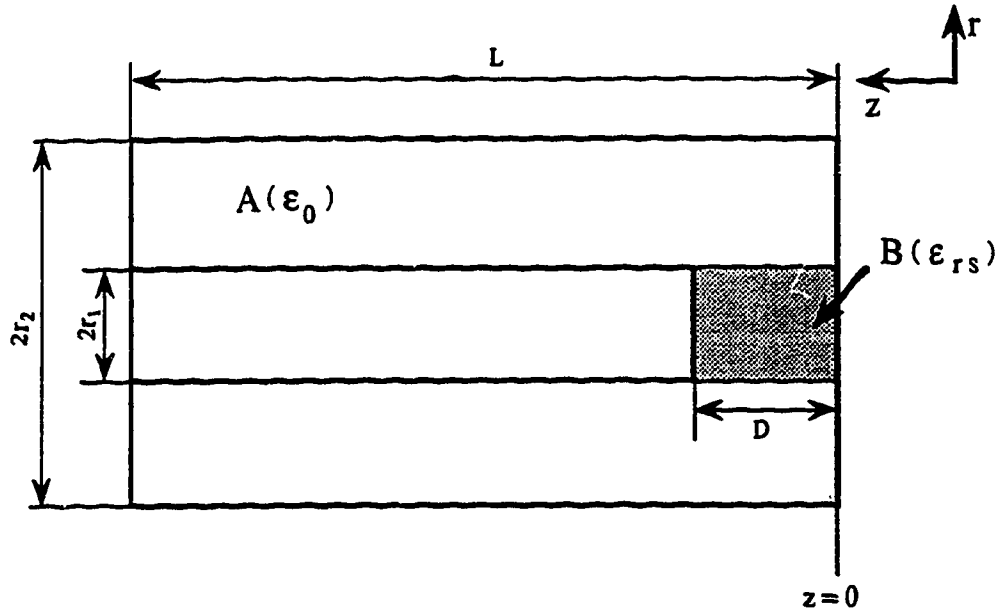


Figure 3.1 Subarea area division for mode-matching formulation of case 1 - gap completely filled with sample.

$$E_r^x = \sum_{i=1}^{\infty} x_i (\beta_1^x / k_1^x) Z_{1i}^x(k_1^x r) \sin \beta_1^x (z + z_0^x) \quad (3.2)$$

$$H_\phi^x = \sum_{i=0}^{\infty} x_i (j\omega \epsilon_0 \epsilon_r^x / k_1^x) Z_{1i}^x(k_1^x r) \cos \beta_1^x (z + z_0^x) \quad (3.3)$$

$$\beta_1^x = i\pi / L^x \quad (3.4)$$

$$(k_1^x)^2 = \epsilon_r^x k_0^2 - (\beta_1^x)^2 \quad (3.5)$$

$$Z_{0i}^x(k_1^x r) = J_0(k_1^x r) - F_1^x \cdot Y_0(k_1^x r) \quad (3.6)$$

$$Z_{1i}^x(k_1^x r) = J_1(k_1^x r) - F_1^x \cdot Y_1(k_1^x r) \quad (3.7)$$

$$k_0 = \frac{2\pi}{\lambda_0} = \frac{2\pi f}{c} = \frac{\omega}{c} \quad (3.8)$$

where:

$z_0^x$  = distance between the coordinate origin and the right boundary;

$\beta_1^x, k_1^x$  = axial and radial wave number;

$k_0$  = free space wave number;

$f_0, \lambda_0$  = resonant frequency and wavelength;

$\epsilon_r^x$  = relative dielectric constant of the medium;

$Z_0^x, Z_1^x$  = a combination of the first and the second kind Bessel functions, referred to as combinational Bessel function in this thesis;

$F_1^x$  = constant associated with the combinational Bessel function;

$J_0, J_1$  = first and second order Bessel function of the first kind;

$Y_0, Y_1$  = first and second order Bessel function of the second kind.

Referring to Figure 3.1, we can write for subarea A

$$i = n \quad (3.9)$$

$$x_1 = a_n \quad (3.10)$$

$$z_0^x = 0 \quad (3.11)$$

$$L^x = L \quad (3.12)$$

$$\epsilon_r^x = \epsilon_r^A = 1 \quad (3.13)$$

$$F_1^x = F_n^A = J_0(k_n^A r_2) / Y_0(k_n^A r_2) \quad (3.14)$$

and for subarea B

$$i = m \quad (3.15)$$

$$x_1 = b_m \quad (3.16)$$

$$z_0^x = 0 \quad (3.17)$$

$$L^x = D \quad (3.18)$$

$$\epsilon_r^x = \epsilon_r^B = \epsilon_{rs} \quad (3.19)$$

$$F_1^x = F_m^B = 0 \quad (3.20)$$

The following explanations may be necessary for understanding the above expressions.

(1) No approximation is made in these expressions except that the cavity walls are assumed to be perfect conductors.

(2) The field expansions are also valid for a complex dielectric constant. To avoid the calculation of a complex resonant frequency, however, a real value is used.

(3) In subarea A,  $r$  does not vanish so that the Bessel functions of the second kind cannot be excluded from the solutions as in subarea B. As a result, the combinational Bessel functions are used.

(4) When  $L/n < \lambda_0/2$  and  $D/m < \lambda_0/(2\sqrt{\epsilon_{rs}})$ ,  $k_n^A$  and  $k_m^B$  become imaginary values and the Bessel functions are reduced to the following modified ones [49]:

$$J_0(jx) = I_0(x) \quad (3.21)$$

$$Y_0(jx) = K_0(x) \quad (3.22)$$

$$J_1(jx) = jI_1(x) \quad (3.23)$$

$$Y_1(jx) = -jK_1(x) \quad (3.24)$$

These imaginary radial wave numbers imply that the corresponding TM modes become cut-off. For instance, If  $\lambda_0=10$ ,  $L=20$  and  $D=1\text{cm}$ , the TM modes are below the cut-off in subarea A for  $n>4$  and in subarea B for all non-zero  $m$  until  $\epsilon_{rs} > 25$ .

(5) It seems that the TEM term should be included in the field expansions for subarea A. Strictly speaking, however, the TEM mode does not exist as long as the gap exists. However, we expect that the cavity fields will be close to those of the TEM mode in the region far away from the gap.

(6)  $E_r$  has already disappeared on the circular surfaces of  $z=0$ ,  $D$  and  $L$  because of using  $\{\sin\beta z\}$  as the axial mode functions.  $E_z$  has also been made zero on the cylindrical surface of  $r=r_2$  by the selection of  $F_n^A$  in Eq.(3.14). The remaining boundary conditions to be satisfied are those at  $r=r_1$ .

## B. Step two: Matching the fields between two subareas

The tangential components  $E_z$  and  $H_\phi$  must be continuous at  $r=r_1$ , that is,

$$E_z^A(r=r_1) = \begin{cases} E_z^B(r=r_1) & 0 \leq z < D \\ 0 & D \leq z \leq L \end{cases} \quad (3.25)$$

$$H_\phi^A(r=r_1) = H_\phi^B(r=r_1) \quad 0 \leq z \leq D \quad (3.26)$$

Substituting the field expressions of Eqs.(3.1)-(3.20) into Eqs. (3.25) and (3.26), we have

$$\sum_{n=0}^{\infty} a'_n \cos\left(\frac{n\pi z}{L}\right) = \begin{cases} \sum_{m=0}^{\infty} b'_m \cos\left(\frac{m\pi z}{D}\right) & 0 \leq z < D \\ 0 & D \leq z \leq L \end{cases} \quad (3.27)$$

$$\sum_{n=0}^{\infty} a'_n R_n^A \cos\left(\frac{n\pi z}{L}\right) = \sum_{m=0}^{\infty} b'_m R_m^B \cos\left(\frac{m\pi z}{D}\right) \quad 0 \leq z \leq D \quad (3.28)$$

where  $a'_n = a_n Z_{0n}^A(k_n^A r_1)$  (3.29)

$$b'_m = b_m Z_{0m}^B(k_m^B r_1) \quad (3.30)$$

$$R_n^A = (\epsilon_r^A / k_n^A) \cdot Z_{1n}^A(k_n^A r_1) / Z_{0n}^A(k_n^A r_1) \quad (3.31)$$

$$R_m^B = (\epsilon_r^B / k_m^B) \cdot Z_{1m}^B(k_m^B r_1) / Z_{0m}^B(k_m^B r_1) \quad (3.32)$$

In order to obtain the relation between  $a_n$  and  $b_m$ , one has to get rid of the variable  $z$  from Eqs.(3.27) and (3.28). To do this, let us first recall the Fourier expansion [50].

A function  $f(x)$ , which is continuous over an interval of  $[0, T]$  can be expanded into a series of  $\{\cos(i\pi x/T)\}$  as

$$f(x) = \sum_{i=0}^{\infty} \xi_i \cos\frac{i\pi x}{T} \quad 0 \leq x \leq T \quad (3.33)$$

where  $\xi_i$  ( $i=0, 1, \dots, \infty$ ) is the Fourier coefficient which is given by

$$\xi_i = \frac{\alpha_i}{T} \cdot \int_0^T f(x) \cdot \cos\frac{i\pi x}{T} \cdot dx \quad (3.34)$$

$$\alpha_i = \begin{cases} 1 & i = 0 \\ 2 & i \neq 0 \end{cases} \quad (3.35)$$

Therefore, considering the left side of Eq.(3.27) as the Fourier expansion

sion of the right side over  $[0, L]$ , we can readily express the Fourier coefficient,  $a'_n$ , as

$$\begin{aligned}
 a'_n &= \frac{\alpha_n}{L} \int_0^D \left( \sum_{m=0}^{\infty} b'_m \cos \frac{m\pi z}{D} \right) \cdot \cos \frac{n\pi z}{L} \cdot dz \\
 &= \frac{D}{L} \alpha_n \cdot \sum_{m=0}^{\infty} b'_m \cdot \left( \frac{1}{D} \int_0^D \cos \frac{m\pi z}{D} \cdot \cos \frac{n\pi z}{L} \cdot dz \right) \\
 &= \frac{D}{L} \alpha_n \cdot \sum_{m=0}^{\infty} b'_m \cdot e_{mn} \left( \frac{D}{L}, 0 \right) \quad (n=0, 1, \dots, \infty) \quad (3.36)
 \end{aligned}$$

where the calculation of  $e_{mn}$  in Appendix 1 results in

$$e_{mn}(a, 0) = \frac{(an)^2}{(an)^2 - m^2} \cdot (-1)^m \cdot \frac{\sin(an\pi)}{an\pi} \quad (3.37)$$

Similarly, treating the right side of Eq.(3.28) as the Fourier expansion of the left over  $[0, D]$ , we can also write

$$\begin{aligned}
 b'_m R_m^B &= \frac{\alpha_m}{D} \int_0^D \left( \sum_{n=0}^{\infty} a'_n R_n^A \cos \frac{n\pi z}{L} \right) \cdot \cos \frac{m\pi z}{D} \cdot dz \\
 &= \alpha_m \cdot \sum_{n=0}^{\infty} R_n^A a'_n \cdot e_{mn} \left( \frac{D}{L}, 0 \right) \quad (m=0, 1, \dots, \infty) \quad (3.38)
 \end{aligned}$$

If the modes with  $n \geq N$  and  $m \geq M$  are truncated, Eqs.(3.36) and (3.38) become a finite linear equation system. Using matrix notation and recalling Eqs.(3.29)-(3.32), we rewrite Eqs.(3.36) and (3.38) as

$$\underline{A} = \underline{P} \cdot \underline{B} \quad (3.39)$$

$$\underline{B} = \underline{Q} \cdot \underline{A} \quad (3.40)$$

where  $\underline{A} = (a_0, a_1, \dots, a_{N-1})^T$  (3.41)

$$\underline{B} = (b_0, b_1, \dots, b_{M-1})^T \quad (3.42)$$

$$\underline{P} = [p_{nm}]_{N \times M} \quad (3.43)$$

$$\underline{Q} = [q_{mn}]_{M \times N} \quad (3.44)$$

$$p_{nm} = \frac{D}{L} \cdot \alpha_n \cdot \frac{Z_{0m}^B(k_n^B r_1)}{Z_{0n}^A(k_n^A r_1)} \cdot e_{mn} \left( \frac{D}{L}, 0 \right) \quad (3.45)$$



$$q_{mn} = \alpha_m \cdot \frac{\epsilon_r^A k_n^B Z_{1n}^A(k_n^A r_1)}{\epsilon_r^B k_n^A Z_{1m}^B(k_n^B r_1)} \cdot e_{mn} \left( \frac{D}{L}, 0 \right) \quad (3.46)$$

for  $n = 0, 1, \dots, N-1$  and  $m = 0, 1, \dots, M-1$ . The superscript T denotes matrix transposition. It should be noted that  $\epsilon_r^A = 1$  and  $Z_{0m}^B = J_0$  and  $Z_{1m}^B = J_1$  since  $F_m^B = 0$  in this case.

### C. Step 3: Solving system equations

Having derived the system equations of (3.39) and (3.40), we can now solve them for the resonant frequencies and modal coefficients. Replacing  $\underline{A}$  in Eq. (3.40) by Eq. (3.39), we obtain a homogeneous equation,

$$\underline{G} \cdot \underline{B} = \underline{0} \quad (3.47)$$

$$\text{where } \underline{G} = [g_{ij}]_{M \times M} = \underline{Q} \cdot \underline{P} - \underline{I} \quad (3.48)$$

and  $\underline{I}$  and  $\underline{0}$  are the unity matrix and the zero vector.

$$\text{Then, } g_{ij} = \sum_{n=0}^{N-1} q_{in} p_{nj} - \delta_{ij}$$

$$= \frac{D}{L} \alpha_i \cdot \frac{\epsilon_r^A k_i^B Z_{0j}^B(k_j^B r_1)}{\epsilon_r^B Z_{1i}^B(k_i^B r_1)} \cdot \sum_{n=0}^{N-1} \frac{\alpha_n Z_{1n}^A(k_n^A r_1)}{k_n^A Z_{0n}^A(k_n^A r_1)} \cdot e_{in} \left( \frac{D}{L}, 0 \right) \cdot e_{jn} \left( \frac{D}{L}, 0 \right) - \delta_{ij} \quad (3.49)$$

$$\delta_{ij} = \begin{cases} 1 & i=j \\ 0 & i \neq j \end{cases} \quad (3.50)$$

One should be aware that all elements of  $\underline{G}$ ,  $g_{ij}$ , are functions of the cavity dimensions,  $r_1$ ,  $r_2$ ,  $L$  and  $D$ , the sample's dielectric constant,  $\epsilon_r$ , and the resonant wavelength,  $\lambda_0$ . To avoid a trivial solution of the homogeneous equation set of (3.47), the determinant of  $\underline{G}$  must be zero, i.e.,

$$\det|\underline{G}| = 0 \quad (3.51)$$

This equation has multiple solutions, thus resulting in a series of resonant wavelengths for a given cavity and sample.

There is a field distribution corresponding to each resonant wavelength. For a given resonant wavelength, cavity dimensions and sample, all elements of  $\underline{G}$  and  $\underline{P}$  become known values. Since only the relative field magnitude is of interest, we can let one of the modal coefficients  $a_n$  or  $b_m$  say  $b_0$ , be equal to unity. Substituting

$$b_0 = 1 \quad (3.52)$$

into Eq. (3.47), we can find  $b_1, b_2, \dots, b_{M-1}$  with no difficulty, from which  $a_0, a_1, \dots, a_{N-1}$  can be calculated immediately by Eq. (3.39).

### 3.2.2 Case 2: Gap partially filled with sample

When the radius of a sample is smaller than that of the center conductor, an extra subarea needs to be added to account for the radius difference as shown in Figure 3.2. The field expansions for subarea A remain unchanged. The expansions for subarea B are almost the same as those in case 1 except that

$$F_m^B \neq 0 \quad (3.53)$$

$$\epsilon_r^B = 1 \quad (3.54)$$

The expansions for subarea C can be readily obtained by assigning the following parameters to Eqs. (3.1)-(3.7).

$$i = m \quad (3.55)$$

$$x_1 = c_m \quad (3.56)$$

$$z_0^X = 0 \quad (3.57)$$

$$L^X = D \quad (3.58)$$

$$\epsilon_r^X = \epsilon_r^C = \epsilon_{rs} \quad (3.59)$$

$$F_1^X = F_m^C = 0 \quad (3.60)$$

The procedure of mode-matching at  $r=r_1$  is the same as that employed in case 1. The results thereof, Eqs. (3.39)-(3.50), are applicable here except that  $F_m^B \neq 0$ . In fact, the  $F_m^B$  have to be determined from the mode-matching between subarea B and C.

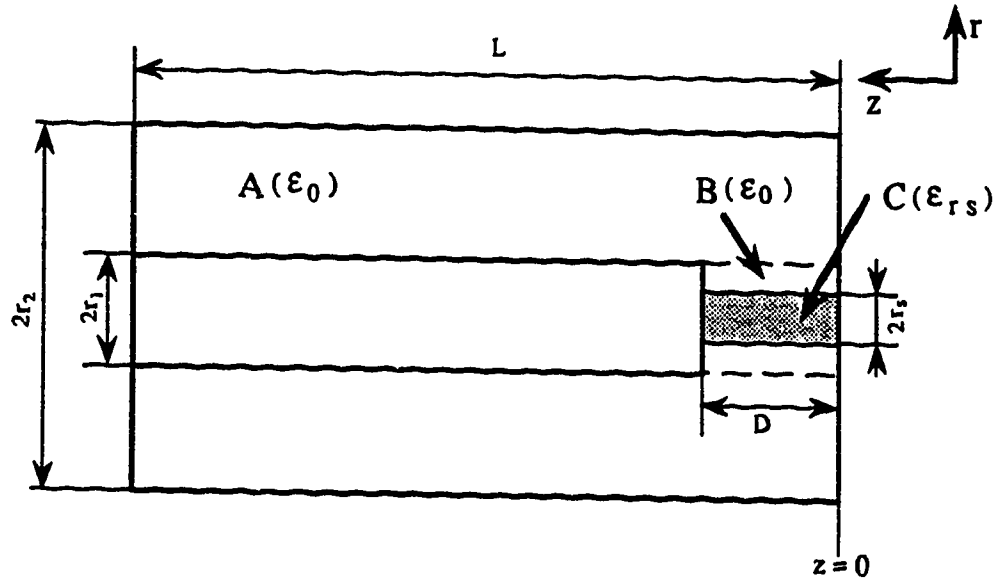


Figure 3.2 Subarea area division for mode-matching formulation of case 2 - gap partially filled with sample.

Applying the continuity property of  $E_z$  and  $H_\phi$  at  $r=r_s$ , one can write

$$E_z^B(r=r_s) = E_z^C(r=r_s) \quad 0 \leq z \leq D \quad (3.61)$$

$$H_\phi^B(r=r_s) = H_\phi^C(r=r_s) \quad 0 \leq z \leq D \quad (3.62)$$

Substituting the field expressions for subarea B and C, the above boundary conditions become

$$\sum_{m=0}^{\infty} b Z_{0m}^B(k_r^B) \cos \beta_m^B z = \sum_{m=0}^{\infty} c J_{0m}^C(k_r^C) \cos \beta_m^C z \quad (3.63)$$

$$\sum_{m=0}^{\infty} b (\epsilon_r^B / k_m^B) Z_{1m}^B(k_r^B) \cos \beta_m^B z = \sum_{m=0}^{\infty} c (\epsilon_r^C / k_m^C) J_{1m}^C(k_r^C) \cos \beta_m^C z \quad (3.64)$$

Examining the above equations and noting that  $\beta_m^C = \beta_m^B$  and  $\cos \beta_m^C z = \cos \beta_m^B z$ , it is clear that we require

$$b Z_{0m}^B(k_r^B) = c J_{0m}^C(k_r^C) \quad (3.65)$$

$$b_m (\epsilon_r^B/k_m^B) Z_{1m}^B(k_m^B r_s) = c_m (\epsilon_r^C/k_m^C) J_1(k_m^C r_s) \quad (3.66)$$

From Eqs. (3.65) and (3.66), we can relate  $c_m$  and  $b_m$  by

$$c_m = \frac{Z_{0m}^B(k_m^B r_s)}{J_0(k_m^C r_s)} b_m \quad (3.67)$$

and derive  $F_m^B$  as

$$F_m^B = \frac{\epsilon_r^B k_m^C J_0(k_m^C r_s) J_1(k_m^B r_s) - \epsilon_r^C k_m^B J_1(k_m^C r_s) J_0(k_m^B r_s)}{\epsilon_r^B k_m^C J_0(k_m^C r_s) Y_1(k_m^B r_s) - \epsilon_r^C k_m^B J_1(k_m^C r_s) Y_0(k_m^B r_s)} \quad (3.68)$$

It should be realized that we have the convenience of deriving  $c_m$  and  $F_m^B$  directly without using the Fourier expansion because subarea B and C share the same metallic boundary at  $z=0$ , D. Otherwise, the derivation would be substantially different as we will see in the case having sample insertion holes.

### 3.2.3 Case 3: Arbitrary gap position

In Figure 3.3, the gap, which contains a sample with  $r_s \leq r_1$ , is located at an arbitrary position between the two endplates of the cavity. Compared with case 2, the only difference in the field expansion is that

$$z_0^A = L_2 \quad (3.69)$$

Consequently, in matching the fields of subarea A with B, we should change Eqs. (3.27) and (3.28) to

$$\sum_{n=0}^{\infty} a_n Z_n^A(k_n^A r_1) \cos \frac{n\pi}{L}(z+L_2) = \begin{cases} \sum_{m=0}^{\infty} b_m Z_m^B(k_m^B r_1) \cos \frac{m\pi}{D} z & 0 < z < D \\ 0 & -L_2 \leq z \leq 0 \text{ and } D \leq z \leq L_1 \end{cases} \quad (3.70)$$

$$\sum_{n=0}^{\infty} a_n (\epsilon_r^A/k_n^A) Z_n^A(k_n^A r_1) \cos \frac{n\pi}{L}(z+L_2) = \sum_{m=0}^{\infty} b_m (\epsilon_r^B/k_m^B) Z_m^B(k_m^B r_1) \cos \frac{m\pi}{D} z \quad 0 < z < D \quad (3.71)$$

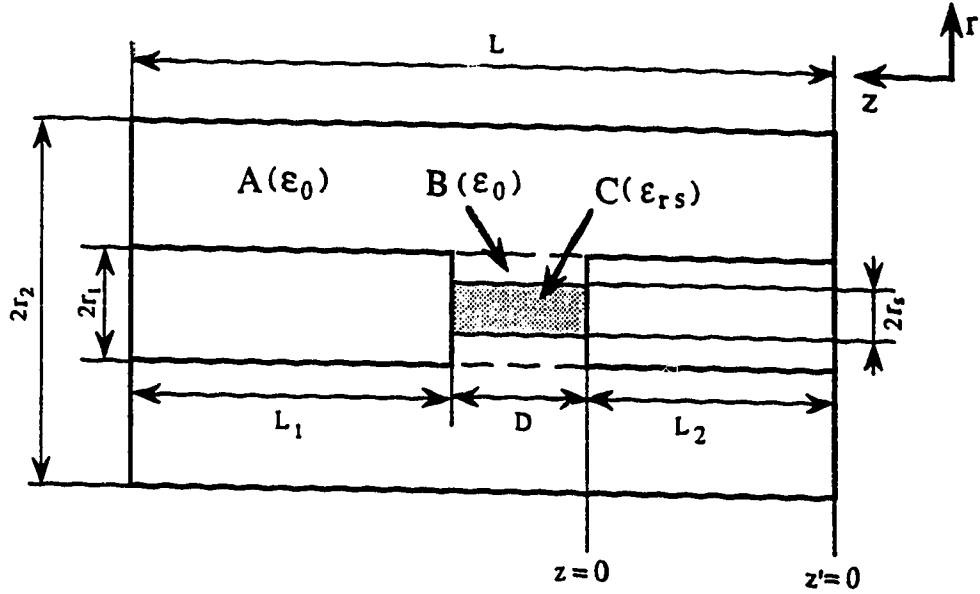


Figure 3.3 Subarea area division for mode-matching formulation of case 3 - arbitrary gap position.

Defining  $z' = z + L_2$  and again using Eqs. (3.29) and (3.30), we can rewrite Eq. (3.70) as

$$\sum_{n=0}^{\infty} a'_n \cos \frac{n\pi}{L} z' = \begin{cases} \sum_{m=0}^{\infty} b'_m \cos \frac{m\pi}{D} (z' - L_2) & L_2 < z' < D + L_2 \\ 0 & 0 \leq z' \leq L_2 \text{ and } D + L_2 \leq z' \leq L \end{cases} \quad (3.72)$$

Using the Fourier expansion procedure as before, we can also derive  $a'_n$  as follows:

$$\begin{aligned} a'_n &= \frac{D}{L} \alpha_n \cdot \sum_{m=0}^{\infty} b'_m \cdot \left[ \frac{1}{D} \int_{L_2}^{D+L_2} \cos \frac{m\pi}{D} (z' - L_2) \cos \frac{n\pi}{L} z' dz' \right] \\ &= \frac{D}{L} \alpha_n \cdot \sum_{m=0}^{\infty} b'_m \cdot \left[ \frac{1}{D} \int_0^D \cos \frac{m\pi}{D} z \cos \frac{n\pi}{L} (z + L_2) dz \right] \\ &= \frac{D}{L} \alpha_n \cdot \sum_{m=0}^{\infty} b'_m \cdot e_{mn} (D/L, L_2/L) \end{aligned} \quad (3.73)$$

Thus, Eq. (3.70) can be rewritten in matrix form as

$$\underline{A} = \underline{P} \cdot \underline{B} \quad (3.74)$$

$$\text{with } p_{nm} = \frac{D}{L} \cdot \alpha_n \cdot \frac{Z_{0m}^B(k_{r1}^B)}{Z_{0n}^A(k_{r1}^A)} \cdot e_{mn}(D/L, L_2/L) \quad (3.75)$$

where

$$e_{mn}(a, b) = \frac{(an)^2}{(an)^2 - m^2} \cdot \left[ \frac{(-1)^m \sin(a+b)n\pi}{an\pi} - \frac{\sin bn\pi}{an\pi} \right] \quad (3.76)$$

as shown in Appendix 1. Likewise, from Eq. (3.71), we acquire

$$\underline{B} = \underline{Q} \cdot \underline{A} \quad (3.77)$$

$$\text{with } q_{mn} = \alpha_m \cdot \frac{\epsilon_r^A k_{rn}^B Z_{0n}^A(k_{r1}^A)}{\epsilon_r^B k_{rn}^A Z_{0m}^B(k_{r1}^B)} \cdot e_{mn}(D/L, L_2/L) \quad (3.78)$$

Finally, we obtain the elements of matrix  $\underline{G}$  as

$$g_{ij} = \sum_{n=0}^{N-1} q_{1n} p_{nj} - \delta_{ij} \\ = \frac{D}{L} \alpha_1 \cdot \frac{\epsilon_r^A k_{r1}^B Z_{0j}^B(k_{r1}^B)}{\epsilon_r^B Z_{11}^B(k_{r1}^B)} \cdot \frac{\sum_{n=0}^{N-1} \alpha_n Z_{1n}^A(k_{r1}^A)}{k_n^A Z_{0n}^A(k_{r1}^A)} \cdot e_{1n}(D/L, L_2/L) e_{jn}(D/L, L_2/L) - \delta_{ij} \quad (3.79)$$

When  $L_2 = 0$ , Eqs. (3.75) and (3.79) reduce to Eqs. (3.45) and (3.49).

It should be mentioned that if the gap is at the midplane of the cavity, i.e.,

$$L_2 = (L-D)/2 \quad (3.80)$$

$e_{mn}$  will vanish unless  $m$  and  $n$  have the same parity, as proved in Appendix 1. This is understandable because the structure symmetry cannot support odd modes in the gap if even modes are established in the coaxial section and vice versa.

### 3.2.4 Case 4: Gap with sample insertion holes

The sample insertion holes in the coaxial re-entrant cavity are provided by the hole in the center conductor and the endplate hole formed by a metallic support tube (Figure 1.1). Using the insertion

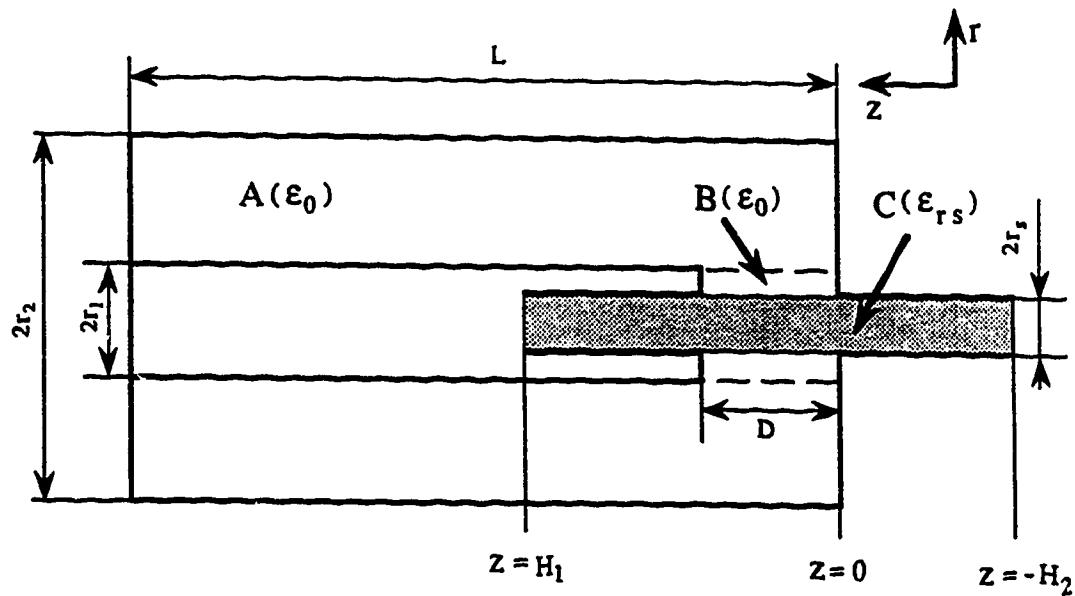


Figure 3.4 Subarea area division for mode-matching formulation of case 4 - gap with sample insertion holes.

hole, a sample can be easily introduced into the cavity without opening it each time, thus ensuring testing repeatability. In addition, the sample inserted through such holes avoids such air gaps that would exist at its ends otherwise. It has been reported that the air gaps may cause significant errors in the dielectric measurement [38]. Furthermore, the insertion holes provide a concentric alignment for a sample in the cavity.

The holes in the center conductor and the endplate are designed to be so small compared with the wavelength that only evanescent modes exist even when an inserted sample has a relatively high permittivity. Therefore, the fields will be strongly attenuated inside the holes, and so the geometrical discontinuities at the sample ends will be invisible to the cavity fields. If we assume that the fields vanish at the points, say,  $z=H_1$  and  $z=-H_2$  as shown in Figure 3.4, a metallic wall can be erected there to simplify the formulation.

In Figure 3.4, subareas A and B are the same as case 2, but subarea C is different since it now includes not only the gap region but also the hole region. This difference makes the mode matching between subarea B and C much more complicated.

All the expressions for the fields in subareas A, B and C in case 2

are valid for this case except that the following parameter changes are made for subarea C.

$$i = \ell \quad (3.81)$$

$$z_0^X = z_0^C = H_2 \quad (3.82)$$

$$L^X = L^C = H = H_1 + H_2 \quad (3.83)$$

where H is the length of subarea C which can be called the effective length of the sample. Note that the symbol for the mode integer in subarea C is changed from m to  $\ell$  to avoid confusion as the axial wave number in subarea C is no longer the same as in B.

To match the fields between subarea C and B as in the last case (Eqs. (3.70) and (3.71)), one can write the continuity conditions at  $r=r_s$  as

$$\sum_{\ell=0}^{\infty} c_{\ell} Z_{\ell}^C(k_{\ell}^C r_s) \cos \frac{\ell \pi}{H} (z + H_2) = \begin{cases} \sum_{m=0}^{\infty} b_m Z_m^B(k_m^B r_s) \cos \frac{m \pi}{D} z & 0 < z < D \\ 0 & -H_2 \leq z \leq 0 \text{ and } D \leq z \leq H_1 \end{cases} \quad (3.84)$$

$$\sum_{\ell=0}^{\infty} c_{\ell} (\epsilon_r^C / k_{\ell}^C) Z_{\ell}^C(k_{\ell}^C r_s) \cos \frac{\ell \pi}{H} (z + H_2) = \sum_{m=0}^{\infty} b_m (\epsilon_r^B / k_m^B) Z_m^B(k_m^B r_s) \cos \frac{m \pi}{D} z \quad (3.85)$$

$0 \leq z \leq D$

As seen in previous cases, these field-matching equations will eventually lead to the relations between  $c_{\ell}$  and  $b_m$  which are expressed in matrix form as

$$\underline{C} = \underline{U} \cdot \underline{B} \quad (3.86)$$

$$\underline{B} = \underline{V} \cdot \underline{C} \quad (3.87)$$

One can find the elements of  $\underline{U}$  and  $\underline{V}$  without lengthy calculations if one recognizes the similarity between the boundary conditions on the common surface of subarea C and B in this case and the conditions of subarea A and B in case 3. As a matter of fact, Eqs. (3.70) and (3.71) will turn out to be the same as Eqs. (3.84) and (3.85) if the parameters of subarea A in case 3 are substituted by those of subarea C in the present case,



and  $r_1$ ,  $L_1$ ,  $L_2$  and  $L$  by  $r_s$ ,  $H_1$ ,  $H_2$  and  $H$ . Making these substitutions in Eqs. (3.75) and (3.78), one can easily obtain  $u_{\ell m}$  and  $v_{m\ell}$  as

$$u_{\ell m} = \frac{D}{H} \alpha_\ell \cdot \frac{Z_{0m}^B(k_{ms}^B)}{Z_{0\ell}^C(k_{\ell s}^C)} \cdot e_{m\ell}(D/H, H_2/H) \quad (3.88)$$

$$v_{m\ell} = \alpha_m \cdot \frac{\epsilon_r^C k_{m1\ell}^B Z_{\ell s}^C(k_{\ell s}^C)}{\epsilon_r^B k_{\ell 1m}^C Z_{ms}^B(k_{ms}^B)} \cdot e_{m\ell}(D/H, H_2/H) \quad (3.89)$$

where  $m=0, 1, \dots, M-1$  and  $\ell=0, 1, \dots, L-1$ .  $L$  is the number of the modes in subarea C considered in practical calculations and it should not be confused with the cavity length. As before, replacing  $\underline{C}$  in Eq. (3.87) by Eq. (3.86) results in

$$\underline{I} \cdot \underline{B} = \underline{0} \quad (3.90)$$

where  $\underline{I} = [t_{ij}]_{M \times M} = \underline{V} \cdot \underline{U} - \underline{I}$  (3.91)

Then,  $t_{ij} = \sum_{\ell=0}^{L-1} v_{i\ell} u_{\ell j} - \delta_{ij}$

$$= \frac{D}{H} \alpha_i \cdot \frac{\epsilon_r^C k_{i1}^B Z_{0j}^B(k_{js}^B)}{\epsilon_r^B Z_{i1}^B(k_{is}^B)} \cdot \frac{\sum_{\ell=0}^{L-1} \alpha_\ell Z_{1\ell}^C(k_{\ell s}^C)}{k_{\ell 0\ell}^C Z_{0\ell}^C(k_{\ell s}^C)} \cdot e_{i\ell}(D/H, H_2/H) e_{j\ell}(D/H, H_2/H) - \delta_{ij}$$

$i, j=0, 1, \dots, M-1$  (3.92)

To this point,  $F_m^B$ , the constant of the combinational Bessel function in subarea B, is still unknown. Unlike case 2, subarea B and C in this case do not share the same axial modal function. As a result,  $F_m^B$  cannot be calculated directly but can be found along with the resonant wavelength,  $\lambda_0$ , by solving simultaneously Eq. (3.90) and

$$\underline{G} \cdot \underline{B} = \underline{0} \quad (3.93)$$

Note that Eq. (3.90) and Eq. (3.93) result from matching the fields of subarea C with B and A with B respectively. To calculate  $F_m^B$  ( $m=0, 1, \dots, M-1$ ) and  $\lambda_0$ , we need  $(M+1)$  equations. Firstly, the  $b_1, b_2, \dots, b_{M-1}$  acquired from Eq. (3.90) should be identical to those from Eq. (3.93).

i.e.,

$$(b_m)_C = (b_m)_T \quad (m = 1, 2, \dots, M-1) \quad (3.94)$$

Secondly, to avoid a trivial solution from Eqs.(3.90) and (3.93), it is required that

$$\det(\underline{G}) = 0 \quad (3.95)$$

and  $\det(\underline{T}) = 0 \quad (3.96)$

Thus, we have just (M+1) equations required to search for  $F_m^B$  and  $\lambda_0$ . It should be noted that all these equations are nonlinear. The numerical algorithm for their solution will be discussed later in this chapter.

### 3.2.4 Case 5: Sample with holder

It is clear that a sample holder is needed when a liquid or powder sample is to be tested. Even for a solid sample, using a non-metallic sample holder is advantageous for thermal insulation since it slows down the thermal conduction between the hot sample and the cool cavity walls. This insulation effect reaches a maximum if a sample is suspended in the gap. In fact, the suspended sample scheme can also be visualized as a holder for which  $\epsilon_{rh} = 1$ . It will also be shown in Chapter 6 that the sample holder made from a low permittivity material can reduce the air gap error.

Adding a sample holder does not present much complexity to the formulation though one more subarea needs to be added. As shown in Figure 3.5, subarea C which denotes the holder has the same length as the subarea D, i.e. the sample; therefore, the field expansions for these two subareas will have the same axial modal functions. It presents no more difficulties to match their fields than to the fields of subarea B and C in case 2.

Subarea A and B still have the same field expansions as before. The field expansions for subarea D can be obtained simply by changing superscript C and  $c_l$  in those for subarea C in case 4 to D and  $d_l$ . To obtain the expansions for subarea C, one can substitute the following into Eqs. (3.1)-(3.7).

$$i = l \quad (3.97)$$

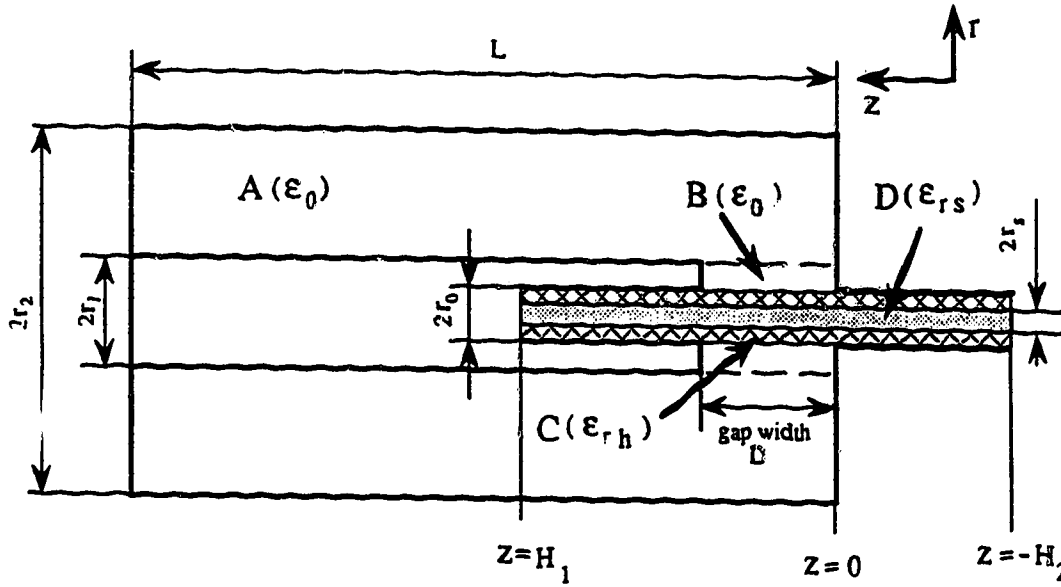


Figure 3.5 Subarea area division for mode-matching formulation of case 5 - sample with sample holder.

$$x_1 = c_\ell \quad (3.98)$$

$$z_0^X = z_0^C = H_2 = z_0^D \quad (3.99)$$

$$L_1^X = L_\ell^C = H = L_\ell^D \quad (3.100)$$

$$\epsilon_r^X = \epsilon_r^C = \epsilon_{rh} \quad (3.101)$$

$$F_1^X = F_\ell^C \neq 0 \quad (3.102)$$

The results of the field matching between subarea A and B are still identical to those in case 2. Using the same procedure as in case 4, the formulation of the field matching between B and C can be easily derived. The fields of C can be matched with those of D directly without Fourier expansion as we have seen in case 2 (Eqs. (3.67) and (3.68)). Therefore, the formulation process for the present case is not given here. Instead, below are listed the results which include all the formulas required for actual calculations of mode coefficients and resonant wavelengths. Some of these have appeared before but are repeated below to make the list complete.

The resonant wavelength,  $\lambda_0$ , and the unknown constants,  $F_m^B$  ( $m=0, 1,$

..., M-1) are determined by

$$(b_m)_G = (b_m)_T \quad (m=1, 2, \dots, M-1) \quad (3.103)$$

$$\det|\underline{G}| = 0 \quad (3.104)$$

$$\det|\underline{I}| = 0 \quad (3.105)$$

where  $(b_m)_G$  are computed by

$$\underline{G} \cdot [1, b_1, b_2, \dots, b_{M-1}]^T = \underline{0} \quad (3.106)$$

and  $(b_m)_T$  by

$$\underline{I} \cdot [1, b_1, b_2, \dots, b_{M-1}]^T = \underline{0} \quad (3.107)$$

The elements of the matrix  $\underline{G}$  and  $\underline{I}$  are given by

$$g_{ij} = \frac{D}{L} \alpha_i \cdot k_i^B \cdot \frac{Z_{0j}^B(k_{j1}^B)}{Z_{11}^B(k_{i1}^B)} \cdot \frac{N-1 \alpha_n Z_{1n}^A(k_{n1}^A)}{\sum_{n=0}^{N-1} \frac{k_n^A Z_{0n}^A(k_{n1}^A)}{k_n^A Z_{0n}^A(k_{n1}^A)}} \cdot e_{in}(\frac{D}{L}, 0) \cdot e_{jn}(\frac{D}{L}, 0) - \delta_{ij} \quad (i, j = 0, 1, \dots, M-1) \quad (3.108)$$

$$t_{ij} = \frac{D}{H} \alpha_i \cdot \epsilon_{rh} k_i^B \cdot \frac{Z_{0j}^B(k_{j0}^B)}{Z_{11}^B(k_{i0}^B)} \cdot \frac{L-1 \alpha_\ell Z_{1\ell}^C(k_{\ell 0}^C)}{\sum_{\ell=0}^{L-1} \frac{k_\ell^C Z_{0\ell}^C(k_{\ell 0}^C)}{k_\ell^C Z_{0\ell}^C(k_{\ell 0}^C)}} \cdot e_{i\ell}(\frac{D}{H}, \frac{H}{2}) e_{j\ell}(\frac{D}{H}, \frac{H}{2}) - \delta_{ij} \quad (i, j = 0, 1, \dots, M-1) \quad (3.109)$$

where

$$\alpha_i = \begin{cases} 1 & i=0 \\ 2 & i \neq 0 \end{cases} \quad (3.110)$$

$$\delta_{ij} = \begin{cases} 1 & i=j \\ 0 & i \neq j \end{cases} \quad (3.111)$$

$$e_{mn}(a, b) = \frac{(an)^2}{(an)^2 - m^2} \cdot \left[ \frac{(-1)^m \sin(a+b)n\pi}{an\pi} - \frac{\sin bn\pi}{an\pi} \right] \quad (3.112)$$

After  $\underline{B}$  is found, the modal coefficients in subarea A, C and D can be calculated by

$$\underline{A} = \underline{P} \cdot \underline{B} \quad (3.113)$$

$$\underline{C} = \underline{U} \cdot \underline{B} \quad (3.114)$$

$$\underline{D} = \underline{W} \cdot \underline{C} \quad (3.115)$$

Elements of the matrices  $\underline{P}$ ,  $\underline{U}$  and  $\underline{W}$  are given by

$$p_{nm} = \frac{D}{L} \cdot \alpha_n \cdot \frac{Z_{0m}^B(k_n^B r_1)}{Z_{0n}^A(k_n^A r_1)} \cdot e_{mn} \left( \frac{D}{L}, 0 \right) \quad (n = 0, 1, \dots, N-1 \text{ and } m = 0, 1, \dots, M-1) \quad (3.116)$$

$$u_{lm} = \frac{D}{H} \cdot \alpha_l \cdot \frac{Z_{0m}^B(k_l^B r_0)}{Z_{0l}^C(k_l^C r_0)} \cdot e_{ml} (D/H, H_2/H) \quad (l = 0, 1, \dots, L-1 \text{ and } m = 0, 1, \dots, M-1) \quad (3.117)$$

$$w_l = \frac{Z_{0l}^C(k_l^C r_s)}{J_0(k_l^D r_s)} \quad (l = 0, 1, \dots, L-1) \quad (3.118)$$

Other parameters involved in the above equations are

$$k_0 = \frac{2\pi}{\lambda_0} = \frac{2\pi f_0}{c} = \frac{\omega}{c} \quad (3.119)$$

$$\beta_n^A = n\pi/L \quad (3.120)$$

$$(k_n^A)^2 = k_0^2 - (\beta_n^A)^2 \quad (3.121)$$

$$Z_{0n}^A(k_n^A r) = J_0(k_n^A r) - F_n^A \cdot Y_0(k_n^A r) \quad (3.122)$$

$$Z_{1n}^A(k_n^A r) = J_1(k_n^A r) - F_n^A \cdot Y_1(k_n^A r) \quad (3.123)$$

$$F_n^A = J_0(k_n^A r_2) / Y_0(k_n^A r_2) \quad (3.124)$$

$$\beta_m^B = m\pi/D \quad (3.125)$$

$$(k_m^B)^2 = k_0^2 - (\beta_m^B)^2 \quad (3.126)$$

$$Z_{0m}^B(k_m^B r) = J_0(k_m^B r) - F_m^B \cdot Y_0(k_m^B r) \quad (3.127)$$

$$Z_{1m}^B(k_m^B r) = J_1(k_m^B r) - F_m^B \cdot Y_1(k_m^B r) \quad (3.128)$$

$$\beta_\ell^C = l\pi/H \quad (3.129)$$

$$(k_\ell^C)^2 = \epsilon_{rh} k_0^2 - (\beta_\ell^C)^2 \quad (3.130)$$

$$Z_{0\ell}^C(k_\ell^C r) = J_0(k_\ell^C r) - F_\ell^C \cdot Y_0(k_\ell^C r) \quad (3.131)$$

$$Z_{1\ell}^C(k_\ell^C r) = J_1(k_\ell^C r) - F_\ell^C \cdot Y_1(k_\ell^C r) \quad (3.132)$$

$$F_\ell^C = \frac{\epsilon_{rh} k_\ell^D J_0(k_\ell^D r_s) J_1(k_\ell^C r_s) - \epsilon_{rs} k_\ell^C J_1(k_\ell^D r_s) J_0(k_\ell^C r_s)}{\epsilon_{rh} k_\ell^D J_0(k_\ell^D r_s) Y_1(k_\ell^C r_s) - \epsilon_{rs} k_\ell^C J_1(k_\ell^D r_s) Y_0(k_\ell^C r_s)} \quad (3.133)$$

$$\beta_\ell^D = l\pi/H \quad (3.134)$$

$$(k_\ell^D)^2 = \epsilon_{rs} k_0^2 - (\beta_\ell^D)^2 \quad (3.135)$$

$$F_\ell^D = 0 \quad (3.136)$$

The above formulation is also applicable to case 4, 2 and 1. If  $\epsilon_{rh} = \epsilon_{rs}$ , then  $k_\ell^C = k_\ell^D$  and  $F_\ell^C = 0$ . Therefore,  $w_\ell = 1$ , that is,  $c_\ell = d_\ell$ . Subarea C and D thus become virtually one subarea. This is case 4. If we further assume that  $H=D$ , or  $H_1=H_2=0$ , we can show that  $u_{\ell m} = 0$  unless  $\ell=m$  since  $e_{m\ell}(1,0) = \delta_{m\ell}/\alpha_m$ . Thus, Eq.(3.117) is the same as Eq.(3.67). We now arrive at case 2. From Eqs.(3.67) and (3.68), we can also see that  $c_m = b_m$  and  $F_m^B = 0$  if  $\epsilon_r^B = \epsilon_r^C = \epsilon_{rs}$ . Now, we have case 1. Moreover, the formulation of the present case can be easily extended to case 3, i.e., arbitrary gap position, by simply replacing  $e(D/L, 0)$  in Eqs.(3.108) and (3.116) by  $e(D/L, L_2/L)$ .

### 3.3 Numerical Algorithm and Computer Program

Without the sample insertion hole, the numerical calculation for the cavity fields and resonant frequency formulated above is a routine task. First, the resonant wavelength can be found from the zero-determi-

nant condition, Eq. (3.104). Then, the linear equation set, Eq. (3.106), is solved for the modal coefficients  $\underline{B}$ , from which,  $\underline{A}$  and  $\underline{C}$  can be readily calculated.

With the introduction of the sample insertion hole, the constants  $F_m^B$  cannot be known before the resonant frequency is found. Instead, they have to be found along with the resonant frequency from the simultaneous equation set of Eqs. (3.103), (3.104) and (3.105). However, direct calculations may not be feasible because these equations are implicit and nonlinear functions of  $F_m^B$  and  $\lambda_0$ . From a practical point of view, we may be content with an approximate solution which can be obtained through a minimization procedure [51]. By constructing the following objective function

$$\text{Ob}(f_0^B, F_0^B, \dots, F_{M-1}^B) = W_1 |\det(\underline{G})| + W_2 |\det(\underline{T})| + W_3 \sum_{m=0}^{M-1} |(b_m)_C - (b_m)_T| \quad (3.137)$$

where  $W_1$ ,  $W_2$  and  $W_3$  are positive constants called weighting factors, we can see that when Ob reaches a minimum value, i.e.,

$$\text{Ob}(f_0^{B*}, F_0^{B*}, \dots, F_{M-1}^{B*}) = \min(\text{Ob}) \quad (3.138)$$

the variables  $f_0^{B*}, F_0^{B*}, \dots, F_{M-1}^{B*}$  satisfy

$$\det(\underline{G}) \approx 0 \quad (3.139)$$

$$\det(\underline{T}) \approx 0 \quad (3.140)$$

$$(b_m)_C \approx (b_m)_T \quad (3.141)$$

Therefore,  $f_0^{B*}, F_0^{B*}, \dots, F_{M-1}^{B*}$  are the approximate solutions which we seek. Such a minimization algorithm can converge rapidly if the number of variables is small and well-chosen initial values are used. In fact, M can be as small as four because the field expansions in subarea B for a gap much smaller than the wavelength are rapidly convergent series.

Computer programs in FORTRAN have been implemented for the coaxial re-entrant cavity field analysis based on the above mode-matching formulation. Different versions are designed specifically for each case; the programs analyzing the structures from case 1 to 5 are named MMCI

to MMC5 respectively. All programs are essentially similar to each other. The main steps involved are as follows:

1. Enter the dimensions of the cavity and the sample, the dielectric constant of the sample (and the holder), and the initial values of the resonant frequency (and  $F_m^B$ );
2. Search for the resonant frequency (and  $F_m^B$ );
3. Compute modal coefficients for each subarea;
4. Integrate the fields to give the Q-factor.

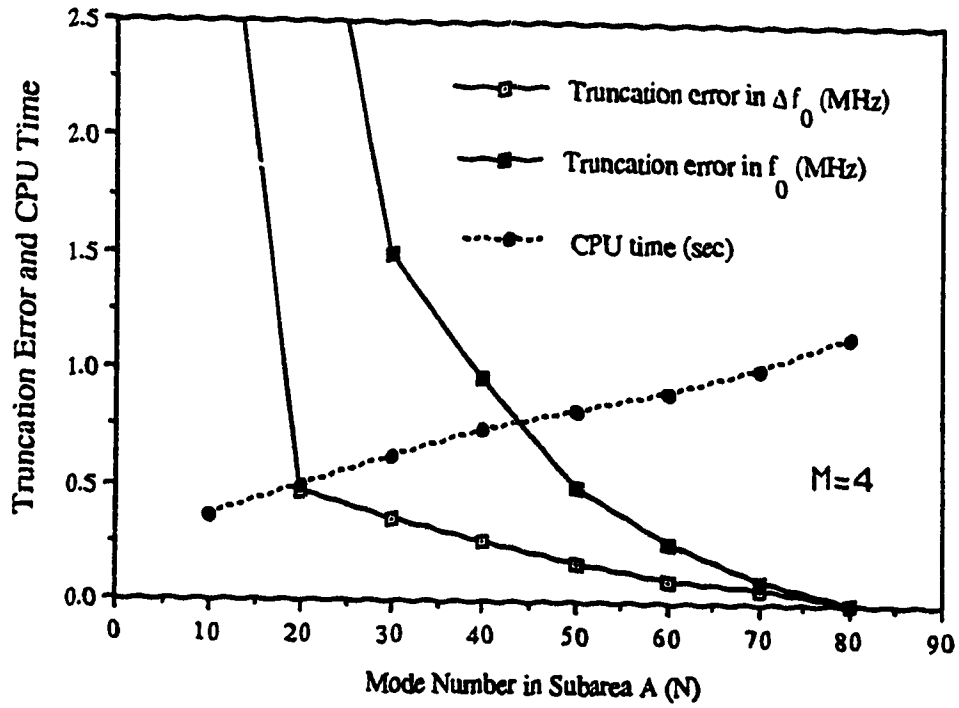
Programs for no-hole cases, MMC1-MMC3, use the Newton method [53] to find the resonant wavelength, or the root of the determinant function. Programs for the cases having the insertion hole, MMC4 and 5, employ the simplex method [51,52] to search for  $\lambda_0$  and  $F_m^B$ . The simplex method is one of the direct minimizing methods which is effective when a small number of variables are involved. The pivot elimination method [53] is chosen to find the inverse matrix and the determinant of  $G$  (and  $I$ ). All the Bessel functions are evaluated by approximating polynomials with an error less than  $10^{-6}$  [54].

### 3.4 Calculation Errors

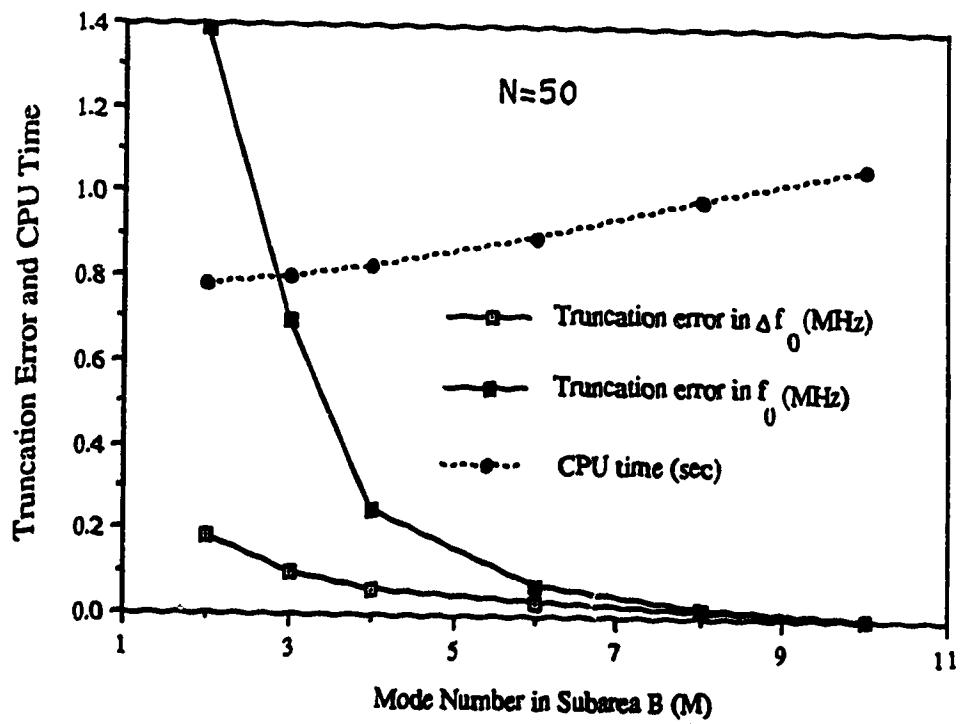
The calculation errors normally consist of the truncation error and the round-off error. Since the amount of calculation outlined above is not very great, the round-off error were found to be insignificant and only the truncation error will be considered here.

Table 3.1 lists the calculated modal coefficients in subarea A and B. It exhibits a fast convergence in both subareas. The modal coefficient in subarea B converges faster than that in subarea A obviously due to  $D \ll L$ . Figure 3.6 shows the variations in the calculated resonant frequency,  $f_0$ , and the frequency shift,  $\Delta f_0$ , versus  $N$  for a fixed  $M$  and versus  $M$  for a fixed  $N$ . It is expected that the truncation error has a lesser effect on  $\Delta f_0$  than on  $f_0$ . In this particular example, the error in  $\Delta f_0$  will not exceed 0.1MHz in the band around 2450MHz if  $M \geq 4$  and  $N \geq 60$ . In this figure, the CPU time spent on the calculation is also plotted and shown to be proportional to  $M \times N$ . Since the round-off error usually increases with the modal number in the calculation, we should choose the minimum  $M$  and  $N$  which satisfy the accuracy requirement.





(a)



(b)

Figure 3.6 Truncation error in  $f_0$  and  $\Delta f_0$  and required computation time on an Amdahl(5870) computer ( $r_a=1.0$ ,  $r_1=1.25$ ,  $r_2=4.5$ ,  $D=1.0$ ,  $L=17.0$ cm,  $f_0=2.8314$  and  $2.4391$ GHz for  $\epsilon_r=1$  and  $51$ , by MMC2).

Table 3.1 Convergence of modal coefficients ( $r_2=4.5$ ,  $r_1=1.25$ ,  
 $r_s=1.0$ ,  $L=17.0$ ,  $D=1.0\text{cm}$ ,  $\epsilon_r=51$ , by MMMC2)

$n$	$ a_n/a_0 $	$m$	$ b_m/b_0 $
0	1.0	0	1.0
1	1.89	1	$2.61 \times 10^{-2}$
2	1.46	2	$5.08 \times 10^{-2}$
3	$1.81 \times 10^{-2}$	3	$1.02 \times 10^{-4}$
4	$1.87 \times 10^{-1}$	4	$2.17 \times 10^{-5}$
5	$3.59 \times 10^{-2}$	5	$6.41 \times 10^{-7}$
6	$8.46 \times 10^{-3}$	6	$1.06 \times 10^{-8}$
7	$2.12 \times 10^{-3}$	7	$1.83 \times 10^{-10}$
8	$5.45 \times 10^{-4}$	8	$3.27 \times 10^{-12}$
9	$1.41 \times 10^{-4}$	9	$5.96 \times 10^{-14}$

The calculated Q-factor is less sensitive to the effect of the truncation error due to the fact that the Q-factor is evaluated by integrating the cavity E-fields and the integration tends to average out the possible random calculation errors. As an example, for the same cavity dimensions and frequency as used in Figure 3.6, the calculated Q-factor varies 0.15% as N is reduced from 80 to 10 and 0.08% as M decreases from 10 to 2.

### 3.5 Verification for Calculation

The calculated results have been compared with our experimental measurement data and with the data published by Karpova [36].

In Table 3.2, the calculated results from this work are listed with Karpova's data. It shows that the difference between the two is less than 0.22%. Karpova determined dielectric constants from the measured resonant frequency and, hence, her data are subject to experimental as well as calculation errors.

The experimental verifications are presented in Tables 3.3, 3.4 and 3.5. Table 3.3 lists the resonant frequency of an empty cavity with a varying gap. It reveals a maximum discrepancy of 0.06%. Such a discrepancy is caused not only by the calculation errors but also by the measurement errors which are to be discussed in Chapter 5. Tables 3.4 and 3.5 give the resonant frequency shifts produced by Teflon and water samples. These results show a larger discrepancy mainly due to the

Table 3.2 Calculated resonant frequencies compared with Karpova's data for the same cavity ( $r_1=0.75$ ,  $r_2=2.56$ ,  $r_s=r_1$ ,  $L=2.0$  and  $D=0.5\text{cm}$ )

$\epsilon_{rs}$	$f_0$ (GHz)		$\delta f_0/f_0$ (%)
	This work	Karpova's	
2.495	1.9741	1.9745	-0.02
2.735	1.9184	1.9223	-0.20
3.734	1.7284	1.7322	-0.22
5.605	1.4854	1.4837	0.11
30.83	0.6969	0.6959	0.14

Table 3.3 Calculated resonant frequency of an empty cavity for varying gap widths, compared with the experimental data ( $r_1=1.23$ ,  $r_2=4.51$ ,  $L=20.0\text{cm}$ , by MMC1)

$D$ (cm)	$f_0$ (GHz)		$\delta f_0/f_0$ (%)
	Calculated	Measured	
0.20	2.3119	2.3131	-0.052
0.50	2.3673	2.3682	-0.038
0.75	2.4047	2.4059	-0.050
1.00	2.4384	2.4380	0.016
1.20	2.4639	2.4649	-0.040
1.50	2.5004	2.5003	0.000
2.00	2.5580	2.5579	0.000
3.00	2.6616	2.6621	-0.019
4.00	2.7375	2.7376	0.000

Table 3.4 Calculated resonant frequency shift produced by Teflon samples, compared with the experimental data ( $r_1=1.23$ ,  $r_2=4.51$ ,  $L=20$ ,  $D=1.0\text{cm}$  and  $\epsilon_r=2.0$ , by MMC2)

$r_s$ (cm)	Mode*	$\Delta f_0$ (MHz)		Difference (MHz)
		Calcu.	Measu.	
0.75	TEM <sub>5/4</sub>	25.9	25.7	0.2
	TEM <sub>7/4</sub>	28.0	27.0	1.0
	TEM <sub>9/4</sub>	24.3	24.7	-0.4
0.35	TEM <sub>5/4</sub>	6.0	6.0	0.0
	TEM <sub>7/4</sub>	6.7	7.3	-0.6
	TEM <sub>9/4</sub>	5.9	5.4	-0.5

\*When the cavity is empty, the measured  $f_0$  at TEM<sub>5/4</sub>, TEM<sub>7/4</sub> and TEM<sub>9/4</sub> are 1.744, 2.4384 and 3.1341GHz respectively. The mode definition will be given in Chapter 4.

Table 3.5 Calculated resonant frequency shift produced by distilled water ( $T \approx 25^{\circ}\text{C}$ ) for varying cavity length, compared with measured data ( $r_2=5.08$ ,  $r_1=1.27$ ,  $r_0=0.35$ ,  $r_s=0.24$ ,  $D=0.25\text{cm}$ ,  $\epsilon_{rs}=79.5$ ,  $\epsilon_{rh}=3.8$ , by MMMC5)

L(cm)	$\Delta f_0$ (MHz)		Difference (MHz)
	Calculated	Measured	
19.5	27.0	27.6	-0.6
19.7	26.6	27.3	-0.7
19.9	26.2	27.1	-0.9
20.1	26.0	26.8	-0.8
20.3	25.9	26.7	-0.8
20.5	25.6	26.5	-0.9

larger experimental errors involved. The Teflon data were obtained using the cavity without the sample insertion hole. As a result, opening the cavity to load the sample degrades the repeatability and causes a significant measurement error. The air gaps at the sample ends will also contribute to the experimental error, causing the measured resonant frequency to be smaller than the true value. However, this air gap error should be negligible for low permittivity materials such as Teflon. The water data, though the sample insertion hole and the holder were used, are also subject to several types of uncertainty such as the value of  $\epsilon_{rs}$  used in the calculation, temperature variation and the dimensional errors in  $D$  and  $r_s$ . Nevertheless, the discrepancy shown in Table 3.5 is less than 4%.

These comparisons have demonstrated the reliability of the mode-matching calculation. As a matter of fact, the high accuracy of the calculated resonant frequency is partly due to the high sensitivity of the determinant function. Figure 3.7 is a typical plot of the function  $\det|\underline{G}|\underline{G}|$  which shows a very steep valley around the resonant frequency. In addition, it is interesting to note that the poles of  $\det|\underline{G}|\underline{G}|$  coincide with the resonant wavelength of the standard coaxial cavity ( $D=0$ ), that is,  $|\underline{G}|=\infty$  at  $\lambda=2L/n$ . The designation and the naming of resonant modes in our re-entrant coaxial cavity will be discussed in the next chapter.

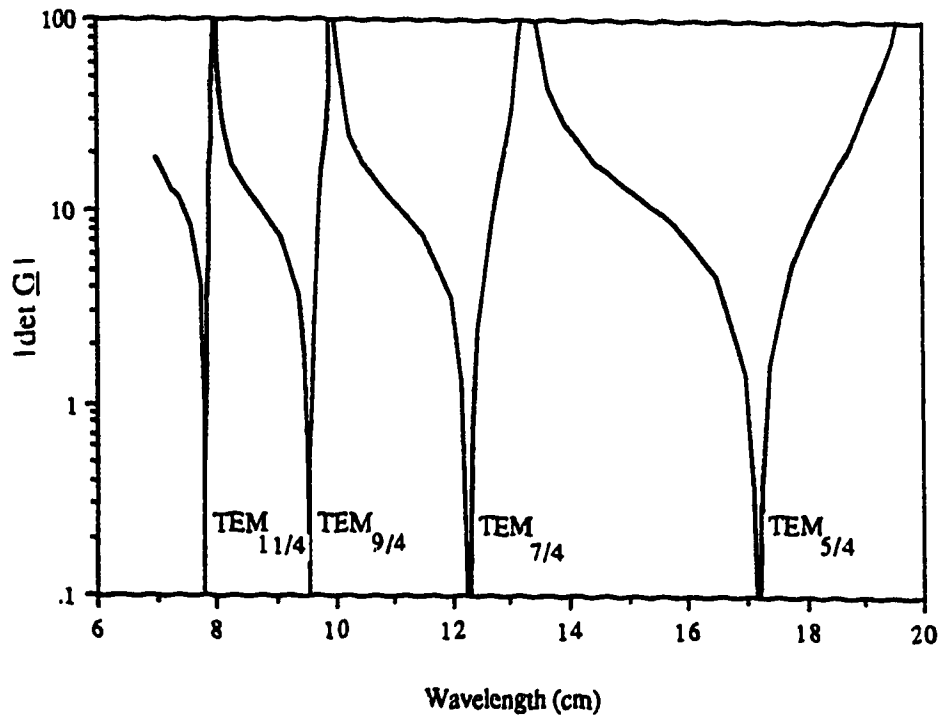


FIGURE 3.7 The determinant of matrix  $\underline{G}$  as a function of wavelength ( $r_1 = 1.25$ ,  $r_2 = 4.5$ ,  $L = 20.0$ ,  $D = 1.0$  cm,  $\epsilon_r = 1.0$ , by MMMC1); its zeros are the solutions for the resonant frequencies.

CHAPTER 4  
THEORETICAL CAVITY RESONANCE CHARACTERISTICS

With the aid of the mode-matching analysis presented in Chapter 3, we are able to quantitatively examine the characteristics of the dielectric sample loaded coaxial re-entrant cavity (Figure 1.1). In this chapter, the major cavity characteristics will be presented based on the numerical results and discussed focusing on the dielectric sample loading effects, namely, changes in the resonant frequency and the electric energy deposition caused by the insertion of a dielectric sample into a cavity [24]. This chapter starts with the description of the cavity field distribution and the definition of the resonant modes. The calculated resonant frequency and Q-factor are then given in the form of mode charts and normalized Q diagrams. It is followed by a discussion of the resulting practical importance and the theoretical insight from these results. Effects of the sample insertion hole and holder [55] are elaborated on, which indicate significant differences between the cavity used in this thesis work and an ordinary coaxial re-entrant cavity. Finally, two calculated calibration curves are proposed for determining the dielectric constant and loss tangent of the sample tested in this cavity. After all, the purpose of this chapter is to provide a theoretical understanding of this cavity and to give practical guidance for designing the cavity into a new high temperature microwave dielectricrometer.

#### 4.1 Field Distribution

It is well known that a standard coaxial cavity has a series of fundamental TEM modes. The TEM field has only a radial electric component,  $E_r$ , and an angular magnetic component,  $H_\phi$ , which can be expressed by [56]

$$E_r = 60(I_0/r)\sin\left(\frac{2\pi z}{\lambda_0}\right) \quad (4.1)$$

$$H_\phi = \left(\frac{I_0}{2\pi r}\right)\cos\left(\frac{2\pi z}{\lambda_0}\right) \quad (4.2)$$

where  $I_0$  is the current flowing through the center conductor, and is here referred to as TEM current. The amplitude ratio of  $E_r$  and  $H_\phi$  is simply the free space impedance, i.e.,

$$\eta_0 = 120\pi \quad (4.3)$$

The resonant wavelength,  $\lambda_0$ , is given by

$$\lambda_0 = \frac{2\ell}{n} \quad (4.4)$$

for a closed cavity and

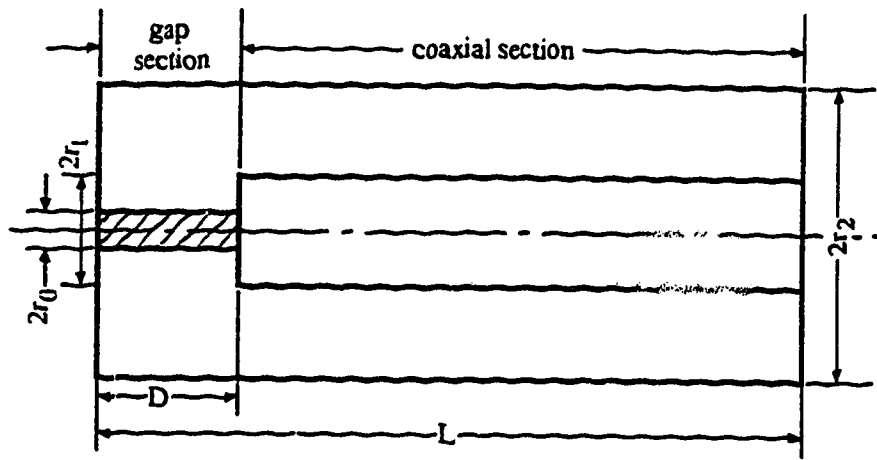
$$\lambda_0 = \frac{4}{2n+1}\ell \quad (4.5)$$

for a cavity opened\* at one end, where  $n = 1, 2, \dots$  and  $\ell$  is the cavity length.

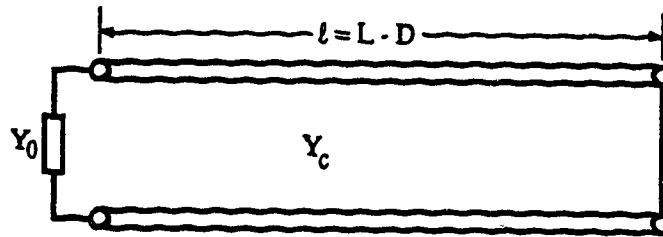
With a gap cut in the center conductor as shown in Figure 4.1a, the axial component  $E_z$  appears in the gap section, hence, the field is no longer an exact TEM field. However, if the gap is much smaller than the wavelength, it is reasonable to expect that the field pattern away from the gap will nearly be TEM except for a change in its resonant wavelength. This can be shown from the calculated field distributions. Figures 4.2a and 4.3a show the axial distribution of  $E_r$ ,  $H_\phi$  and  $E_z$  at  $(r_1+r_2)/2$  before and after a sample of  $\epsilon'_r=50$  is loaded in the cavity gap, plotted together with the TEM field of the same wavelength. We see that at a distance of about  $3D$  away from the gap,  $E_r$  and  $H_\phi$  are almost the same as those of the TEM field and  $E_z$ , a component associated with TM modes, decays to about 10%. Moreover, the field pattern of  $\epsilon'_r=50$  is almost the same as that obtained by stretching the field pattern of  $\epsilon'_r=1$  along the  $z$  axis, since it is only the resonant wavelength that changes in the coaxial section. However, the net energy stored in the gap section is substantially different. Figures 4.2b and 4.3b demonstrate the radial distribution of gap fields normalized by the TEM current, and clearly show that the gap with  $\epsilon'_r=1$  is electrically dominant, i.e., it has much more electric energy than magnetic energy, while the gap with

---

\* In this thesis, "opened" is referred to "ideally opened" which corresponds to a zero fringe capacitance.



(a)



(b)

Figure 4.1 Coaxial re-entrant cavity with a gap partially filled with a dielectric sample. (a) Schematic diagram of the structure and (b) Equivalent circuit.

$\epsilon'_r=50$  is magnetically dominant. Therefore, it is justified to call the former gap capacitive and the latter inductive.

The gap fields shown in Figures 4.2b and 4.3b are close to those of the  $TM_{010}$  mode of a cylindrical cavity if  $r$  is small, i.e.,  $E_z = \text{constant}$ ,  $H_\phi \propto J_1(kr)$  and  $E_r = 0$ . As a result, a rather uniform temperature profile will be achieved when the cavity is used as a microwave heater. In addition, since the resonant field pattern in the coaxial section is very close to the TEM pattern as shown in Figures 4.2a and 4.3a, one can expect that the cavity field and the resonant frequency will not change if the cavity length increases or decreases by one half of the wavelength.



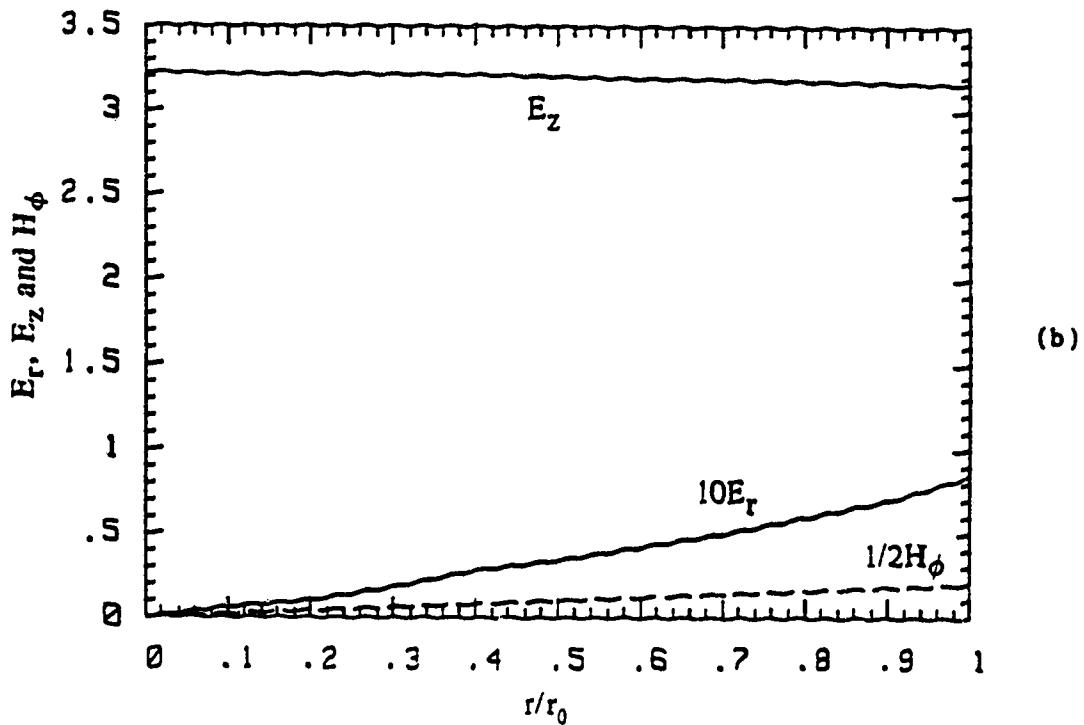
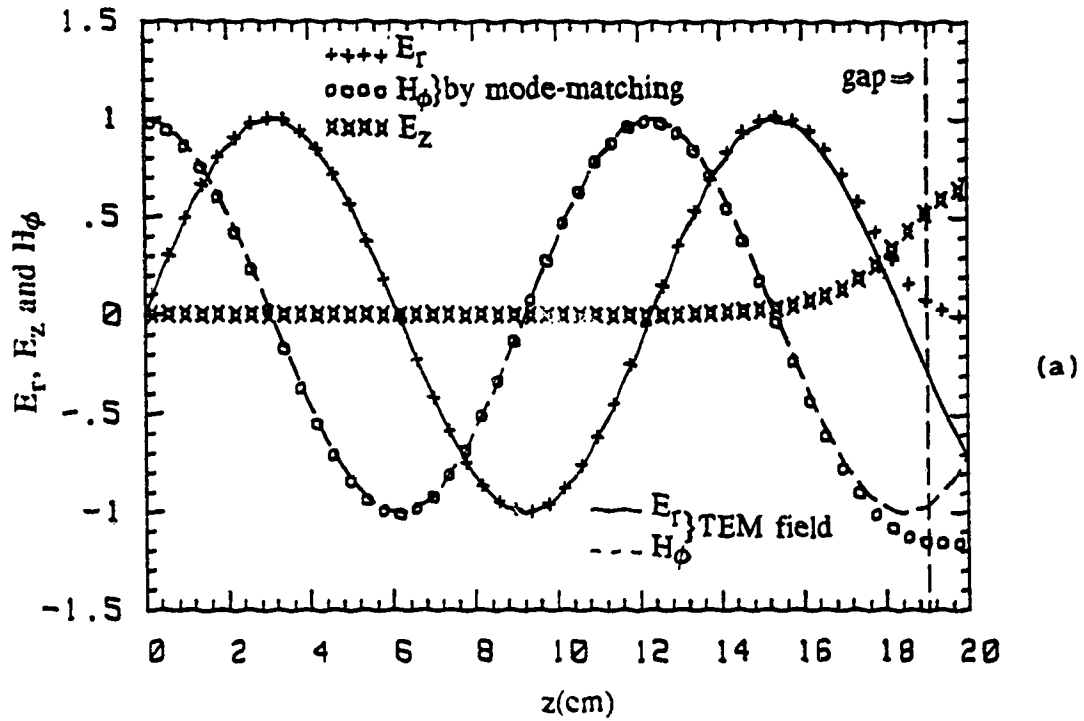


Figure 4.2 E and H fields for a capacitive mode ( $r_1=1.25, r_2=4.5, D=1.0, L=20.0\text{cm}, \epsilon_{r_g}=1.0, f_0=2.438\text{GHz}$ ), normalized by the TEM field in the coaxial section. (a) Axial distribution between the center and outer conductor, compared with TEM fields and (b) Radial distribution in the gap midplane.

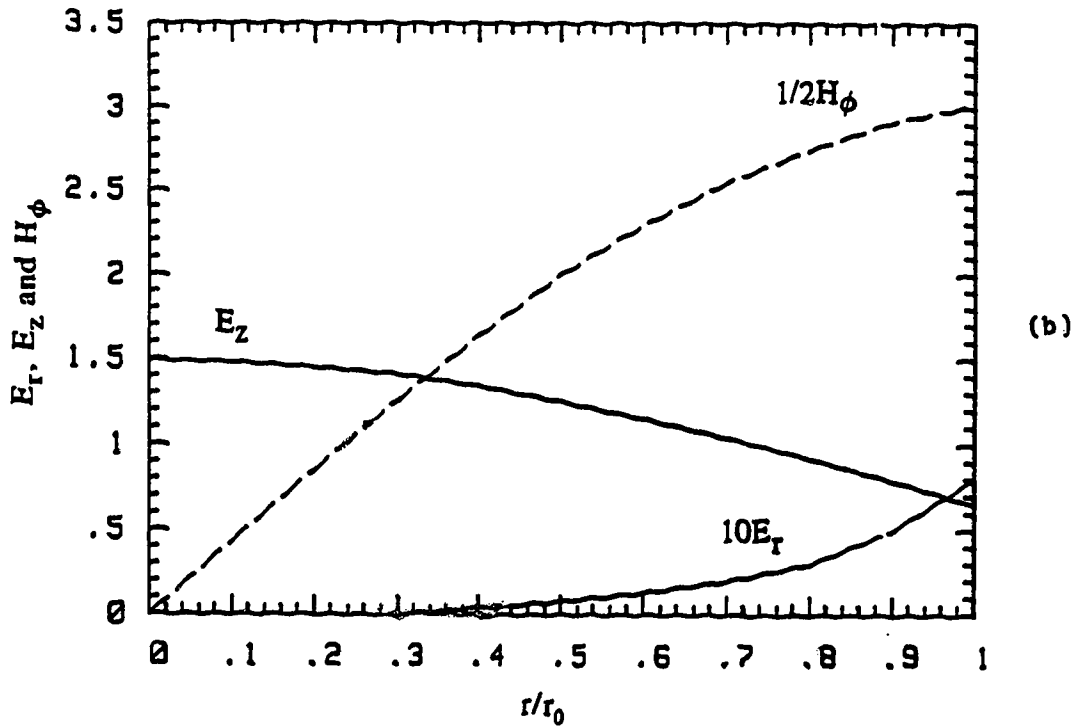
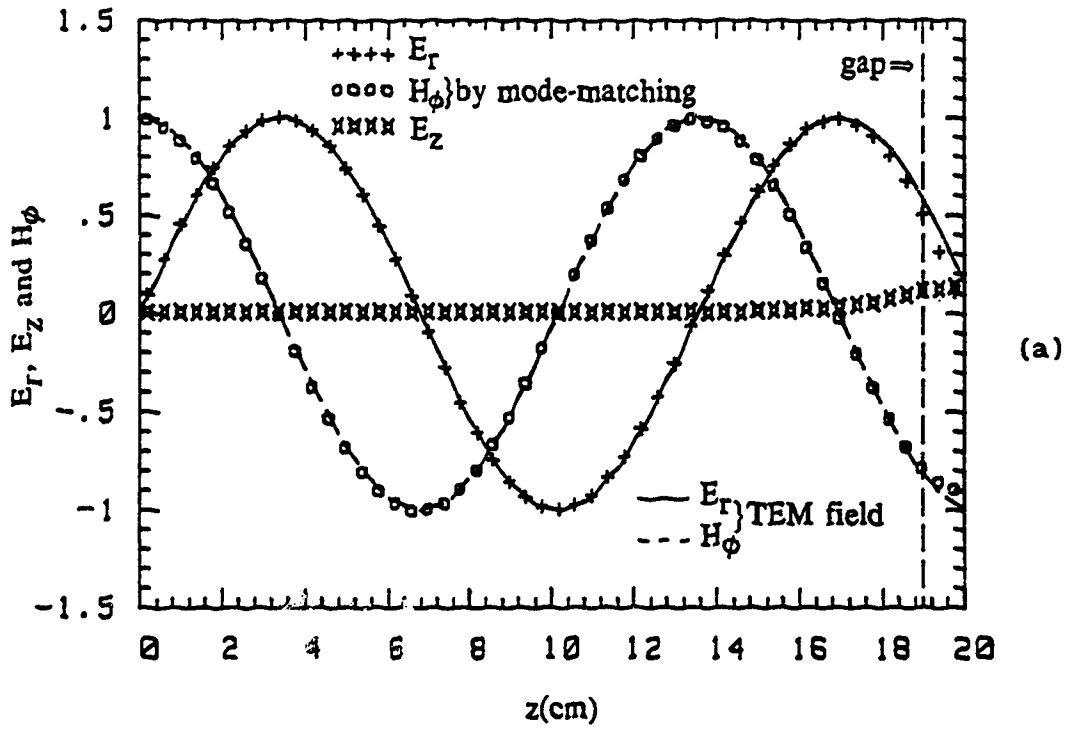


Figure 4.3 E and H fields for an inductive mode ( $r_1=1.25, r_2=4.5, D=1.0, L=20.0\text{cm}, \epsilon_{r_s}=50.0, f_0=2.212\text{GHz}$ ), normalized by the TEM field in the coaxial section. (a) Axial distribution between the center and outer conductor, compared with TEM fields and (b) Radial distribution in the gap midplane.

## 4.2 Quasi-TEM Resonant Modes

In general, a coaxial re-entrant cavity can be reduced to an equivalent circuit as shown in Figure 4.1b, where the transmission line represents the coaxial section and the admittance,  $Y_0$ , models the gap section of the cavity. Thus, the resonant condition can be easily written as [56]

$$\cot(\ell\omega/c) = -jY_0/Y_c \quad (4.6)$$

where  $Y_0 = j\omega C_0$  (4.7)

for a capacitive gap and

$$Y_0 = 1/j\omega L_0 \quad (4.8)$$

for an inductive gap.  $C_0$  and  $L_0$  are the equivalent lumped gap capacitance and inductance and  $Y_c$  is the characteristic admittance of the coaxial section which is given by

$$Y_c = \frac{1}{60 \ln(r_2/r_1)} \quad (4.9)$$

If  $C_0$  and  $L_0$  are independent of the resonant frequency, the resonant frequency can be solved for graphically as shown in Figure 4.4. Such a graphical solution will help to make the following mode definition more illustrative.

Figure 4.4 shows that the solutions for the resonant frequency of a capacitive gap are all above the horizontal axis and between  $(n-1)\pi$  and  $(n-1/2)\pi$ , i.e.,

$$(n-1)\lambda_0/2 < \ell < (2n-1)\lambda_0/4 \quad (4.10)$$

or  $4\ell/(2n-1) < \lambda_0 < 2\ell/(n-1)$  (4.11)

These modes are defined as capacitive quasi-TEM modes and designated as  $TEM_{(2n-1)/4}$ . For an inductive gap, the solutions are all located below the axis and between  $(n-1/2)\pi$  and  $n\pi$ , i.e.,

$$(2n-1)\lambda_0/4 < \ell < 2n\lambda_0/4 \quad (4.12)$$

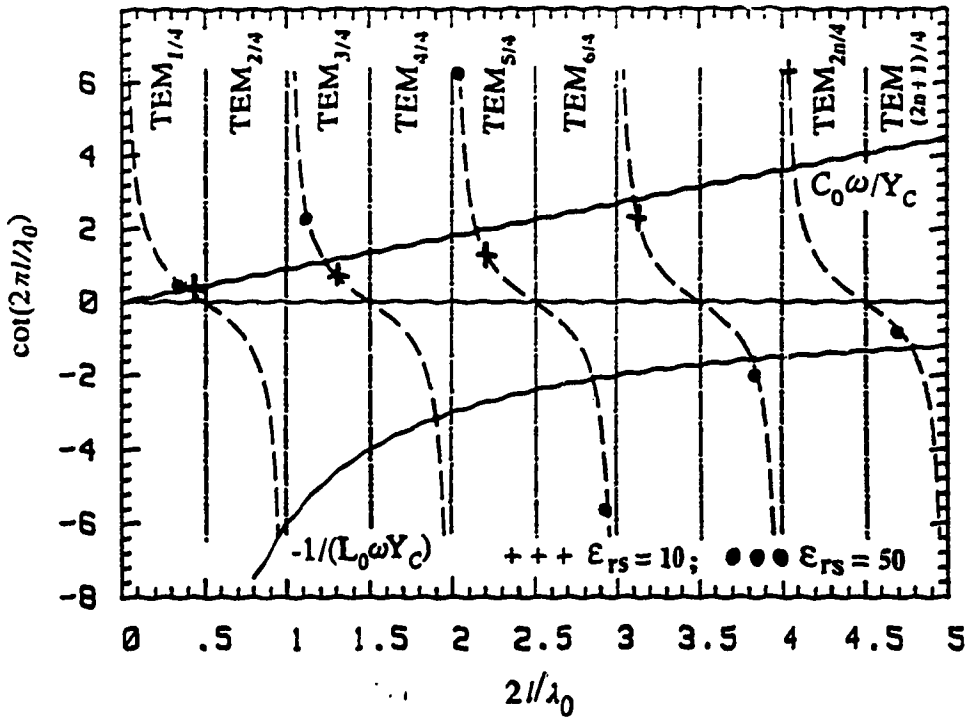


Figure 4.4 Graphic solution for resonant frequencies of an ideal coaxial re-entrant cavity with lumped gap parameters  $C_0$  and  $L_0$  and the loci of the resonant frequencies of a real cavity.

$$\text{or} \quad 2L/n < \lambda_0 < 4L/(2n-1) \quad (4.13)$$

Similarly, these modes are named inductive quasi-TEM modes and designated as  $TEM_{2n/4}$ . As the gap capacitance disappears or approaches an infinite value, all these quasi TEM modes become exact TEM modes as in an ideally opened or closed coaxial cavity. Compared with a coaxial cavity opened at one end, a capacitive mode (or gap) virtually shortens the cavity whereas an inductive mode (or gap) lengthens the cavity.

Understanding these two types of modes is helpful in making more efficient use of coaxial re-entrant cavities. For example, when designing a microwave applicator [23], a capacitive mode should be chosen for heating non-magnetic materials and an inductive mode for magnetic materials so that a maximum material-field interaction and, therefore, a high temperature or a high heating rate can be achieved.

### 4.3 Equivalent Gap Capacitance

Generally speaking, the lumped gap parameter  $C_0$  or  $L_0$  depends not only on cavity dimensions and the sample in the gap but also on resonant modes (or frequency). As shown in Figure 4.4, the resonant frequencies of a given cavity, marked by crosses ( $\epsilon'_r=10$ ) and dots ( $\epsilon'_r=50$ ), are no longer located along a straight line or a hyperbolic curve, which means that  $C_0$  and  $L_0$  are frequency dependent. Nevertheless, it will be shown below that a gap capacitance can be frequency independent under certain conditions.

As mentioned above, a capacitive gap can be represented by a lumped capacitance, which can be derived from the known resonant frequency via Eqs. (4.6) and (4.7), i.e.,

$$C_0 = Y_c \cot(lw/c)/\omega \quad (4.14)$$

On the other hand, Marcuvitz [57] gave an expression for the equivalent capacitance for an empty coaxial re-entrant gap as follows:

$$C_0^\circ = \epsilon_0 \pi r_1^2 / D + 4\epsilon_0 r_1 \ln((r_2 - r_1)/D) \quad (4.15)$$

This capacitance is composed of a parallel plate capacitance

$$C_{0p}^\circ = \epsilon_0 \pi r_1^2 / D \quad (4.16)$$

and a fringe capacitance

$$C_{0f}^\circ = 4\epsilon_0 r_1 \ln((r_2 - r_1)/D) \quad (4.17)$$

To extend the expression to the case of a gap partially filled with a dielectric,  $C_{0p}^\circ$  can be modified to

$$C_{0p}^\circ = \epsilon_0 \pi (r_0^2 (\epsilon'_r - 1) + r_1^2) / D \quad (4.18)$$

and  $C_{0f}^\circ$  remains unchanged. Therefore, Eq. (4.15) becomes

$$C_0^\circ = \epsilon_0 \pi (r_0^2 (\epsilon'_r - 1) + r_1^2) / D + 4\epsilon_0 r_1 \ln((r_2 - r_1)/D) \quad (4.19)$$

To examine the validity of Eq. (4.19), a comparison between  $C_0^\circ$  of Eq. (4.19) and  $C_0$  of Eq. (4.14) is made and presented in Figure 4.5 for dif-

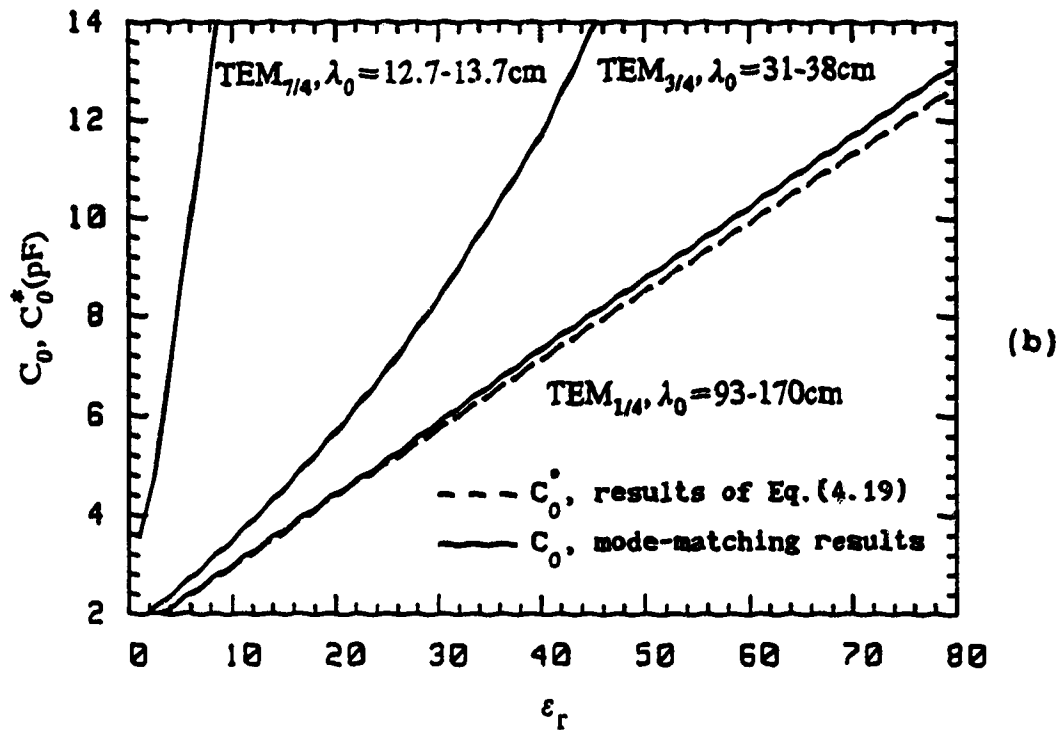
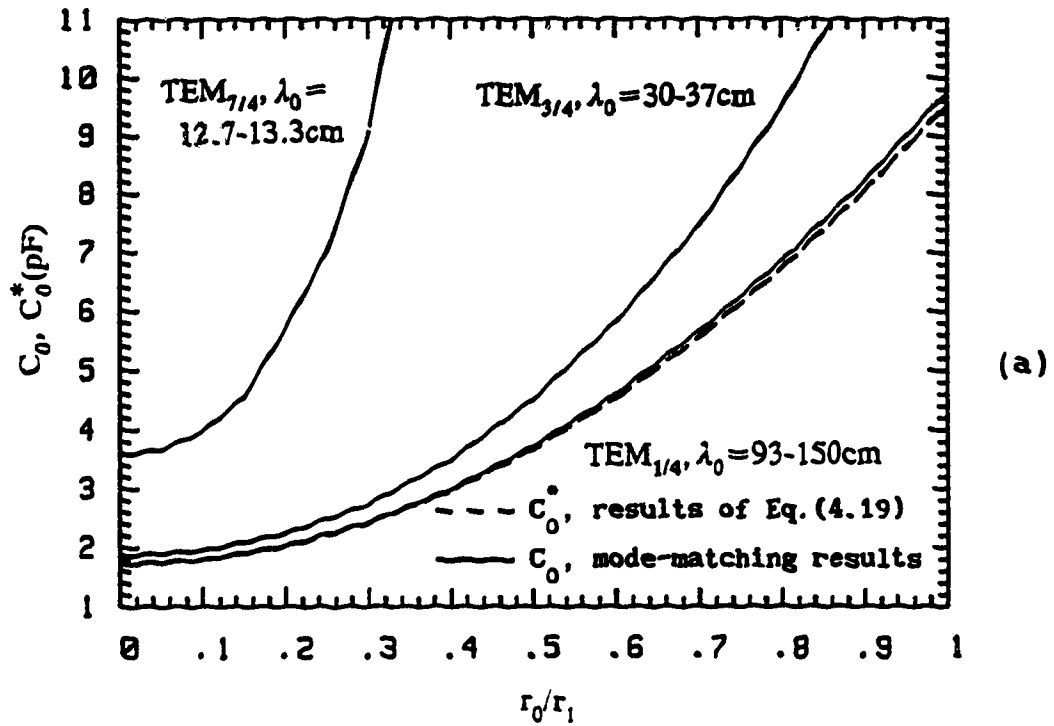


Figure 4.5 Equivalent gap capacitance ( $r_1=1.25, r_2=4.5, L=20.0, D=0.5$ , in cm) versus (a) sample radius ( $\epsilon_{rs}=10$ ) and (b) dielectric constant ( $r_0=0.5$ cm).

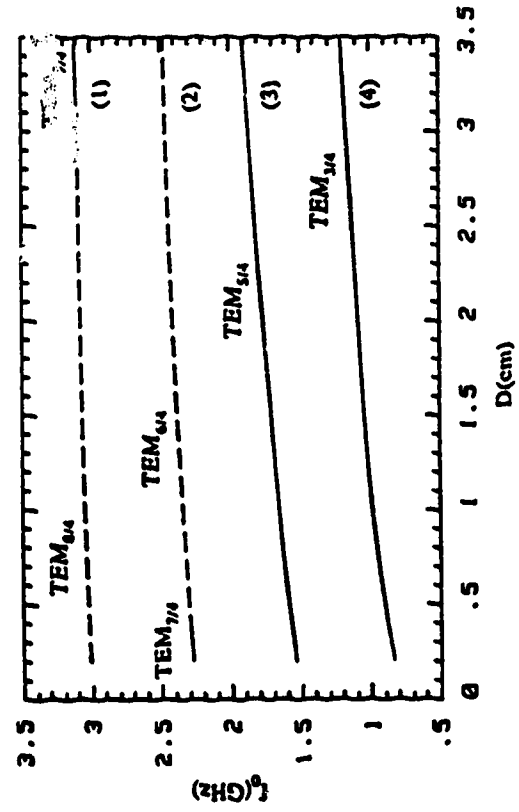
ferent radii and dielectric constants of the sample. These curves show that Eq.(4.19) is valid if the gap width is much smaller than the wavelength in the dielectric. We can adopt the same conditions as given by Marcuvitz, that is,  $2\pi D/\lambda \ll 1$  and  $D/(r_2 - r_1) \ll 1$ , where  $\lambda = \lambda_0 / \sqrt{\epsilon_r}$ .

#### 4.4 Resonant Frequency

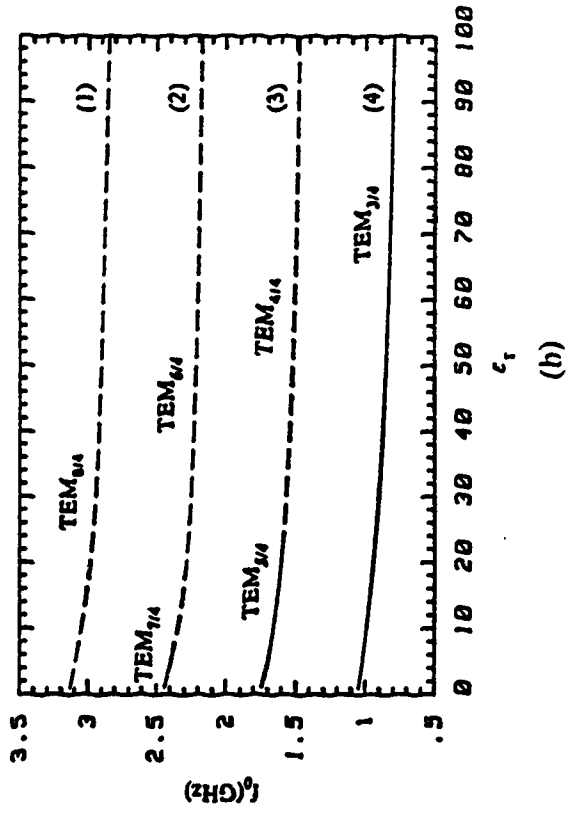
Resonant frequencies are computed for a typical gap width,  $D$ , sample radius,  $r_0$ , and sample dielectric constant,  $\epsilon_r'$ , and are presented in Figure 4.6 in the form of mode charts. On these mode charts, capacitive modes are shown by solid lines and inductive modes by dashed lines.

First of all, we see that reducing the gap width and increasing the dielectric constant or radius of the sample have an equivalent effect on the reduction of resonant frequencies. Recalling that the sample loading factor is proportional to the sample's dielectric constant and volume and the square of the gap E-field (Eq.(2.37)), we see that the larger the loading factor, the greater the frequency reduction. For a loaded cavity, the frequency reduction with decreasing gap width slows down especially at a wider gap or for a higher mode because the length or the volume of the sample decreases as well.

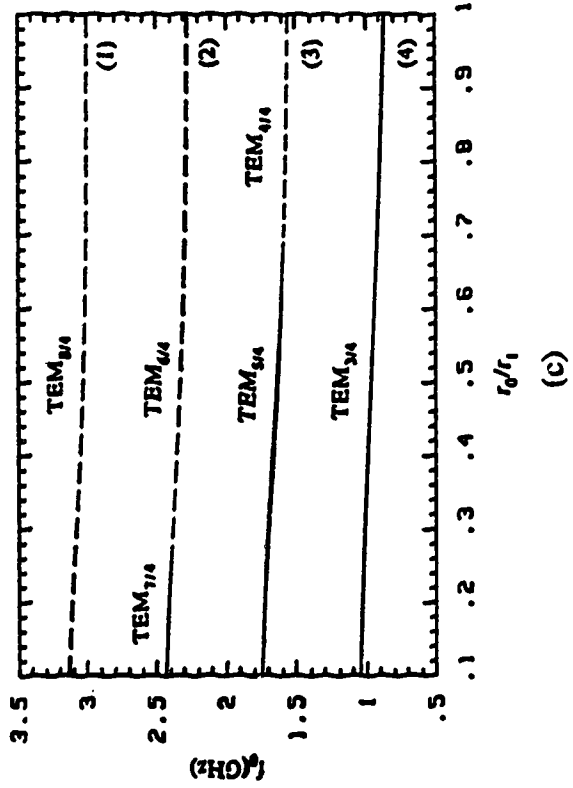
Secondly, in contrast to the modes in standard cavities which are distinct from each other, capacitive and inductive modes exhibit a smooth transition between each other as  $D$ ,  $r_0$  and  $\epsilon_r'$  are varied. At the transition point, both the coaxial and gap sections have equal electric and magnetic energy and are therefore loosely coupled. It is important to understand the mode transition due to the variations in the sample, in particular, changes of dielectric properties with temperature. The mode transition from a capacitive mode to an inductive mode may weaken the interaction of the sample with the electric field. This will cause problems in high temperature material heating since the dielectric constant of most oxides, ceramics and glasses increases with temperature. On the other hand, it is possible to make use of this mode transition to suppress the temperature run-away which arises from the positive temperature coefficient of the material's loss factor. It is understandable that the mode transition happens more frequently for a larger sample radius. Figure 4.7 is an example, where a smaller slope corres-



(a)



(b)



(c)

Figure 4.6 Resonant frequency ( $r_1=1.25$ ,

$r_2=4.5$ ,  $L=20.0\text{cm}$ ) versus:

(a) Gap width,  $D$ ;

( $r_0=0.5\text{cm}$ ,  $\epsilon_r=10$ )

(b) Dielectric constant,  $\epsilon_r$ ;

( $r_0=0.5$ ,  $D=1.0\text{cm}$ )

(c) Sample radius,  $r_0$ .

( $\epsilon_r=10$ ,  $D=1.0\text{cm}$ )



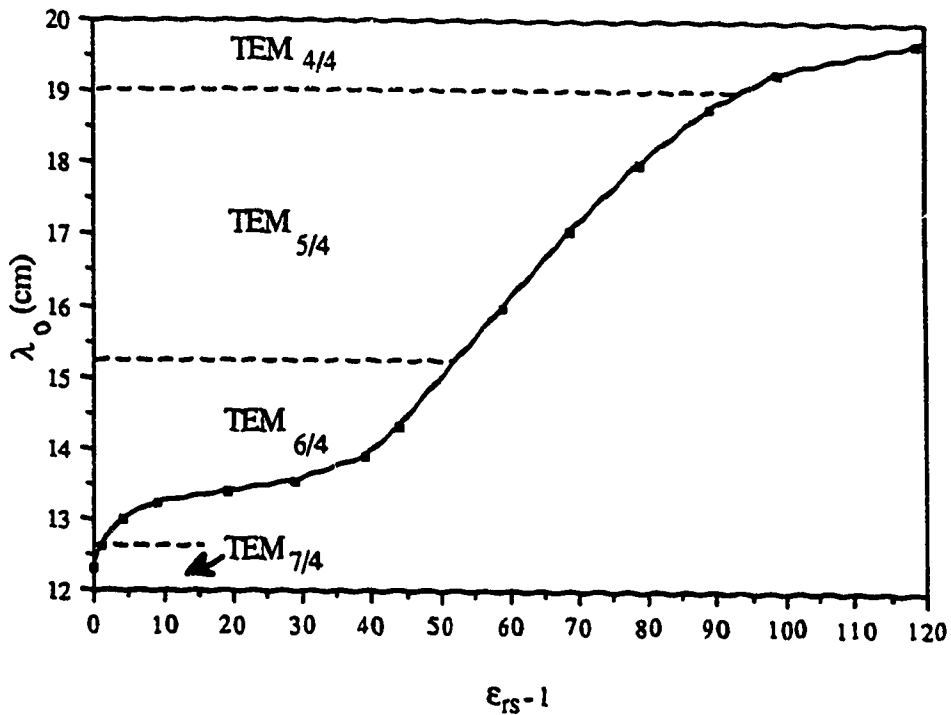


Figure 4.7 Resonant wavelength as a function of the dielectric constant of a sample with the same diameter as the center conductor ( $r_1=r_s=1.25$ ,  $r_2=4.5$ ,  $L=20.0$ ,  $D=1.0$ cm, by MPMC1).

ponds to an inductive mode which relates to a weaker gap E-field. This curve also reveals that the mode transition is responsible for a non-linear frequency shift with increasing dielectric constant.

#### 4.5 Cavity Q-factor

The Q-factor of a dielectric loaded cavity is expressed in two parts as

$$1/Q_L = 1/Q_C + 1/Q_D \quad (4.20)$$

where  $Q_C$  is the cavity Q due to the wall loss, and  $Q_D$  is the cavity Q due to the sample's dielectric loss, i.e.,

$$Q_C = \omega W_E / P_W \quad (4.21)$$

$$\text{and } Q_D = W_E / (W_D \tan \delta) = 1 / (F_\ell \tan \delta) \quad (4.22)$$

where  $W_E$  and  $W_D$  are the stored energy in the whole cavity and in the sample,  $P_W$  is the power dissipated in the cavity walls which is inversely proportional to the square root of the wall conductivity,  $\sigma$ , and  $F_\ell$  is the sample loading factor. If  $Q_D$  and  $Q_C$  differ by a factor more than 10, the lower one dominates the loaded cavity Q-factor. From this point of view, when a very lossy sample is loaded into a cavity,  $Q_L$  will not be very high no matter how high the  $Q_C$  is.

#### 4.5.1 Normalized $Q_C$

To be useful generally, we define a normalized Q-factor,  $\bar{Q}_C$ , which is independent of  $\sigma$ , as follows

$$\bar{Q}_C = Q_C / \sqrt{\sigma} \quad (4.23)$$

The inverse of  $\bar{Q}_C$  is presented as a function of  $D$ ,  $\epsilon'_r$  and  $r_0/r_1$  in Figure 4.8. Although it seems that the cavity Q-factor varies with  $D$ ,  $\epsilon'_r$  and  $r_0$  in different ways, it is almost always true that  $Q_C$  for a set of arbitrary parameters is intrinsically determined by the cavity resonant frequency, that is,  $Q_C$  increases with the resonant frequency. An exception may occur if the frequency is so high that the increase in wall loss overrides the increase in the stored energy as shown in Figure 4.8a.

The cavity Q-factor,  $Q_C$ , may be approximated by the value for a zero-gap cavity, i.e., a standard coaxial cavity. As derived in Appendix 2, if  $L \gg D$  and  $\lambda_0/4\pi$ ,  $\bar{Q}_C$  can be expressed by

$$\bar{Q}_C = 0.4\pi\sqrt{f_0} \frac{\ln(r_2/r_1)}{1/r_1 + 1/r_2 + (4/L)\ln(r_2/r_1)} \quad (4.24)$$

where  $f_0$  is in GHz and  $r_1$ ,  $r_2$  and  $L$  in cm. This formula is actually the same as the Q expression of a standard coaxial cavity [56]. To examine its accuracy, let  $r_1=1.25$ ,  $r_2=4.5$  and  $L=20.0$ , Eq. (4.24) becomes

$$\bar{Q}_C = 1.26\sqrt{f_0} \quad (4.25)$$

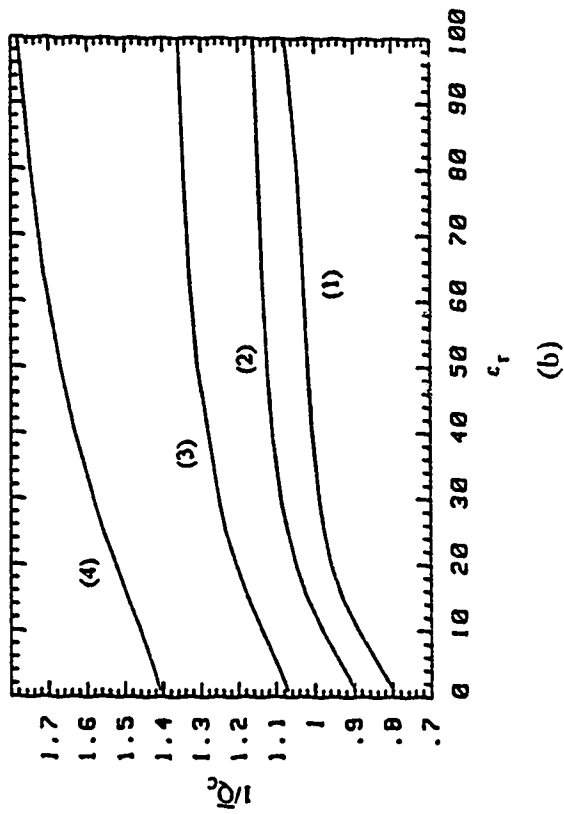
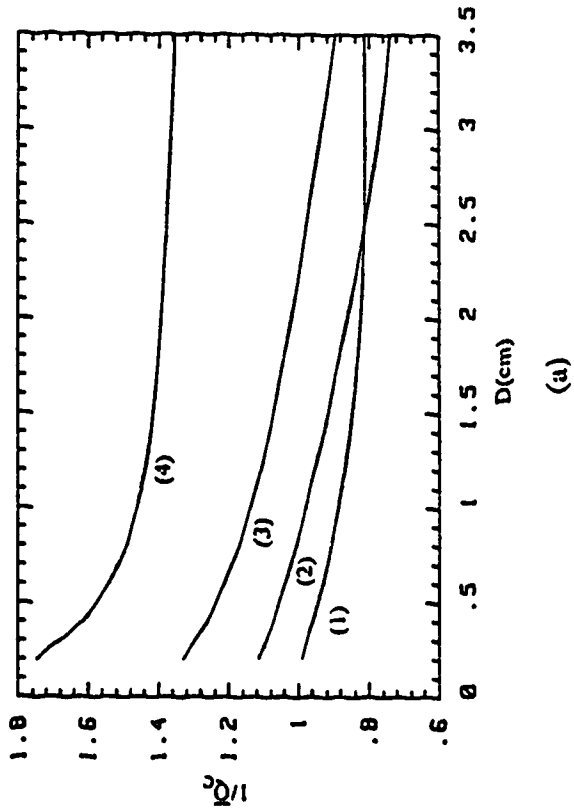


Figure 4.8 Inverse normalized cavity  $Q$ -factor ( $r_1=1.25$ ,  $r_2=4.5$ ,  $L=20.0\text{cm}$ ) versus:

(a) Gap width,  $D$ ;

( $r_0=0.5\text{cm}$ ,  $\epsilon_r=10$ )

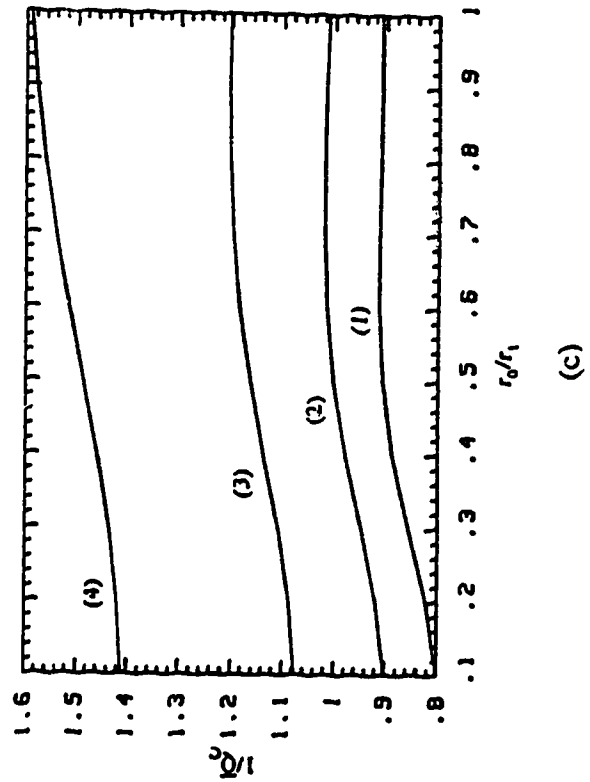
(b) Dielectric constant,  $\epsilon_r$ ;

( $r_0=0.5$ ,  $D=1.0\text{cm}$ )

(c) Sample radius,  $r_0$ .

( $\epsilon_r=10$ ,  $D=1.0\text{cm}$ )

The Curve numbers correspond to those of Figure 4.6.



Using this formula,  $\bar{Q}_c$  is calculated and compared with the results of the mode-matching analysis for selected  $D$ ,  $r_0$  and  $\epsilon'_r$  in Table 4.1. As expected, the error decreases with reducing gap width and wavelength. What is not expected is that the accuracy becomes better for a larger  $\epsilon'_r$  and  $r_0$ . This may be due to the fact that a dielectric loaded gap makes a re-entrant cavity behave more like a zero-gap cavity than would an unloaded gap.

**Table 4.1** Calculated Normalized  $Q_c$ , Approximated Analytical results (Eq. (4.24)) vs. numerical results ( $r_1=1.25, r_2=4.5, L=20.0\text{cm}$ ).

D/L	$r_0/r_1$	$\epsilon_r$	$\lambda_0/(4\pi L)$	$\bar{Q}_c$		Difference
				Eq. (2.24)	MMMC2	
0.05	0.5	10	0.121	1.37	1.25	-8.6%
0.05	0.5	10	0.072	1.76	1.62	-7.7%
0.05	0.5	10	0.051	2.04	1.93	-5.5%
0.05	0.5	10	0.039	2.25	2.20	-2.4%
0.10	0.5	10	0.039	2.42	2.20	-8.9%
0.05	0.5	1.0	0.038	2.52	2.24	-11.2%
0.05	0.5	20	0.040	2.10	2.18	4.0%
0.05	0.2	10	0.038	2.44	2.22	-8.6%

#### 4.5.2 Normalized $Q_D$ and sample energy density

As  $\bar{Q}_c$ , the normalized dielectric cavity Q-factor is defined as

$$\bar{Q}_D = Q_D \tan \delta = W_E / W_D = 1 / F_\ell \quad (4.26)$$

We see that the inverse of  $\bar{Q}_D$  is simply the sample loading factor,  $F_\ell$ , which is the ratio of the energy stored in the sample to that in the cavity. To be more meaningful,  $F_\ell$  is divided by a volume filling factor  $F_0$ , resulting in an energy density ratio  $f_\ell$  as follows:

$$f_\ell = F_\ell / F_0 = (W_D / V_D) / (W_E / V_C) \quad (4.27)$$

$$F_\ell = W_D / W_E \quad (4.28)$$

$$F_0 = V_D / V_C \quad (4.29)$$

where  $V_D$  and  $V_C$  are the volume of the sample and the cavity. Therefore,  $Q_D$  is related to  $f_\ell$  by

$$1/Q_D = \tan\delta/\bar{Q}_D = F_C \cdot f_\ell \cdot \tan\delta \quad (4.30)$$

Curves of  $f_\ell$  versus  $D$ ,  $\epsilon'_r$  and  $r_0/r_1$  are plotted in Figure 4.9. They clearly exhibit a strongly focused electric field existing in the gap which explains the high heating rate obtained from this structure [23]. However, the focused gap field also imposes limitations on processable volume and loss range of the sample. For example, if  $f_\ell=500$  and  $\tan\delta=0.1$ , a sample with a filling factor of  $1/500$  will deteriorate the total cavity Q-factor from any high value, say 2000, to a Q of less than 10. Therefore, it is necessary to reduce the sample volume or increase the input power to maintain a certain heating rate.

In addition, the following conclusions can be made based on the results of the  $f_\ell$  curves:

(1) The sample energy density rises exponentially as the gap is reduced in Figure 4.9a. An increase in wavelength virtually reduces the gap width which suggests that low frequency operation is preferred to heat samples with practical dimensions.

(2) In Figure 4.9b, the sample energy density increases almost linearly with  $\epsilon'_r$  for low  $\epsilon'_r$ . It then tends to saturate and drop off slowly with increasing  $\epsilon'_r$  due to the mode shifting away from being a capacitive mode. This relatively flat portion of the curve is advantageous in maintaining a stable heating rate while the sample's permittivity varies with temperature.

(3) The decrease in sample energy density in Figure 4.9c with increase of sample radius is mainly due to the gap E-field being approximately a  $J_0(kr)$  function which decreases with large  $r$ . In order to have a relatively uniform radial field profile, the sample radius should be restricted to less than 40% of the center conductor radius.

#### 4.6 Effects of Insertion Hole

The presence of the sample insertion hole in the re-entrant gap has similar effects on cavity characteristics as widening the gap. Using this analogy, we may qualitatively expect that the holes will cause the

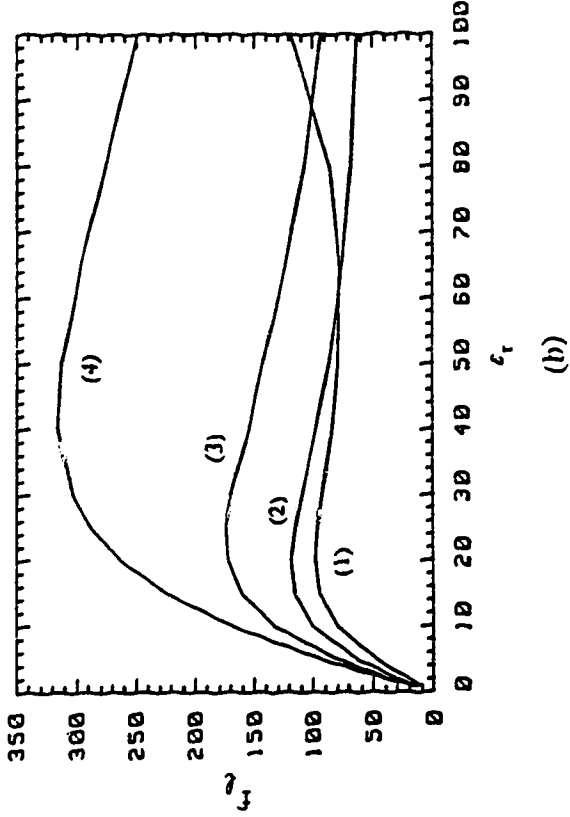


Figure 4.9 Sample energy density ratio

( $r_1=1.25$ ,  $r_2=4.5$ ,  $L=20.0\text{cm}$ )  
versus:

(a) Gap width,  $D$ ;

( $r_0=0.5\text{cm}$ ,  $\epsilon_r=10$ )

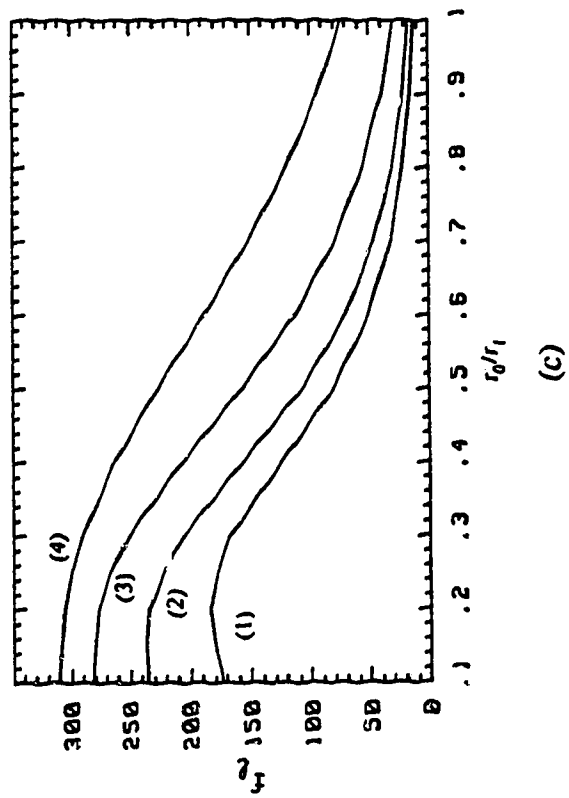
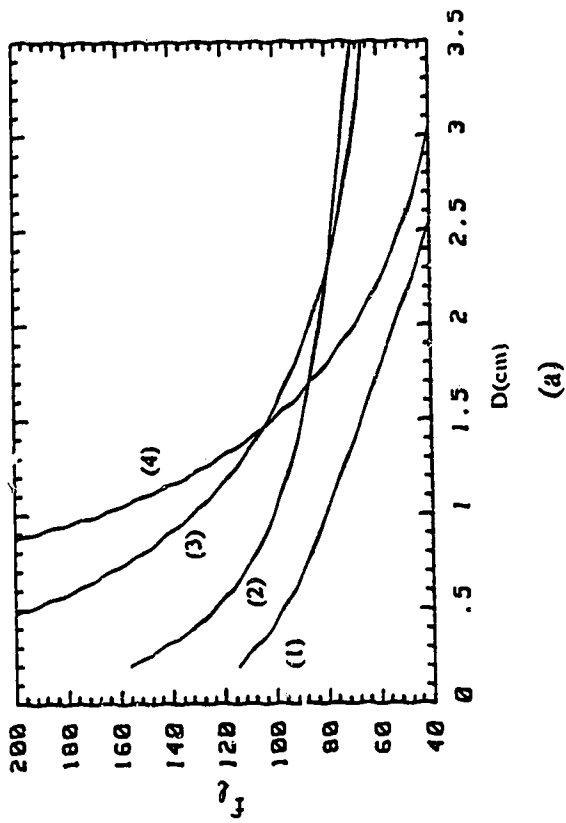
(b) Dielectric constant,  $\epsilon_r$ ;

( $r_0=0.5$ ,  $D=1.0\text{cm}$ )

(c) Sample radius,  $r_0$ .

( $\epsilon_r=10$ ,  $D=1.0\text{cm}$ )

The Curve numbers correspond to those of Figure 4.6.



gap capacitance and gap E-field to decrease or the resonant frequency to increase. The reduced gap fields will in turn lessen the sample loading effects, namely the frequency shift and Q-factor drop caused by the sample. On the other hand, some of the electric energy now also exists inside the holes, equivalently increasing the sample length or volume. In this section, we will closely examine these effects by comparing the numerical results with those of the no-hole case. Also discussed is the case using a sample holder, which acts to enhance the hole effects.

#### 4.6.1 Hole field attenuation

Due to the hole diameter being much less than the wavelength, fields cannot propagate but decay along the path deeper into the holes. As shown in Figure 4.10, the E-field at some distance into the hole is attenuated to a negligible level, say 5%, a number corresponding to a negligible variation in the calculated resonant frequency. This distance may be called effective hole depth,  $z_h$ . It will increase with sample permittivity. The dependence of the effective depth on the permittivity is illustrated in Figure 4.11. It shows that as the dielectric constant increases the effective depth increases, and eventually reaches infinity where the hole is no longer cut-off.

#### 4.6.2 Gap field distribution

As expected, the E-field intensity in the gap is weakened and its peak value shifts away from the axis when the holes appear in the gap. This is demonstrated in Figure 4.12, where radial distributions of  $E_z$  in the midplane of the gap are plotted for three cavities: (1) without hole or a sample holder; (2) with holes but without the holder; and (3) with both holes and the holder. It shows that the peak field is shifted from the axis to the radial edge of the holes and the presence of a sample holder further reduces the gap field.

#### 4.6.3 Resonant frequency shift

For the same cavity structures of (1), (2) and (3) as in Figure

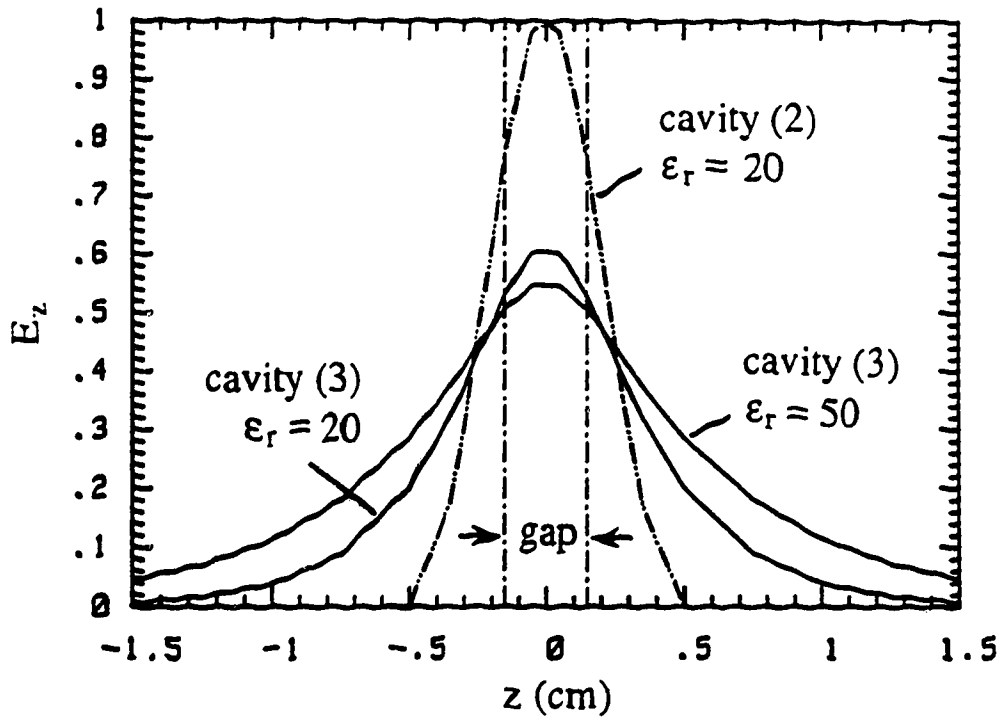


Figure 4.10 Axial distribution of the normalized  $E_z$  in the gap and adjacent hole region at  $r=0$  and at about 3GHz ( $r_s=0.24, r_1=1.23, r_2=4.51, L=20.5, D=0.3$ cm, for cavity (2) and (3) see Figure 4.12).

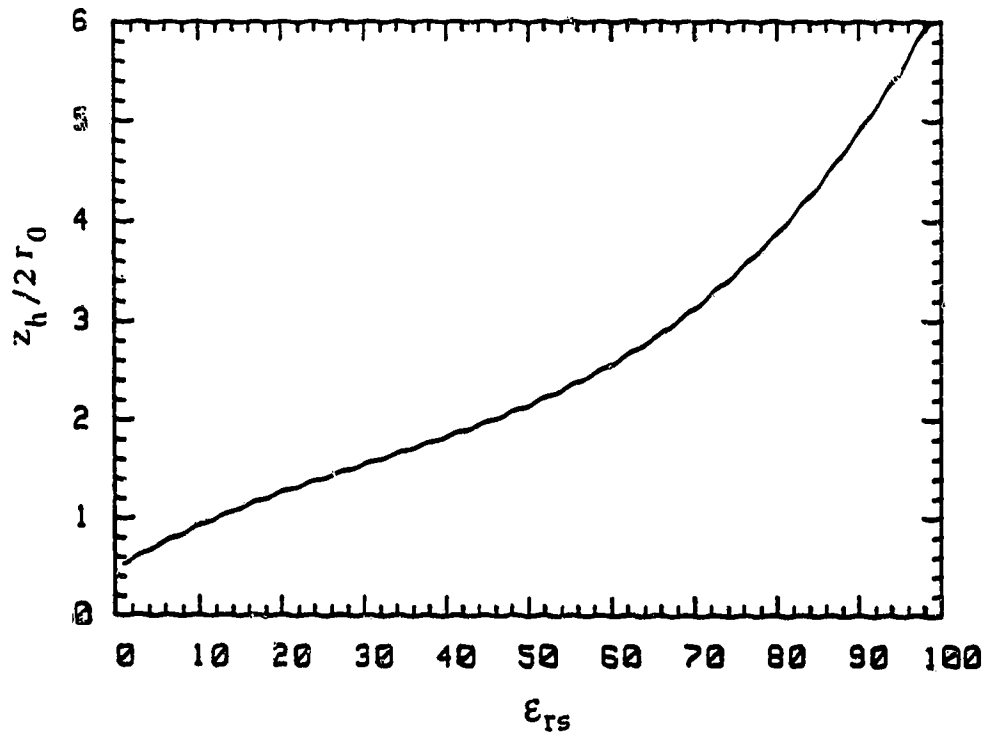
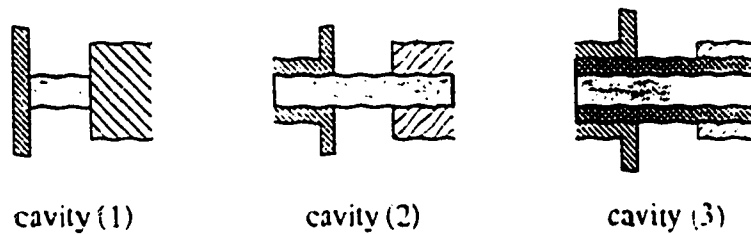


Figure 4.11 The effective hole depth of cavity (3) (see Figure 4.12) as a function of dielectric constant.





cavity (1) - without hole and holder ( $r_0=0$ )  
 cavity (2) - with hole and without holder ( $r_0=r_s$ )  
 cavity (3) - with both hole and holder ( $r_0=0.37\text{cm}$ ,  $\epsilon_{rs} \approx 3.78$ )

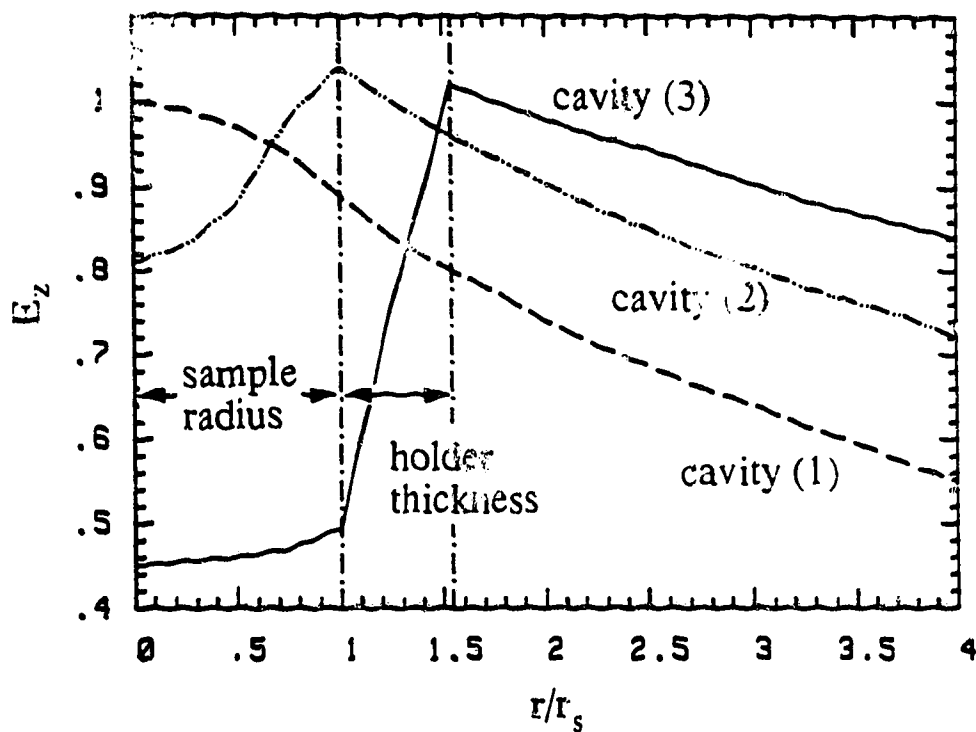


Figure 4.12 Radial distribution of the normalized  $E_z$  at the gap mid-plane at about 3GHz in three structures (The other cavity dimensions are the same as in Figure 4.10 and  $\epsilon_{rs} \approx 20$ ).

4.12, resonant frequency shifts are calculated and plotted as a function of permittivity in Figure 4.13. The results are in qualitative agreement with those of the gap field in Figure 4.12. In other words, the stronger the gap field, the greater the shift in resonant frequency when

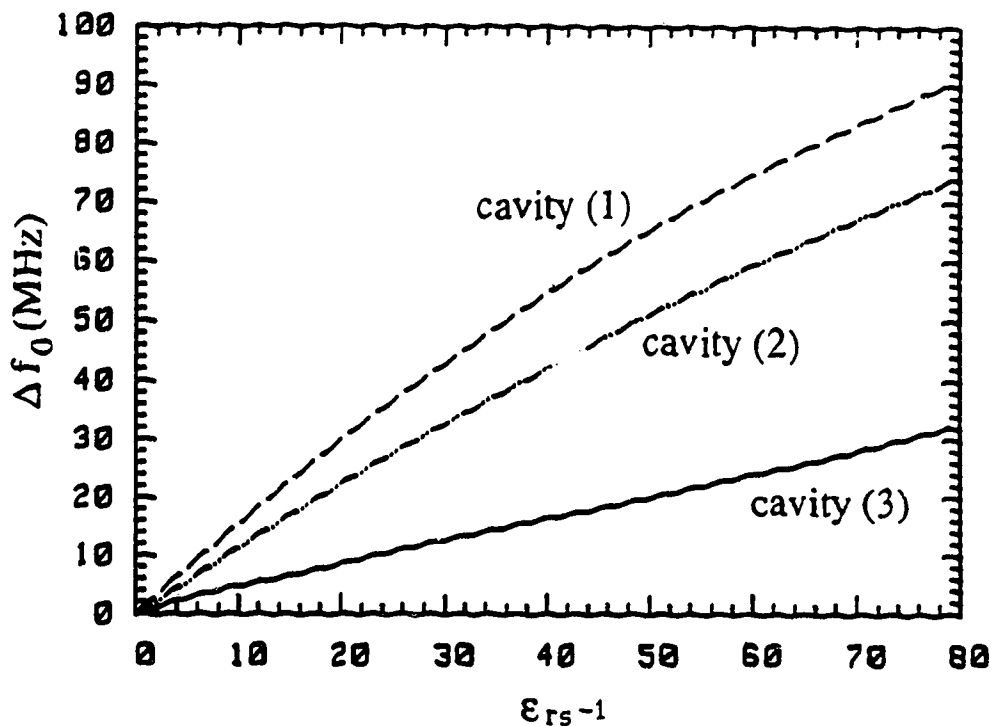


Figure 4.13 Resonant frequency shift produced by a sample at about 3GHz in cavity (1), (2) and (3) (see Figure 4.12).

loading the gap. The slope of  $\Delta f_0$  versus  $\epsilon'_r$  determines the sensitivity of dielectric determinations. However, it also controls the measurable range of dielectric properties because a larger detuning of a resonator tends to bring about more difficulties such as impedance mismatch in practical measurements. Therefore, a coaxial cavity with sample insertion holes and holder can extend the measurable range of dielectric properties. Moreover, it presents a better linearity of frequency shift as a function of dielectric constant. As shown in Figure 4.13, curve (3) is almost a straight line up to  $\epsilon'_r = 80$ , which is a great convenience in dielectric determinations. For instance, one can have a linear cavity length variation in the length variation method (see section 4.7). This improvement in linearity is not only the consequence of a reduction of the gap field but also the outcome of an increased effective hole depth at a higher dielectric constant which offsets the saturation exhibited in a normal detuning curve, such as the curve for cavity (1) in Figure 4.13.

#### 4.6.4 Energy stored and dissipated in sample

The electric energy stored in a dielectric sample loaded through an insertion hole can be broken into two parts, namely the gap portion and the hole portion energy. The presence of the holes reduces the gap portion energy because of the decreased gap field but also yields an additional amount of energy in the holes. To examine these two portions of energy closely, the stored energy in a sample is integrated over the volume of the gap and the holes separately for varied dielectric constants, and presented in Figure 4.14 together with the results of the no-hole case. It shows that the hole portion contributes an appreciable percentage of the total energy and that it increases with dielectric constant at an increasing rate. It is this hole portion energy that compensates for the reduction of the E-field in the sample due to the increase of the dielectric constant, thus extending the linear range in the curve of the resonant frequency shift versus dielectric constant.

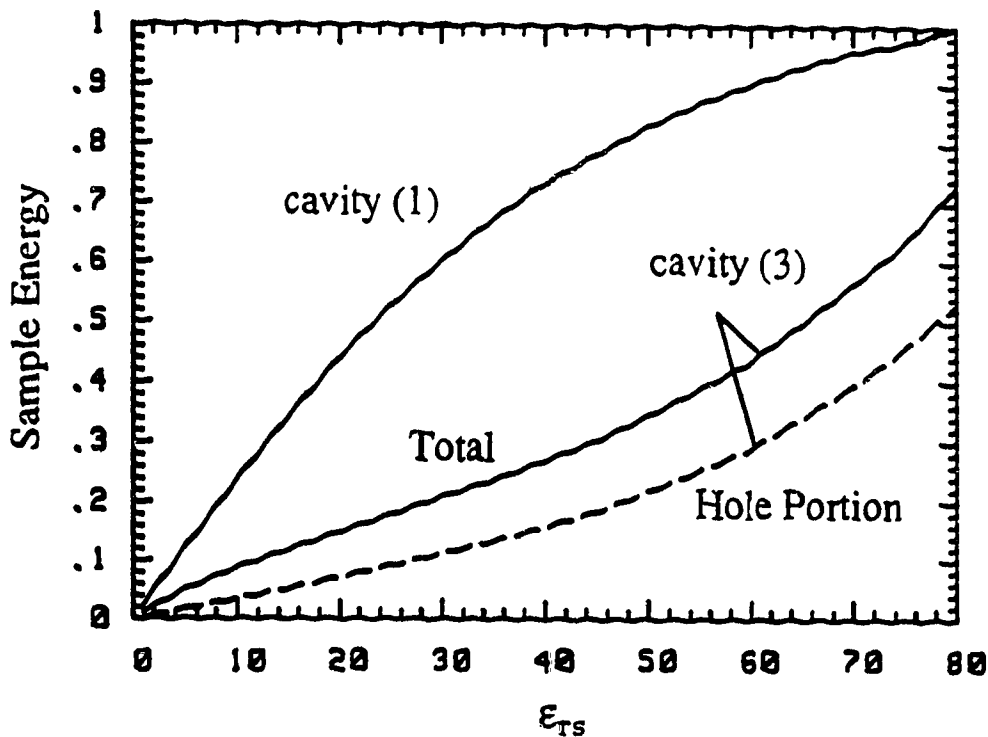


Figure 4.14 Normalized electric energy stored in a sample as a function of the sample's dielectric constant of cavity (1) and (2) (see Figure 4.12).

As stated in Eq. (2.31), the dissipated energy in a sample is directly proportional to the stored energy, with the proportionality constant being the loss tangent of the sample. Consequently, for a constant loss tangent, the dissipated energy in the sample increases with the dielectric constant,  $\epsilon'_r$ , in the same manner as the stored energy, i.e., at a nearly constant rate in a lower range of  $\epsilon'_r$  and at an increasing rate at higher  $\epsilon'_r$ . When the cavity is loaded with a sample having both a high dielectric constant and a high loss tangent, it will present a very low Q-factor and will be severely under-coupled. Therefore, in order to obtain a wider measurable permittivity range, the volume of samples must still be limited, even though the insertion hole has already lowered the gap field.

#### 4.6.5 Hole effect and wavelength

It is evident that the hole effects discussed above depend on the wavelength. Considering the hole as a dielectric filled cylindrical waveguide operating in  $TM_{01}$  mode, we can write the cutoff condition as [31]

$$\lambda_0 > \lambda_c \quad (4.31)$$

$$\lambda_c = 2.62r_0\sqrt{\epsilon'_r} \quad (4.32)$$

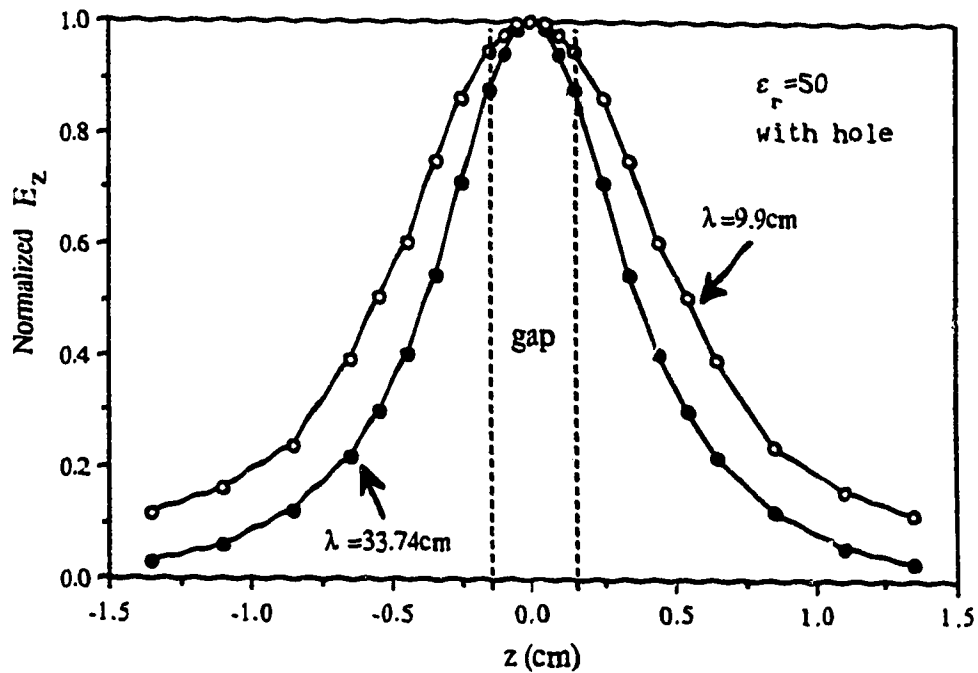
$$\text{or } r_0 < \lambda_0 / (2.62\sqrt{\epsilon'_r}) \quad (4.33)$$

We can define a critical hole radius as

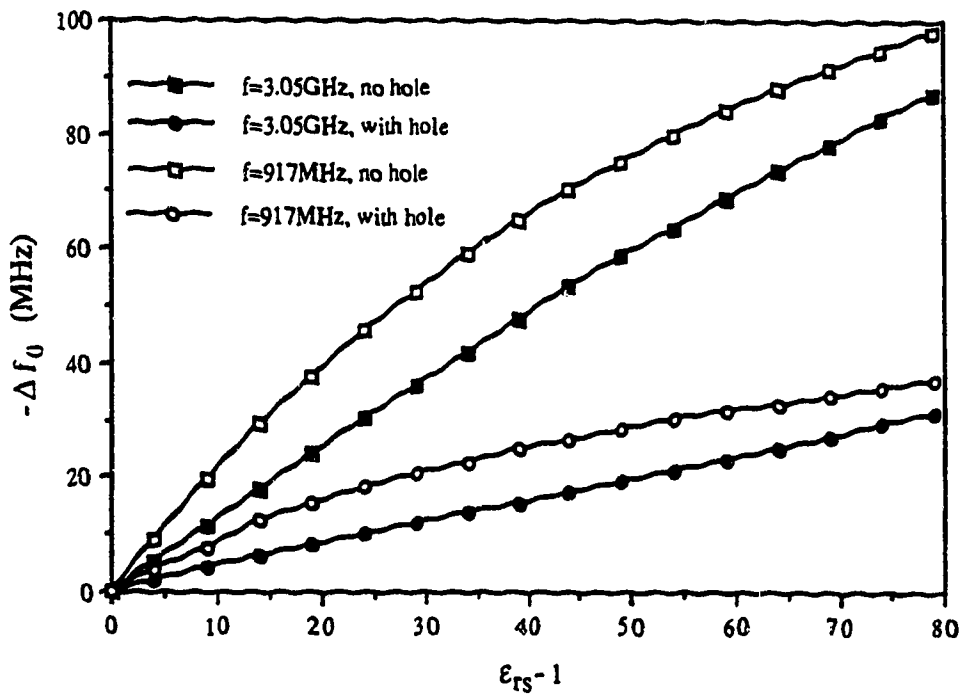
$$r_{0c} = \lambda_0 / (2.62\sqrt{\epsilon'_{rmax}}) \quad (4.34)$$

where  $\epsilon'_{rmax}$  is the maximum dielectric constant to be measured. This equation gives the maximum hole size one can use in practice.

Under the cutoff condition, the decay rate of the hole fields is determined by the ratio of  $\lambda_0/\lambda_c$ . For a given hole, the hole effects on the cavity characteristics is weakened by the increase of wavelength. To show this, the hole field distribution and the frequency shifts by the sample are plotted in Figure 4.15 for two different frequency bands. We can see that the hole field is attenuated faster and the frequency shift curve becomes less linear at 915MHz than at 3GHz.



(a)



(b)

Figure 4.15 (a) The axial distribution ( $r=0$ ) of normalized  $E_z$  and (b) the resonant frequency shift as a function of sample's dielectric constant in two different frequency bands ( $r_s=0.24$ ,  $r_0=0.355$ ,  $r_1=1.244$ ,  $r_2=5.0$ ,  $L=20.0$ ,  $D=0.3\text{cm}$ , and  $r_0=0$  for the no-hole case and  $r_0=0.355\text{cm}$  and  $\epsilon_{rh}=3.78$  for the hole case).

#### 4.7 Calibration Curves for Dielectric Determination

To determine dielectric constants and loss tangents, it is essential to find their relationships to the measurable parameters which are the resonant frequency shift and the Q-factor change produced by the sample in most cases. Such relationships can be readily obtained by the mode-matching analysis. In fact, they have implicitly been presented already in the above discussions of cavity characteristics.

The calibration curve for determining dielectric constants can be constructed by plotting curves of  $\epsilon'_r$  vs.  $\Delta f_0$ . The steeper the curve, the wider the range of dielectric constant that can be measured for a given maximum  $\Delta f_0$  but the poorer the accuracy of the determination.

The loss tangent can be related to the cavity Q change via the sample loading factor as

$$\tan\delta = \frac{1}{F_\ell} \cdot \left( \frac{1}{Q_L} - \frac{1}{Q_C} \right) \quad (4.35)$$

The loading factor  $F_\ell$  has been plotted in Figure 4.9 as a function of  $\epsilon'_r$ , in the form of the sample energy density,  $f_\ell$ , which is equal to  $F_\ell$  divided by the volume filling factor  $F_0$ . It should be pointed out that  $Q_C$  is not a constant but a function of  $\epsilon'_r$ , hence; it is hardly a measurable parameter. Nevertheless, we can use the empty cavity Q-factor,  $Q_0$ , as an approximation of  $Q_C$ , so that Eq. (4.35) becomes

$$\tan\delta \approx \frac{1}{F_\ell} \cdot \left( \frac{1}{Q_L} - \frac{1}{Q_0} \right) = \frac{1}{F_\ell} \cdot \Delta(1/Q_0) \quad (4.36)$$

We now see that  $F_\ell$  is the only parameter required to determine  $\tan\delta$  from the measured  $\Delta(1/Q_0)$ . Therefore,  $F_\ell = F_\ell(\epsilon'_r)$  is the calibration curve for the determination of the loss tangent.

The approximation made in Eq. (4.36) may cause an error in loss tangent determinations since  $Q_0$  is only the value of  $Q_C$  at  $\epsilon'_r=1$ . Such an error may be reduced by a simple correction. Recalling that  $Q_C$  is proportional to the square root of  $f_0$  (Eq. (4.24)), one can express  $Q_C$  by  $Q_0$  approximately as follows

$$Q_C = Q_0 \sqrt{(f_0 + \Delta f_0)/f_0} \approx Q_0 (1 + 0.5 \Delta f_0 / f_0) \quad (4.37)$$

where  $f_0$  is the resonant frequency of the empty cavity and  $\Delta f_0$  is the frequency shift produced by the sample and always has negative values.

As discussed in Chapter 2, if the sample loading factor is very small and the perturbation condition is satisfied, the loss tangent can also be found from the frequency shift, thus eliminating the need for the calibration curve of  $F_\ell(\epsilon'_r)$ . Rewriting Eq.(2.17) as follows

$$\tan\delta = \frac{1}{F'_\ell} \cdot \Delta(1/Q_0) \quad (4.38)$$

$$F'_\ell = - \frac{\epsilon'_r}{\epsilon'_r - 1} \cdot \frac{2\Delta f_0}{f_0} \quad (4.39)$$

We expect that  $F'_\ell$  of Eq.(4.39) should be equal to  $F_\ell$  of Eq.(4.28) for a small sample with a low dielectric constant. This is confirmed by the plot of  $F'_\ell$  and  $F_\ell$  in Figure 4.16 which are the calculated results for a given cavity. The figure indicates that the difference between  $F'_\ell$  and  $F_\ell$  is rather small for  $\epsilon'_r \leq 10$ .

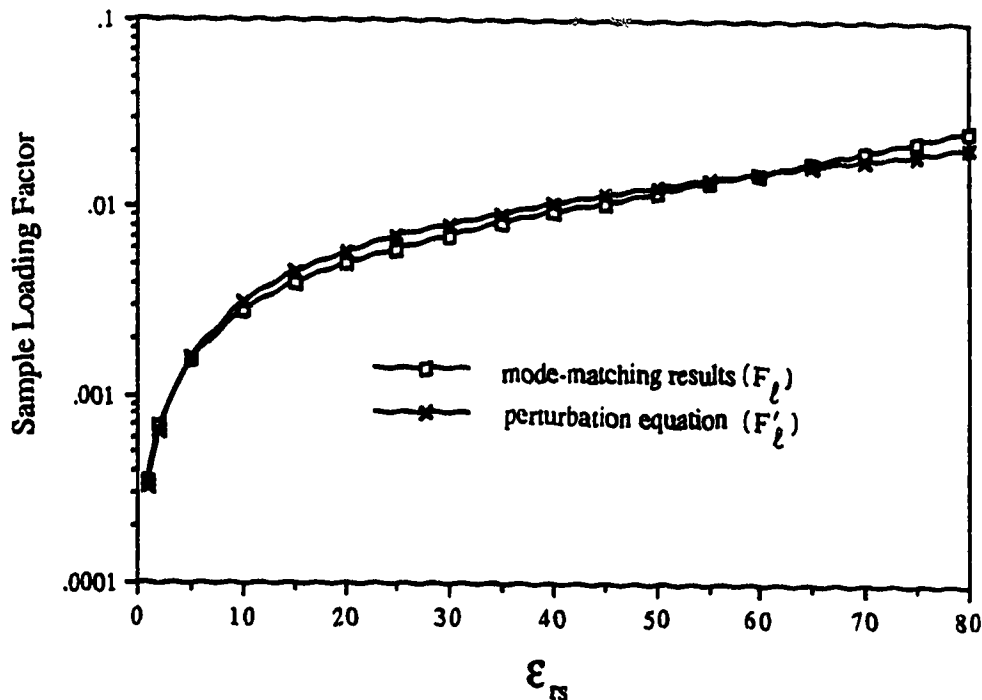


Figure 4.16 The sample loading factor as a function of the sample's dielectric constant; perturbation compared with mode-matching results. The cavity is the same as that in Figure 4.15a.

The dielectric constant can also be determined in a CW mode, i.e., at a single frequency, rather than in the sweeping mode, by the so-called length variation method [9]. In this method, a sample loaded cavity is re-resonated by an adjustment of the cavity length; thus the dielectric constant of the sample is found from the length variation. To do so, a calibration curve is required to relate the dielectric constant to the length variation. It can be obtained from the mode-matching analysis as well. Figure 4.17 is an example of such a calibration curve. It is calculated for a cavity having an insertion hole and operating at 3GHz. Since both functions of  $\Delta L$  vs.  $\Delta f_0$  and  $\Delta f_0$  vs.  $\epsilon'_r$  are almost linear, the obtained calibration curve is roughly a straight line. In this length variation method, one can also adjust the gap width instead of the cavity length to re-resonate the loaded cavity. For this purpose, a calibration curve of  $\epsilon'_r$  vs.  $\Delta D$  is calculated and presented in Figure 4.18. It shows that the curve tends toward saturation at larger  $\epsilon'_r$  due to the increase of the sample volume with the gap width.

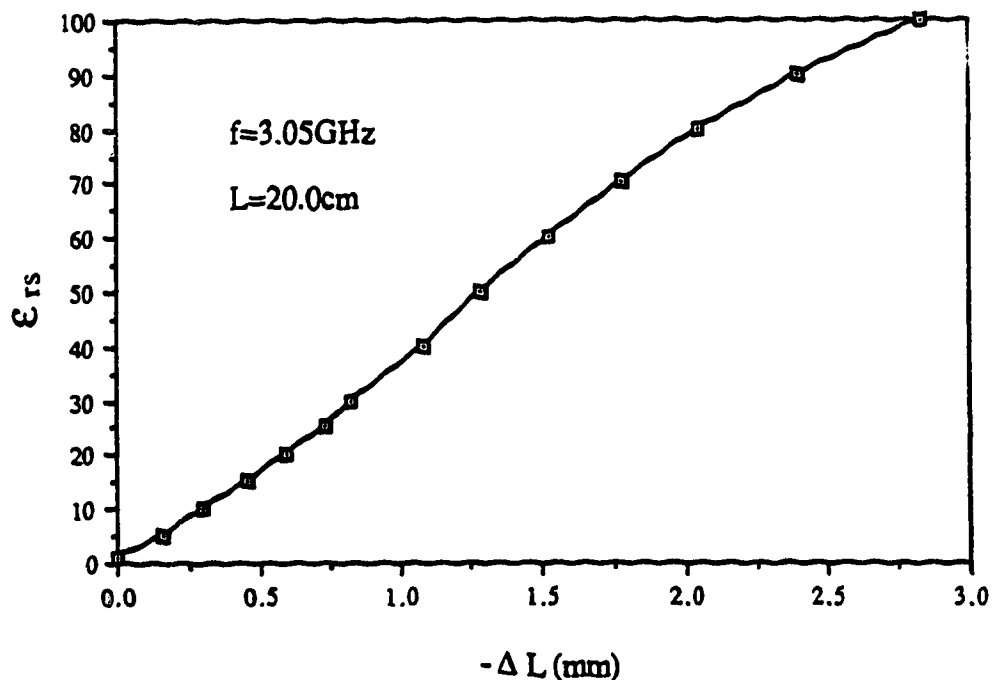


Figure 4.17 Calibration curve for determining dielectric constant in the length variation method. The cavity is the same as that in Figure 4.15a.



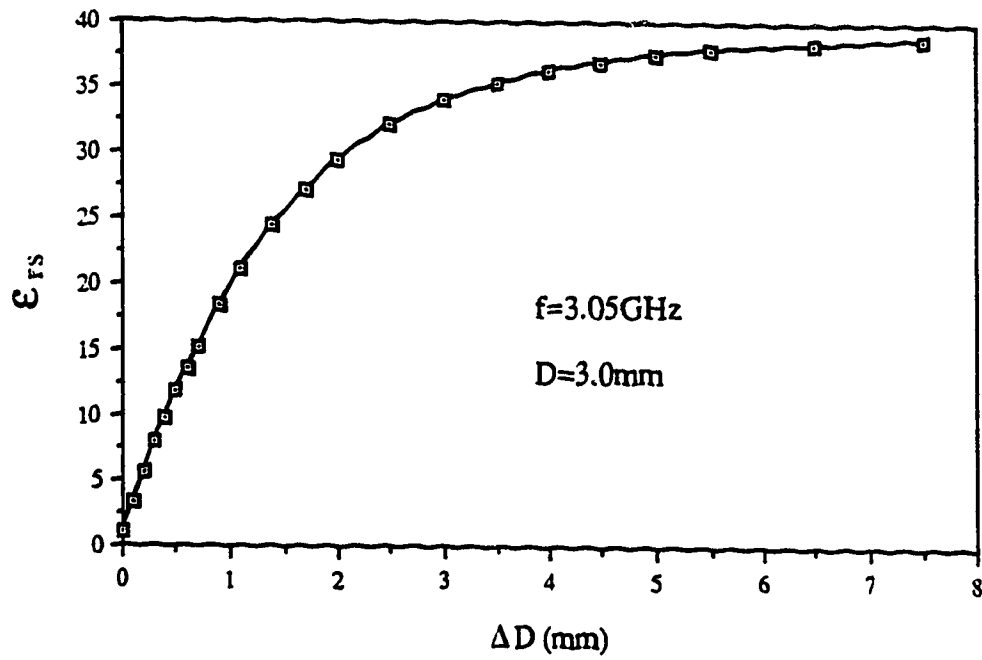


Figure 4.18 Calibration curve for determining dielectric constant in the gap variation method. The cavity is the same as that in Fig. 4.15a.

CHAPTER 5  
MEASUREMENT AND CONTROL SYSTEM

The high temperature dielectric measurement technique proposed in this thesis, as stated in Chapter 1, is a resonant cavity method in which a coaxial re-entrant cavity is designed as a sample heater as well as a test chamber. As a test chamber, the cavity resonates in the testing band and the measurement of the changes in the resonant parameters produced by a sample allows the determination of its complex dielectric constant. As a sample heater, the cavity supplies a focused E-field which is also a resonant field to raise the sample's temperature via its microwave absorption. A sample is tested and heated simultaneously in different frequency bands to avoid the cross coupling of heating power and measurement signal.

To realize this scheme, an experimental system is implemented and shown in the block diagram of Figure 5.1 [58,59]. In such a setup, the cavity is connected with three channels. The testing channel is basically a reflectometer which measures the reflection spectrum, that is, reflection coefficient versus frequency, of the cavity in S-band (2-

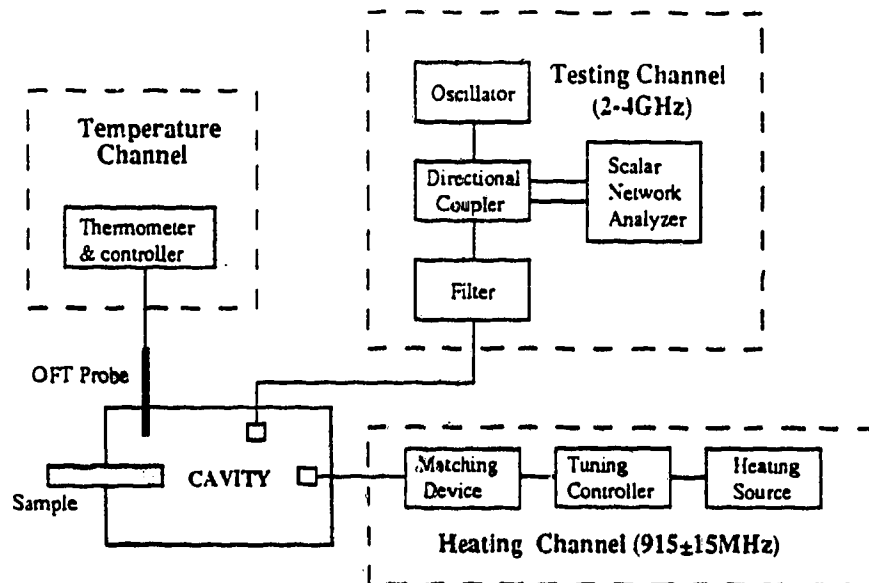


Figure 5.1 Experimental system for high temperature dielectric measurements.

4GHz). The resonant frequency shift and Q-factor can then be derived from the reflection spectrum. The heating channel is mainly a solid state microwave power source at 915MHz, tunable over a 30MHz band and capable of providing a maximum output of 120W. The power is delivered to the sample loaded cavity via a matching device and a tuning controller which ensure maximum power delivery to the cavity. A high pass filter is connected between the cavity and the reflectometer operating over S-band to block the power from the 915MHz heating source. The third channel is a thermometer for measuring and controlling the sample's temperature, using an optical fiber probe which does not disturb microwave fields as much as a thermocouple. In this chapter, the design of the cavity will be addressed first due to the central role which it plays in the system. The testing, heating and temperature measuring techniques involved in this system will then be presented. Thereafter, the associated errors and the dynamic measurement range are discussed.

## 5.1 Cavity Design

### 5.1.1 Design considerations

The cavity to be designed is schematically shown in Figure 5.2. The main considerations for such a design are:

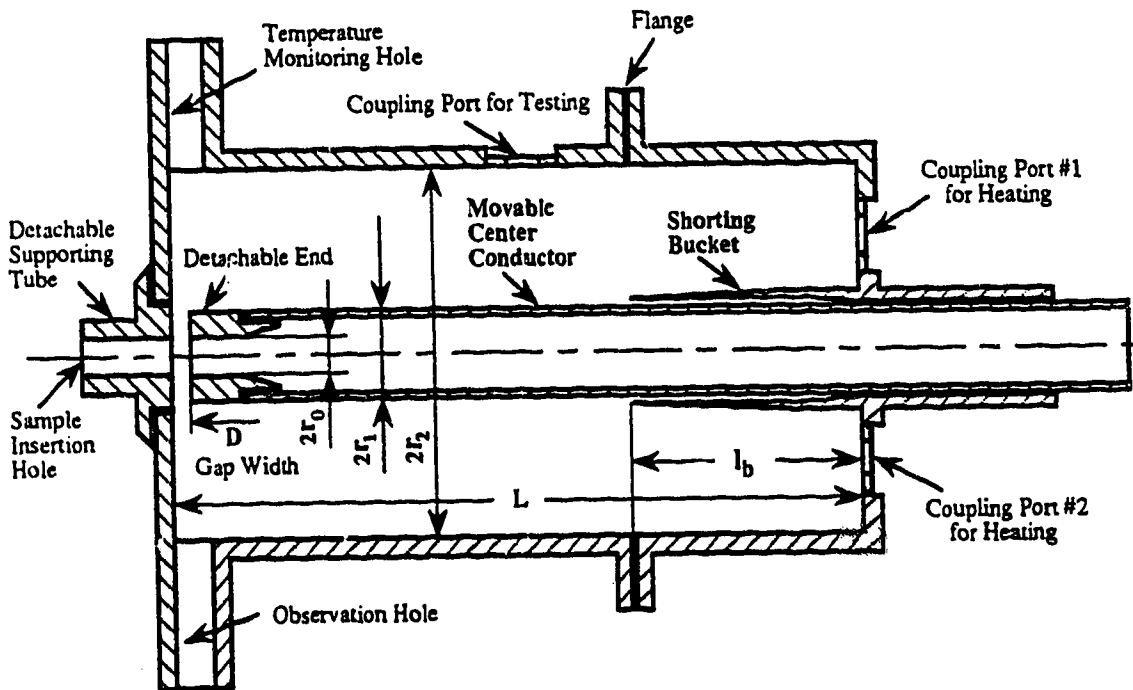


Figure 5.2 Cavity structure of dielectrometer.

1. The heating and testing operations require two resonant modes. One is within the band for which the heating power source is available, namely  $915 \pm 15$  MHz; the other is chosen to be around 3 GHz.

2. To ensure good measurement reliability and a high cavity Q-factor, we prefer that all the cavity dimensions could be fixed. However, we often need to change cavity dimensions, particularly the gap width and the cavity length. In order to maintain mechanical simplicity, we choose the gap width as the only adjustable dimension.

3. The sample volume which interacts with the cavity E-field is determined by the gap width and the insertion hole diameter. These dimensions are chosen based on a compromise between the test sensitivity and the dynamic measurement and heating range. Though a larger sample volume produces a greater resonant frequency shift and Q change, and therefore, better sensitivity in dielectric determinations, it causes more detuning and mismatching problems in a practical testing and heating situation.

### 5.1.2 Determination of cavity dimensions

#### A. Cavity radius

As indicated in Appendix 2, at a given frequency, the unloaded Q-factor of a coaxial cavity is proportional to the radius of its outer conductor,  $r_2$ , and for a fixed  $r_2$ , it reaches a maximum value when  $r_2/r_1 = 3.58$ , a ratio which corresponds to a characteristic impedance of  $77 \Omega$  [60]. We choose  $r_2 = 5.1$  cm (2"), then  $r_1 = 5.1/3.58 = 1.42$  cm (0.56"). 1" standard pipe is used for the center conductor, i.e.,  $r_1 = 1.27$  cm at the machining stage.

It is necessary to check for the existence of possible transverse modes. In a coaxial line of  $r_1 = 1.27$  cm and  $r_2 = 5.1$  cm, the cutoff frequencies of all the transverse modes are above 3.8 GHz except for  $TE_{11}$  and  $TE_{21}$  modes whose  $f_c$  is 1.55 GHz and 2.83 GHz respectively [31]. Neglecting the gap effect and assuming  $L = 20$  cm, we can find that there are two transverse resonant modes,  $TE_{211}$  and  $TE_{212}$ , whose resonant frequencies are close to 3 GHz.  $f_0(TE_{211}) = 2.9$  GHz and  $f_0(TE_{212}) = 3.2$  GHz. The testing band should be chosen in between these two modes, i.e., centered at 3.05 GHz.

## B. Cavity length

The cavity length is mainly determined by the resonant modes and the frequency band. For capacitive modes, the length of the coaxial section is given by Eq.(4.10), i.e.,

$$(n-1)\lambda_0/2 < l < (2n-1)\lambda_0/4 \quad (5.1)$$

Considering that the short-circuit design of Figure 5.2 requires the cavity length to be larger than a quarter wavelength, we choose the second lowest mode ( $n=2$ ), i.e.,  $TEM_{3/4}$ , in the heating band. Substituting  $\lambda_0=30(\text{cm}\cdot\text{ns}^{-1})/0.930(\text{GHz})=32.26\text{cm}$  and  $n=2$  into Eq.(5.1), we have

$$16.13\text{cm} < l < 24.19\text{cm} \quad (5.2)$$

Similarly, in the testing band,  $f_0=3.05\text{GHz}$ ,  $\lambda_0=9.84\text{cm}$ , so the length required for the  $TEM_{9/4}$  mode, i.e.,  $n=5$ , is

$$19.66\text{cm} < l < 22.12\text{cm} \quad (5.3)$$

The exact cavity length cannot be determined until other cavity dimensions are given. Neglecting the hole effects and taking  $D=0.3\text{cm}$ , we can compute the unloaded resonant frequencies of the  $TEM_{3/4}$  and  $TEM_{9/4}$  modes for  $L$  varying from 19.5cm to 20.5cm, using the mode-matching analysis program MMMC1. The calculated results plotted in Figure 5.3 show that the cavity of  $L=20\text{cm}$  can resonate at both 917MHz and 3.05 GHz. It may be useful to know that this cavity also resonates at 2.32GHz( $TEM_{7/4}$ ) which is the closest to the 2.45GHz band. The actual resonant frequencies will be slightly higher because of the presence of the insertion hole and the coupling loop. The insertion hole reduces the gap capacitance and the coupling loop tends to shorten the cavity length, both resulting in a higher resonant frequency.

## C. Insertion hole radius and gap width

The insertion hole radius,  $r_0$ , and gap width,  $D$ , actually determine the effective sample volume which interacts with the gap E-field. As developed in section 5.5,  $r_0$  and  $D$  determine the measurement range of dielectric constant and loss tangent. The requirements for extending the upper and lower limit of measurable  $\epsilon'_r$  and  $\tan\delta$  are in conflict with one

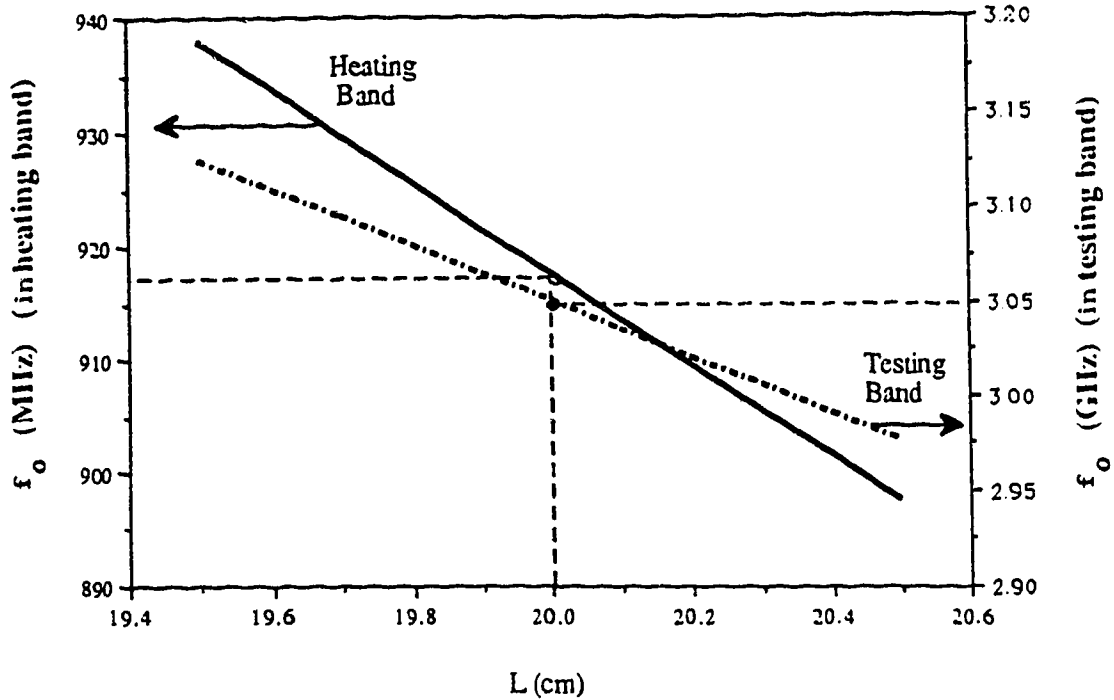


Figure 5.3 Resonant frequency plotted as a function of cavity length in both the testing and heating bands ( $r_1=1.27$ ,  $r_2=5.1$ ,  $D=0.3\text{cm}$ ,  $\epsilon_{rs}=1.0$ , by MMMC1).

another. Moreover, a wider measurement range is usually obtained at the price of losing the measurement sensitivity. To be flexible, therefore, the gap width is made adjustable by moving the center conductor, while the sample insertion hole radius can be altered by replacing the detachable end of the center conductor and the insertion hole supporting pipe on the endplate, as indicated in Figure 5.2.

The maximum  $r_0$  is limited by the cutoff condition expressed by Eq. (4.34). Using  $\epsilon'_{r\max}=81$  and  $\lambda_0=10\text{cm}$  ( $f_0=3.0\text{GHz}$ ), we find  $r_{0c}=0.42\text{cm}$ . To ensure sufficient cutoff, we can take  $r_0=85\%r_{0c}=0.36\text{cm}$ . In order to use standard quartz tubes as sample holders,  $2r_0$  is chosen to be the outer diameter of the standard tubes, say, 7mm and 6mm. Using 7mm and 6mm sample holders, the sample radius is about 2.4 and 2.0mm. The gap width may be as large as permitted by the detuning and mismatching limits of the testing and heating channels. It can also be very small as long as arcing does not occur in the gap. However, the sample cannot be arbitrarily small for practical reasons.

### 5.1.3 Design of the non-contact short circuit

To allow the gap width to be adjustable, we have to design a movable center conductor. A non-contact short circuit design is thus required to ensure electrical reliability. A bucket structure as shown in Figure 5.4 is selected. To evaluate its performance, we should inspect the normalized input impedance at the effective shorting plane which is found to be [61]

$$\begin{aligned}\bar{Z}_s &= Z_s/Z_c = \bar{R}_s + j\bar{X}_s \\ &= \frac{1 + j\bar{Z}_g \tan\theta_b}{[1 + (1 + \bar{Z}_g) \tan^2\theta_b] + j[(1/\bar{Z}_g - 1) + \tan^2\theta_b/\bar{Z}_g] \tan\theta_b}\end{aligned}\quad (5.4)$$

where  $Z_c$  is the characteristic impedance of the coaxial section, i.e.,

$$Z_c = 60 \ln(r_2/r_1) \quad (5.5)$$

$\bar{Z}_g$  is the normalized characteristic impedance of the gap space between the bucket and the center conductor:

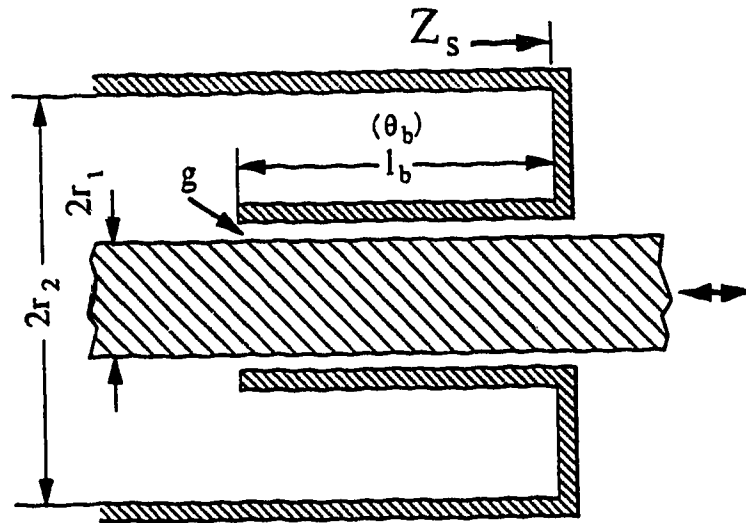


Figure 5.4 Simplified cross section of the shorting bucket.

$$\bar{Z}_g = \frac{60}{Z_c} \ln\left(\frac{r_1 + g}{r_1}\right) \approx \frac{60}{Z_c} g/r_1 \quad (5.6)$$

and  $\theta_b$  is the electrical length of the bucket:

$$\theta_b = 2\pi\ell_b/\lambda \quad (5.7)$$

The real part of  $\bar{Z}_s$  is the energy loss through the short circuit and it is usually expressed in decibel form as

$$L_R = 10\log(\bar{R}_s) \quad (\text{dB}) \quad (5.8)$$

It should be mentioned that this energy loss does not include the bucket surface loss, which is estimated to be about -35dB if the plunger is made of brass or is silver plated [62]. For this reason, it is unnecessary to reduce  $L_R$  below -35dB. The imaginary part of  $\bar{Z}_s$  is the reactance created by the short circuit assembly and can be viewed as an electrical length variation in degrees:

$$\Delta\theta_b = \tan^{-1}(\bar{X}_s) \quad (5.9)$$

or as an equivalent length shift

$$\Delta\ell_b = \lambda\Delta\theta_b/2\pi \quad (5.10)$$

In Figure 5.5,  $L_R$  and  $\Delta\theta_b$  are plotted against  $\theta_b$  from  $50^\circ$  to  $90^\circ$  for the structure of Figure 5.4 with  $r_2=5.1$ ,  $r_1=1.27$  and  $g=0.1\text{cm}$ . The curve of  $L_R$  is symmetric and  $\Delta\theta_b$  is anti-symmetric about  $90^\circ$ . Both  $L_R$  and  $\Delta\theta_b$  are periodic functions with a period of  $180^\circ$ .

The shorting bucket under design must have a very small  $\bar{R}_s$  and  $\bar{X}_s$  in both the testing and the heating band. If  $\ell_b=7.5\text{cm}$ , the electrical length of the bucket deviates from  $90^\circ$  by less than  $10^\circ$  in both the 3.0-3.1GHz and 900-930MHz bands. From Figure 5.5, we see that  $L_R$  and  $\Delta\theta_b$  corresponding to  $80^\circ$  are about -58dB and  $0^\circ$ , which means that a bucket with  $\ell_b=7.5\text{cm}$  and  $g=1\text{mm}$  simulates an ideal short circuit very well.

#### 5.1.4 Mechanical tolerances of cavity dimensions

Permissible mechanical tolerance can be evaluated from the maximum tolerable resonant frequency changes produced by cavity dimension variations. The results of such an evaluation are summarized in Table 5.1.



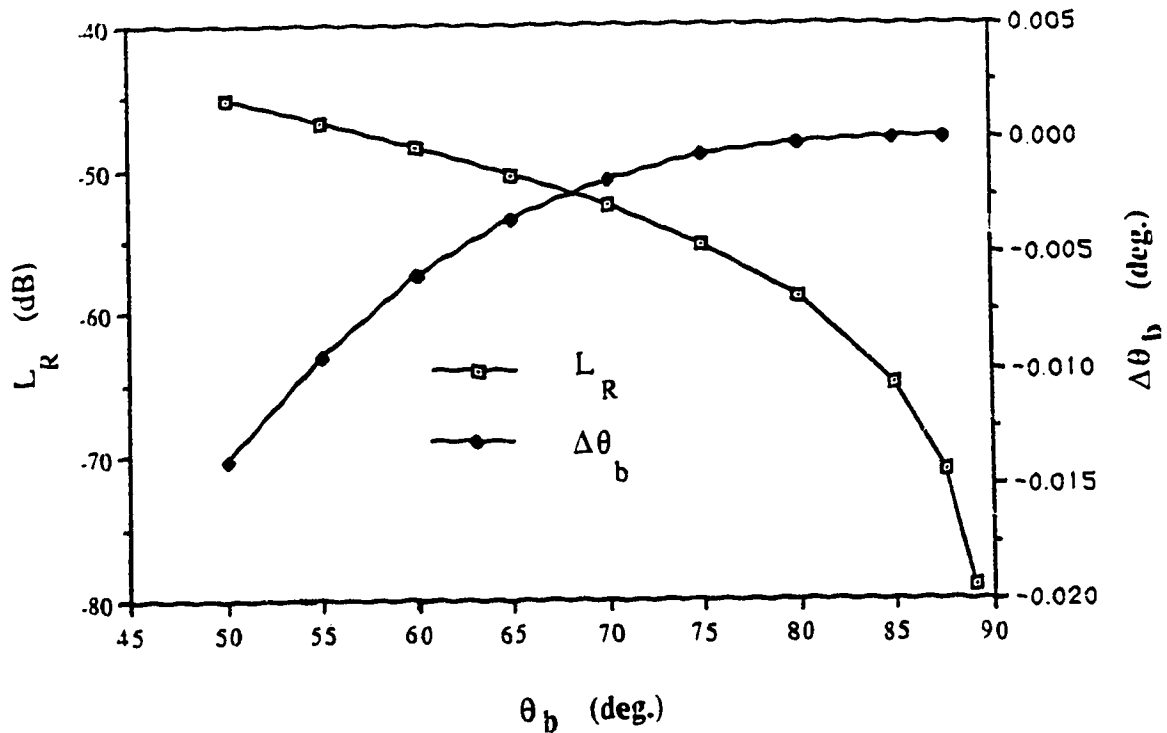


Figure 5.5 Normalized input impedance of the shorting bucket. Its real part,  $L_R$ , plotted in decibels and its imaginary part,  $\Delta\theta$ , in electrical length variation,  $\Delta\theta$  ( $r_1=1.27$ ,  $r_2=5.1$ ,  $g=0.1\text{cm}$ ).

Table 5.1 Evaluation of mechanical tolerance of cavity ( $f_0=3\text{GHz}$ ,  $r_2=5.0$ ,  $r_1=1.25$ ,  $r_0=0.35$ ,  $L=20.0$ ,  $D=0.3\text{cm}$ ,  $\epsilon_{r,s}=1.0$ , by MIMC4)

Dimension x	$\Delta\lambda/\Delta x$ mm/mm	$\Delta f/\Delta x$ MHz/mm	$\Delta x(\text{mm})$ at $\Delta f=\pm 1.0\text{MHz}$	$\Delta x(\text{mm})$ at $\Delta f=\pm 0.5\text{MHz}$
$r_2$	+0.088	-2.8	$\mp 0.36$	$\mp 0.18$
$r_1$	+0.088	-2.7	$\mp 0.37$	$\mp 0.19$
$r_0$	-0.030	+0.90	$\pm 1.1$	$\pm 0.56$
L	+0.48	-15.0	$\mp 0.068$	$\mp 0.034$
D	-0.35	+11.0	$\pm 0.091$	$\pm 0.045$

It should be mentioned that, although the resonant frequency is not sensitive to the variation in the hole radius,  $r_0$ , when the cavity is empty as shown in Table 5.1, it will become rather sensitive if a high permittivity sample is loaded. The error in the dielectric determination due to such a variation is analyzed in Chapter 6.

## 5.2 Testing Channel Operation

The requirement for the test channel is to measure the resonant frequency and the Q-factor of a sample loaded cavity precisely and rapidly. Standard measurement methods are adopted which are briefly summarized in this section. However, the associated errors will be discussed in detail. The program designed for automatic measurements is also described.

With a swept reflectometer, which consists of a scalar network analyzer, a sweep oscillator and a dual directional coupler as shown in Figure 5.1, it is straightforward to measure the resonant frequency. Using the HP8756A analyzer, the resonant frequency can be found using the Cursor Min function [63]. In determining dielectric constants, it is the resonant frequency shift not the frequency itself that must be accurate. The factors affecting the accuracy of  $\Delta f_0$  include the linearity of the sweep voltage-frequency correlation, the frequency stability and the frequency display resolution. The nonlinearity of the HP8623A sweep oscillator plug-in is less than  $\pm 0.154\%$  of the swept band [64], or  $\pm 0.045\text{MHz}$  over a 30MHz band. The frequency of the plug-in output fluctuates typically  $\pm 0.2\text{MHz}$  per 10 minute interval after 1 hour warm-up [64], due to the changes in temperature, line voltage and load SWR. The frequency display resolution is found to be better than 0.01MHz [63]. Therefore, the total measurement uncertainty in frequency shift is less than 0.26 MHz. For a short test period of 1 minute, this uncertainty can be as small as 0.05MHz.

The determination of the cavity Q-factor is much more complicated. The cavity Q-factor cannot be measured directly but is derived from the measured Q-factor,  $Q_m$ , and the coupling factor,  $\beta$ . Both of them can be determined from the measured reflection spectrum  $\Gamma(f)$  as shown in Figure 5.6 [65].

$$Q = (1+\beta)Q_m \quad (5.11)$$

$$\beta = \begin{cases} \text{SWR} & \text{if over-coupled} \\ 1/\text{SWR} & \text{if under-coupled} \end{cases} \quad (5.12)$$

$$\text{SWR} = (1+\Gamma_0)/(1-\Gamma_0) \quad (5.13)$$

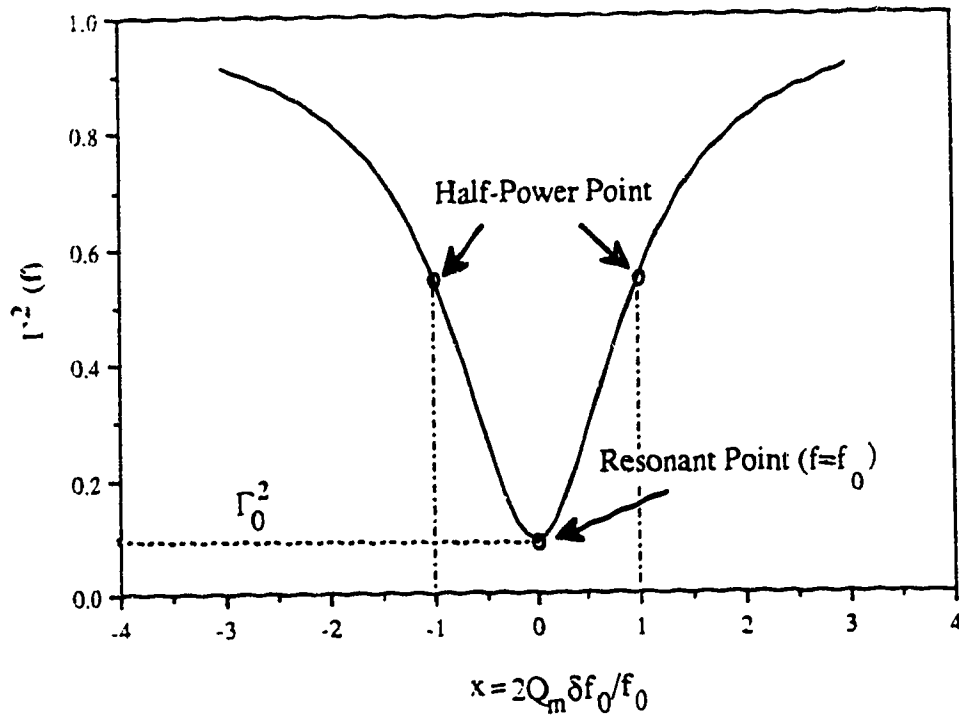


Figure 5.6 The square of the reflection coefficient as a function of the normalized frequency increment,  $x$  ( $\Gamma_0=0.3$ ).

$$Q_m = \frac{f_0}{2\delta f_0} \cdot x \quad (5.14)$$

$$\delta f_0 = f_0 - f_x \quad (5.15)$$

$$x^2 = (\Gamma_x^2 - \Gamma_0^2) / (1 - \Gamma_x^2) \quad (5.16)$$

Where,

$x$  = the normalized frequency increment;

$f_0, f_x$  = the resonant frequency and its neighboring point;

$\Gamma_0, \Gamma_x$  = the reflection coefficient at  $f_0$  and  $f_x$ .

When

$$\Gamma_x^2 = (1 + \Gamma_0^2) / 2 \quad (5.17)$$

then  $x=1$  and

$$Q_m = \frac{f_0}{2\delta f_0} \quad (5.18)$$

where  $\delta f_0 = f_0 - f_{1/2}$  (5.19)

This is the case for the half-power point usually used in practice. As analyzed in Appendix 3, the uncertainty of  $Q_m$  determined at the half-power point can be expressed by

$$(dQ_m/Q_m)^\pm = \frac{\ln 10}{20} \cdot \frac{(1+\Gamma_0^2)}{(1-\Gamma_0^2)} \cdot dRL^\pm \quad (5.20)$$

Eq.(5.20) indicates that the  $Q_m$  error increases with the degree of mismatch and is proportional to the amount of return loss uncertainty. In practice, one cannot do much about the former factor because the required matching adjustment in the testing band would disturb the resonant frequency of the cavity. The latter factor depends on the return loss itself. In a well calibrated reflectometer, the uncertainty in return loss measurements is mainly due to the finite directivity of the directional coupler and the effective source mismatch. For low load reflection, a finite coupler directivity is the dominant error source, while for high load reflection, source mismatch is the primary error source. If the equivalent source mismatch is neglected and the directivity of the dual directional coupler employed is 30dB or 40dB, we find that  $|dQ_m/Q_m| = 12.5\%$  or  $3.5\%$  in the worst case. Details of this error analysis are presented in Appendix 3.

The error in the cavity Q determined by Eq.(5.11) is contributed by both the  $Q_m$  error discussed above and the error in the coupling factor,  $\beta$ . The  $\beta$  error is a minor one unless the cavity is over coupled and is seriously mismatched as indicated in Appendix 3.

As a sample is being heated rapidly in the cavity, manual measurements of the frequency shift and Q-factor are unsatisfactory in terms of both reliability and speed. Therefore, a computer is employed to carry out the measurement automatically. A program called DIELEC is written in BASIC for instrument setup, data acquisition and dielectric data calculations. Via the HP-IB instrument interface, the computer can receive an entire measured resonant trace with 401 points and 0.01dB resolution from the HP8756A analyzer within 40 milliseconds [63]. The frequency resolution is therefore 0.25% of the sweep bandwidth, that is, 0.1MHz for a 40MHz band. This resolution is improved in the program by a para-

bolic interpolation technique in determining  $f_0$  and  $\delta f_0$  required for the  $Q$  calculations. The program uses the half-power point for  $\delta f_0$  unless this point is rather close to the trace shoulder. The dielectric constant and loss factor are evaluated by the polynomial obtained through fitting the calibration data from the mode-matching analysis (see Chapter 6). As each trace is transferred, the program also logs the sample's temperature data from an Accufiber thermometer via the RS232 serial interface. In this manner, one data point takes about one second and one complete curve of complex dielectric constant versus temperature is obtained in only one minute.

### 5.3 Heating Channel Operation

The heating channel consists of a heating power source, a matching device and a tuning device. Its aim is to deliver a sufficient power level to the cavity to raise the sample's temperature effectively. For a given power level, the main task is to minimize the reflection which arises from detuning and mismatching.

A solid-state microwave power source (AMT-1120A) is employed. It has 8 independent channels, each providing a maximum output of 60W in the band of  $915 \pm 15$  MHz. Four channels are used at the present time via a power combiner so that a power level of 120W is obtained. The output level can be varied either manually or electronically. Using the temperature control mode, the power level can be automatically adjusted to hold the sample's temperature at a given temperature setpoint. To realize electronic tuning, we use an external voltage controlled oscillator (VCO) as the input to this power source as shown in Figure 5.7a.

A three stub coaxial tuner is chosen as the matching device due to its wide matching range. For example, it can match both an empty cavity ( $Q \approx 4000$ ) and the cavity loaded with a saline (0.1M) sample ( $Q \approx 80$ ), whereas, an internal movable coupling loop [66] can only match samples less lossy than distilled water ( $Q \approx 400$ ). On the other hand, the disadvantages of using a stub tuner include the difficulty in automating its operation and its disturbance to the testing band response. It is preferable not to adjust the stub tuner during the data collection for dielectric determinations. Experiments show that, after several pilot runs of heating, an optimum stub position can be found for a given

sample and temperature range so that the stub tuner can be fixed at such an optimum position during the heating and testing.

It is essential to tune the heating power source frequency automatically. Due to the variation of the dielectric properties of a sample with temperature, the resonant frequency of a loaded cavity in the heating band changes all the time. A slight detuning will cause a large heating power reflection. For example, if  $Q_m = 2250$  and  $f_0 = 900\text{MHz}$ , a  $0.2\text{MHz}$  deviation of the heating source frequency from the resonant point can produce a power reflection of 50%. The objective of the automatic tuner is to sweep the heating band, i.e.,  $915 \pm 15\text{MHz}$ , and search for the resonant point and then to adjust the source frequency accordingly. An analog circuit, as described in Appendix 4, has been designed using common type circuit blocks [67-69].

This tuning circuit uses as input the reflection voltage,  $V_r$ , from the heating band and its output is a frequency tuning voltage,  $V_f$ , used to control the heating source's external VCO. As illustrated in Figure 5.7, the timing cycle of the circuit can be divided into a searching

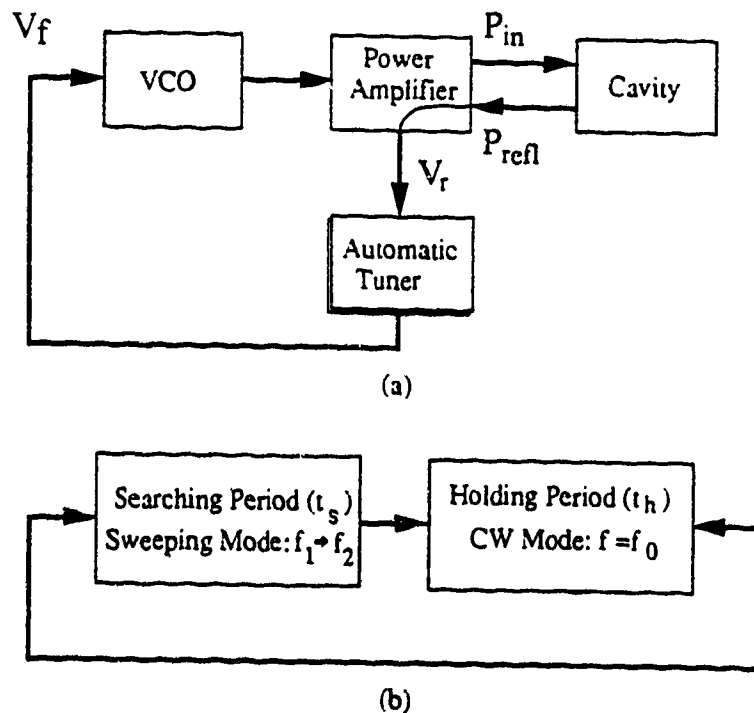


Figure 5.7 (a) Block diagram of the external tuning system and (b) time cycle of the automatic tuner ( $f_1 = 900$ ,  $f_2 = 930\text{MHz}$ ,  $f_0 = \text{resonant frequency}$ ,  $t_s = 0.1$  and  $t_h = 1.0\text{s}$ ).

period and a holding period. Within the searching period, two frequency sweeps are triggered. During the first frequency sweep, the value of  $V_R$  at the resonant point,  $V_R(f_0)$ , is found by a peak detector. This is followed by the second sweep during which the frequency at the resonant point,  $f_0$ , is located by a comparator which compares the current  $V_R$  with  $V_R(f_0)$  obtained from the first sweep. A sample/hold circuit then captures the correct tuning voltage  $V_f$ . The circuit then enters the holding period in which  $V_f$ , and hence the heating source frequency, is kept unchanged. At the end of the holding period, the circuit starts another searching period. Typical waveforms of  $V_R$  and  $V_f$  are plotted in Figure 5.8.

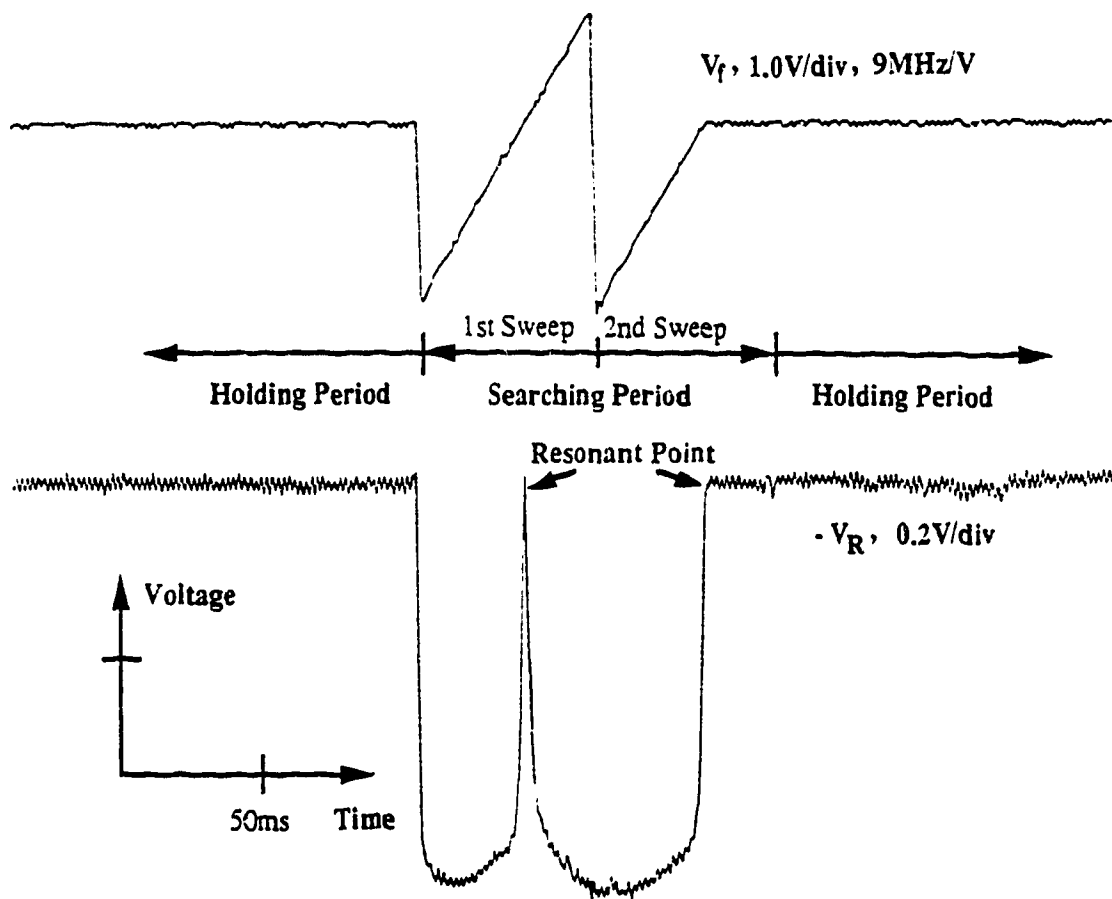


Figure 5.8 Typical waveform of the reflection voltage,  $V_R$ , and the tuning voltage,  $V_f$ , in the circuit of the automatic tuner, obtained by a digital storage oscilloscope (TEKTRONIX 2220).

## 5.4 Temperature Measuring Channel

An optical fiber thermometer (OFT) [70] is employed in sample temperature measurements. The reason for using the OFT is not only its extraordinary performance [71] such as wide range (300–1900°C), high accuracy (0.2% at 1000°C), high resolution (0.1°C at 1000°C) and fast response, but also its minimal disturbance to the microwave field due to its non-metallic optical sensor. In a microwave environment, commonly-used thermocouples directly perturb the field and hence give a false temperature indication. Moreover, RF current coupled into the thermocouple-detector circuit is mixed with the true temperature change signal, thereby further corrupting the results [72].

Using the OFT to monitor the temperature of a small sample, one cannot obtain the accuracy it promises if it is not properly placed. If a lightpipe probe is chosen, it should be placed in close proximity to

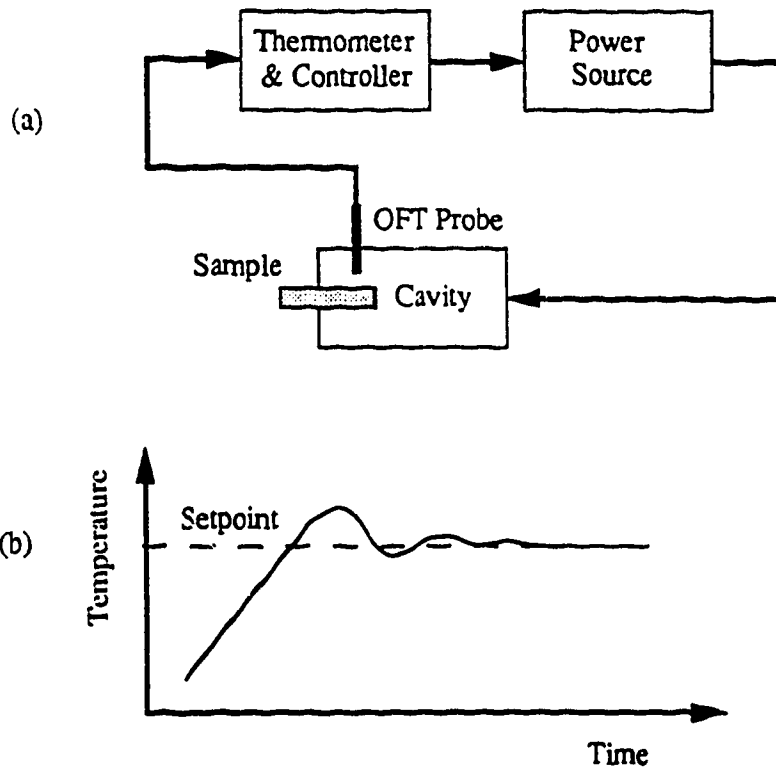


Figure 5.9 Sample's temperature control. (a) Block diagram of the control loop and (b) Temperature response of a properly tuned PID controller.



the sample though a direct contact with the sample is not necessary. It is found that the temperature reading does not vary greatly with the probe-sample distance but will be misleading if the probe does not aim right at the hot zone of the sample.

In addition to the measurement function, our Accufiber (M100C) OFT has a temperature controller option installed. Selecting its output control function and connecting the analog output to the power level controller in the heating source, as illustrated in Figure 5.9, a negative feedback loop is formed. The proportional, integral and derivative (PID) controller [73] in the Accufiber is then able to control the sample's temperature at the set point with an error less than  $0.5^{\circ}\text{C}$  at  $1000^{\circ}\text{C}$ . This allows us to measure dielectric properties as a function of temperature in a programmed manner, ensuring a stable and repeatable test and heating process and also eliminating the common temperature run-away phenomenon. In the simplest temperature control mode the setpoint increases in equal increments so that the heating rate of a sample is nearly constant. In Figure 5.10, a heating curve of Macor obtained in this step-wise fashion is compared with one without temperature control. The dielectric measurement made on these steps is more reliable.

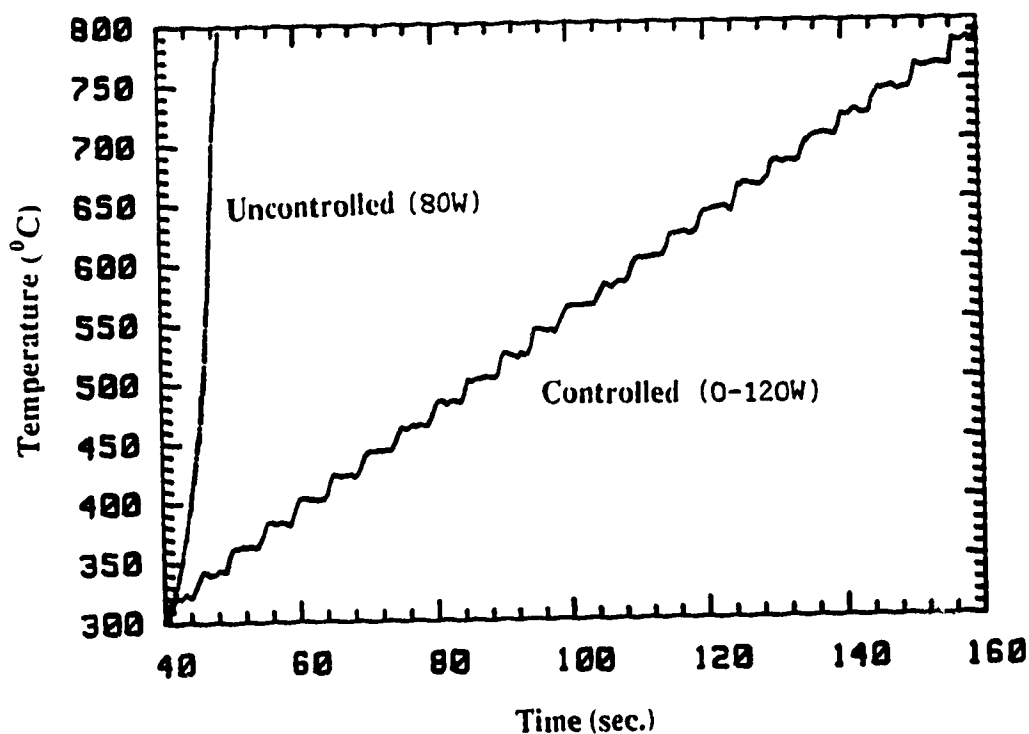


Figure 5.10 Controlled and uncontrolled microwave heating curve of Macor.

## 5.5 Dynamic Measurement Range

The evaluation of the dynamic range is quite involved since it needs the knowledge of both the sample loading degree and the testing and heating ability of the system. In this section, such an evaluation is attempted using an analytical approach based on the numerical results obtained from the mode-matching analysis. This approach can overcome experimental limitations such as the unavailability of samples with the required dielectric data and it also gives better insight into the dielectric sample loading effect.

### 5.5.1 Dielectric constant range

The upper limit of the measurement range of dielectric constant for a given sample geometry depends on the maximum detuning, or the resonant frequency shift,  $\Delta f_0$ , which the system will allow. In the testing band, the maximum  $\Delta f_0$  is limited by the presence of transverse modes; whereas in the heating band, it is restricted by the tunable range of the heating source. Due to the narrow tuning range of medium and high power microwave sources, the latter factor is dominant over the former in determining the maximum  $\Delta f_0$ . Given  $(\Delta f_0)_{\max} = 30\text{MHz}$  in the heating band, the maximum measurable  $\epsilon'_r$  is calculated as a function of the gap width and shown in Figure 5.11. It shows that the smaller the sample's radius and gap width, the higher the upper measurement limit of  $\epsilon'_r$ .

On the other hand, the minimum dielectric constant which can be measured is only limited by the frequency measurement resolution of the testing channel. For the same cavity dimensions as in Figure 5.11, a sample of  $\epsilon'_r = 2$  and  $r_s = 0.24$  and  $0.2\text{cm}$  produces a frequency shift of  $0.5$  and  $0.4\text{MHz}$ , so that the minimum  $\epsilon'_r$  is  $1.10$  and  $1.13$ , respectively, if the measurement error in frequency shift is  $0.05\text{MHz}$ .

### 5.5.2 Loss factor or loss tangent range

The maximum loss tangent of a sample which can be effectively heated and measured depends on the maximum mismatch which the system can tolerate. Assuming that the empty cavity is matched in both the testing and heating channel, we can express the normalized input resistance of the loaded cavity as

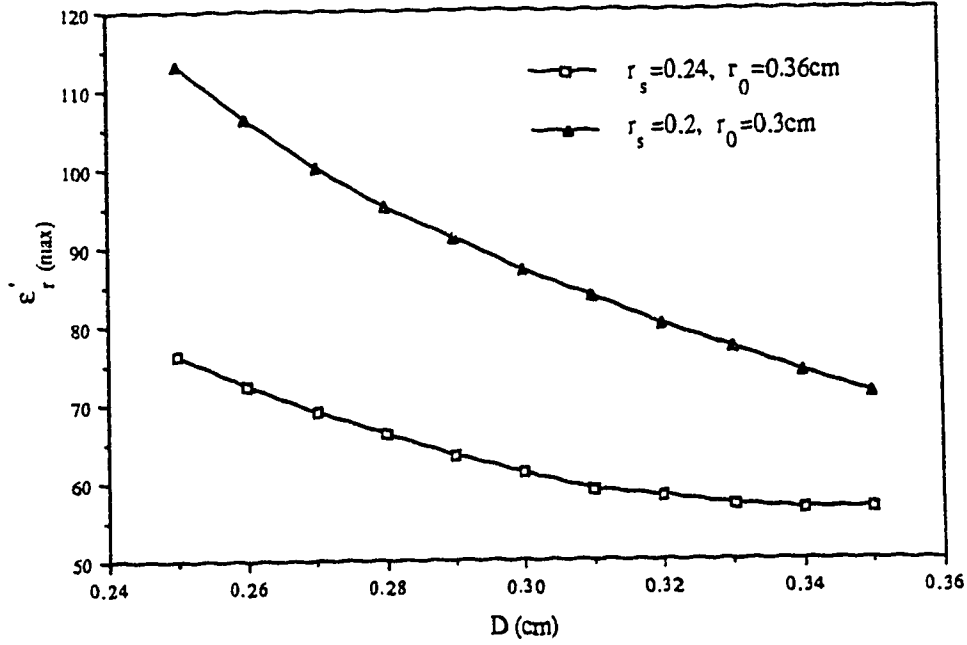


Figure 5.11 Maximum measurable dielectric constant,  $\epsilon'_{r(\max)}$ , as a function of the gap width, calculated from the maximum detuning allowed in the heating band, i.e., 30MHz ( $r_1 = 1.244$ ,  $r_2 = 5.0$ ,  $L = 20.0$ cm,  $\epsilon_{rh} = 3.8$ , by MM4C5).

$$\bar{R} = Q_0/Q_L = Q_0(1/Q_c + 1/Q_D) \approx 1 + Q_0/Q_D \quad (5.21)$$

Note that  $Q_0 \approx Q_c$  is assumed throughout this section. The reflection coefficient at the resonant frequency can then be expressed in terms of  $Q_0/Q_D$  as

$$\Gamma = (\bar{R} - 1)/(\bar{R} + 1) = \frac{Q_0/Q_D}{Q_c/Q_D + 2} \quad (5.22)$$

In the testing channel, the error in measured Q-factor,  $Q_m$ , normally increases with  $\Gamma_0$ , so that the maximum  $Q_0/Q_D$  must be limited. For example, using a reflectometer with a directivity of 30dB, the return loss uncertainty will cause a  $Q_m$  error larger than 13% if  $\Gamma_0 > 0.5$ . If a 13%  $Q_m$  error is intolerable, then according to Eq. (5.22), the maximum  $Q_0/Q_D$  allowed is found to be 2.0. Likewise, in the heating channel,  $(Q_0/Q_D)_{\max}$  is restricted by the matching ability of the matching device. The three stub tuner employed can match a loaded cavity with  $\Gamma_0 \leq 0.8$  which corresponds to a  $Q_0/Q_D \leq 7.7$ . Recalling Eq. (4.22), we can write

$$Q_0/Q_D = Q_0 F_\ell \tan\delta \quad (5.23)$$

$$\text{Then, } \tan\delta_{(\max)} = (Q_0/Q_D)_{\max} / (Q_0 F_\ell) \quad (5.24)$$

$$\text{or, } \epsilon''_{r(\max)} = (Q_0/Q_D)_{\max} \cdot \frac{\epsilon'_r}{Q_0 F_\ell} \quad (5.25)$$

This equation simply shows us that for a given  $(Q_0/Q_D)_{\max}$ , the maximum measurable  $\tan\delta$  is inversely proportional to the sample loading factor which increases with the gap E-field and the sample's dielectric constant and volume. It should also be noted that  $(\tan\delta)_{\max}$  decreases with an increase of the unloaded cavity Q. Conversely, we require a high Q cavity for testing and heating a low loss sample as analyzed below.

At the other end of the range, the minimum measurable loss tangent is limited by the heating ability and the Q measurement uncertainty. In the heating band, sample heating tends to be very ineffective when the sample loss is comparable to the cavity wall loss. In this situation, the competition between microwave absorption by the sample and the cavity wall may result in an overheated cavity and a cool sample. It is true that the positive temperature dependence of loss factors for most ceramics should help to raise the sample's temperature. However, the metal surface loss also tends to increase with temperature. To account for this limit, we can define a minimum loss tangent as

$$\tan\delta_{(\min)} = 1/(Q_0 F_\ell) \quad (5.26)$$

at which the sample loss or  $Q_D$  equals the wall loss or  $Q_0$ . In the practical use of this relation,  $Q_0$  should also include external losses due to the stub tuner, the coupling loop and the cable. As a result,  $\tan\delta_{(\min)}$  is higher than that given in Eq.(5.26).

However, the minimum loss tangent may be lower than that of Eq. (5.26) if thermal loss factors are considered. A hot object invariably loses thermal energy from its surface via conduction, convection and radiation. The larger the volume-surface ratio the slower the thermal loss. This ratio is approximately equal to  $r_s/2$  for a cylindrical sample and equal to the skin depth for a metal cavity body. Since the skin depth of a cavity at microwave frequencies is of the order of  $10\mu\text{m}$  which is smaller than a sample radius by several orders of magnitude, the

thermal loss on the internal cavity wall surface is enormous compared with that on the sample's surface. Besides the difference in the volume-surface ratio, the thermal loss of a sample can be further reduced by suspending the sample in the gap or using a thermally insulating sheath around the sample to avoid a direct contact with the cavity wall. As a result, the heating rate of the sample can still be much higher than that of the cavity even if an equal or lesser amount of microwave power is absorbed by the sample at the beginning of heating. With the help of a positive temperature coefficient of its loss factor, the sample will absorb more power once its temperature starts to rise.

In the testing band, the measurable  $\tan\delta$  also reaches a lower limit when the Q change due to the sample loss, that is

$$\Delta(1/Q) \approx 1/Q_D \quad (5.27)$$

is close to that due to the measurement error, namely,

$$\Delta(1/Q) \approx 1/(Q_0 + \delta Q) - 1/Q_0 \approx \frac{1}{Q_0} \left( \frac{\delta Q}{Q} \right) \quad (5.28)$$

where  $\delta Q/Q$  is the relative error in Q measurements as evaluated in section 5.3. Equating Eq. (5.27) and Eq. (5.28) gives

$$\frac{Q_0}{Q_D} = \frac{\delta Q}{Q} \quad (5.29)$$

or  $Q_0 F_\ell \tan\delta = \delta Q/Q \quad (5.30)$

Similar to the case for the heating band, a minimum loss tangent can also be defined as

$$\tan\delta_{(\min)} = \frac{1}{Q_0 F_\ell} \cdot \frac{\delta Q}{Q} \quad (5.31)$$

It should be pointed out that the values of the parameter  $Q_0 F_\ell$  in Eq. (5.31) and in Eq. (5.26) are different because they are defined in different frequency bands. If  $Q_0 F_\ell$  of the testing band is the same as that in the heating band, the low limit of  $\tan\delta$  in the testing band is only  $\delta Q/Q$  percent of that in the heating band as indicated by Eqs. (5.26) and (5.31).

The above analysis, resulting in Eqs. (5.24), (5.26) and (5.31),

shows that both the upper and lower limit of measurable loss tangent or loss factor are determined by the same parameter, namely  $1/(Q_0 F_\ell)$ , which actually is the ratio of the energy stored in the sample to that lost on the cavity wall. This reveals the fact that the upper and lower limits of the allowed loss tangent in the testing and heating bands cannot be extended at the same time. To evaluate these limits,  $\epsilon'_r/(Q_0 F_\ell)$  is calculated and plotted against  $\epsilon'_r$  for both bands in Figure 5.12. Let  $(Q_0/Q_D)_{\max} = 2.0$  and  $7.7$  for the testing and heating band respectively, and assume the  $Q$  measurement error to be  $\delta Q/Q = 10\%$ ; then the upper and lower limits of the loss tangent and loss factor are shown in Table 5.2.

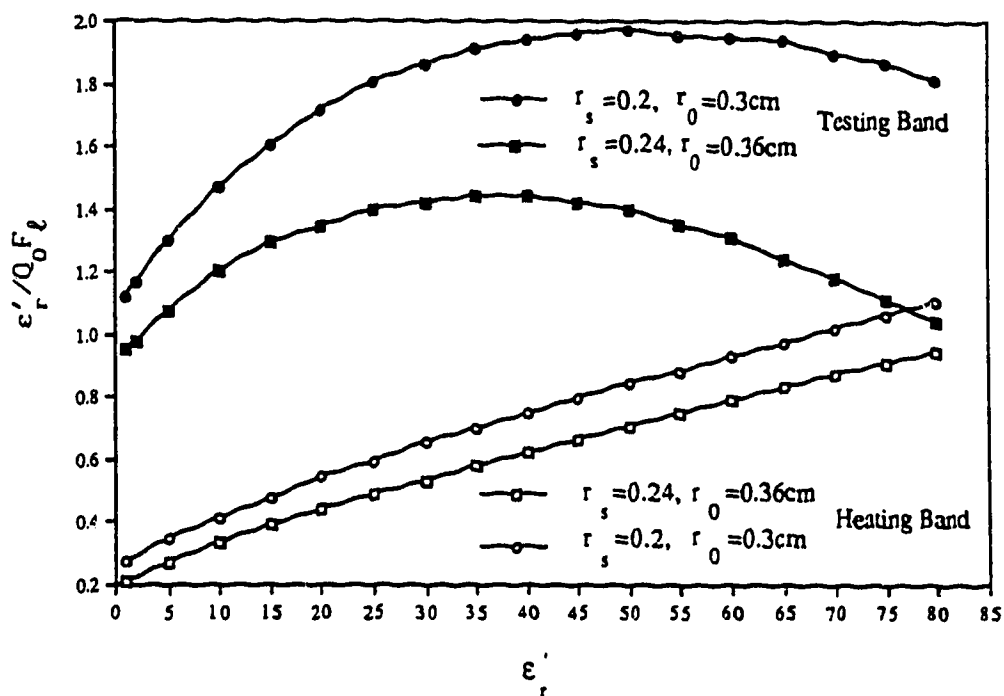


Figure 5.12 The parameter  $(\epsilon'_r / Q_0 F_\ell)$  used for estimating the maximum and minimum loss factor which can be covered by the testing and heating systems, plotted as functions of dielectric constant ( $Q_c = 3000$  and  $2000$  in the testing and heating bands,  $r_1 = 1.244$ ,  $r_2 = 5.0$ ,  $L = 20.0$ ,  $D = 0.3\text{cm}$ ,  $\epsilon_{rh} = 3.8$  by MMCS).

**Table 5.2** Lower and upper limits of loss factor and loss tangent, evaluated from  $\epsilon'_r/(Q_0 F_t)$  of Figure 5.12.

		Testing Band				Heating Band			
		$\epsilon'_r=10$	$\epsilon'_r=30$	$\epsilon'_r=50$	$\epsilon'_r=70$	$\epsilon'_r=10$	$\epsilon'_r=30$	$\epsilon'_r=50$	$\epsilon'_r=70$
$\epsilon''_r(\min)$	$r_s=0.24$	0.120	0.140	0.138	0.117	0.350	0.550	0.730	0.880
	$r_s=0.20$	0.147	0.185	0.197	0.185	0.420	0.650	0.870	1.04
$\tan\delta(\min)$	$r_s=0.24$	0.012	0.005	0.003	0.002	0.035	0.018	0.015	0.013
	$r_s=0.20$	0.015	0.006	0.004	0.003	0.042	0.022	0.017	0.015
$\epsilon''_r(\max)$	$r_s=0.24$	2.40	2.80	2.76	2.34	2.70	4.24	5.62	6.78
	$r_s=0.20$	2.95	3.70	3.95	3.70	3.23	5.01	6.70	8.01
$\tan\delta(\max)$	$r_s=0.24$	0.240	0.093	0.055	0.033	0.270	0.141	0.112	0.097
	$r_s=0.20$	0.295	0.123	0.079	0.053	0.323	0.167	0.134	0.114

CHAPTER 6  
EXPERIMENTAL RESULTS AND ERROR ANALYSIS

In this chapter, the calculated calibration curves for determining dielectric constants and loss factors are presented first. These are followed by an error analysis of the determined dielectric data. The final part reports on the dielectric measurement results. The experimental system outlined in Chapter 5 is checked by measuring a number of well characterized materials at room temperature. Using this system, various ceramic and oxide samples are heated and tested simultaneously. The obtained data are plotted as a function of temperature. These results are discussed and some important measurement details are also emphasized.

### 6.1 Calibration Curves

The dielectric constant,  $\epsilon'_r$ , and loss tangent,  $\tan\delta$ , or loss factor,  $\epsilon''_r$ , are determined from the measured resonant frequency shift,  $\Delta f_0$ , and cavity Q-factor change,  $\Delta(1/Q)$ . To do this, two theoretically calculated calibration curves are proposed in section 4.7. The first is  $\epsilon'_r$  versus  $\Delta f_0$ .

$$\epsilon'_r = \epsilon'_r(\Delta f_0) \quad (6.1)$$

which is obtained by calculating  $\Delta f_0$  as a function of  $\epsilon'_r$  for a given cavity and sample geometry, in the frequency band of interest, by the cavity mode-matching analysis program. The second is the loading factor,  $F_\ell$ , which is a function of  $\epsilon'_r$ ,

$$F_\ell = F_\ell(\epsilon'_r) \quad (6.2)$$

and can also be calculated by the mode-matching program. Knowing  $F_\ell$ ,  $\tan\delta$  or  $\epsilon''_r$  can be determined readily by

$$\tan\delta = (1/F_\ell) \cdot \Delta(1/Q) \quad (6.3)$$

or 
$$\epsilon''_r = (\epsilon'_r/F_\ell) \cdot \Delta(1/Q) \quad (6.4)$$

In fact, the parameter  $\epsilon'_r/F_\ell$  is simply the loss factor for unit  $\Delta(1/Q)$ .



For this reason, it is more convenient to use  $\epsilon'_r/F_\ell$  than  $F_\ell$  as the second calibration curve.

In Figures 6.1, 6.2 and 6.3, calibration curves for both  $\epsilon'_r$  and  $\epsilon''_r$  are presented for different sample holders, sample radii and gap widths. The other cavity dimensions used in the calculation are  $r_1=1.244$ ,  $r_2=5.0$ , and  $L=20.0$ cm. The frequency of the calculation is around 3GHz which corresponds to the testing band. In Figure 6.1, the curves of a suspended sample ( $\epsilon_{rh}=1.0$ ) are presented together with those using two different quartz sample tubes ( $\epsilon_{rh}=3.78$ ), the larger one having an OD of 0.71cm and an ID of 0.48cm; the smaller having an OD of 0.6cm and an ID of 0.4cm. Since the air space between the sample and the insertion hole wall reduces the gap E-field, the suspended sample produces less frequency shift and a smaller loading factor. The calibration curves for various gap widths and sample radii are given in Figures 6.2 and 6.3. As expected, the larger the gap width and sample radius, the greater the frequency shift and loading factor, because of the increased sample volume which interacts with the cavity field.

For the convenience of dielectric determinations, the calibration curves can also be expressed by polynomials using a least square fit as

$$\epsilon'_r = 1 + a_1 |\Delta f_0| + a_2 |\Delta f_0|^2 + a_3 |\Delta f_0|^3 + \dots \quad (6.5)$$

$$\epsilon''_r/F_\ell = b_0 + b_1 \epsilon'_r + b_2 (\epsilon'_r)^2 + b_3 (\epsilon'_r)^3 + \dots \quad (6.6)$$

The coefficients  $a_1$  and  $b_1$  are listed in Tables 6.1, 6.2 and 6.3 for the curves presented in Figures 6.1, 6.2 and 6.3. Note that the coefficients  $a_1$  correspond to the  $\Delta f_0$  measured in MHz and r.m.s.e. stands for root-mean-square-error.

## 6.2 Error Analysis

To estimate the error in the dielectric constant determined by Eq. (6.1), we need to examine the differential of Eq. (6.1)

$$\Delta \epsilon'_r = \frac{\partial \epsilon'_r}{\partial (\Delta f_0)} \cdot \Delta (\Delta f_0) \quad (6.7)$$

where  $\partial \epsilon'_r / \partial (\Delta f_0)$  is the slope of the calibration curve and  $\Delta (\Delta f_0)$  is the

Figure 6.1a Calibration curves for determining the dielectric constant,  $\epsilon_r'$ , from the measured resonant frequency shift,  $\Delta f_0$ , in MHz, for three types of sample holders ( $r_1=1.244$ ,  $r_2=5.0$ ,  $L=20.0$ ,  $D=0.3$ cm).

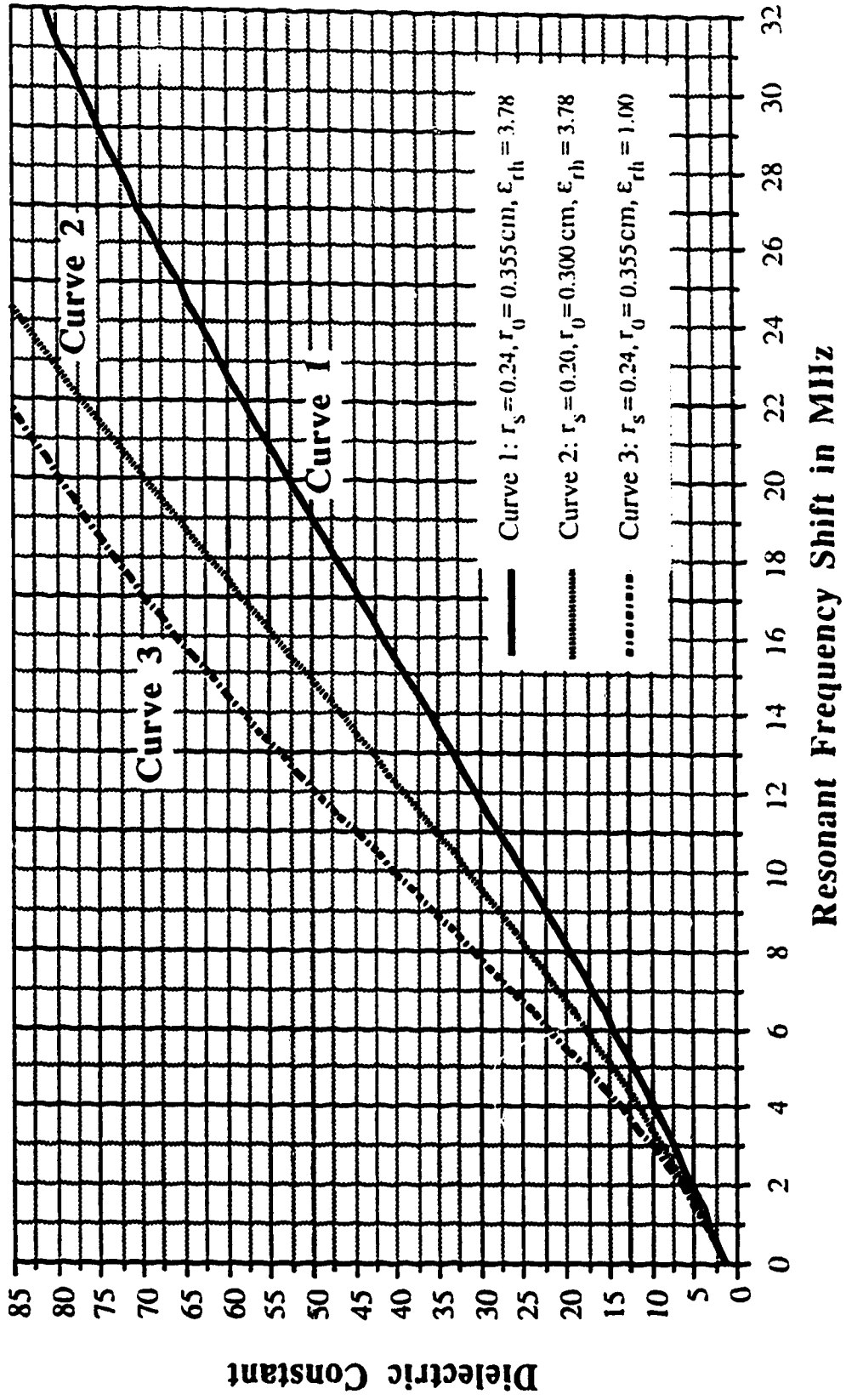
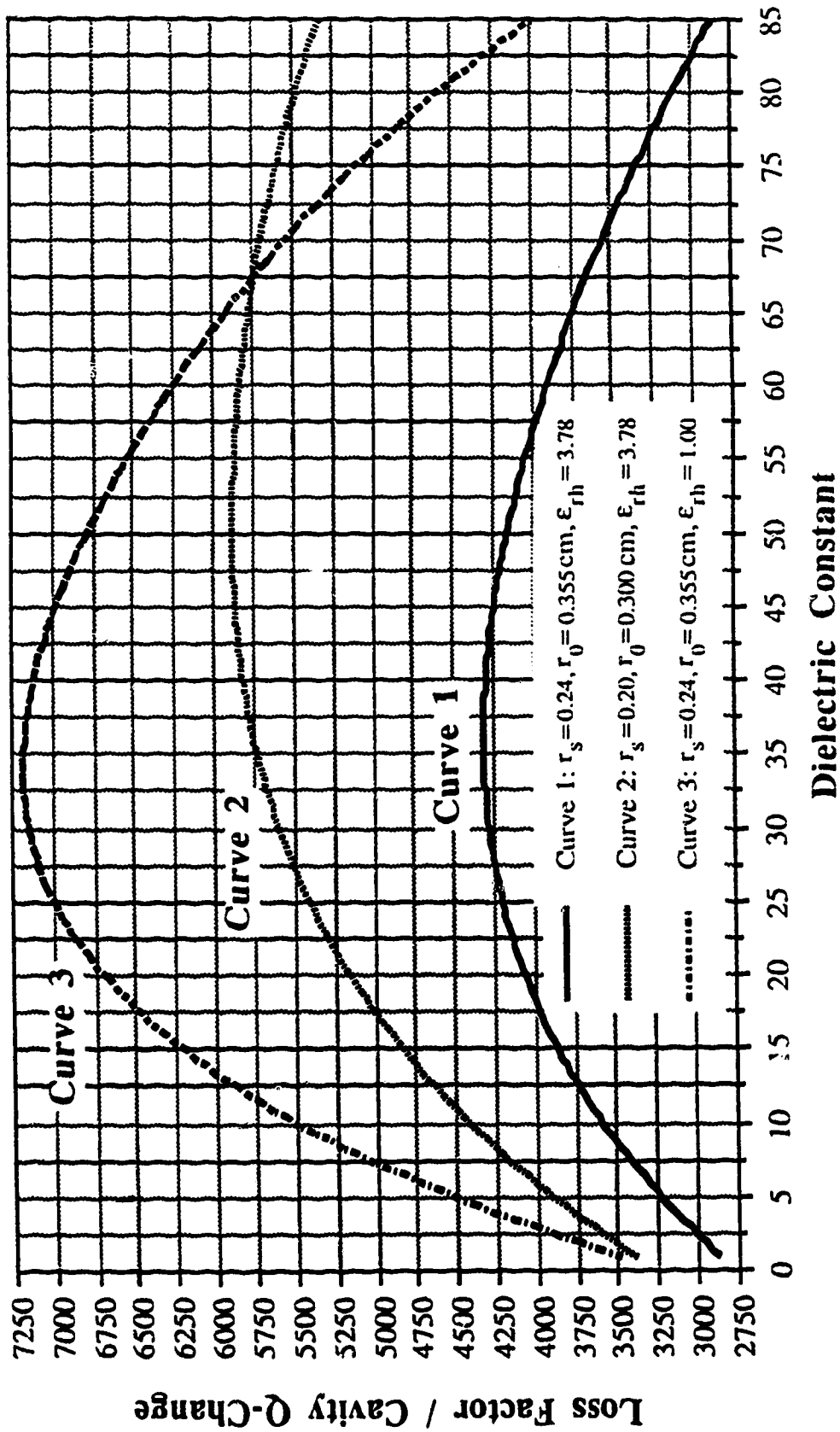


Figure 6.1b Calibration curves for determining the loss factor,  $\epsilon_r''$ , from the measured cavity Q change,  $\Delta(1/Q)$ , and dielectric constant,  $\epsilon_r'$ , for three types of sample holders ( $r_1=1.244$ ,  $r_2=5.0$ ,  $L=20.0$ ,  $D=0.3\text{cm}$ ).



**Figure 6.2a** Calibration curves for determining the dielectric constant,  $\epsilon'_r$ , from the measured resonant frequency shift,  $\Delta f_0$ , in MHz, for different gap widths ( $r_1 = 1.244$ ,  $r_2 = 5.0$ ,  $L = 20.0$ ,  $D = 0.3\text{cm}$ ).

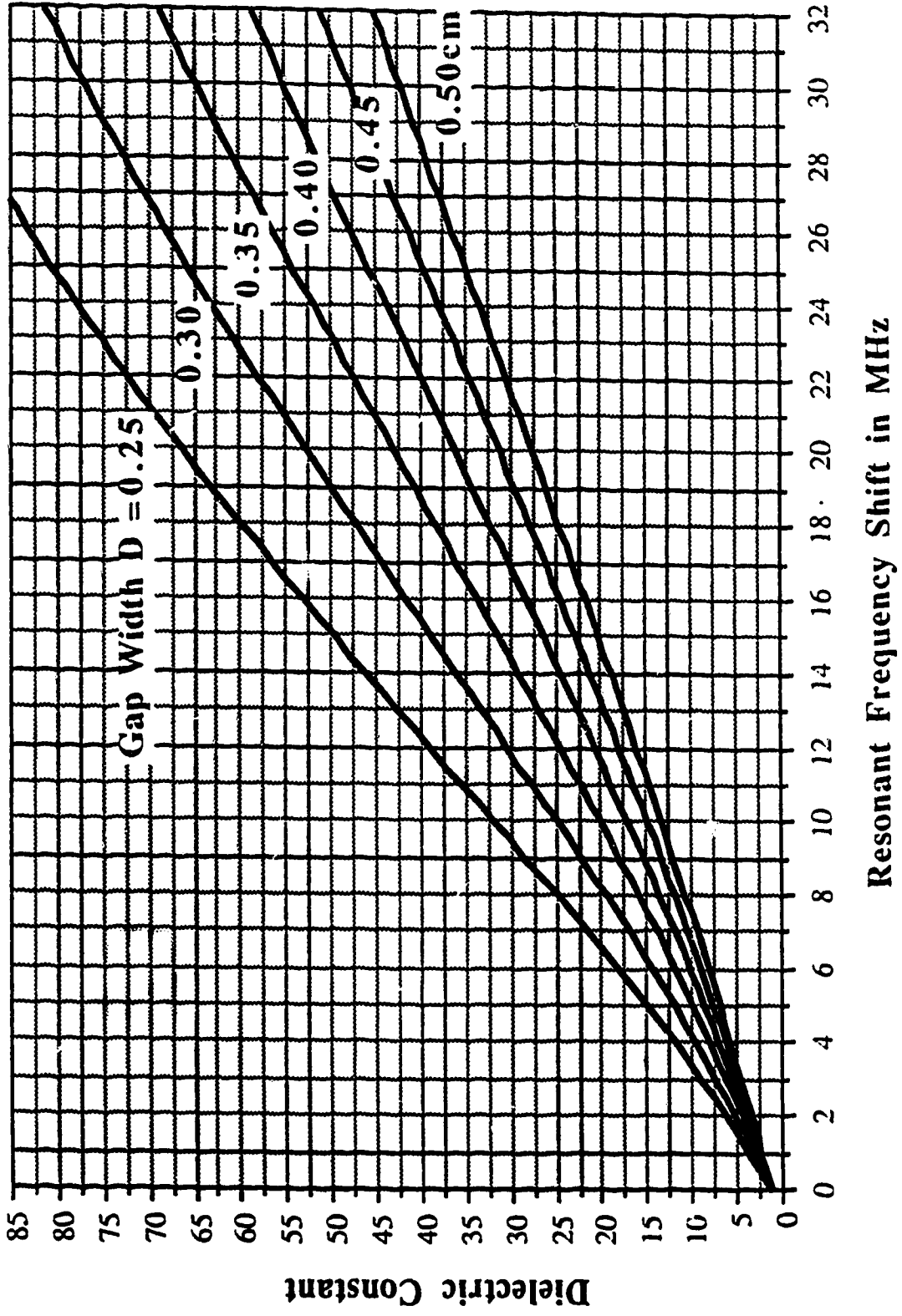


Figure 6.2b Calibration curves for determining the loss factor,  $\epsilon''$ , from the measured cavity Q change,  $\Delta(1/Q)$ , and dielectric constant,  $\epsilon'$ , for different gap widths ( $r_1=1.244$ ,  $r_2=5.0$ ,  $L=20.0$ ,  $D=0.3\text{cm}$ ).

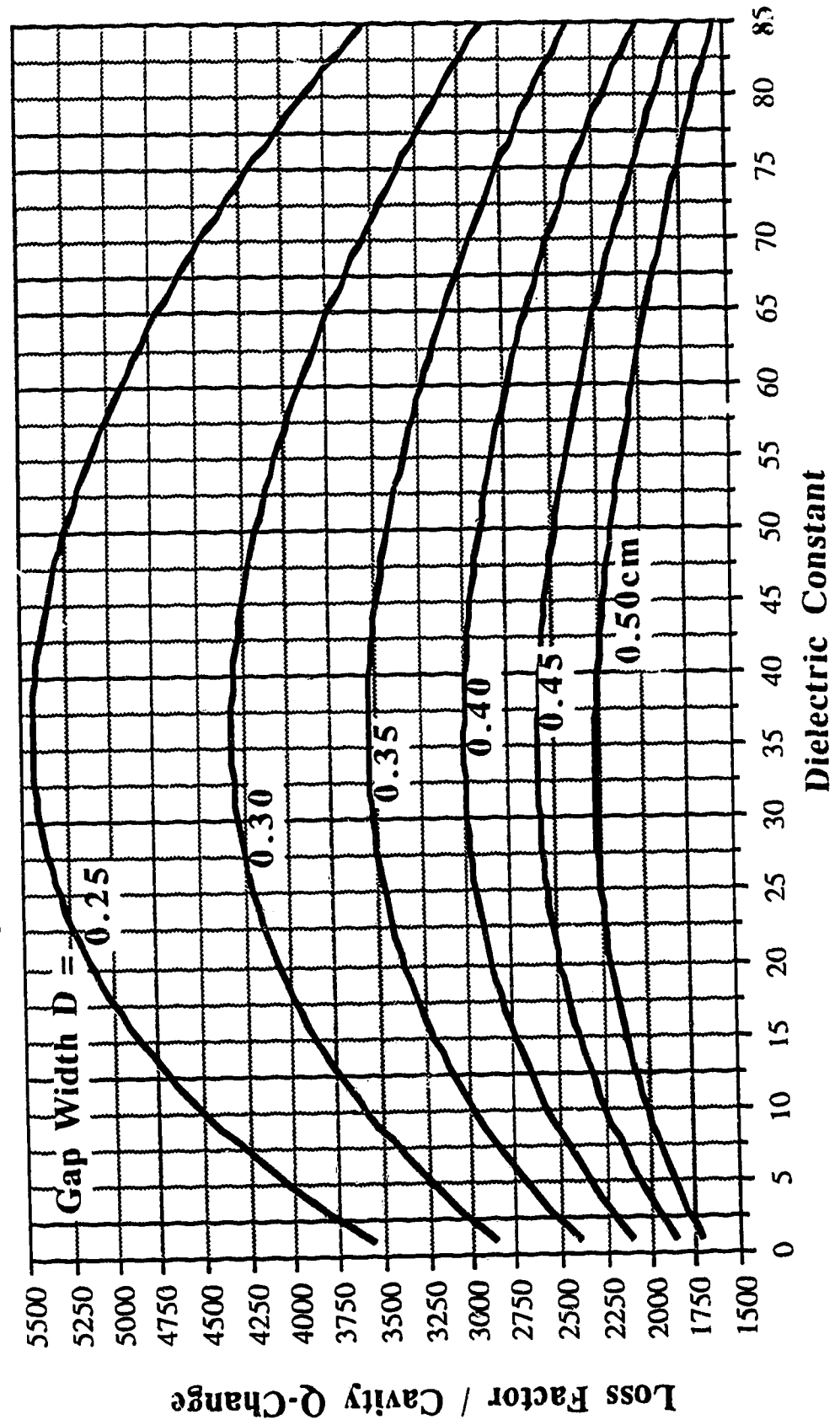


Figure 6.3a Calibration curves for determining the dielectric constant,  $\epsilon'_r$ , from the measured resonant frequency shift,  $\Delta f_0$ , in MHz, for different sample radii ( $r_1=1.244$ ,  $r_2=5.0$ ,  $L=20.0$ ,  $D=.3\text{cm}$ ).

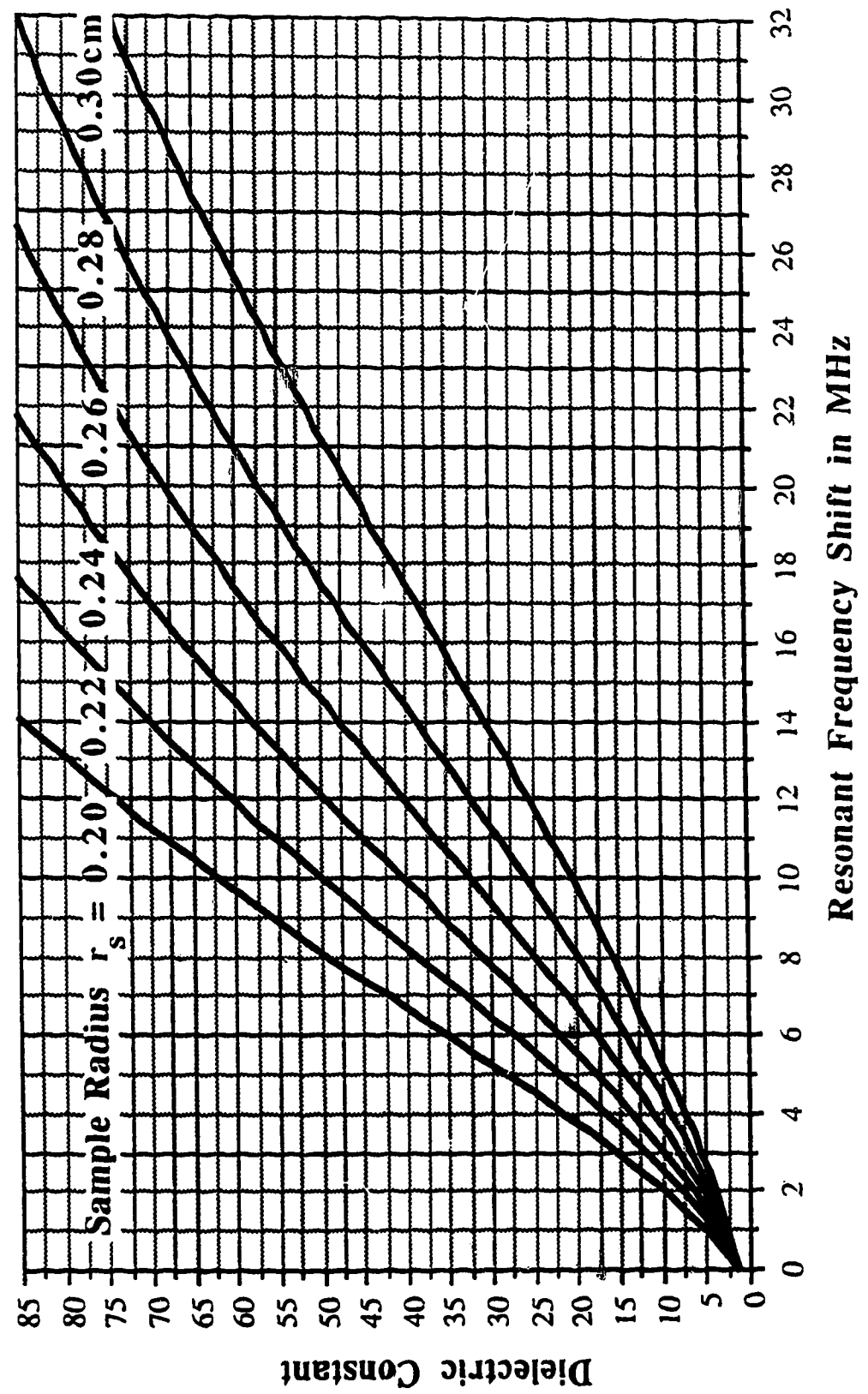
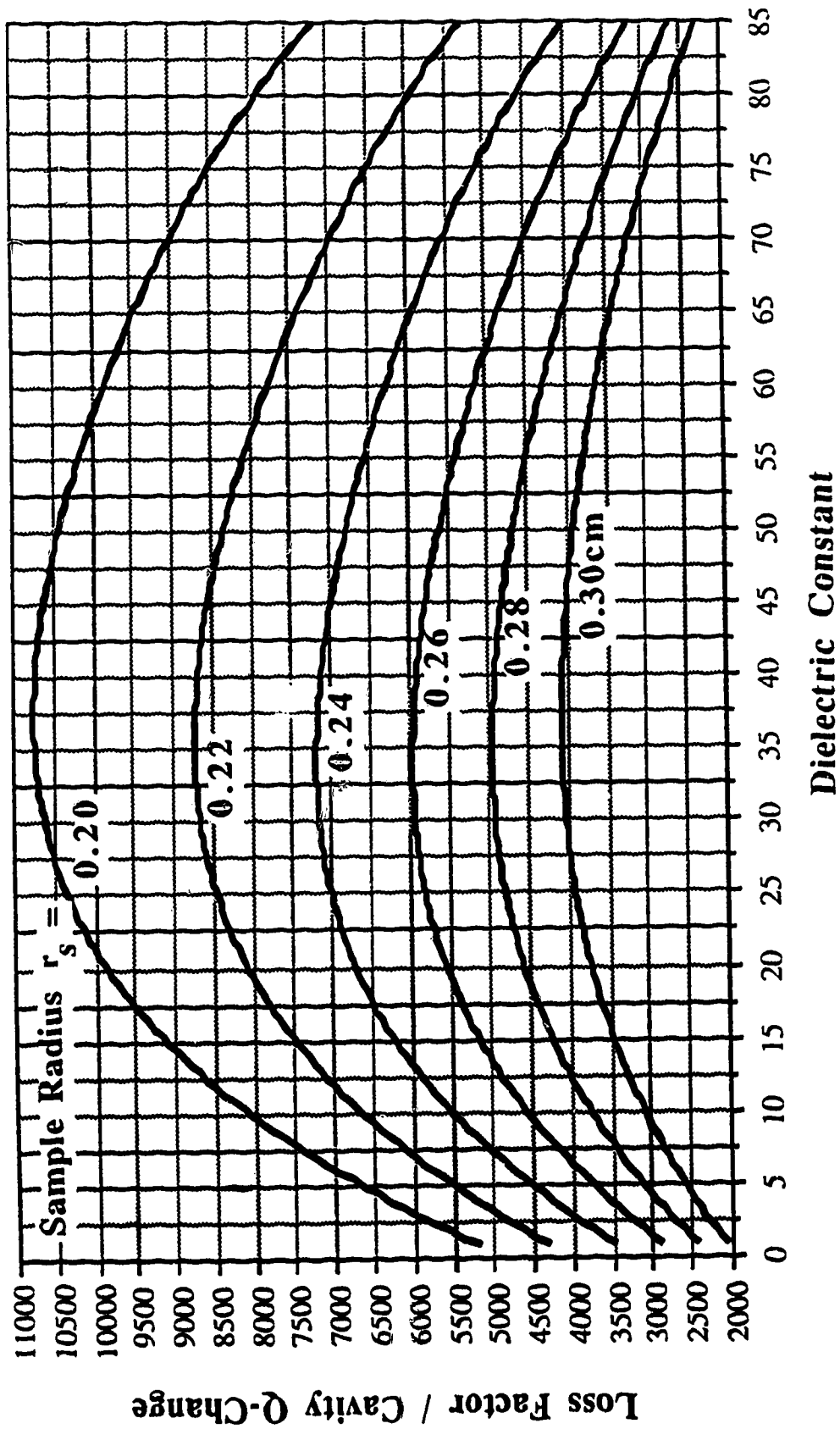


Figure 6.3b Calibration curves for determining the loss factor,  $\epsilon''$ , from the measured cavity Q change,  $\Delta(1/Q)$ , and dielectric constant,  $\epsilon'$ , for different sample radii ( $r_1=1.244$ ,  $r_2=5.0$ ,  $L=20.0$ ,  $D=0.3\text{cm}$ ).



**Table 6.1** Polynomial fitting coefficients for the permittivity calibration curves in Figure 6.1 (Curve 1:  $r_s=0.24\text{cm}, r_o=0.355\text{cm}, \epsilon_{rh}=3.78$ ; curve 2:  $r_s=0.20\text{cm}, r_o=0.30\text{cm}, \epsilon_{rh}=3.78$ ; curve 3:  $r_s=0.24\text{cm}, r_o=0.355\text{cm}, \epsilon_{rh}=1.0$ ; the other cavity dimensions are  $r_1=1.244, r_2=5.0, L=20.0$  and  $D=0.3\text{cm}$ )

Curve	$a_1$	$a_2$	$a_3$	$a_4$	r.m.s.e.
1	1.835	7.2955E-2	-2.1011E-3	1.4779E-5	0.037
2	2.157	1.1107E-1	-2.3930E-3	0.0	0.035
3	2.060	3.1812E-1	-1.5546E-2	2.1540E-4	0.028

Curve	$b_0$	$b_1$	$b_2$	$b_3$	$b_4$	r.m.s.e./ $b_0$
1	2.764E+3	1.005E+2	-2.083	1.5231E-2	-5.2645E-5	0.24%
2	3.249E+3	1.392E+2	-2.630	2.2036E-2	-8.2244E-5	0.28%
3	3.175E+3	2.978E+2	-7.538	7.7304E-2	-3.3555E-4	0.75%

**Table 6.2** Polynomial fitting coefficients for the permittivity calibration curves in Figure 6.2 ( $r_s=0.24\text{cm}, r_o=0.355\text{cm}, \epsilon_{rh}=3.78$ )

D(cm)	$a_1$	$a_2$	$a_3$	$a_4$	r.m.s.e.
0.25	2.228	1.2545E-1	-4.5256E-3	4.1137E-5	0.040
0.30	1.835	0.7296E-1	-2.1011E-3	1.4779E-5	0.037
0.35	1.525	0.4723E-1	-1.0710E-3	0.5365E-5	0.074
0.40	1.333	0.3210E-1	-0.6454E-3	0.3082E-5	0.038
0.45	1.180	0.2374E-1	-0.4341E-3	0.1962E-5	0.064
0.50	1.070	0.1794E-1	-0.3133E-3	0.1499E-5	0.094

D(cm)	$b_0$	$b_1$	$b_2$	$b_3$	$b_4$	r.m.s.e./ $b_0$
0.25	3417	133.14	-2.865	2.3103E-2	-8.9896E-5	0.31%
0.30	2764	100.54	-2.083	1.5231E-2	-5.2645E-5	0.24%
0.35	2313	82.12	-1.784	1.4422E-2	-5.5333E-5	0.24%
0.40	2026	67.12	-1.540	1.3870E-2	-6.0026E-5	0.20%
0.45	1804	54.72	-1.249	1.0478E-2	-4.0675E-5	0.22%
0.50	1661	43.37	-0.991	0.7805E-2	-2.7422E-5	0.21%



Table 6.3 Polynomial fitting coefficients for the permittivity calibration curves in Figure 6.3 ( $r_0=0.355\text{cm}$ ,  $\epsilon_{rh}=1.0$ ,  $D=0.3\text{cm}$ )

$r_s$ (cm)	$a_1$	$a_2$	$a_3$	$a_4$	r.m.s.e.
0.20	3.137	6.520E-1	-4.4054E-2	8.4806E-4	0.032
0.22	2.400	4.739E-1	-2.7534E-2	4.6491E-4	0.082
0.24	2.060	3.181E-1	-1.5546E-2	2.1540E-4	0.028
0.26	1.709	2.202E-1	-0.3949E-2	1.0189E-4	0.036
0.28	1.432	1.475E-1	-0.4837E-2	0.4331E-4	0.042
0.30	1.217	0.924E-1	-0.2301E-2	0.1436E-4	0.050

$r_s$ (cm)	$b_0$	$b_1$	$b_2$	$b_3$	$b_4$	r.m.s.e./ $b_0$
0.20	4759	417.62	-10.104	1.0214E-1	-4.3711E-4	0.73%
0.22	3559	339.68	-8.252	0.8136E-1	-3.4277E-4	0.65%
0.24	3174	297.80	-7.538	0.7730E-1	-3.3555E-4	0.69%
0.26	2643	243.53	-6.060	0.6023E-1	-2.5663E-4	0.69%
0.28	2229	192.07	-4.544	0.4227E-1	-1.7343E-4	0.62%
0.30	1911	143.28	-3.131	0.2648E-1	-1.0417E-4	0.36%

total frequency shift uncertainty. For a given  $\Delta f_0$ , the greater the curve slope, the larger the dielectric constant error but the wider the measurement range. Neglecting the higher order terms in Eq.(6.5), we have

$$\partial \epsilon'_r / \partial (\Delta f_0) \approx a_1 \quad (6.8)$$

$a_1 \approx 1-3$  as listed in Tables 6.1-6.3; therefore, one MHz  $\Delta(\Delta f_0)$  will produce a  $\Delta \epsilon'_r$  of 1-3.

The total frequency shift uncertainties are the sum of the uncertainties in calculated  $\Delta f_0$  and measured  $\Delta f_0$ , i.e.,

$$\Delta(\Delta f_0) = \Delta(\Delta f_0)_{\text{calc.}} + \Delta(\Delta f_0)_{\text{meas.}} \quad (6.9)$$

The uncertainty in calculated  $\Delta f_0$  includes not only numerical but also other errors. One such error is due to the uncertainties in cavity dimensions. The other error arises from departures of a real cavity from the ideal mathematical model due to eccentricity of the sample placement and presence of the movable short circuit and coupling loop. Being a

relative parameter,  $\Delta f_0$  is affected little by these errors. Numerical errors in  $\Delta f_0$  are also negligible if the modal number used in the field calculation is large enough, as demonstrated in section 3.3.

The uncertainty in measured  $\Delta f_0$  includes the measurement error and also includes other possible experimental errors due to the sample, sample holder and cavity as described below.

(1) Error due to the sample. The variations in sample radii due to size measurement uncertainty and thermal expansion can cause a significant error. In Figure 6.4, the relative error in  $\epsilon'_r$  due to one percent  $r_s$  variation is plotted as a function of  $\epsilon'_r$  for different sample radii. It is shown that the error does not exceed 3% for  $r_s/r_0=0.676$  but it increases drastically when the sample radius approaches the insertion hole radius, especially for high permittivity samples. For this reason, even a slight looseness of the sample in the hole would produce a significant error if there was not sufficient air space between the sample

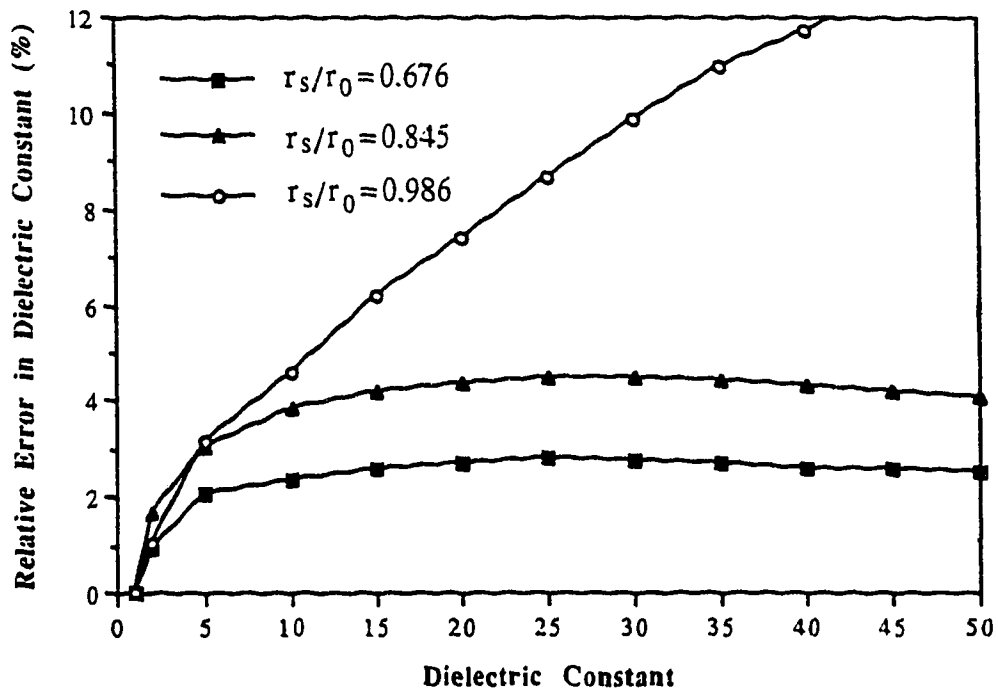


Figure 6.4 The relative error in the dielectric constant due to a 1% variation in sample's radius at different sample radii ( $r_0 = 0.355$ ,  $r_1 = 1.244$ ,  $r_2 = 5.0$ ,  $L = 20.0$ ,  $D = 0.3\text{cm}$ ,  $\epsilon_{rh} = 1.0$ ).

and the hole wall or if a sample holder made of a low permittivity material was not used. Besides radius variations, sample length variations can also cause errors if the length is not longer than the effective hole depth.

(2) Errors due to the sample holder. Since there are always dimensional variations in sample holders, one particular sample holder should be used in both the empty and loaded cavity tests to avoid an erroneous  $\Delta f_0$ . Moreover, in the case of liquid samples, the variation in the holder's inner diameter causes the same variation in the sample's diameter, thus resulting in a sample radius error as examined in (1).

(3) Errors due to the cavity. Since the resonant frequency is a sensitive function of the cavity dimensions, for example,  $\Delta f_0 = 15\text{MHz}$  for a 1mm length variation, the thermal expansion during the sample test can produce a misleading  $\Delta f_0$ . For example, the linear expansion coefficient of brass is about  $2 \times 10^{-5}/^\circ\text{C}$ , thus, a 10-degree change in overall cavity temperature will bring about a length change of 0.04mm to a 20cm long brass cavity, leading to a resonant frequency shift of  $0.04\text{mm} \times 15\text{MHz}/\text{mm} = 0.6\text{MHz}$ . By our use of localized microwave sample heating and a small sample volume, cavity expansion is very minimal while this same design feature also shortens heating time.

It should be mentioned that the cavity structure with the sample insertion holes not only makes the sample insertion easier but also reduces some of the experimental errors which would be significant otherwise. Firstly, loading a sample without opening the cavity each time ensures greater test repeatability. Secondly, the insertion holes also help to reduce the eccentricity of sample placement. Finally, the contact of the sample ends with cavity walls is avoided, thus eliminating the usual air gap error which typically is greater than 10% in a cavity without insertion holes [38].

However, the presence of the insertion hole can also be a drawback. The hole effects, as discussed in Chapter 4, make the axial distribution of the E-field, and therefore the temperature, non-uniform in the sample. Always being a function of temperature, the sample's dielectric constant will not be a constant. The dielectric constant determined under the assumption of homogeneous dielectric properties is really some type of average value. This value is between  $\epsilon'_r(T_1)$  and  $\epsilon'_r(T_2)$  where  $T_1$  and  $T_2$  are the highest and the lowest temperatures over the sample volume which

interacts with the E-field. Ideally, in order to reduce the difference in  $\epsilon'_r(T_1)$  and  $\epsilon'_r(T_2)$ , the sample must reach a temperature equilibrium. In practice, however, the temperature equilibrium is not necessary and a slightly longer sample heating time can reduce this difference to a negligible degree. This is confirmed by a detailed analysis and experimental results presented in Appendix 5.

Errors in the loss tangent can be calculated by Eq. (6.3). Differentiating Eq. (6.3), we have

$$\frac{\Delta(\tan\delta)}{\tan\delta} = \frac{\Delta(\Delta(1/Q))}{\Delta(1/Q)} + F_\ell \Delta(1/F_\ell) \quad (6.10)$$

This equation indicates that the relative error in  $\tan\delta$  is composed of two parts, the part due to the Q-measurement error

$$\left[ \frac{\Delta(\tan\delta)}{\tan\delta} \right]_Q = \frac{\Delta(\Delta(1/Q))}{\Delta(1/Q)} = \frac{Q_L^2 \Delta Q_0 - Q_0^2 \Delta Q_L}{Q_L Q_0 (Q_0 - Q_L)} \quad (6.11)$$

and the part due to the error in dielectric constant transferred through the loading factor

$$\left[ \frac{\Delta(\tan\delta)}{\tan\delta} \right]_\epsilon = F_\ell \Delta(1/F_\ell) = F_\ell \left[ \partial(1/F_\ell) / \partial \epsilon'_r \right] \cdot \Delta \epsilon'_r \quad (6.12)$$

where the calculation error in  $F_\ell$  is neglected. If the approximation is made that  $\bar{Q} = (Q_L + Q_0)/2 \gg (Q_0 - Q_L)$  and  $\Delta Q_L \approx \Delta Q_0 \approx \Delta \bar{Q}$ , Eq. (6.11) becomes

$$\left[ \frac{\Delta(\tan\delta)}{\tan\delta} \right]_Q = -2\Delta \bar{Q} / \bar{Q} \quad (6.13)$$

where  $\Delta \bar{Q} / \bar{Q}$  can be treated as an average relative error in Q measurements. Because the parameter  $\epsilon'_r / F_\ell$  is used as the calibration curve, we express the second part of the loss tangent error in terms of  $\epsilon'_r / F_\ell$  and its derivative as follows

$$\left[ \frac{\Delta(\tan\delta)}{\tan\delta} \right]_\epsilon = F_\ell \cdot \frac{\partial(1/F_\ell)}{\partial \epsilon'_r} \cdot \Delta \epsilon'_r = \left[ \left( \frac{\epsilon'_r}{F_\ell} \right)^{-1} \cdot \frac{\partial(\epsilon'_r / F_\ell)}{\partial \epsilon'_r} - 1/\epsilon'_r \right] \cdot \Delta \epsilon'_r \quad (6.14)$$

Defining

$$\zeta = \left(\frac{\epsilon'_r}{F_\ell}\right)^{-1} \cdot \frac{\partial(\epsilon'_r/F_\ell)}{\partial\epsilon'_r} \epsilon'_r - i \quad (6.15)$$

then 
$$\left[\frac{\Delta(\tan\delta)}{\tan\delta}\right]_\epsilon = \zeta \cdot \Delta\epsilon'_r/\epsilon'_r \quad (6.16)$$

We may call  $\zeta$  the error transfer function which amplifies the error in  $\epsilon'_r$  when  $\zeta > 1$  and compresses the error when  $\zeta < 1$ . This function can be easily derived from the calibration curve  $\epsilon'_r/F_\ell$ . According to Eq. (6.15), it can be shown that the  $\epsilon'_r/F_\ell$  curve with a steep rising section and a flat falling section leads to a small  $\zeta$ . In Figure 6.5,  $\zeta$  is plotted for the case of the calibration curves in Figure 6.1b. It shows that  $\zeta$  is dielectric constant dependent and  $\zeta < 1$  if  $\epsilon'_r < 35$ . We also see that  $\zeta$  varies greatly with sample size and a small sample size results in a small  $\zeta$ . However, this may not reduce the  $\tan\delta$  error of Eq. (6.16) as the error of  $\Delta\epsilon'_r/\epsilon'_r$  tends to increase with decreasing sample radius (see curve 1 and 2 in Figure 6.1a).

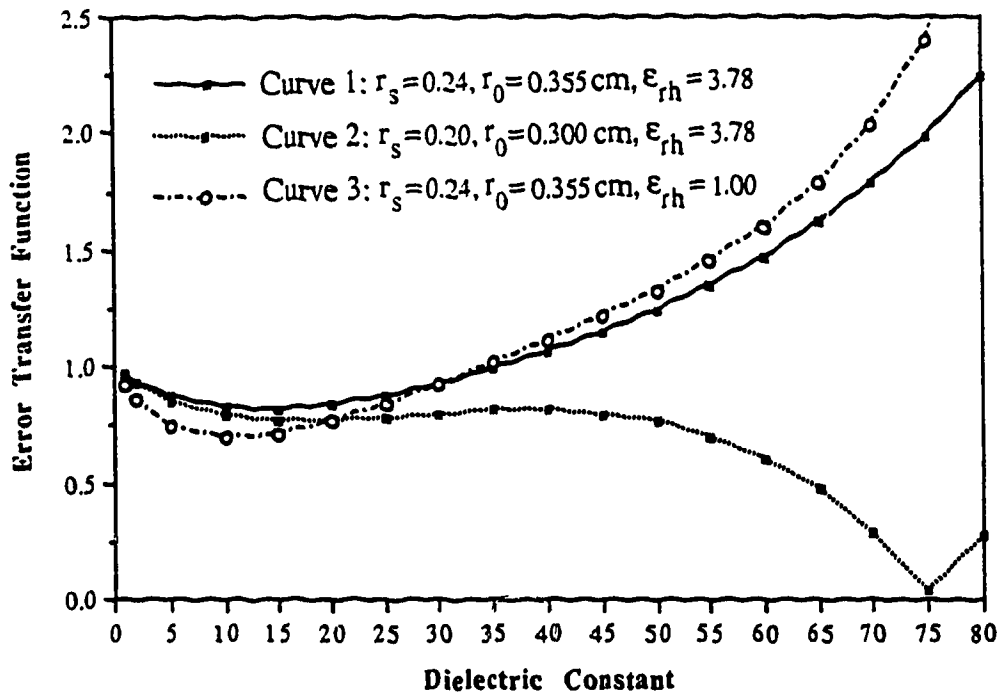


Figure 6.5 The error transfer function, i.e. the relative error in the loss tangent due to an error of 100% in the dielectric constant for three types of sample holders (see Figure 6.1).

To summarize the above error analysis, we will calculate the worst-case error in the dielectric constant and loss tangent for a suspended sample with  $r_s=0.24$  and  $D=0.3\text{cm}$ . As discussed above, for this case, the calculational errors and most experimental errors are minimal. Only the  $\Delta f_0$ -measurement uncertainty, sample radius variation and Q-measurement error needs to be considered. Therefore, we can express the error limit as

$$|\Delta \epsilon'_r| = \frac{\partial \epsilon'_r}{\partial |\Delta f_0|} \cdot |\Delta f_0|_m + |(\Delta \epsilon'_r)_{r_s}| \quad (6.17)$$

$$\left| \frac{\Delta \tan \delta}{\tan \delta} \right| = 2|\Delta Q/Q|_m + |\zeta \cdot (\Delta \epsilon'_r / \epsilon'_r)| \quad (6.18)$$

where  $\partial \epsilon'_r / \partial |\Delta f_0|$  is the slope of the calibration curves for dielectric constant given in Figures 6.1a, 6.2a and 6.3a,  $|\Delta f_0|_m$  is the  $\Delta f_0$ -measurement uncertainty limit which has been estimated to be 0.05MHz for the HP8623A sweep oscillator plug-in,  $(\Delta \epsilon'_r)_{r_s}$  is the error due to sample radius variations as shown in Figure 6.4,  $|\Delta Q/Q|_m$  is the Q-measurement uncertainty limit which has been found to be 12.5% or 3.5% for a direc-

Table 6.4 Evaluation of the worst-case error in the determined dielectric constant and loss tangent ( $r_s=0.24$ ,  $r_0=0.355$ ,  $r_1=1.244$ ,  $r_2=5.0$ ,  $D=0.3$ ,  $L=20.0\text{cm}$  and  $\epsilon_{rh}=1.0$ )

$\epsilon'_r$	2	5	10	20	30	40	50	60
$\partial \epsilon'_r / \partial  \Delta f_0 $	2.33	2.94	3.61	4.31	4.60	4.62	4.44	4.10
$ \Delta f_0 _m \times \partial \epsilon'_r / \partial  \Delta f_0 $	0.12	0.15	0.18	0.22	0.23	0.23	0.22	0.21
$ (\Delta \epsilon'_r)_{r_s} $	0.03	0.15	0.38	0.87	1.33	1.73	2.04	2.20
$ \Delta \epsilon'_r $	0.15	0.30	0.56	1.09	1.56	1.96	2.26	2.41
$ \Delta \epsilon'_r / \epsilon'_r $ (%)	7.5	6.0	5.6	5.5	5.2	4.9	4.5	4.0
$ \zeta $	0.86	0.75	0.69	0.77	0.92	1.11	1.32	1.59
$ \zeta \cdot (\Delta \epsilon'_r / \epsilon'_r) $ (%)	6.5	4.5	3.9	4.2	4.8	5.4	5.9	6.4
$ \Delta \tan \delta / \tan \delta $ (%) (Directivity=30dB)	31.5	29.5	28.9	29.2	29.8	30.4	30.9	31.4
$ \Delta \tan \delta / \tan \delta $ (%) (Directivity=40dB)	10.0	8.0	7.4	7.7	8.3	8.9	9.4	9.9

tional coupler with a directivity of 30dB or 40dB, and  $\zeta$  is the error transfer function as given in Figure 6.5. Assuming  $\Delta r_s / r_s = 1\%$ , we can evaluate Eqs. (6.17) and (6.18) as shown in Table 6.4. We can find that the worst-case error in the dielectric constant is 4-7% and that in the loss tangent is 30% or 10% for 30dB or 40dB directivity. It should be pointed that these errors are typically much less in practice because the random error vectors are seldom in phase.

### 6.3 Room Temperature Measurements

To verify the accuracy of the high temperature dielectric measurement method presented in this thesis, a number of different samples were measured at room temperature and their dielectric data were determined using the calculated calibration curves. The results are listed in Table 6.5 along with the published data for the sake of comparison.

The samples chosen are in solid, powder and liquid form and they cover a wide range of dielectric properties:  $\epsilon'_r = 2-75$  and  $\tan\delta = 0.001-0.7$ . We see that the discrepancy between this work and the published data, in most cases, is less than 0.1+5% for  $\epsilon'_r$  and 0.005+10% for  $\tan\delta$ , which is well within the worst-case error estimated in the last section. It should be emphasized that the method of dielectric determination based on the calculated calibration curves is an absolute method which does not rely on the reference data. Nevertheless, it still gives results in good agreement with the reference data as shown in Table 6.5.

### 6.4 High Temperature Measurement Procedure

The principle and method for the high temperature dielectric measurements have already been addressed. This section is intended to outline major experimental steps involved. Although not all the details can be covered, those critical to the measurement accuracy will be emphasized.

#### 6.4.1 Sample preparation

Samples to be measured are cylinders with a diameter smaller than the insertion hole and a length not shorter than twice the effective hole depth (see Figure 4.11). For a 0.3cm re-entrant gap and a 0.36cm hole, the minimum sample length is about  $(0.75 + 0.05\epsilon'_r)$  cm and the maxi-

**Table 6.5** Experimental results of dielectric constants and loss tangent at  $f=3.0\text{GHz}$  and  $T=23^{\circ}\text{C}$  as compared with published data

Sample	Present Work		Reference Data		Discrepancy	
	$\epsilon'_r$	$\tan\delta$	$\epsilon'_r$	$\tan\delta$	$\Delta\epsilon'_r$	$\Delta\tan\delta$
Teflon	1.94	0.0025	2.05	0.0083 (1)	-0.11	-0.0058
			2.10	0.0002 (2)	-0.16	+0.0023
Nylon	2.94	0.010	3.04	0.012 (2)	-0.10	-0.002
Quartz (Corning)	3.74	0.0006	3.78	0.0005 (3)	-0.04	+0.0001
Soda Lime Glass (0080, Corning)	6.45	0.012	6.71	0.013 (2)	-0.16	-0.001
Alumina (AL-23, JM)	8.70	0.0008	9.30	0.0002 (4)	-0.60	+0.0006
CuO (powder, 2.7g/cc)	3.44	0.247	3.20	0.28 (5)	+0.22	-0.033
Benzene	2.24	0.004	2.28	0.002 (6)	-0.04	+0.002
Monochlorobenzene	5.39	0.110	5.54	0.120 (7)	-0.15	-0.01
Methanol	19.9	0.744	18.9	0.75 (8)	+1.0	-0.06
			21.0	0.62 (2)	-1.1	-0.124
Distilled Water	76.5	0.153	77.3	0.155 (2)	-0.8	-0.002
NaCl (0.1M)	73.3	0.219	75.2	0.225 (9)	-1.9	-0.006
10%A, 20%M and 70%B	6.66	0.278	7.30	0.22 (7)	-0.64	+0.058
40%W and 60%M	45.9	0.426	46.0	0.37 (7)	-0.1	+0.056
20%W and 80%D	10.6	0.236	9.19	0.257 (10)	+1.41	-0.021
40%W and 60%D	23.6	0.267	23.5	0.290 (10)	+0.1	-0.023
60%W and 40%D	42.8	0.243	39.3	0.275 (10)	+3.5	-0.032
80%W and 20%D	58.9	0.207	59.5	0.194 (10)	-0.6	+0.013

A-Acetone, B-Benzene, D-Dioxane, M-Methanol and W-Distilled Water

- (1) HP Product Note 8510-3, Aug. 1985.
- (2) A.R.von Hippel, Dielectric Materials and Application, MIT Press, 1954.
- (3) A.C.Metaxas, et al, Industrial Microwave Heating, IEE England, UK, 1988.
- (4) Data from Superior Technical Ceramics Corp., St. Albans, VT, USA.
- (5) W.R. Tinga, Electromagnetic Energy Reviews, vol.1, p.47, 1988.
- (6) B.Terselius, et al, J. of Microwave Power, 13(4), p.327, 1978.
- (7) P.O. Risman, et al, J. of Microwave Power, 6(2), p.101, 1971.
- (8) B.P.Jordan, et al, J. Phys. D: Appl. Phys., vol.11, p.695, 1978.
- (9) A. Stogryn, IEEE Trans., vol.MTT-19, p.733, Aug. 1971.
- (10) D. Misra, et al, IEEE Trans., vol.MTT-38, p.8, Jan. 1990.



mum sample diameter is around 80% of the hole size. If a sample diameter is too close to the hole diameter, arcing may occur in that narrow space. Also, a small variation in sample diameters will produce a significant error in the dielectric data as discussed in the previous section. On the other hand, a smaller sample will be subject to a larger error for the given measurement system accuracy.

Whether to use a sample holder or not depends on several factors. Obviously, powdered and fibrous samples must be contained in a holder, usually a quartz tube. Even in the case of solid samples, a holder makes sample inserting and positioning easier. It also improves the sample temperature uniformity and prevents possible contamination to the cavity. However, a holder which contacts the cavity wall is a heat sink; thus greatly lowering the sample heating rate [59].

#### 6.4.2 System setup check

After having set up the measurement and heating system as described by the block diagram of Figure 5.1, one should check the following:

1. Choose a proper sweep band and CRT scale. A resonant curve should appear on the right end of the screen, free of noise and irregularities and having a reasonable resolution;
2. Tighten every connector reasonably so that a stable resonant curve can be maintained even with a gentle knock on the bench;
3. Allow the analyzer a two-hour warm-up period to ensure a stable measurement;
4. Adjust the orientation of the coupling loop on the testing port to a roughly matched but slightly under-coupled condition;
5. Adjust the coupling loop and the three-stub tuner on the heating port to obtain critical coupling for a low loss sample and over-coupling for a medium loss sample;
6. Measure some of the samples listed in Table 6.5 at room temperature and compare the results with those in the table;
7. Heat one of the samples to be tested to make sure that the microwave heating power source, the tuning circuit and the temperature controller operate properly.

### 6.4.3 Heating and testing

The whole sample heating and testing process is controlled by the BASIC program DIELEC on an HP200 computer. The steps involved are (1) calibrating the reflectometer by replacing the cavity by a short; (2) testing the empty cavity; (3) heating and testing the sample at each temperature set point assigned; and (4) calculating the dielectric data. At the end of the test, the empty cavity is measured again to check the thermal expansion effect. Water cooling is used to keep the center conductor near room temperature. Even then, to minimize the thermal expansion effects, the time for measuring a sample up to 1000<sup>0</sup>C has to be limited to 2-3 minutes; typically 20-30 points and about 4-6 seconds for each point.

### 6.5 Experimental Results and Discussion

Samples of various types of materials are measured and their results are summarized in Table 6.6. The data of dielectric constants and loss factors are plotted as functions of temperature in Figures 6.6a through 6.6m, where dots are experimental results and lines are results of polynomial fitting. The results presented are typical ones among several sample tests using the same material.

The machinable ceramic has the usual ceramic properties of good chemical and thermal stability and high compressive strength and, at the same time, offers the ease of conventional machining. By virtue of its machinability, the sample dimension can be controlled accurately. The samples used are Cotronics Rescor Series Machinable Ceramics. The measured data of three types of machinable ceramics are shown in Figures 6.6a-c [58]. Macor(915) is an opaque white, odorless, porcelain-like material composed of 55% fluorophlogopite mica and 45% borosilicate glass [74]. This composition makes its dielectric properties similar to borosilicate glasses (see Figures 6.6e and f). Macor is usable until 1000<sup>0</sup>C; however, after being heated to 500<sup>0</sup>C, it becomes more transparent and less machinable. The second type is alumina silicate(902) which offers the highest machinability with the lowest cost. With a simple heat treatment at 1000<sup>0</sup>C after machining, its operation temperature can be extended from 600<sup>0</sup>C to 1150<sup>0</sup>C. If not heat treated, it tends

Table 6.6 High temperature dielectric properties of ceramics, measured at 3GHz while the sample is being heated by a 120W, 915MHz solid state power source.

Material	@25 <sup>0</sup> C	@300 <sup>0</sup> C	@500 <sup>0</sup> C	@800 <sup>0</sup>	@T <sub>max</sub>	T <sub>max</sub> <sup>0</sup> C	Remarks
	$\epsilon'_r$						
	$\epsilon''_r$						
Macor (915) (Cotronics)	5.8 0.05	6.5 0.32	7.0 0.52	9.0 2.3	9.0 2.3	800	softens at 850 <sup>0</sup> C
Alumina silicate (Cotronics)	4.8 <0.05	5.1 <0.05	5.4 0.05	5.9 0.28	6.6 0.66	1100	heat treatment before test; melted at 1200 <sup>0</sup> C
Machinable alumina (Cotronics)	4.1 <0.05	/ /	4.2 0.05	4.3 0.20	7.2 1.90	1600	preheated to 500 <sup>0</sup> C volume reduced by 70% at 1600 <sup>0</sup> C
Soda lime glass (Corning 0080)	6.7 0.08	7.5 0.10	8.0 0.70	/ /	21.5 14.5	750	softens at 700 <sup>0</sup> C
Borosilicate glass (Corning 7740)	4.1 <0.05	4.5 <0.05	4.9 0.24	6.6 1.8	7.5 3.2	880	softens at 800 <sup>0</sup> C
Borosilicate glass (Corning 3320)	4.2 <0.05	4.7 <0.05	4.9 0.12	5.8 0.80	8.1 3.3	950	softens at 800 <sup>0</sup> C
Mullite (McDanel MV20)	5.4 <0.05	/ /	6.4 0.05	7.0 0.27	8.8 1.6	1350	local melting at 1400 <sup>0</sup> C
Alumina (Coors AD995)	9.1 <0.05	/ /	/ /	9.8 <0.05	/ /	/ /	externally heated to 800 <sup>0</sup> C
CuO; pressed powder; 4.3g/cc (J. T. Baker)	5.4 <0.27	8.8 9.0	14.5 17.0	42.6 31.0	49.6 27.0	850	large power re- flection & local melting at 900 <sup>0</sup>
Al <sub>2</sub> O <sub>3</sub> (10%H <sub>2</sub> O) pressed powder; 1.5g/cc; (JM)	4.2 0.6	3.8 0.2	3.5 0.08	/ /	/ /	/ /	air gap occurs & density changes
SiC powder 1.63g/cc (C-Axis)	10.3 2.4	13.0 /	13.4 /	22.0 /	/ /	/ /	unstable heating; data show oscil- lation pattern

(Table 6.6 continued)

Material	@25 <sup>0</sup> C	@300 <sup>0</sup> C	@500 <sup>0</sup> C	@800 <sup>0</sup>	@T <sub>max</sub>	T <sub>max</sub> <sup>0</sup> C	Remarks
$\epsilon'_r$							
$\epsilon''_r$							
Aluminum nitride powder; 1.68g/cc (C-Axis)	2.7 <0.05	3.7 0.2	3.4 0.2	4.1 1.1	5.6 2.4	1150	thermal radiation loss & power reflection
Zeolite pressed powder; 0.9g/cc (Linde 13X)	3.1 0.27	4.5 1.75	5.8 4.7	/ /	5.8 4.7	500	local melting at 600 <sup>0</sup> C
Alumina cement dried; 0.5g/cc (Zircar AC56)	3.6 <0.05	4.3 <0.05	4.8 0.04	5.1 0.08	5.4 0.29	1150	local melting at 1200 <sup>0</sup> C
Zirconia cement dried; 1.4g/cc (Zircar ZC89)	3.6 0.17	3.3 0.14	3.1 0.05	3.3 0.34	4.1 1.0	1100	burnt at 1200 <sup>0</sup> C
Zirconia felt (Zircar ZYF100)	1.6 <0.05	1.8 <0.05	2.0 0.20	2.3 0.60	2.5 1.1	1000	local temperature oscillation

to crack or melt beyond 600<sup>0</sup>C with a heating rate greater than 25<sup>0</sup>C/sec. As shown in Figure 6.6b, its dielectric data have a quite linear temperature dependence over the range of 500<sup>0</sup>C to 1100<sup>0</sup>C. The third type is the machinable alumina (960) which is porous 96% alumina. It can be used continuously to 1660<sup>0</sup>C with no post-machining heat treatment required. However, it can be densified to 70% of the original volume after being heated to 1500<sup>0</sup>C over a period of 2 minutes. Due to this volume reduction, the high temperature data shown in Figure 6.6c are lower than the true values. It should also be mentioned that the pre-heat is used because of its low dielectric loss at room temperature. The sample is first heated in a resistance heater to about 500<sup>0</sup>C and then quickly inserted into the cavity. At this temperature, 960 is able to effectively absorb microwave energy.

Three types of glass from Corning are measured and their results are presented in Figures 6.6d-f. All the dielectric data show a sharp

cant concentration of alkali ions ( $\text{Na}^+$ ,  $\text{Ca}^{++}$ , etc), i.e., modifiers, whose mobility increases exponentially with temperature. Also, the network-forming ions ( $\text{Si}^{+4}$ ,  $\text{B}^{+3}$ , etc) become more mobile at temperatures above the freezing point (several hundred degrees) [75]. As a consequence, the ionic polarization and the dipole orientation contribution increase, resulting in a dramatic rise in the dielectric constant at high temperatures. Since the conductivity is proportional to the ion mobility, the dielectric loss will be an exponential function of temperature. Actually, the relaxation curves of glasses have a loss peak at frequencies below the microwave range. As temperature is increased, the peak shifts to higher frequencies [76]. If the peak shape remains the same, the shift gives rise to the positive temperature coefficient of the dielectric loss. By comparing Figure 6.6d with 6.6e and 6.6f, we can see that soda lime glass has a higher dielectric constant and loss factor than borosilicate glasses at all temperatures. This is probably due to the fact that the alkali ion concentration is higher in soda lime glass (15% $\text{Na}_2\text{O}$ , 7% $\text{CaO}$ , 4% $\text{MgO}$  and others) than in borosilicate glasses (4% $\text{MgO}$ , 3% $\text{Al}_2\text{O}_3$  and others) [77].

The measured dielectric data of MV20 is given in Figure 6.6g over the temperature range of 500°C to 1350°C. The MV20 is a dense mullite ( $\text{Al}_6 \cdot \text{Si}_2 \cdot \text{O}_{13}$ ) in a glassy matrix. It is a silica-alumina binary system with 55% $\text{Al}_2\text{O}_3$  and 42% $\text{SiO}_2$  [78]. This composition and structure makes the dielectric properties fall between those of amorphous glass and microcrystalline materials such as pure alumina. Attempts were made to measure the high temperature dielectric properties of high purity alumina by microwave absorption. A sample of 99.5% purity alumina from Coors is almost transparent to the microwave field in the cavity with a Q-factor of 2000 and its temperature cannot be raised by microwave heating. Using a conventional furnace to preheat the sample and then measuring it in the cavity, we find that its dielectric constant increases only slightly (from 9.1 to 9.8) and loss factor is almost unchanged (<0.05) up to 800°C.

Powder samples of several types of materials are measured. The obtained data from cupric oxide, aluminum nitride and zeolite are plotted in Figures 6.6h-j. It is known that the dielectric properties are very dependent on the density. The density variation during heating

lectric properties. Moreover, local melting and arcing are more likely to take place in a non-uniform sample. Therefore, the powder is pressed so that the density can remain relatively constant. The cupric oxide data in Figure 6.6h show a rapid increase in both  $\epsilon'_r$  and  $\epsilon''_r$  with temperature. The fall of  $\epsilon''_r$  after 730°C cannot be easily explained since the pressed sample after being heated has almost the same density as before. Also, the phase change of CuO does not take place below 1200°C and at one atmosphere [14]. On the curves of alumina nitride powder in Figure 6.6i, the slight drop at 450°C is more likely due to a local density change because the sample is not pressed. Figure 6.6j is the data of pressed 13X zeolite powder from Linde, showing that zeolite is a strong microwave absorber as reported in [79]. Without using temperature control, zeolite can be melted in a matter of seconds with only a few watts of microwave power. Zeolite has a cage structure formed by linking  $\text{SiO}_4$  and  $\text{AlO}_4$  tetrahedra at all the corners. The possible dielectric loss mechanism is ionic "rattling" in the cage [80]. Another ceramic powder with a large microwave absorption which we measured is silicon carbide powder. The measurement reveals that the data of SiC powder are unstable and unrepeatable at elevated temperatures [58], exhibiting an oscillation pattern, especially in the loss factor. Also measured is 90% aluminum oxide powder. We fail to obtain consistent dielectric data from this material due to the density changes. It should be pointed out that the data of powder samples presented here are always subject to the density uncertainty though care has been taken.

Other samples measured are alumina cement, zirconia cement and zirconia felt from Zircar. The cement samples are cast in the test tube, fully dried and baked at about 400°C for one hour. The sample of zirconia felt is cut and fits the test tube, maintaining the original density of 0.24g/cc. The data obtained from these samples are presented in Figures 6.6k-m. Figures 6.6k and 6.6l show that alumina cement has much less loss than zirconia cement. Figure 6.6m shows that zirconia felt, though having 90% voids, has a pronounced rise in the loss factor beyond 400°C. It is also noticed that the heating is intermittent, indicated by a flickering glow of the sample.

Figure 6.6 Measured dielectric constants and loss factors of various ceramics, at 3GHz, as functions of temperature. The worst case error is about  $\pm 8\%$  and  $\pm 30\%$  for dielectric constant and loss tangent (see Table 6.4).

- (a) Macor (Cotronics 915), one type of machinable ceramics;
- (b) Alumina silicate (Cotronics 902), one type of machinable ceramics;
- (c) Machinable alumina (Cotronics 960), one type of machinable ceramics;
- (d) Soda lime glass (Corning 0080);
- (e) Borosilicate glass (Corning 7740);
- (f) Borosilicate glass (Corning 3320);
- (g) Mullite (McDanel MV20);
- (h) Cupric oxide powder (J.T.Baker, pressed, 4.3g/cc);
- (i) Aluminum nitride powder (C-AXIS, 1.67g/cc);
- (j) Zeolite powder (Linde 13X, pressed, 0.9g/cc);
- (k) Alumina cement (Zircar AC56, fully dried, 0.5g/cc);
- (l) Zirconia cement (Zircar ZC89, fully dried, 1.4g/cc);
- (m) Zirconia felt (Zircar ZYF100).

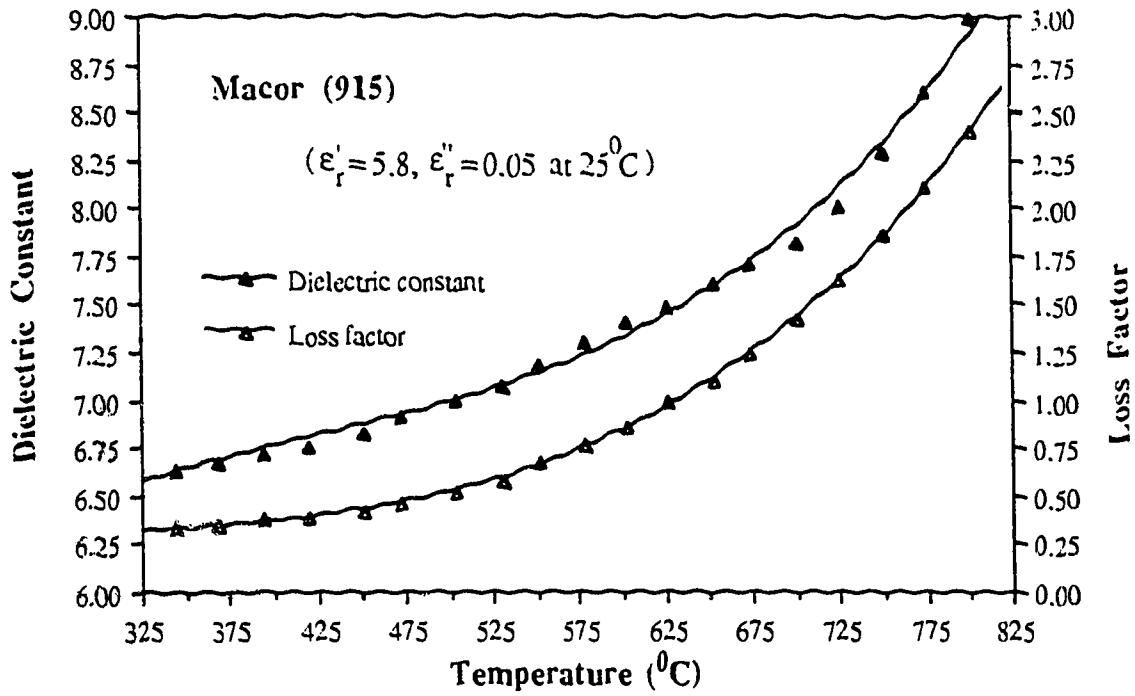


Figure 6.6a

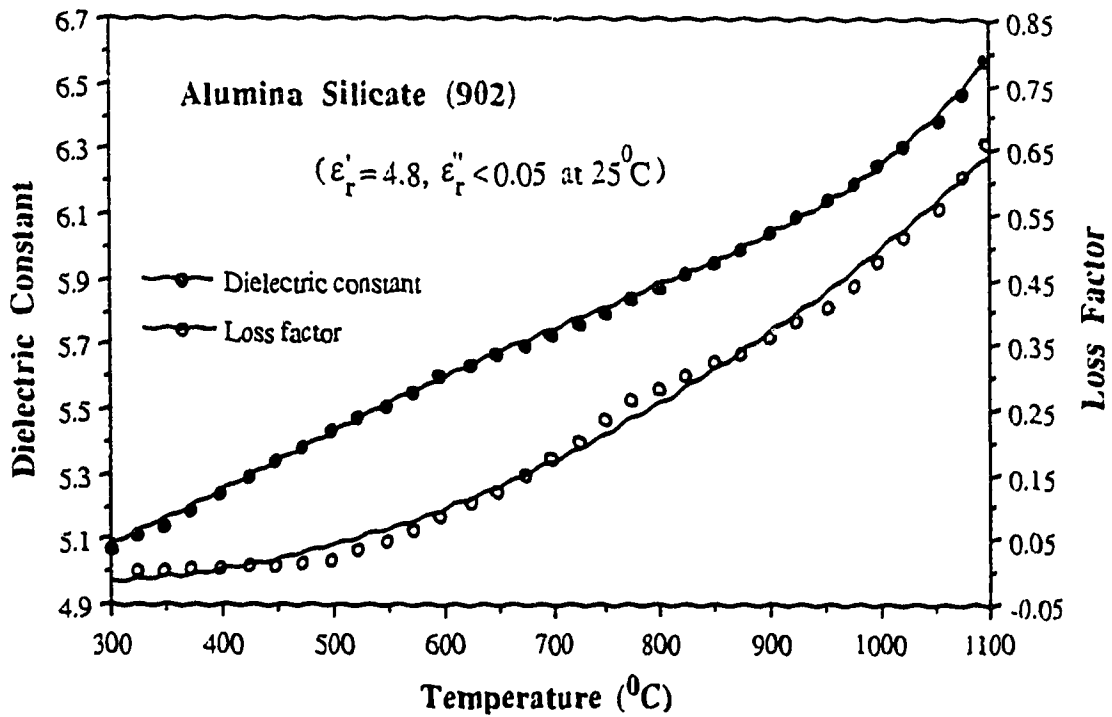


Figure 6.6b



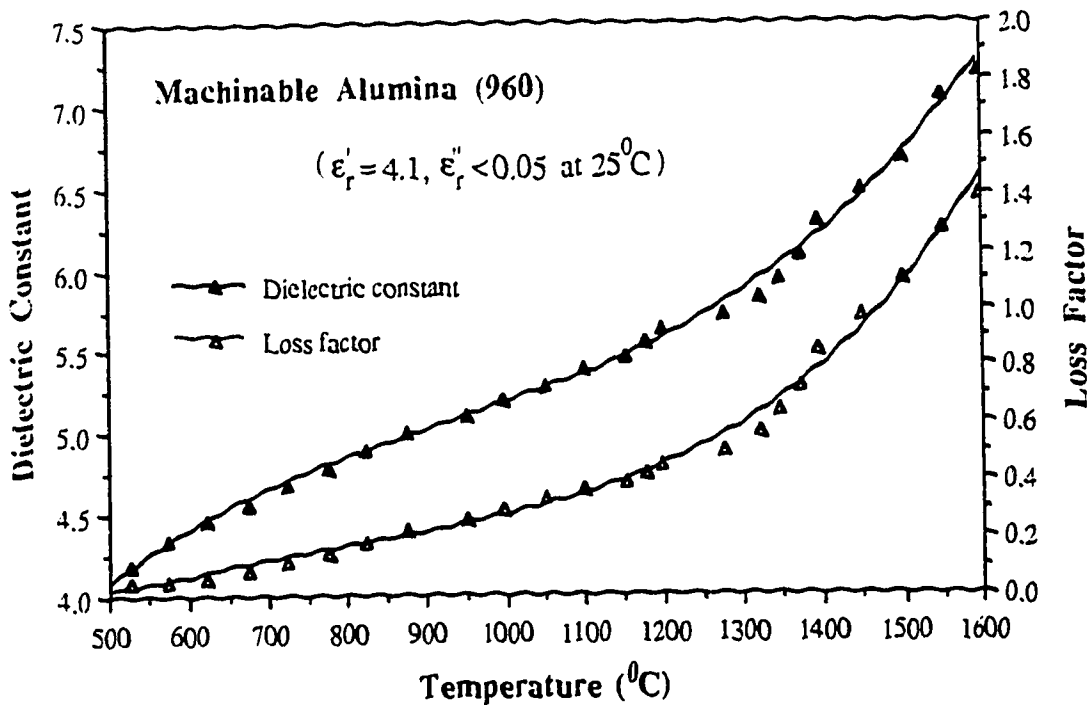


Figure 6.6c

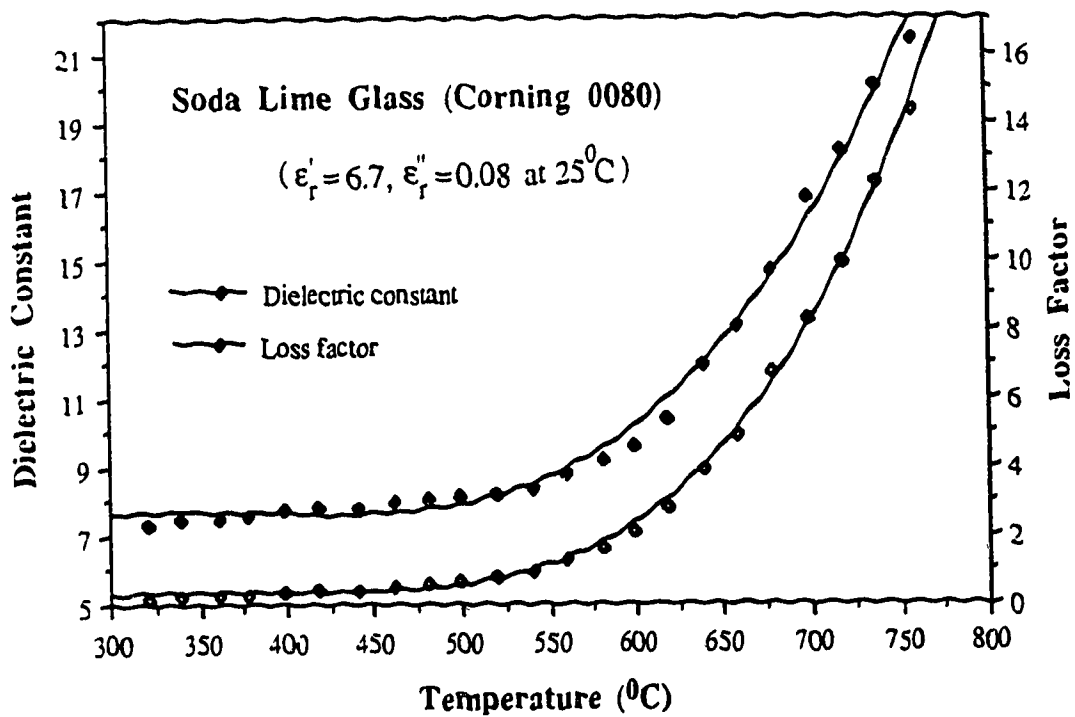


Figure 6.6d

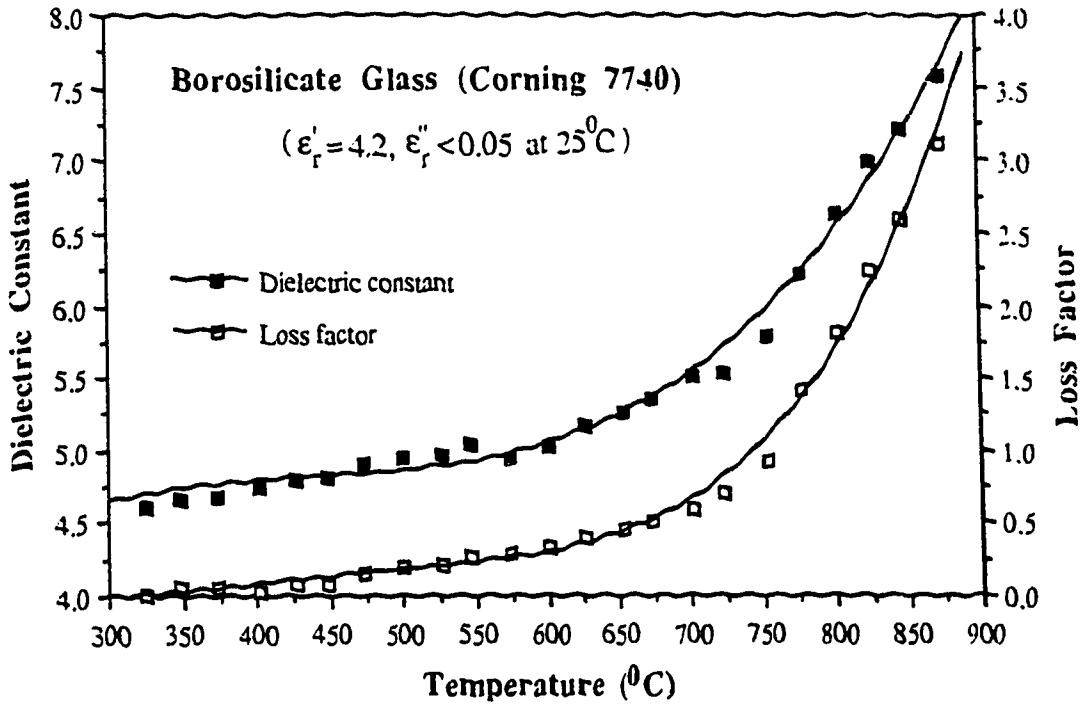


Figure 6.6e

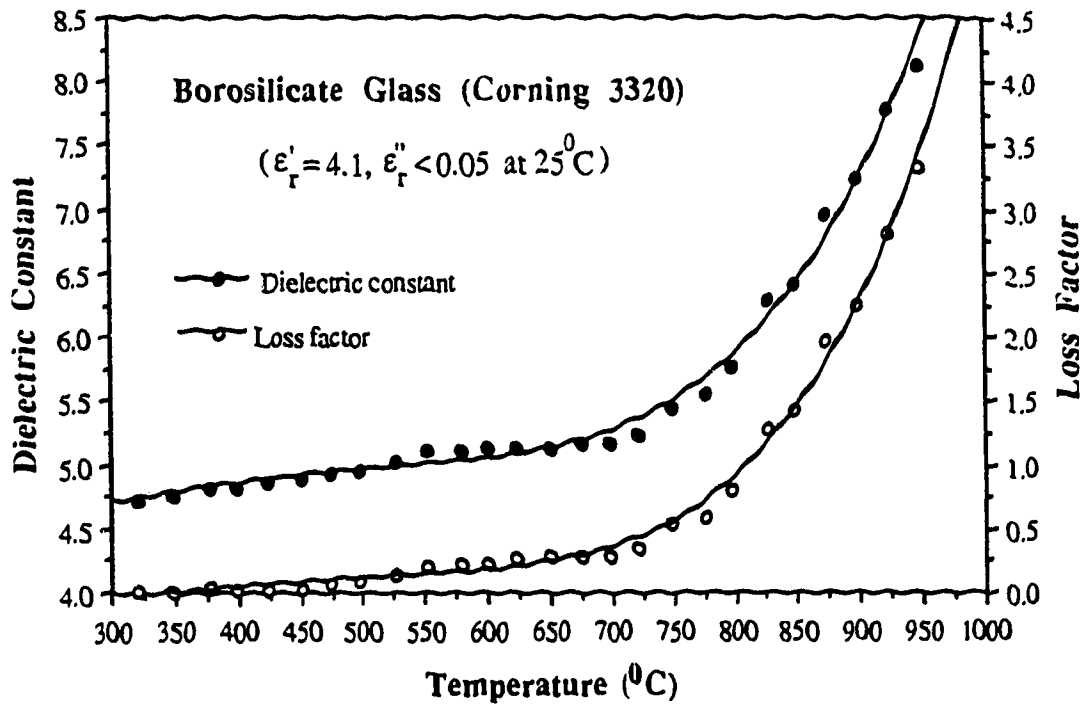


Figure 6.6f

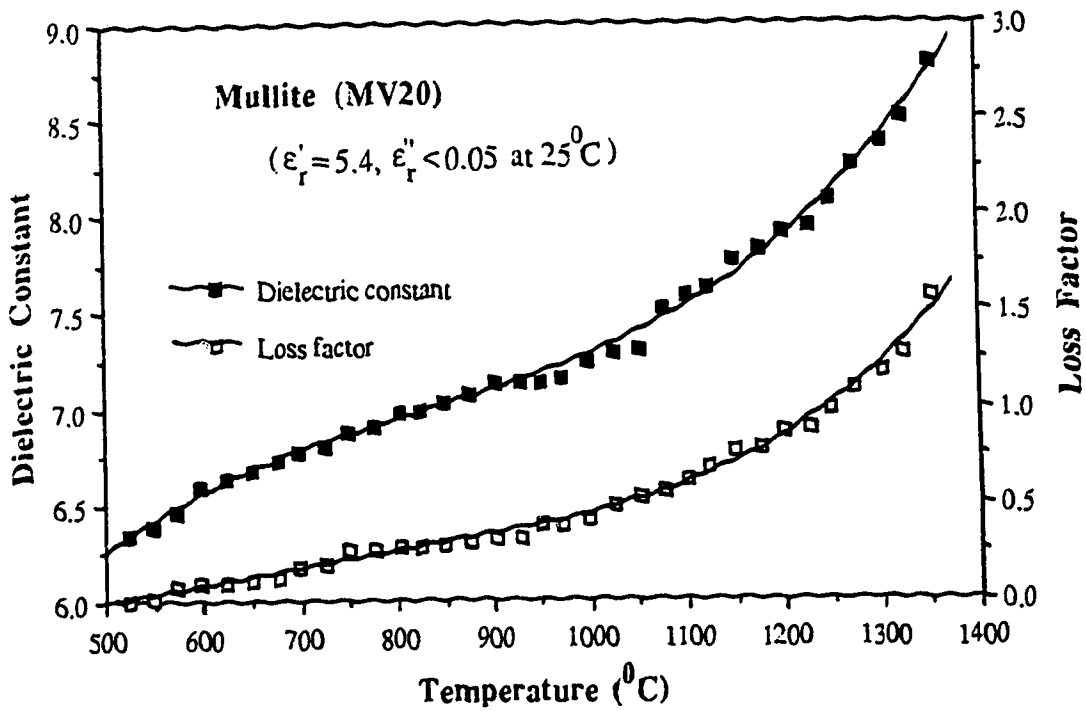


Figure 6.6g

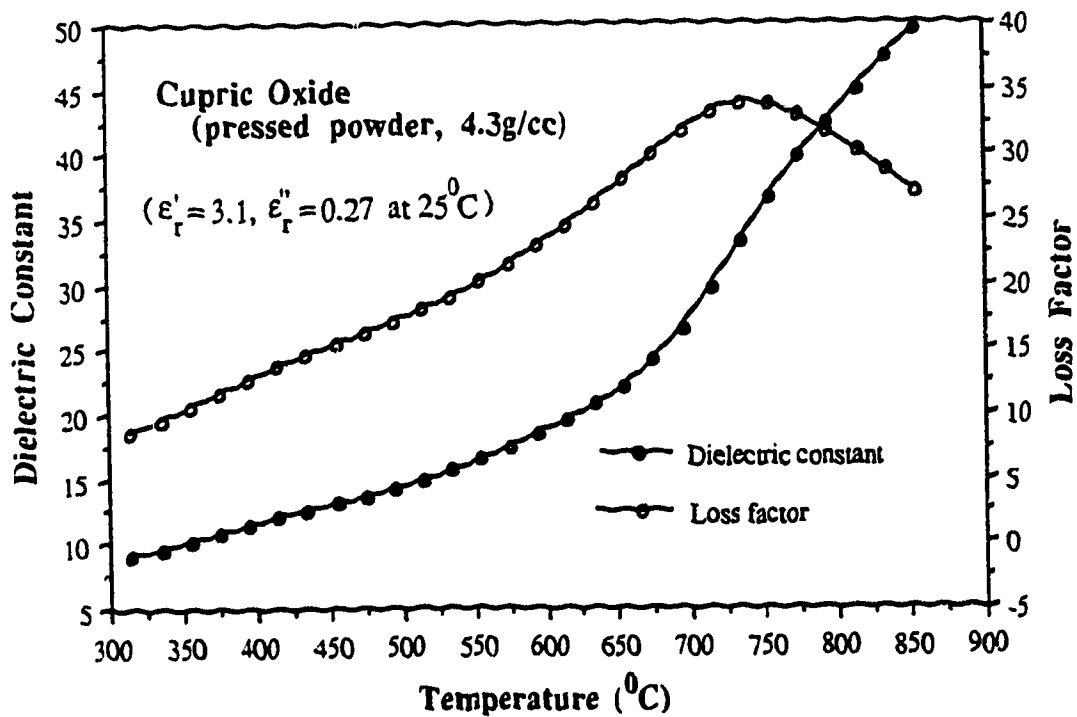


Figure 6.6h

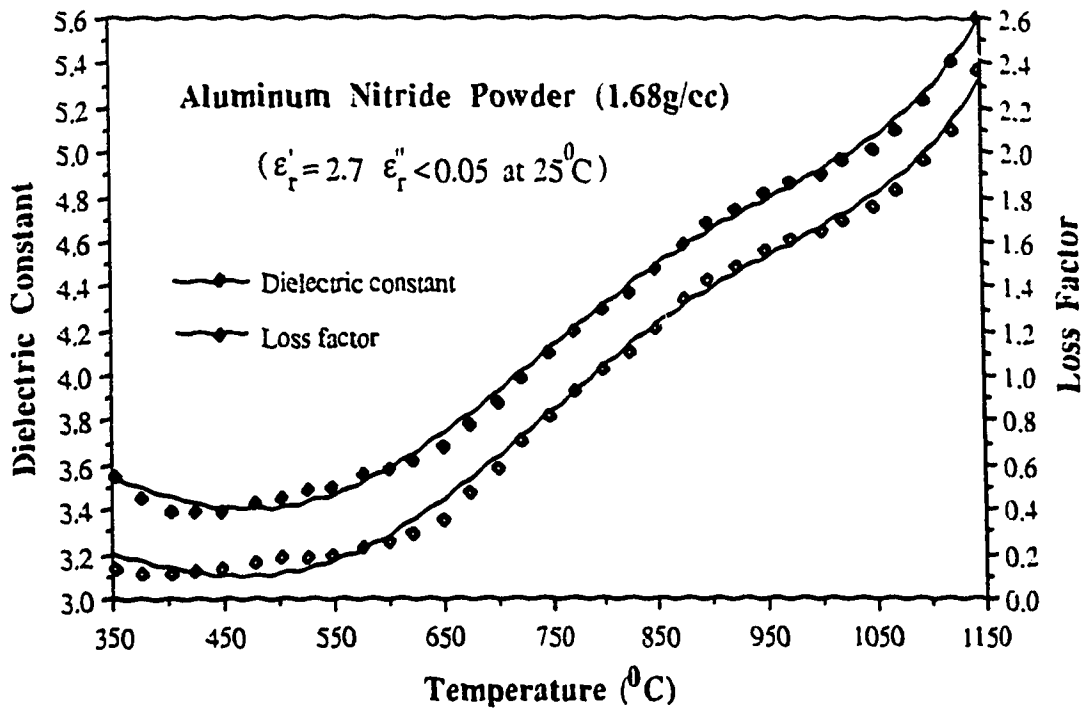


Figure 6.6i

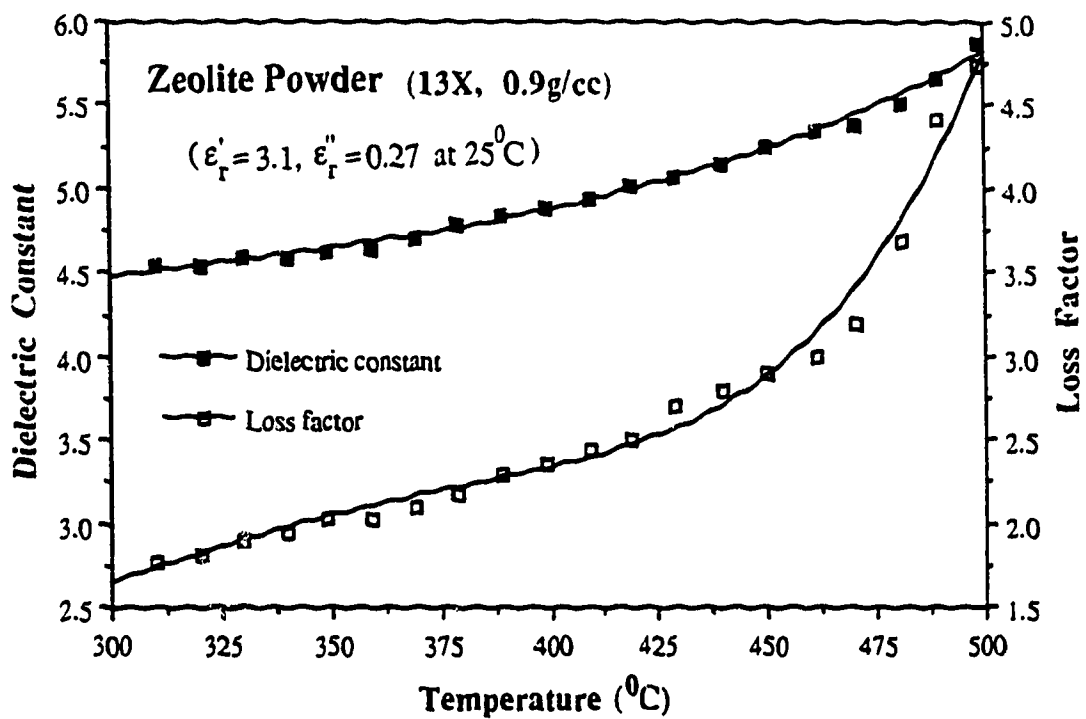


Figure 6.6j

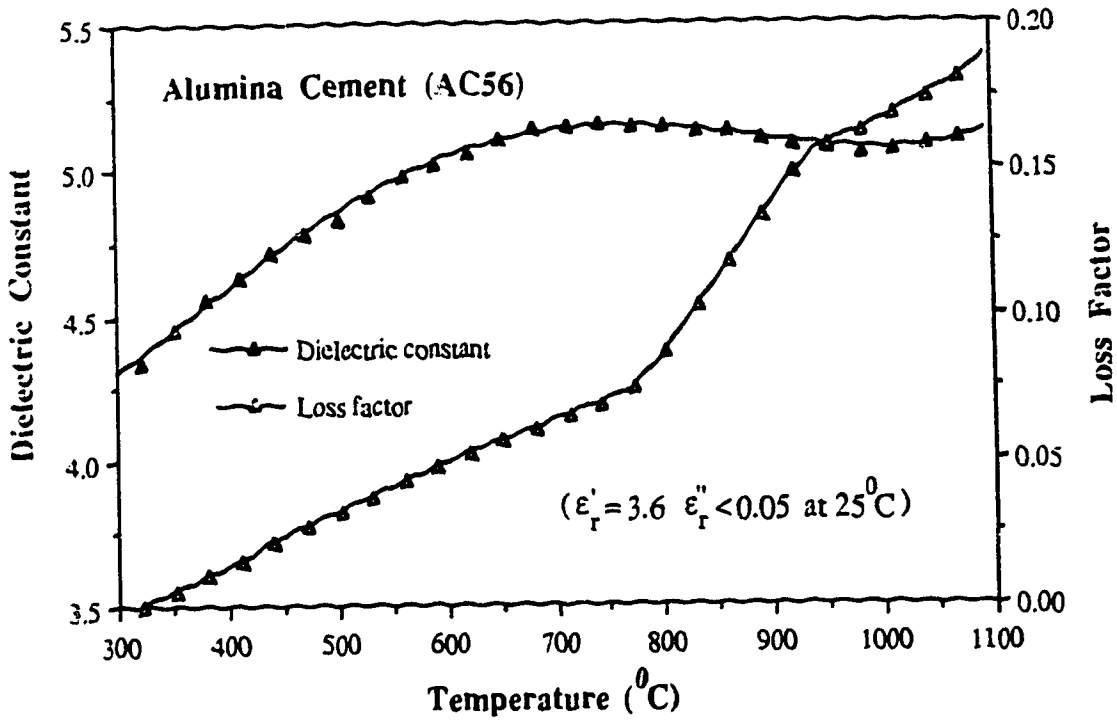


Figure 6.6k

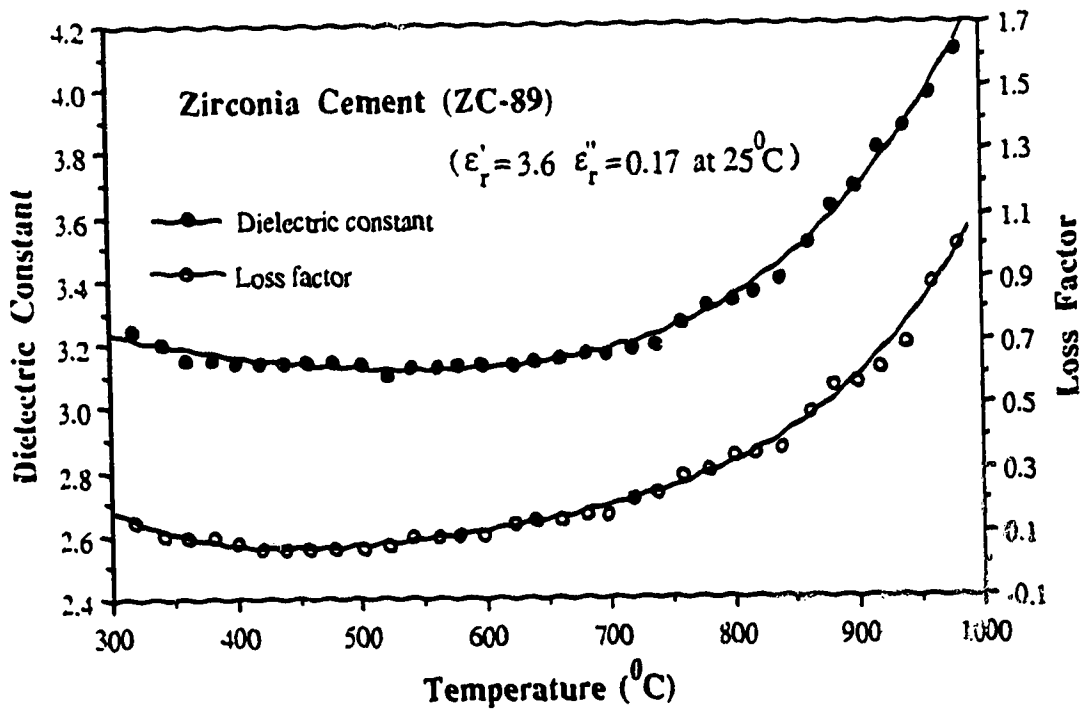


Figure 6.61

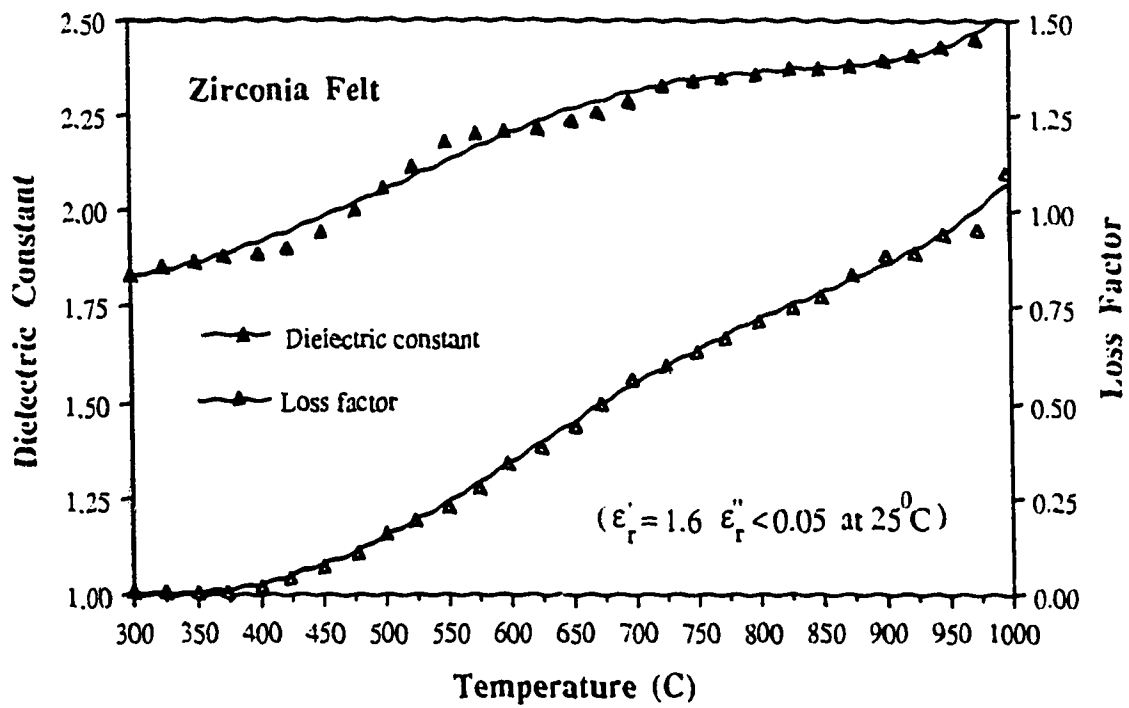


Figure 6.6m

## CHAPTER 7

### CONCLUSION

An automatic high temperature microwave dielectrometer system has been presented which is demonstrated to be capable of measuring complex dielectric constant versus temperature curves up to 1600<sup>o</sup>C, at 3GHz, in a few minutes, while the sample is being rapidly heated by 120W of 915 MHz microwave power. Four main features characterize this system.

(1) A coaxial re-entrant cavity is designed to be used both as a test chamber and as a microwave sample heater. By virtue of a strongly focused E-field in the re-entrant gap, a high heating rate and high measurement sensitivity have been achieved. The use of fast and selective microwave sample heating together with a small sample volume greatly reduces the cavity thermal expansion errors which exist in a conventional sample heating scheme.

(2) Sample heating and testing are conducted at the same time but in different frequency bands, i.e., 915MHz and 3GHz. As a result, the testing signal can easily be isolated from the heating power by a high-pass filter. If interested in dielectric properties at 915MHz, one can interchange the testing and heating source and use a low-pass filter instead. Moreover, this dual frequency approach allows a much higher heating power level.

(3) Dielectric data are determined from the calculated instead of experimentally obtained calibration curves. The accuracy in this absolute method does not suffer from the uncertainty in the reference data. The calibration curves can be easily obtained for arbitrary sample and cavity dimensions without repeating experimental calibration procedures.

(4) The use of a sample insertion hole and hollow center conductor greatly eases the sample preparation and loading, making instant on-line measurement possible. It also avoids the contact of the sample ends with the cavity walls and thus eliminates the usual air gap errors in a cavity without insertion holes. Furthermore, the analysis shows that the hole effects linearize the resonant frequency shift by the sample.

The cavity characteristics are fully explored with the aid of a mode-matching analysis. They can be summarized as follows.

(1) There exists a series of quasi TEM modes, which are the TEM

from the gap region, the TEM field pattern is a good approximation for the cavity field distribution.

(2) The gap field cannot be represented by a lumped capacitor or an inductor. Instead, it varies greatly with the frequency or gap parameters such as gap width, sample radii and permittivity.

(3) The electric energy density in a sample loaded in a narrow gap can be higher than the average cavity value by a factor of several hundred, though the stored energy in the sample is only a fraction of the total energy in the cavity. The power dissipation in a medium loss sample ( $\tan\delta=0.01-0.1$ ) is comparable to that on the cavity wall.

(4) The presence of the sample insertion holes reduces the gap E-field but causes an additional amount of stored energy inside the holes. This portion of energy compensates the sensitivity drop in the dielectric determination, and hence, provides a nearly linear frequency shift with dielectric loading.

(5) For a given sample radius, the use of a sample holder equivalently increases the hole size (by the holder's wall thickness), thereby enhancing the hole effects, especially for a low permittivity holder. It also considerably reduces the sample radius variation error which is minimized when the holder's permittivity is unity, i.e., the sample is suspended in the gap.

The resultant errors in the determined dielectric data are examined in detail. The analysis shows that the measurement error of the dielectrometer is the single largest error source. For example, for a total loss tangent error of 30%, 25% is due to the uncertainty in the return loss measurement. This error can be reduced to 4% if the directivity of the reflectometer is improved from 30dB to 40dB. It is also shown that the cavity thermal expansion will cause a larger error in the resonant frequency shift than the measurement uncertainty if the cavity body temperature is raised by  $10^{\circ}\text{C}$ .

The dynamic measurement range is mainly limited by the measurement uncertainty of the testing channel and the heating ability of the heating channel. Clearly, it is difficult to heat a very low loss sample effectively by microwave absorption. Sample preheating and sample thermal insulation can overcome this limitation to a certain degree.

The main disadvantage of this system is the complexity due to the



heating also increases the complexity due to the requirement for dynamic tuning and matching. Nevertheless, the methodology used has resulted in a microwave dielectrometer exceeding the high temperature limitation of other methods. Its speed, convenience and reliability make it useful not only in laboratory measurements but also in industry processing and quality control, especially for fiber, rod or liquid products. With both microwave testing and heating capability, this system can also be used in dynamic studies of microwave heating of ceramics. The dielectric data obtained as functions of time, temperature or heating rate or power level will be very informative in understanding the mechanism of microwave-material interaction.

It is believed that the work, as reported in this thesis, has laid the basis for a better understanding of the characteristics of the dielectric loaded coaxial re-entrant cavity. This work will also contribute substantially to the technique of high temperature dielectric measurement and to the more effective industrial utilization of microwave power in general.

## REFERENCES

- [1] J.M. Osepchuk, "A history of microwave heating application", IEEE Trans. MTT, vol.30(9), pp.1200-1224, 1984.
- [2] R.C. Jain, Microwave Dielectric Measurement and Layer Heating, Ph.D Thesis, University of Alberta, pp.1-2, 1988.
- [3] S. Das and T.R. Curlee, "Microwave sintering of ceramics: can we save energy?", Ceramic Bulletin, vol.66(7), pp.1093-1094, 1987.
- [4] W.H. Sutton, "Microwave processing of ceramic materials", Ceramic Bulletin, vol.68, pp.376-386, 1989.
- [5] W.R. Tinga, "Design principles for microwave heating and sintering", Mat. Res. Soc. Symp. Proc., vol.60, pp.105-116, 1986.
- [6] R.E. Collin, Field Theory of Guided Waves, ch.1, McGraw-Hill, NY, 1960.
- [7] R.M. Redheffer, "The Measurement of Dielectric Constant", in Technique of Microwave Measurements, C. Montgomery, Ed., ch.10, McGraw-Hill, NY, 1947.
- [8] A.R. von Hippel, Ed., Dielectric Materials and Application, ch.2, MIT Press, 1954.
- [9] H.M. Altschuler, "Dielectric Constant", in Handbook of Microwave Measurements (vol.II), Max Sucher and Jerome Fox, Ed., ch. IX, John Wiley & Sons, 1963.
- [10] M.N. Afsar, J.R. Birch and R.N. Clarke, "The measurement of properties of materials", Proc. IEEE, vol.74(1), pp.183-199, 1986.
- [11] W.R. Tinga and S.O. Nelson, "Dielectric properties of materials for microwave processing - Tabulated", J. of Microwave Power, 8(1), pp. 23-65, 1973.
- [12] G.M. Brydon and D.J. Hepplestone, "Microwave measurement of permittivity and  $\tan\delta$  over the temperature range 20-700<sup>o</sup>C ", Proc. IEE, vol.112, pp.421-425, 1965.
- [13] W.R. Tinga, "Microwave dielectric constants of metal oxides at high temperatures", Electromagnetic Energy Reviews, vol.1(4), pp.47-51, 1988; vol.2(1), pp.1-6, 1989.
- [14] D.K. Wong, Dielectric Constants of Metal Oxides, M.Sc. Thesis, University of Alberta, 1975.
- [15] W.W. Ho, "High-temperature dielectric properties of polycrystalline ceramics", Mat. Res. Soc. Symp., vol.124, pp.137-148, 1988.

- [16] R.M. Hutcheon, M.S.de Jong, P.F. Adams, L. Hunt, F. Iglesias, G.W. Wood and G.Parkinson, "A technique for rapid scoping measurements of RF properties up to 1000<sup>0</sup>C", *Electromagnetic Energy Reviews*, 2(4), pp.46-51, 1989.
- [17] J.B. Salsman, "Measurement of dielectric properties in the frequency range of 300MHz to 3GHz as a function of temperature and density", *Amer.Cer.Soc., Ceramic Transactions*, vol.21, "Microwave: Theory and Applications in Materials Processing", pp.203-214, 1991.
- [18] T.W. Athey, M.M. Stuchly and S.S. Stuchly, "Measurement of radio frequency permittivity of biological tissues with an open-ended coaxial line, Part I", *IEEE Trans. MTT*, vol.30, pp.82-86, 1982.
- [19] E.C. Burdette, F.L. Cain and J. Seals, "In Vivo probe measurement technique for determining dielectric properties at VHF through microwave frequencies", *IEEE Trans. MTT*, vol.28, pp.414-427, 1980.
- [20] D. Couderc, M. Giroux and R.G. Bosisio, "Dynamic high temperature microwave complex permittivity measurements of samples heated via microwave absorption", *J.of Microwave Power*, 8(1), pp.69-82, 1973.
- [21] M.Ollivon, S.Quinquenet, M. Seras, M. Delmotte and C. More, "Microwave dielectric measurements during thermal analysis", *Thermo-chimica Acta*, 125, pp.141-153, 1988.
- [22] J. Jaw, M. Finzel, J. Asmussen and M.C. Hawley, "Dielectric and temperature measurements during microwave curing of epoxy in a sweeping resonant cavity", *IEEE MTT-S Digest*, pp.465-468, 1987.
- [23] W.R. Tinga, B.Q. Tian and W.A.G. Voss, "New high temperature multi-purpose applicator", *Mat. Res. Soc. Proc.*, vol.189, pp.111- 116, 1991.
- [24] Weiguo Xi, W.R. Tinga, W.A.G. Voss and B.Q. Tian, "New results for coaxial re-entrant cavity with partially dielectric filled gap", *IEEE Trans. MTT*, vol.40(4), pp.747-753, 1992.
- [25] P.O. Risman and N.E. Bengtsson, "Dielectric properties of food at 3 GHz as determined by a cavity perturbation technique", *J. of Microwave Power*, 6(2), pp.101-124, 1971.
- [26] C.M.B. Walker, *Dielectric Constant of Water-DMSO Solutions and Numerical Modelling of Microwave Heating*, Ph.D Thesis, University of Alberta, pp.13-41, 1977.
- [27] R.C. Jain, *Microwave Dielectric Measurement and Layer Heating*, Ph.D

- Thesis, University of Alberta, pp.8-38, 1988.
- [28] H.B.G. Casimir, "On the theory of electromagnetic waves in resonant cavities", Philips. Res. Rep., 6, pp.161-182, 1951.
  - [29] R.A. Waldron, "Perturbation theory of resonant cavities", Proc. IEE, vol.107C, pp.272-274, 1960.
  - [30] O.P. Gandhi, Microwave Engineering and Applications, ch.2-4, Pergamon Press, NY, 1981.
  - [31] N.Marcuvitz, Waveguide Handbook, ch.2, McGraw-Hill, 1951.
  - [32] R.E. Collin, Fundamentals for Microwave Engineering, ch.3, McGraw-Hill, NY, 1966.
  - [33] B.W. Hakki and P.D. Coleman, "A dielectric resonator method of measuring inductive capacities in the millimeter range", IRE Trans. MTT vol.8(7), pp.402-410, 1960.
  - [34] F. Horner, T.A. Taylor, R. Dunsmuir, J. Lamb and W. Jackson, "Resonance methods of dielectric measurement at centimeter wavelengths", J. IEE, vol.93, pp.53-67, 1946.
  - [35] A. Parkash, J. K. Vaid and A. Mansingh, "Modified relations for evaluation of dielectric parameters in cylindrical cavities operating in  $E_{010}$  mode", J. Phys. E: Sci. Instrum., vol.12, pp.308-310, 1979.
  - [36] O.V. Karpova, "On an absolute method of measurement of dielectric properties of a solid using a  $\pi$ -shaped resonator", (in Russian) Fiz. Tverd. Tela, vol.1, pp.246-255, Feb 1959.
  - [37] A Milewski, "Coaxial lumped capacitance resonator for the investigations of dielectrics". Electron Technol., vol.10, pp.71-98, Jan 1977.
  - [38] A.Kaczkowski and A. Milewski, "High-accuracy wide range measurement method for determination of complex permittivity in re-entrant cavity-Part A and B", IEEE Trans. MTT, vol.28(3), pp.225-231, 1980.
  - [39] Shihe Li, C. Akyel and R.G. Bosisio, "Precise calculations and measurements on the complex dielectric constant of lossy materials using  $TM_{010}$  cavity perturbation techniques", IEEE Trans. MTT, vol. 29(10), pp.1041-1047, 1981.
  - [40] Shihe Li and R.G. Bosisio, "Composite hole conditions on complex permittivity measurements using microwave cavity perturbation techniques", IEEE Trans. MTT, vol.30(1), pp.100-103, 1982.

- [41] G. Roussy and M. Felden, "A sensitive method for measuring complex permittivity with a microwave resonator", IEEE Trans. MTT, vol.14 (4), pp.171-175, 1966.
- [42] B. Manring and J. Asmussen, "Electromagnetic modelling of single mode excited material loaded applicators", Amer. Cer. Soc., Ceramic Transactions, vol.21, "Microwaves: Theory and applications in materials processing", pp.159-166, 1991.
- [43] A Wexler, "Computation of electromagnetic fields", IEEE Trans. MTT, vol.17(8), pp.416-439, 1969.
- [44] T.Itoh, Ed., Numerical Techniques for Microwave and Millimeter Wave Passive Structures, John Wiley & Sons, NY, 1989.
- [45] W.C. Hahn, "A new method for the calculation of cavity resonators", J. of Applied Physics, vol.12, pp.63-68, 1941.
- [46] J.R. Whinnery, H.W. Jamiesen and Theo E. Robbins, "Coaxial-line discontinuities", Proc. of IRE, pp.695-709, 1944.
- [47] R. Mittra and S.W. Lee, Analytical Techniques in the Theory of Guided Waves, ch.2, Macmillan Company, NY, 1971.
- [48] B.Q. Tian and W.R. Tinga, "A wide range tunable and matchable high temperature applicator", Amer.Cer.Soc., Ceramic Transactions, vol. 21, "Microwave: Theory and Applications in Materials Processing", pp.647-654, 1991.
- [49] N.W. McLachlan, Bessel Functions for Engineers, Clarendon Press, 1955.
- [50] G.P. Tolstov, Fourier Series, Dover Pub., NY, 1962
- [51] R. Fletcher, Practical Methods of Optimization, John Wiley & Sons, NY, 1987.
- [52] D.R. Wong, Algorithm for Nonlinear Equations and Optimization Methods, (In Chinese), ch.2.7, Education Press, Beijing, 1979.
- [53] S.D. Conte and Carl de Boor, Elementary Numerical Analysis: An Algorithm Approach, McGraw-Hill, 1975.
- [54] M. Abramowitz and I.A. Stegun, Ed., Handbook of Mathematical Functions, ch.9, Dover Pub., NY, 1965.
- [55] Weiguo Xi and W.R. Tinga, "Field analysis of new coaxial dielectrometer", to be published on IEEE Trans. MTT, vol.40(10), 1992.
- [56] O.P. Gandhi, Microwave Engineering and Applications, ch.8, Pergamon Press, NY, 1981.
- [57] N. Marcuvitz, Waveguide Handbook, ch.4.5, McGraw-Hill, 1951.

- [58] Weiguo Xi and W.R. Tinga, "High temperature microwave dielectrometer", Amer. Cer. Soc., Ceramic Transactions, vol.21, "Microwave: Theory and Applications in Materials Processing", pp.215-224, 1991.
- [59] Weiguo Xi and W.R.Tinga, "Microwave heating and characterization of machinable ceramics" in Microwave Processing of Materials III, W.B. Snyder, Jr., W.H. Sutton, M. Iskander and P.L. Johnson, Ed., (Mat. Res.Soc.Proc. vol.269, San Francisco, CA 1992), 10 pages, in press.
- [60] H. J. Reich, Ed., Very High Frequency Techniques (vol.II), ch.28.17, McGraw-Hill, NY, 1947.
- [61] *ibid*, ch.32.30.
- [62] *ibid*, ch.32.34.
- [63] Hewlett Packard, HP 8756A Scalar Network Analyzer, Operating Manual.
- [64] Hewlett Packard, HP 86235A, 86240A/B/C RF Plug-in, Operating Information.
- [65] Z.Y. Shen, Microwave Techniques, (in Chinese), ch.8.9, Defense Industry Press, Beijing, 1980.
- [66] B.Q. Tian, W.R. Tinga and Weiguo Xi, "Single frequency high temperature microwave applicator and dielectrometer system" in Microwave Processing of Materials III, W.B. Snyder, Jr., W.H. Sutton, M. Iskander and P.L. Johnson, Ed., (Mat. Res. Soc. Proc. vol.269, San Francisco, CA 1992), 7 pages, in press.
- [67] D.A. Bell, Solid State Pulse Circuits, Reston Pub. Co., NY, 1976.
- [68] J.G. Webster, Ed., Medical Instrumentation: Application and Design, ch.1-3, Houghton Mifflin Company, Boston, 1978.
- [69] P. Horowitz and W. Hill, The Art of Electronics, ch.3-5, Cambridge University Press, NY, 1989.
- [70] R.R. Dils, "High-temperature optical fiber thermometer", J. Appl. Phys., 54(3), pp.1198-1201, 1983.
- [71] Luxtron Co., Accufiber Division, High Temperature Measurement and Control System, User's Manual of Accufiber Model 100C.
- [72] D.P. Chakraborty and I.A. Brezovich, "Error sources affecting thermocouple thermometry in RF electromagnetic fields", J. of Microwave Power, 17(1), pp.17-28, 1982.
- [73] P.W. Murrill, Fundamentals of Process Control Theory, Measur. Soc. Amer., NY, 1981.
- [74] D.G. Grossman, American Machinist, May 1978.

- [75] W.D.Kingery, H.K.Bowen and D.R.Uhlmann, Introduction to Ceramics, ch.18, John Wiley & Sons, NY, 1975.
- [76] R.H.Doremus, Glass Science, ch.2.11, John Wiley & Sons, NY, 1973.
- [77] N.P.Bansal and R.H.Doremus, Handbook of Glass Properties, Academic Press, NY, 1986.
- [78] McDanel Refractory Company, Data Sheet of Ceramic Tubing, Rods and Insulators, Beaver Falls, PA, USA.
- [79] S.Komarneni and R. Roy, "Anomalous microwave melting of zeolites", Materials Letters, vol.4(2), pp.107-110, 1986.
- [80] J.Thiebaut, C. Akyel, G.Roussy and R.G.Bosisio, "Dehydration and dielectric permittivity measurements of porous, inorganic material (13X Zeolite) heated with microwave power", IEEE Trans. IM, vol. 37(1), pp.114-120, 1988.
- [81] K.Crandell and P.A.Crandell, "Reflectometer for millimeter-wave measurements", Microwave Journal, pp.59-63, June 1980.
- [82] Hewlett Packard, "Microwave mismatch error analysis", Application Note 56, Oct 1967.
- [83] F.M. Mims, "Analog arithmetic", Modern Electronics, pp.57-61, Nov 1990.
- [84] W.R. Tinga, "Rapid high temperature measurement of microwave dielectric properties" in Microwave Processing of Materials III, W.B. Snyder, Jr., W.H. Sutton, M. Iskander and P.L. Johnson, Ed., (Mat. Res. Soc. Proc. vol.269, San Francisco, CA 1992), 12 pages, in press.

APPENDIX 1 INTEGRATION FUNCTION OF  $e_{ij}(a,b)$

This appendix evaluates and discusses the following integration

$$e_{ij} = \frac{1}{A} \int_0^A \cos \frac{j\pi}{B} (z+z_0) \cos \frac{i\pi}{A} z dz \quad (A1.1)$$

$i, j = 0, 1, \dots, \infty$

$e_{ij}$  can be directly integrated as follows:

$$\begin{aligned} e_{ij} &= \frac{1}{A} \int_0^A \cos \frac{j\pi}{B} (z+z_0) \cos \frac{i\pi}{A} z dz \\ &= \frac{1}{2A} \int_0^A \left\{ \cos \left[ \left( \frac{j+i}{B} \right) \pi z + \frac{z_0}{B} j \pi \right] + \cos \left[ \left( \frac{j-i}{B} \right) \pi z + \frac{z_0}{B} j \pi \right] \right\} dz \\ &= \frac{1}{2A} \left\{ \frac{1}{j/B+i/A} \cdot \sin \left[ \left( \frac{j+i}{B} \right) \pi z + \frac{z_0}{B} j \pi \right] + \frac{1}{j/B-i/A} \cdot \sin \left[ \left( \frac{j-i}{B} \right) \pi z + \frac{z_0}{B} j \pi \right] \right\} \Big|_0^A \\ &= \frac{1}{2A} \left\{ \frac{1}{jA/B+i} \cdot \left[ \sin \left[ \left( \frac{j+i}{B} \right) \pi + \frac{z_0}{B} j \pi \right] - \sin \frac{z_0}{B} j \pi \right] \right. \\ &\quad \left. + \frac{1}{jA/B-i} \cdot \left[ \sin \left[ \left( \frac{j-i}{B} \right) \pi + \frac{z_0}{B} j \pi \right] - \sin \frac{z_0}{B} j \pi \right] \right\} \\ &= \frac{1}{2\pi} \cdot [(-1)^i \sin \left[ \left( \frac{j+i}{B} \right) \pi + \frac{z_0}{B} j \pi \right] - \sin \frac{z_0}{B} j \pi] \cdot \left( \frac{1}{jA/B+i} + \frac{1}{jA/B-i} \right) \end{aligned}$$

Let  $A/B=a$  (A1.2)

and  $z_0/B=b$ , (A1.3)

Then,  $e_{ij} = e_{ij}(a, b)$

$$\begin{aligned} &= \frac{1}{2\pi} \cdot [(-1)^i \sin(a+b)j\pi - \sin bj\pi] \cdot \left( \frac{1}{ja+i} + \frac{1}{ja-i} \right) \\ &= \frac{1}{\pi} \cdot \frac{ja}{(ja)^2 - i^2} \cdot [(-1)^i \sin(a+b)j\pi - \sin bj\pi] \\ &= \frac{(ja)^2}{(ja)^2 - i^2} \cdot \left[ (-1)^i \frac{\sin(a+b)j\pi}{ja\pi} - \frac{\sin bj\pi}{ja\pi} \right] \quad (A1.4) \end{aligned}$$

First let's prove that  $e_{ij}$  is a convergent sequence.

$$\begin{aligned} \lim_{i \rightarrow \infty} |e_{ij}| &= \lim_{i \rightarrow \infty} \left| \frac{(ja)^2}{(ja)^2 - i^2} \cdot \left[ (-1)^i \frac{\sin(a+b)j\pi}{ja\pi} - \frac{\sin bj\pi}{ja\pi} \right] \right| \\ &= \lim_{i \rightarrow \infty} \frac{ja}{i^2} \cdot |(-1)^i \sin(a+b)j\pi - \sin bj\pi| \end{aligned}$$



$$\leq \lim_{j \rightarrow \infty} \frac{2ja \cdot 1}{\pi} \cdot \frac{1}{j^2} = 0$$

$$\lim_{j \rightarrow \infty} |e_{ij}| = \lim_{j \rightarrow \infty} \frac{1}{ja\pi} \cdot [(-1)^i \sin(a+b)j\pi - \sin bj\pi]$$

$$\leq \lim_{j \rightarrow \infty} \frac{2}{\pi} \cdot \frac{1}{j^2} = 0$$

Now let's look at some special cases.

(1)  $i \neq 0$  and  $j = 0$

$$e_{i0} = 0 \tag{A1.5}$$

(2)  $i = 0$  and  $j \neq 0$

$$e_{0j} = \frac{1}{ja\pi} \cdot [\sin(a+b)j\pi - \sin bj\pi] \tag{A1.6}$$

(3)  $i = j = 0$

$$\begin{aligned} e_{00} &= \lim_{j \rightarrow 0} e_{0j} \\ &= \lim_{j \rightarrow 0} \left[ \frac{a+b}{a} \cdot \frac{\sin(a+b)j\pi}{(a+b)j\pi} - \frac{b}{a} \cdot \frac{\sin bj\pi}{jb\pi} \right] \\ &= \frac{a+b}{a} - \frac{b}{a} \\ &= 1 \end{aligned} \tag{A1.7}$$

(4)  $b = 0$

$$e_{ij}(a, 0) = \frac{(-1)^i (ja)^2 \sin ja\pi}{(ja)^2 - 1^2} \cdot \frac{1}{ja\pi} \tag{A1.8}$$

$$e_{ij}(1, 0) = \delta_{ij} / \alpha_i \tag{A1.9}$$

(5)  $ja = i$  but  $i \neq 0$

$$\begin{aligned} e_{ij} &= \lim_{ja \rightarrow i} \frac{1}{\pi} \cdot \frac{ja}{(ja)^2 - 1^2} \cdot [(-1)^i \sin(a+b)j\pi - \sin bj\pi] \\ &= \lim_{ja \rightarrow i} \frac{1}{\pi} \cdot \frac{1}{2(ja-1)} \cdot [(-1)^i \sin[(ja-i)\pi + i\pi + b]j\pi - \sin bj\pi] \\ &= \lim_{x \rightarrow 0} \frac{1}{2\pi x} \cdot [\sin(x+bj)\pi - \sin bj\pi] \\ &= \lim_{x \rightarrow 0} \frac{1}{2\pi x} \cdot 2\cos(x+2bj)\frac{\pi}{2} \cdot \sin x \frac{\pi}{2} \end{aligned}$$

$$\begin{aligned}
&= \lim_{x \rightarrow 0} \frac{1}{2} \cdot \cos bj\pi \cdot \frac{\sin(\pi x/2)}{\pi x/2} \\
&= \frac{1}{2} \cdot \cos bj\pi
\end{aligned} \tag{A1.10}$$

(6)  $a=1-2b$  or  $z_0=(b-a)/2$

Since  $(-1)^i \sin(a+b)j\pi - \sin bj\pi = (-1)^i \sin(1-b)j\pi - \sin bj\pi$

$$\begin{aligned}
&= -\sin bj\pi [(-1)^{i+j} + 1] \\
&= \begin{cases} -2\sin bj\pi & (i+j) \text{ is an even number} \\ 0 & (i+j) \text{ is an odd number} \end{cases}
\end{aligned} \tag{A1.11}$$

then  $e_{ij}(a, b) = \begin{cases} \frac{-2j a \sin bj\pi}{(ja)^2 - i^2} & (i+j) \text{ is an even number} \\ 0 & (i+j) \text{ is an odd number} \end{cases}$  (A1.12)

This means that  $e_{ij}$  will vanish if  $i$  and  $j$  do not have the same parity.

## APPENDIX 2 APPROXIMATED CALCULATION OF CAVITY Q-FACTOR

In this appendix, the Q-factor of a dielectric loaded re-entrant coaxial cavity is evaluated. The main approximation made in this evaluation is that the gap width is very narrow compared with the cavity length and the wavelength. The cavity structure considered is case 2 as shown in Figure A2.1.

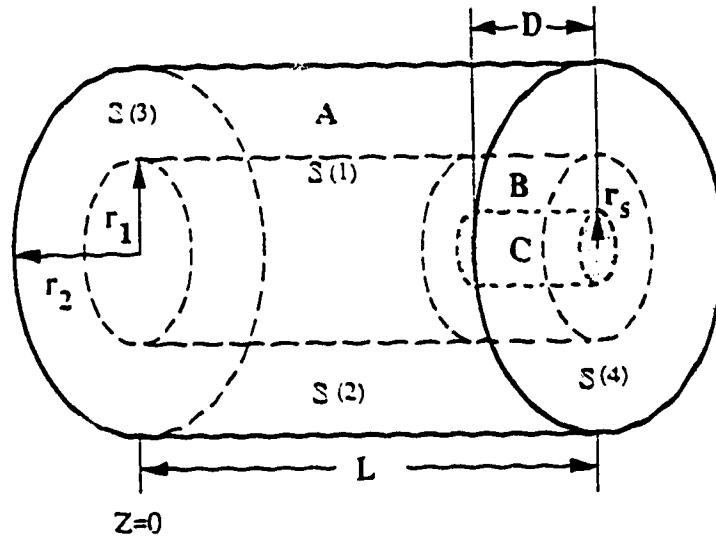


Figure A2.1 Schematic diagram of a coaxial re-entrant cavity with a partially dielectric loaded gap.

Cavity Q-factor is defined as angular frequency times the ratio of the stored energy to the dissipated power in the cavity, that is,

$$Q = \omega W_E / P = \omega W_E / (P_W + P_D) \quad (A2-1)$$

The stored electric energy is given by

$$W_E = \frac{1}{2} \epsilon_0 \iiint_V \epsilon_r (E_z^2 + E_r^2) dv \quad (A2-2)$$

The dissipated power consists of the metal surface loss

$$P_W = \frac{R_s}{2} \iint_S H_\phi^2 ds \quad (A2-3)$$

$$R_s = \sqrt{\omega \mu_0 / (2\sigma)} \quad (A2-4)$$

and the dielectric loss

$$P_D = \omega \tan \delta W_E^C \quad (A2-5)$$

$$W_E^C = \frac{1}{2} \epsilon_0 \iiint_V \epsilon_r (E_z^2 + E_r^2) dv \quad (A2-6)$$

First, let's consider subarea A. For a narrow gap, we need only consider the TEM fields which are expressed by

$$E_r = \frac{60I_0}{r} \sin \frac{2\pi z}{\lambda_0} \quad (A2-7)$$

$$E_z = 0 \quad (A2-8)$$

$$H_\phi = \frac{I_0}{2\pi r} \cos \frac{2\pi z}{\lambda_0} \quad (A2-9)$$

Therefore, the stored energy and the dissipated power on surfaces (1)-(4) can be evaluated as the follows

$$W_E^A = \frac{\epsilon_0}{2} \int_{r_1}^{r_2} \int_0^L E_r^2 \cdot 2\pi r dr dz = \frac{\epsilon_0}{4} (60I_0)^2 \pi L \left( \ln \frac{r_2}{r_1} \right) \left( 1 - \frac{\lambda_0}{4\pi L} \sin \frac{4\pi L}{\lambda_0} \right) \quad (A2-10)$$

$$P_W^{(1)} = \frac{R}{2} \int_{r_1}^{r_2} \int_0^{L-D} H_\phi^2 (r=r_1) dz = \frac{I_0^2 R}{8\pi r_1} \cdot (L-D) \cdot \left[ 1 + \frac{\lambda_0}{4\pi(L-D)} \sin \frac{4\pi(L-D)}{\lambda_0} \right] \quad (A2-11)$$

$$P_W^{(2)} = \frac{R}{2} \int_{r_2}^{r_1} \int_0^L H_\phi^2 (r=r_2) dz = \frac{I_0^2 R}{8\pi r_2} L \left( 1 + \frac{\lambda_0}{4\pi L} \sin \frac{4\pi L}{\lambda_0} \right) \quad (A2-12)$$

$$P_W^{(3)} = \frac{R}{2} \int_{r_1}^{r_2} H_\phi^2 (z=0) 2\pi r dr = \frac{I_0^2 R}{4\pi} \ln \frac{r_2}{r_1} \quad (A2-13)$$

$$P_W^{(4)} = \frac{R}{2} \int_{r_1}^{r_2} H_\phi^2 (z=L) 2\pi r dr = \frac{I_0^2 R}{4\pi} \ln \frac{r_2}{r_1} \cos^2 \left( \frac{2\pi L}{\lambda_0} \right) \quad (A2-14)$$

Since  $L \gg D$  and  $4\pi L \gg \lambda_0$ , the above results can be simplified as

$$W_E^A = \frac{\epsilon_0}{4} (60I_0)^2 \pi L \ln \frac{r_2}{r_1} \quad (A2-15)$$

$$P_W^{(1)} = \frac{I_0^2 R_s L}{8\pi r_1} \quad (A2-16)$$

$$P_W^{(2)} = \frac{I_0^2 R_s L}{8\pi r_2} \quad (A2-17)$$

$$P_W^{(3)} = \frac{I_0^2 R_s}{4\pi} \ln \frac{r_2}{r_1} \quad (A2-18)$$

For the same reason, the contribution of subarea B and C to  $W_E$  and  $P_W$  can be negligible. However, the dielectric loss cannot be ignored. To estimate  $P_D$ , we first need to evaluate the electric energy stored in the sample, i.e.,  $W_E^C$ . For a narrow gap and a small sample radius, we can assume the E-field in the sample to be uniform and in axial direction only. Thus

$$W_E^C = \frac{1}{2} \epsilon_0 \epsilon_r V_D E_0^2 \quad (A2-19)$$

$$\text{and } P_D = \frac{1}{2} \omega \tan \delta \epsilon_0 \epsilon_r V_D E_0^2 \quad (A2-20)$$

where,  $V_D$  is the sample volume

$$V_D = \pi r_0^2 D \quad (A2-21)$$

Substituting  $W_E^A$ ,  $P_W^{(1)} - P_W^{(4)}$  and  $P_D$  into Eq. (A2-1), we finally have

$$Q = 0.003974 \sqrt{\sigma f_0} \cdot \ln(r_2/r_1) / \{1/r_1 + 1/r_2 + (2/L) \cdot [1 + \cos^2(2\pi L/\lambda_0)] \cdot \ln(r_2/r_1) + 0.003974 \sqrt{\sigma f_0} \cdot \left(\frac{r_0^2 D}{L}\right) \cdot \left(\frac{E_0}{60 I_0}\right)^2 \epsilon_r''\} \quad (A2-22)$$

The last term in the denominator relates to the dielectric loss. Take a typical numerical example:

$$\sigma = 10^7 / (\Omega m), f_0 = 3 \text{GHz}, \lambda_0 = 10 \text{cm}, 0.003974 \sqrt{\sigma f_0} = 6882 / \text{cm}$$

$$r_1 = 1.25, r_2 = 5.0, L = 20.0, D = 0.3, r_0 = 0.25 \text{cm}$$

$$E_0 / (60 I_0 / r_2) = 2.5, E_0 / (60 I_0) = 2 / r_2 = 0.5 / \text{cm}, (E_0 / (60 I_0))^2 = 0.25 \text{cm}^{-2}$$

$$r_0^2 D/L = 0.938 \times 10^{-3} \text{ cm}^2$$

The wall loss term = 2.04/cm

The dielectric loss term =  $1.614 \epsilon_r''/\text{cm}$

We see that the dielectric loss is comparable to the wall loss in this example.

If the resonant wavelength is close to that of TEM modes in a closed coaxial cavity,  $\cos(2\pi L/\lambda_0) \approx 1$  and the empty cavity  $Q$  becomes

$$Q_0 = 0.003974 \sqrt{\epsilon_r} \cdot \frac{\ln(r_2/r_1)}{1/r_1 + 1/r_2 + (4/L) \ln(r_2/r_1)} \quad (\text{A2-23})$$

This is identical to the formula for the  $Q$ -factor of a coaxial cavity given in [56]. This equation can be rewritten as

$$Q_0 = 0.003974 \sqrt{\epsilon_r} r_2 \cdot H \quad (\text{A2-24})$$

$$H = \frac{\ln(r_2/r_1)}{1 + r_2/r_1 + (4r_2/L) \ln(r_2/r_1)} \quad (\text{A2-25})$$

If take a derivative of  $H$  against  $r_2/r_1$ ,

$$\frac{dH}{d(r_2/r_1)} = \frac{r_1/r_2 + 1 - \ln(r_2/r_1)}{[1 + r_2/r_1 + (4r_2/L) \ln(r_2/r_1)]^2} \quad (\text{A2-26})$$

and let it equal to zero, we find that  $H$  therefore  $Q_0$  reaches maximum when  $r_2/r_1 = 3.58$ .

## APPENDIX 3

### EVALUATION OF RETURN LOSS AND Q-MEASUREMENT UNCERTAINTY

This appendix covers the error analysis of the cavity Q-factor determined from a reflectometer. This error mainly originates from uncertainties in the measured return loss. In this appendix, the return loss uncertainty is analyzed first. The Q-factor error limit is then evaluated.

#### A3.1 Return Loss Uncertainty

Using a reflectometer configuration, the uncertainty of measured return loss of a device under test (DUT) has two primary sources, namely the finite directivity of the directional coupler and the mismatch of the signal source. Due to the phase ambiguity of a reflectometer, we are only able to estimate these errors limits, i.e., the errors in the worst case. Moreover, it should be noted that in this appendix, RL denotes the positive value of return loss and  $\Gamma$  is only the amplitude of the reflection coefficient.

##### A3.1.1 Directivity uncertainty

With a finite directivity,  $D$ , the measured return loss,  $RL_m$ , will be [81]

$$-20\log(\Gamma + \Gamma_D) \leq RL_m \leq -20\log(\Gamma - \Gamma_D) \quad (A3.1)$$

where

$$\Gamma_D = 10^{-D/20} \quad (A3.2)$$

$$\Gamma = 10^{-RL/20} \quad (A3.3)$$

and  $RL$  is the true return loss of DUT. Thus, the error

$$\delta RL = RL_m - RL \quad (A3.4)$$

can be expressed by

$$-20\log(\Gamma + \Gamma_D) - RL \leq \delta RL \leq -20\log(\Gamma - \Gamma_D) - RL \quad (A3.5)$$

Using Eqs. (A3.2) and (A3.3) in Eq. (A3.5), we obtain the error range

$$-20\log(1+10^{-(D-RL)/20}) \leq \delta RL \leq -20\log(1-10^{-(D-RL)/20}) \quad (A3.6)$$

Hence, the upper error limit is given by

$$\delta RL^+ = -20\log(1-10^{-(D-RL)/20}) \quad (A3.7)$$

and the lower error limit is

$$\delta RL^- = -20\log(1+10^{-(D-RL)/20}) \quad (A3.8)$$

$$\text{or } (\delta RL^\pm)_D = -20\log(1 \mp 10^{-(D-RL)/20}) \quad (A3.9)$$

where subscript D denotes the directivity uncertainty. Expressing this in terms of  $\Gamma_D$  and  $\Gamma$ , we have

$$\delta RL^\pm = -20\log(1 \mp \Gamma_D/\Gamma) \quad (A3.10)$$

It is shown that the return loss error is significant when the return loss (or  $\Gamma$ ) is close to the directivity value (or  $\Gamma_D$ ) and its upper limit will be infinite if the return loss equals the directivity. If  $D-RL > 20$ , that is, the return loss is 20dB lower than the directivity, the error will not exceed  $\pm 1$ dB.

### A3.1.2 Source mismatch uncertainty

If there is a source mismatch, i.e., a mismatch looking back to the source, the reflected power from the DUT will be re-directed to the DUT. This amount of power is added to the incident power, resulting in a measured return loss error which is given by [82]

$$20\log(1-\Gamma_S) \leq \delta RL \leq 20\log(1+\Gamma_S) \quad (A3.11)$$

$$\text{or } (\delta RL^\pm)_S = 20\log(1 \pm \Gamma_S) \quad (A3.12)$$

$$\text{where } \Gamma_S = (SWR_S - 1)/(SWR_S + 1) \quad (A3.13)$$

and  $SWR_S$  is the effective source mismatch. Define  $RL_S$  as

$$RL_S = -20\log\Gamma_S \quad (A3.14)$$

we can rewrite Eq.(A3.12) as



$$(\delta RL^{\pm})_S = 20 \log_{10} (1 \pm 10^{-(RL+RL_S)/20}) \quad (A3.15)$$

It can also be shown that the RL error due to a source mismatch is smaller than  $\pm 1$ dB when  $RL+RL_S > 20$ dB. Therefore,  $(\delta RL^{\pm})_S$  will never exceed  $\pm 1$ dB if  $RL_S > 20$ dB which corresponds to  $SWR_S < 1.22$ . In practice, the source mismatch can be reduced by connecting a matched attenuator (6-10dB) at the source output.

### A3.1.3 Graphical presentation of return loss uncertainty

By comparing Eq. (A3.9) and Eq. (A3.15), we see that  $(\delta RL^{\pm})_S = -(\delta RL^{\mp})_D$  if  $RL+RL_S = D-RL$ . This fact suggests us to use a single graph to present both the directivity and source mismatch uncertainty as shown in Figure A3.1.

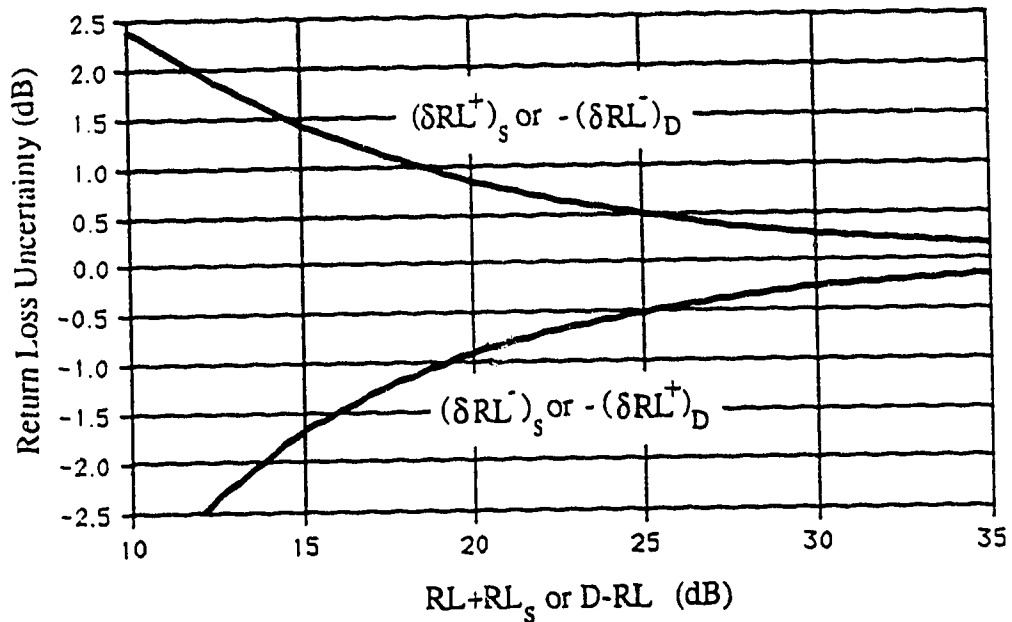


Figure A3.1 Return loss uncertainty in a reflectometer;  $(\delta RL^{\pm})_S$  and  $(\delta RL^{\pm})_D$  are the upper and lower limit of source mismatch and directivity uncertainty.

#### A3.1.4 Total return loss uncertainty

The total RL uncertainty is the superposition of the directivity and the source mismatch uncertainty. Adding Eq.(A3.10) to Eq.(A3.12) gives

$$\delta RL^{\pm} = (\delta RL^{\pm})_S + (\delta RL^{\pm})_D = 20 \log \frac{1 \pm \Gamma \cdot \Gamma_S}{1 \mp \Gamma_D / \Gamma} \quad (A3.16)$$

Since the directivity error is the dominant error term for a high RL (small reflection) and the source mismatch is the main error term for a low RL (large reflection), we expect that the total RL uncertainty will arrive at a minimum at a medium RL. It can be found that when

$$\Gamma = \Gamma_D [\sqrt{1+1/(\Gamma_D \Gamma_S)} + 1] \approx \sqrt{\Gamma_D / \Gamma_S} \quad (A3.17)$$

the upper limit,  $\delta RL^+$ , is minimized and when

$$\Gamma = \Gamma_D [\sqrt{1+1/(\Gamma_D \Gamma_S)} - 1] \approx \sqrt{\Gamma_D / \Gamma_S} \quad (A3.18)$$

the lower limit,  $\delta RL^-$ , is maximized. In other words, the return loss around  $\sqrt{\Gamma_D / \Gamma_S}$  can be measured most accurately.

#### A3.2 Uncertainty of Measured Cavity Q-factor

A measured Q-factor includes the loss of both the cavity under test and the measurement system used. This Q-factor can be determined from a measured reflection spectrum (see Figure 5.6) which can be expressed by

$$\Gamma^2(x) = \frac{\Gamma_0^2 + x^2}{1 + x^2} \quad (A3.19)$$

where  $x$  is the normalized frequency increment defined as

$$x = 2Q_m \cdot (f - f_0) / f_0 \quad (A3.20)$$

and  $\Gamma_0$  is the reflection coefficient at the resonant point,  $f=f_0$  or  $x=0$ . Therefore,

$$Q_m = \frac{f_0}{2(f-f_0)} \cdot x \quad (A3.21)$$

$$\text{and } x^2 = (\Gamma^2 - \Gamma_0^2) / (1 - \Gamma^2) \quad (\text{A3.22})$$

At the half power point,

$$\Gamma^2 = (1 + \Gamma_0^2) / 2 \quad (\text{A3.23})$$

$$x=1 \quad (\text{A3.24})$$

$$\text{and } Q_m = \frac{f_0}{2(f_{1/2} - f_0)} \quad (\text{A3.25})$$

This is the commonly used method for Q-determination.

In order to find the variation of  $Q_m$  caused by an error in the return loss

$$\text{RL} = -20 \log \Gamma \quad (\text{A3.26})$$

we take the differential of Eqs. (A3.21), (A3.22) and (A3.26) as follows

$$dQ_m / Q_m = dx / x \quad (\text{A3.27})$$

$$dx / x = \frac{(1+x^2)^2}{(1-\Gamma_0^2)x^2} \cdot \Gamma d\Gamma \quad (\text{A3.28})$$

$$\Gamma d\Gamma = -(20 / \ln 10) \cdot \Gamma^2 d\text{RL} = -(20 / \ln 10) \cdot \frac{\Gamma_0^2 + x^2}{1+x^2} \cdot d\text{RL} \quad (\text{A3.29})$$

Substituting Eq. (A3.29) into Eq. (A3.28) and then into Eq. (A3.27) results in

$$\frac{dQ_m / Q_m}{d\text{RL}} = -\frac{\ln 10}{20} \cdot \frac{(\Gamma_0^2 + x^2)(1+x^2)}{(1-\Gamma_0^2)x^2} \quad (\text{A3.30})$$

$$\text{or } \frac{dQ_m / Q_m}{d\text{RL}} = -\frac{\ln 10}{20} \cdot \frac{\Gamma^2(1-\Gamma_0^2)}{(1-\Gamma^2)(\Gamma^2-\Gamma_0^2)} \quad (\text{A3.31})$$

This equation gives the relative error of measured Q-factor due to a 1dB RL uncertainty for different increments,  $x$ , at which the  $Q_m$  is calculated. This relative error is plotted in Figure A3.2 as a function of  $x$  for  $\Gamma_0 = 0.1, 0.3$  and  $0.5$  which shows that there is an  $x$  at which, for the same amount of RL uncertainty,  $Q$  can be determined with a

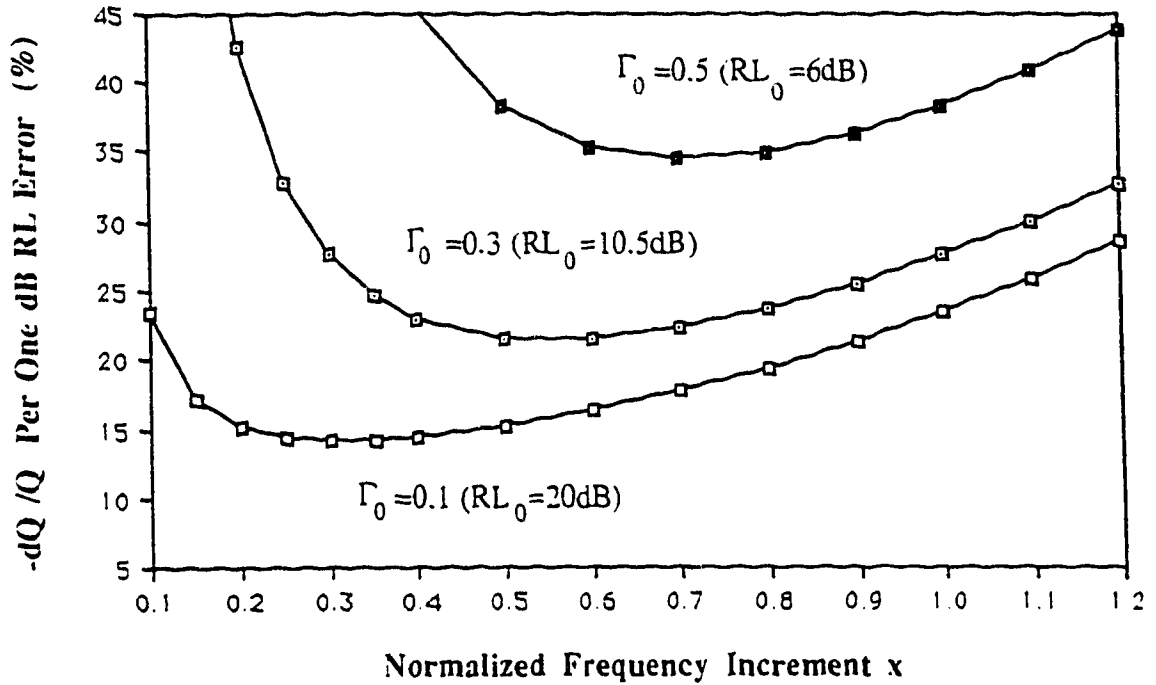


Figure A3.2 Relative error in measured Q-factor caused by a one dB return loss uncertainty as a function of the normalized frequency increment,  $x$ , at which  $Q_m$  is determined.

minimum error. This point is found to be

$$x^* = \sqrt{\Gamma_0} \quad (\text{A3.32})$$

which corresponds to the steepest point of a reflection resonant curve.

At  $x=x^*$ , we get

$$\Gamma = \Gamma^* = \sqrt{\Gamma_0} \quad (\text{A3.33})$$

and 
$$\frac{dQ_m/Q_m}{dRL} = \left(\frac{dQ_m/Q_m}{dRL}\right)_{\min} = -\frac{\ln 10}{20} \cdot \frac{1+\Gamma_0}{1-\Gamma_0} = -0.1155\text{SWR}_0 \quad (\text{A3.34})$$

It should be emphasized that Eq. (A3.34) gives only the minimum of  $dQ_m/Q_m$  per one dB RL uncertainty not the minimum of  $dQ_m/Q_m$  itself. In fact,  $dQ_m/Q_m$  may be rather large at  $x^*$  as a significant error occurs in RL for a large RL if the directivity uncertainty is considered. Substituting Eq. (A3.10) into Eq. (A3.31), we have

$$(dQ_m/Q_m)^{\pm} = \frac{\Gamma^2(1-\Gamma_0^2)}{(1-\Gamma^2)(\Gamma^2-\Gamma_0^2)} \cdot \ln(1 \pm \Gamma_D/\Gamma) \quad (\text{A3.35})$$

This equation gives the limits of relative error in the  $Q_m$  which is determined at an arbitrary point on a reflection resonant curve. There should also be a point at which  $Q_m$  can be determined most accurately. Detailed calculations show that the half-power point is a fairly good approximation of such a point. Substituting  $\Gamma$  at the half-power point given in Eq. (A3.23) into Eq. (A3.35) gives

$$(dQ_m/Q_m)_{\min}^{\pm} \approx \frac{(1+\Gamma_0^2)}{(1-\Gamma_0^2)} \cdot \ln(1 \pm \Gamma_D / (\frac{1+\Gamma_0^2}{2})^{1/2}) \quad (\text{A3.36})$$

$$\approx \pm \frac{(1+\Gamma_0^2)^{1/2}}{(1-\Gamma_0^2)} \cdot \sqrt{2}\Gamma_D \quad (\text{A3.37})$$

In Figure A3.3, these  $Q_m$  limits are plotted against  $\Gamma_0$  for  $D=30$  and  $40$  dB.

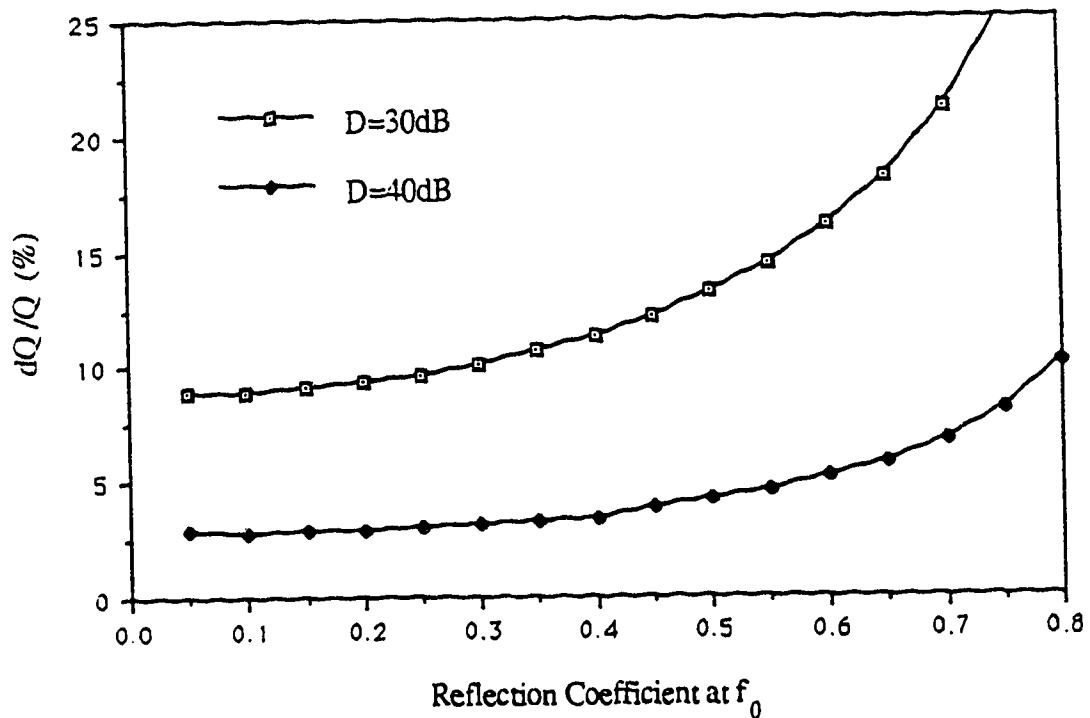


Figure A3.3 Relative error in measured  $Q$ -factor versus the reflection coefficient,  $\Gamma_0$ , at the resonant frequency for a reflectometer directivity of  $D=30$  and  $40$  dB.

We see that  $dQ_m/Q_m$  is within  $\pm 12.5\%$  and  $3.5\%$  for  $D=30$  and  $40\text{dB}$  respectively, if  $\Gamma_0 < 0.47$  or  $RL > 6.5\text{dB}$ .

### A3.3 Uncertainty of Intrinsic Cavity Q-factor

The Q-factor of a cavity which may include a sample is derived from the measured Q-factor,  $Q_m$ , and the coupling factor,  $\beta$ , as

$$Q = (1+\beta)Q_m \quad (\text{A3.38})$$

where

$$\beta = \begin{cases} \text{SWR}_0 & \text{if over-coupled} \\ 1/\text{SWR}_0 & \text{if under-coupled} \end{cases} \quad (\text{A3.39})$$

We can write the relative error of Q as

$$dQ/Q = d\beta/(1+\beta) + dQ_m/Q_m \quad (\text{A3.40})$$

The term of  $dQ_m/Q_m$  has been evaluated above and  $d\beta/(1+\beta)$  can be found to be

$$|d\beta/(1+\beta)| = \frac{d\Gamma_0}{1 \mp \Gamma_0} = \frac{\ln 10}{20} \cdot \frac{\Gamma_0}{1 \mp \Gamma_0} \cdot |dRL_0| \quad (\text{A3.41})$$

for over- and under-coupling respectively. It shows that the error in coupling factor due to return loss uncertainty is larger in the over coupling case. If only under coupling is assumed and the directivity uncertainty of Eq. (A3.10) at  $f_0$  is used, Eq. (A3.41) becomes

$$\left(\frac{d\beta}{1+\beta}\right)^\pm = \frac{\Gamma_0}{1 \mp \Gamma_0} \ln(1 \pm \Gamma_D/\Gamma_0) \quad (\text{A3.42})$$

The calculation can show that this  $\beta$  term contributes to cavity Q-factor error less than  $3.5\%$  or  $0.9\%$  for  $D=30$  or  $40\text{dB}$  if  $\Gamma_0 > 0.1$  ( $RL_0 < 20\text{dB}$ ).

#### APPENDIX 4 AUTOMATIC TUNING CIRCUIT

Designed for automatically tuning the frequency of the microwave heating source, the control circuit is illustrated by the block diagram of Figure A4.1. The idea is to operate a sample loaded cavity at resonance to maximize the heating power delivered to the load. The actual circuit is given in Figure A4.2. Since each function block in this circuit is a common type which is well explained in most text books [67-69], this appendix will only cover the operation principle of the circuit.

The inputs of the circuit are analog voltages,  $V_i$  and  $V_r$ , which are proportional to the incident and reflected power, while the output is the frequency tuning voltage,  $V_f$ , for the voltage controlled oscillator (VCO) which drives the heating source. The circuit structure mainly consists of a sweeping circuit and a searching circuit. The operation sequence of the entire circuit can be divided into the searching period and the holding period as shown in Figure A4.1. During the searching period which includes two consecutive sweeps, the input resonant curve is searched for the resonant frequency. The first sweep is used to determine the resonant curve magnitude at the resonant point, whereas the second sweep is used to determine the tuning voltage at the resonant point. During the holding period, this voltage, and therefore the heating source frequency, is kept unchanged, resulting in a minimized power reflection. The length of the holding period is about 0.5-2 seconds. This can be set low or high depending on the rate of change in the sample's dielectric constant with heating time. The searching period should be as short as possible since there is virtually no power coupling to the cavity within this period. However, it can be no less than about one tenth of the holding period primarily due to the limited tuning rate of our power source.

Referring to the sweeping circuit in Figure A4.1, an astable multivibrator (AMV) generates a train of negative-going pulses,  $V_1$ , which serve as a clock signal for the entire circuit. The rising edge of the pulse is used to trigger a monostable multivibrator (MMV) to produce a single negative-going pulse,  $V_2$ , with about the same width. Therefore, the AMV acts as a master, while the MMV works as a slave. The pulses  $V_1$  and  $V_2$  are then used to trigger two separate bootstrap ramp generators (BRG). Adding the two ramps together, we obtain two consecutive sweep

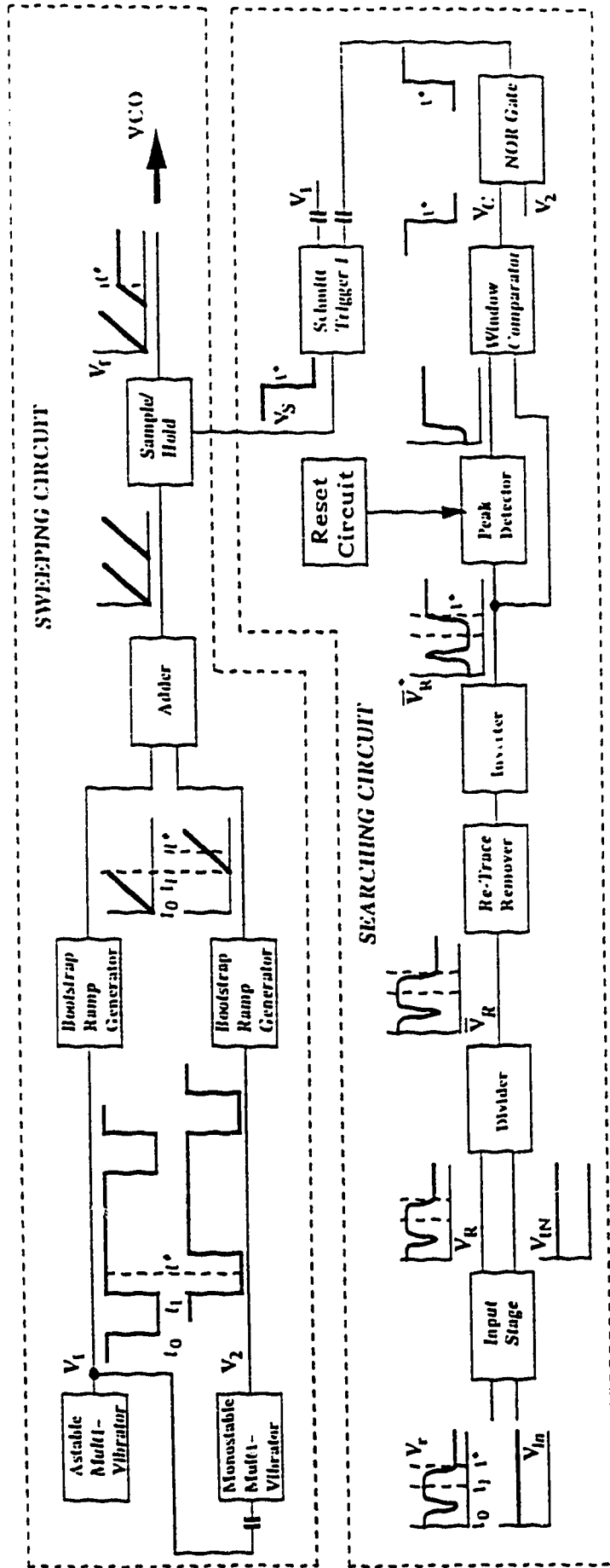
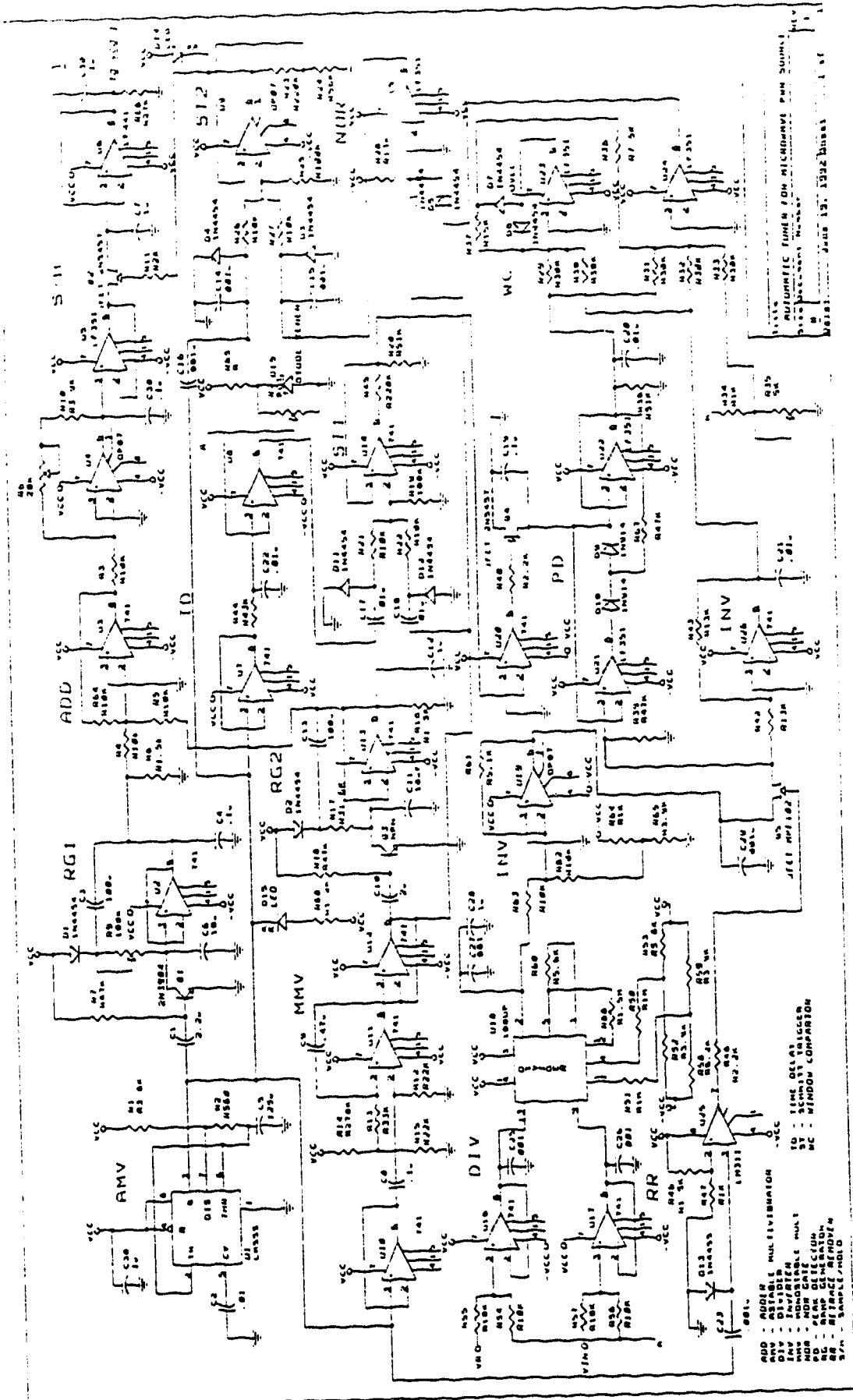


FIGURE A4.1 Block diagram of the automatic tuning circuit.



FIGURE A4.2 Automatic tuning circuit



voltages which drive the VCO via a sample-hold (S/H). When the S/H's control signal,  $V_S$ , is high, the S/H is simply a voltage follower which replicates the sweeping voltage. During this state, the power source is operating in a sweep mode. Conversely, at the instant  $V_S$  switches from high to low, the S/H holds the oscillator control voltage at a fixed value. Thereafter, the power source operates in the CW mode at the last found resonant frequency.

In the searching circuit, the input signals  $V_r$  and  $V_i$  are first conditioned to produce  $V_R$  and  $V_I$  in the range of 0.5 to 5V.  $V_R$  is then divided by  $V_I$  by an analog divider (DIV100) [83], resulting in a normalized reflection voltage,  $\bar{V}_R$ , which is proportional to the reflection coefficient. Using this normalization procedure, the circuit still functions correctly when the incident power or  $V_i$  changes. After being inverted,  $\bar{V}_R$  becomes  $\bar{V}_R^*$  which has a maximum instead of a minimum at the resonant point. This maximum is found and held by a peak detector (PD) and is compared with  $\bar{V}_R^*$  by a window comparator (WC). When  $\bar{V}_R^*$  is within a given  $\Delta V$  of the PD's output, the WC switches to low. This low output is used to trigger the S/H into the hold state through a NOR gate and a Schmitt trigger. Note that the WC goes into the low state not only at the resonant point during the second sweep but also on the rising portion of  $\bar{V}_R^*$  during the first sweep. This ambiguity is removed by using a NOR gate which disables the WC's output ( $V_C$ ) during the first sweep because the NOR gate has a high output only if both  $V_C$  and  $V_2$  are low. Therefore, at the instant the NOR gate goes high, the tuning voltage corresponding to the resonant point, i.e.,  $V_r(t^*)$ , has been determined. The NOR gate output then drives the Schmitt trigger (ST1) into the low state which causes the S/H to shift to the hold state. As shown the ST1 has two derivative inputs, one from the NOR gate and the other from the AMV, connected to the ST1 through a summing network. In this way, the ST1 is triggered to its low output state as the NOR gate goes high, and to its high output state as  $V_i$  goes negative.

The function blocks yet to be explained are the retrace remover and the reset circuit. It should be noted that at the beginning of the first and second sweep, or  $t=t_0$  and  $t_1$ , the VCO may also respond to the switching transients in the sweep voltage. As a result, two spikes may appear in the input signal  $V_r$  and confuse the searching operation. The second spike is blocked from the PD's input by a circuit called retrace

remover (RR). This circuit is basically a JFET switch which is turned off for a short period (less than half a percent of the sweep period) centered at  $t_1$ , i.e., the transition point from the first sweep to the second. The first spike is not removed; instead, its effect is avoided by the design of the reset circuit. It is necessary to reset the PD so that it holds only the most recent peak value. With this circuit, the PD is virtually disabled by shorting the capacitor ( $C_{19}$  in Figure A4.2). The interval in which the PD is enabled almost coincides with the length of the entire searching period, i.e., the first plus the second sweep time, except that it starts slightly later than  $t_0$ . In this manner, the first spike which occurs at  $t_0$  does not affect the searching operation because the PD has not been enabled yet.

The experiment shows that this automatic tuning circuit works satisfactorily though its design is by no means optimized.

APPENDIX 5  
ANALYSIS OF SAMPLE TEMPERATURE NON-UNIFORMITY

In this appendix, we will analyze the problem illustrated in Figure A5.1, in which, (a) is a schematic diagram of a sample positioned in the cavity re-entrant gap and extending into both the holes in the center conductor and the endplate; (b) and (c) are the distributions of  $E_z^T$  and  $E_z^H$ , the E-fields inside the sample in the testing and heating band, with  $E_z^H$  exhibiting a sharper profile due to its longer wavelength; (d) and (e) are the sample's temperature and permittivity profiles associated with the  $E_z^H$  distribution. The field  $E_z^T$  determines the amount of the cavity's resonant frequency shift and Q-factor change produced by the sample. These disturbances to the cavity are measured and used to determine the sample's dielectric properties which are assumed to be uniform within the effective sample volume. However, the dielectric properties throughout the volume are not uniform at elevated temperatures due to the heating field and temperature distributions. Hence, an error in the determined permittivity will result.

To analyze the error in the determined dielectric data due to the temperature non-uniformity, one can use the perturbation equation of Eq. (2.6) which is rewritten below

$$\frac{\Delta f_0}{f_0} = - \frac{\epsilon_0 \int_V \epsilon_r' (\epsilon_r' - 1) E_0^T E_1^T dv}{4W_E} \quad (A5.1)$$

$$\Delta\left(\frac{1}{Q_0}\right) = - \frac{\epsilon_0 \int_V \epsilon_r'' E_0^T E_1^T dv}{2W_E} \quad (A5.2)$$

where  $E_0^T$  and  $E_1^T$  are the testing field before and after the sample is inserted. First, we examine Eq. (A5.1). Let

$$f_0 \epsilon_0 / (4W_E) = c \quad (A5.3)$$

and  $\chi = \epsilon_r' - 1$  (A5.4)

then  $\Delta f_0 = c \int_V \chi E_0^T E_1^T dv$  (A5.5)

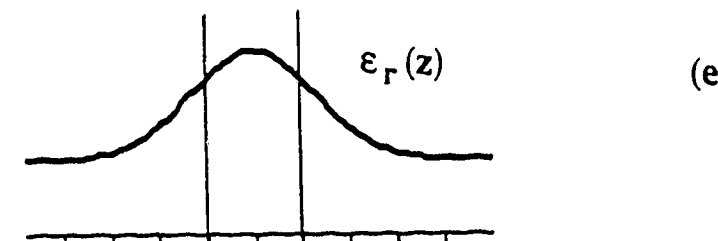
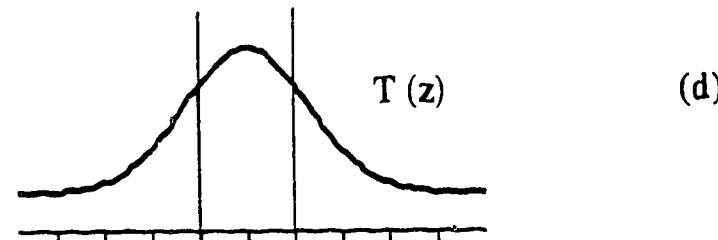
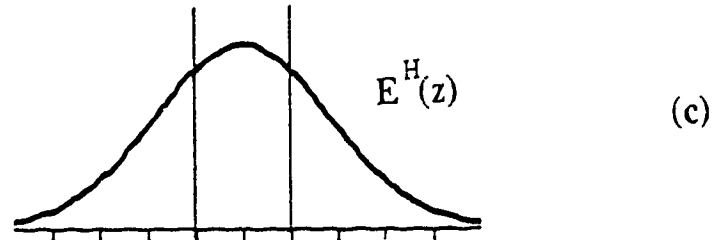
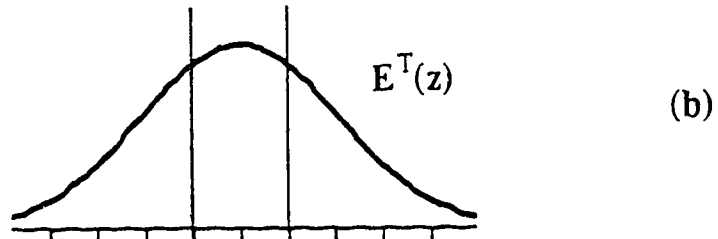
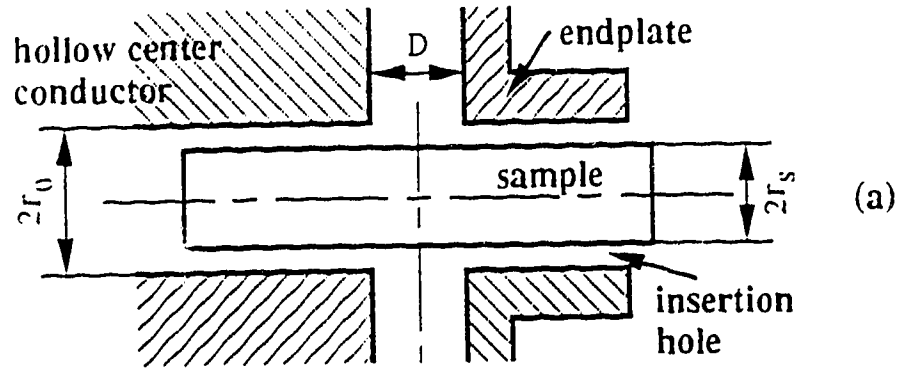


Figure A5.1 Dielectric non-uniformity due to the E-fields and the sample temperature distribution.

where  $c$  is a constant and  $\chi$  is the sample's dielectric susceptibility. Assuming that the E-field inside the sample is uniform in the  $r$ -direction, symmetrical about the gap midplane and oriented only in the  $z$ -direction, i.e.,  $E^T = E_z^T$  and  $E_r^T = 0$ , we can write Eq. (A5.5) as

$$\Delta f_0 = 2\pi r_s^2 c \int_0^\infty \chi E_{z0}^T E_{z1}^T dz \quad (\text{A5.6})$$

which is also valid for an inhomogeneous sample. Since we have assumed in our method that,

$$\chi = \chi_0$$

then 
$$\Delta f_0 = 2\pi r_s^2 c \chi_0 \int_0^\infty E_{z0}^T E_{z1}^T dz \quad (\text{A5.7})$$

Dividing Eq. (A5.7) by Eq. (A5.6), we have

$$\chi_0 = \frac{\int_0^\infty \chi E_{z0}^T E_{z1}^T dz}{\int_0^\infty E_{z0}^T E_{z1}^T dz} \quad (\text{A5.8})$$

This equation shows that the determined  $\chi_0$  is really a weighted average value of distributed  $\chi$  over the entire sample volume with  $E_{z0}^T E_{z1}^T$  as the weighting factor. The temperature dependence of  $\chi$ , as a first order approximation, can be considered to be a linear function, i.e.,

$$\chi = \chi_H + (\chi_G - \chi_H) \cdot \frac{T - T_H}{T_G - T_H} \quad (\text{A5.9})$$

where subscripts G and H denote the values at  $z=0$  (gap midplane) and  $z=z_h$  (inside the hole). If we further assume that only the heating field distribution is responsible for the temperature gradient, we can write Eq. (A5.9) as

$$\chi = \chi_H + (\chi_G - \chi_H) \cdot (E_z^H)^2 \quad (\text{A5.10})$$

Note here that the effect of thermal diffusion is neglected and  $E_z^H$  is the normalized value. Substituting this expression into Eq. (A5.8) produces

$$\chi_0 = \frac{\int_0^\infty [\chi_H + (\chi_G - \chi_H) \cdot (E_Z^H)^2] \cdot E_{z0}^T E_{z1}^T dz}{\int_0^\infty E_{z0}^T E_{z1}^T dz}$$

$$= \chi_H + p \cdot (\chi_G - \chi_H) \quad (\text{A5.11})$$

$$p = \frac{\int_0^\infty (E_Z^H)^2 \cdot E_{z0}^T E_{z1}^T dz}{\int_0^\infty E_{z0}^T E_{z1}^T dz} \quad (\text{A5.12})$$

Therefore, when the sample's temperature in the gap midplane is measured, as in our method, the error in the determined dielectric constant is found to be

$$\Delta \epsilon'_r = \epsilon'_{r0} - \epsilon'_{rG} = \chi_0 - \chi_G$$

$$= -(\chi_G - \chi_H) \cdot (1-p) = -(\epsilon'_{rG} - \epsilon'_{rH}) \cdot (1-p) \quad (\text{A5.13})$$

Obviously,  $p=1$  and  $\Delta \epsilon'_r=0$  if  $E_Z^H$  is a constant. To evaluate the E-field integral in  $p$ , we approximate the axial distribution of  $E_Z$  by a normal function

$$y(z) = e^{-(z/\alpha)^2} \quad (\text{A5.14})$$

where,  $\alpha$  is a parameter signifying the flatness of the distribution, or the degree of the hole effect in this case. Actual calculations show that this function is a valid approximation for  $E_Z$  if  $\epsilon'_r \leq 20$ . Recalling that the effective hole depth,  $z_h$ , is defined as the distance into the hole where the gap E-field is attenuated to 5% in section 4.6.1, we can find that  $\alpha = z_h / 3$  since  $y(3\alpha) = e^{-9} \approx 0.05 = y(z_h)$ . Making use of the result

$$\int_0^\infty e^{-(x/\alpha)^2} dx = \sqrt{\pi} \alpha / 2 \quad (\text{A5.15})$$

we can calculate  $p$  of Eq. (A5.12) as follows

$$\begin{aligned}
p &= \frac{\int_0^{\infty} e^{-2(z/\alpha_2)^2} \cdot e^{-(z/\alpha_0)^2} \cdot e^{-(z/\alpha_1)^2} \cdot dz}{\int_0^{\infty} e^{-(z/\alpha_0)^2} \cdot e^{-(z/\alpha_1)^2} \cdot dz} \\
&= \frac{\int_0^{\infty} \exp\{-[2/\alpha_2^2 + 1/\alpha_0^2 + 1/\alpha_1^2]z^2\} \cdot dz}{\int_0^{\infty} \exp\{-[1/\alpha_0^2 + 1/\alpha_1^2]z^2\} \cdot dz} \\
&= \left[ \frac{1/\alpha_0^2 + 1/\alpha_1^2}{2/\alpha_2^2 + 1/\alpha_0^2 + 1/\alpha_1^2} \right]^{1/2} \tag{A5.16}
\end{aligned}$$

where,  $\alpha_0$ ,  $\alpha_1$  and  $\alpha_2$  are the  $\alpha$  parameters corresponding to the E-fields of  $E_{z0}^T$ ,  $E_{z1}^T$  and  $E_z^H$ . For a small dielectric perturbation to the cavity,  $\alpha_0 \approx \alpha_1$ , then

$$p \approx \frac{1}{\sqrt{1 + (\alpha_1/\alpha_2)^2}} \tag{A5.17}$$

This indicates that the larger the ratio  $\alpha_2/\alpha_1$ , the closer  $p$  is to unity and the less the difference between the permittivity's measured average value,  $\epsilon'_{r0}$ , and its true value in the gap,  $\epsilon'_{rG}$ . To give examples,  $\alpha$  and  $p$  values for different sample geometries and dielectric constants are calculated and listed in Table A5.1. Since the testing field has a shorter wavelength than that of the heating field,  $\alpha_1 > \alpha_2$  and  $p$  is about 0.6-0.8.

If the temperature distribution is also approximated by a normal function, Eq.(A5.9) is rewritten as

$$\chi = \chi_H + (\chi_G - \chi_H) \cdot e^{-(z/\alpha_t)^2} \tag{A5.18}$$

Comparing with Eq. (A5.10) and noting that  $(E_z^H)^2 = e^{-2(z/\alpha_2)^2}$ , we find that

$$\alpha_t^2 = \alpha_2^2/2 \tag{A5.19}$$

Therefore, Eq. (A5.17) becomes



**Table AS.1** The parameter  $\alpha$  and  $p$  for evaluating the error of the sample's temperature non-uniformity.

Cavity Gap Parameters	$\epsilon'_r$	$\alpha_0$	$\alpha_1$	$\alpha_2$	$p$
$r_s=0.24, r_o=0.355\text{cm}, \epsilon_{rh}=3.78$	5	0.44	0.46	0.32	0.58
$r_s=0.24, r_o=0.355\text{cm}, \epsilon_{rh}=1.0$	5	0.47	0.51	0.42	0.65
"	10	"	0.53	0.49	0.71
"	20	"	0.63	0.61	0.76
$r_s=0.24, r_o=0.30\text{cm}, \epsilon_{rh}=1.0$	5	0.32	0.37	0.31	0.67
"	10	"	0.42	0.41	0.75
"	15	"	0.50	0.47	0.78

$$p \approx \frac{1}{\sqrt{1+0.5(\alpha_1/\alpha_t)^2}} \quad (\text{A5.20})$$

If the sample's temperature profile is close to or flatter than that of the testing field, i.e.,  $\alpha_t \approx \alpha_1$ , then  $p \approx 0.82$ . In practice, this condition can be satisfied if a longer sample heating time is used. Using a thermal insulating material as the sample holder can also increase  $\alpha_t$ .

To have an estimation of the error analyzed above, let's take a numerical example. A sample has a temperature of  $1000^\circ\text{C}$  and  $700^\circ\text{C}$  at  $z=0$  (gap midplane) and  $z=1.5\text{cm}$  (zero-field point inside the hole). Assuming that  $\epsilon'_r(1000)=11.0$ ,  $\epsilon'_r(700)=10.0$  and  $p=0.9$ , we find that the determined  $\epsilon'_{r0} = 10 + 0.9 \times (11 - 10) = 10.9$  and  $\Delta\epsilon'_r/\epsilon'_r(1000) = (10.9 - 11)/11 = -0.9\%$  which is negligible compared with other measurement errors (5-10%).

To find the error in the loss factor due to a non-uniform sample temperature, we can make use of the results derived for the dielectric constant because of the similarity between Eq.(A5.1) and (A5.2). Simply replacing  $\epsilon'_r$  by  $\epsilon''_r$  in Eq. (A5.13) leads to

$$\Delta\epsilon''_r = \epsilon''_{r0} - \epsilon''_{rG} = -(\epsilon''_{rG} - \epsilon''_{rH}) \cdot (1-p) \quad (\text{A5.21})$$

Here the parameter  $p$  is the same as that given by Eq. (A5.16).

In Figure AS.2, the measured sample temperature distribution at  $700^\circ\text{C}$  along the  $z$ -axis is plotted together with the testing and heating

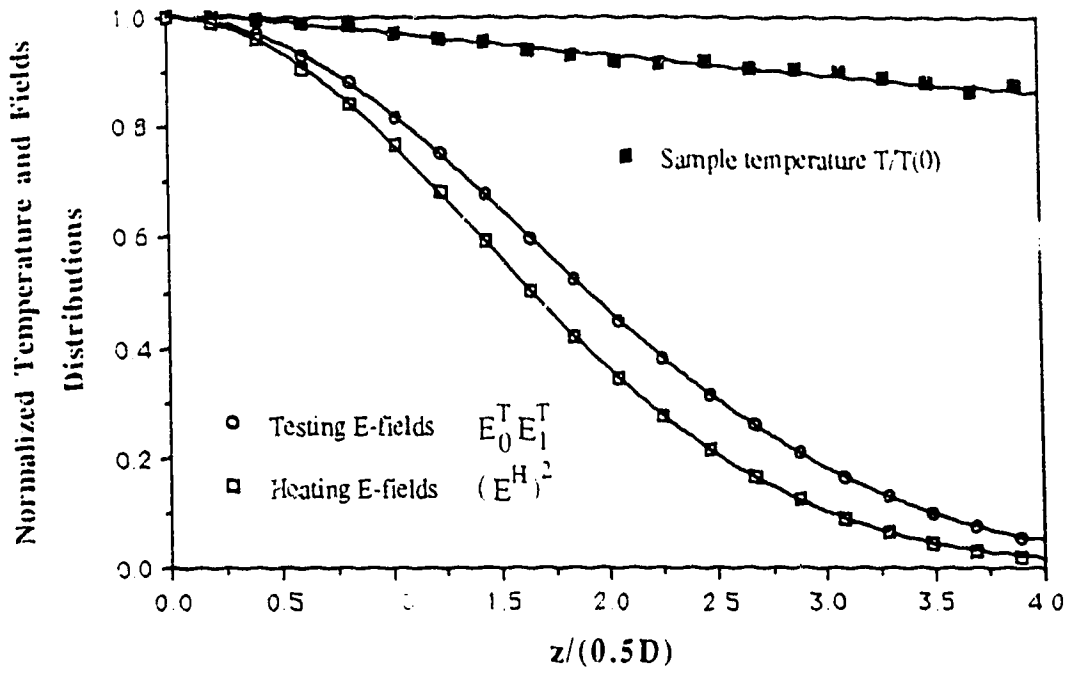


Figure A5.2 The measured axial temperature distribution of a glass sample (Corning 3320) at 700°C for 1.5 minutes, compared with the calculated testing and heating field profiles.

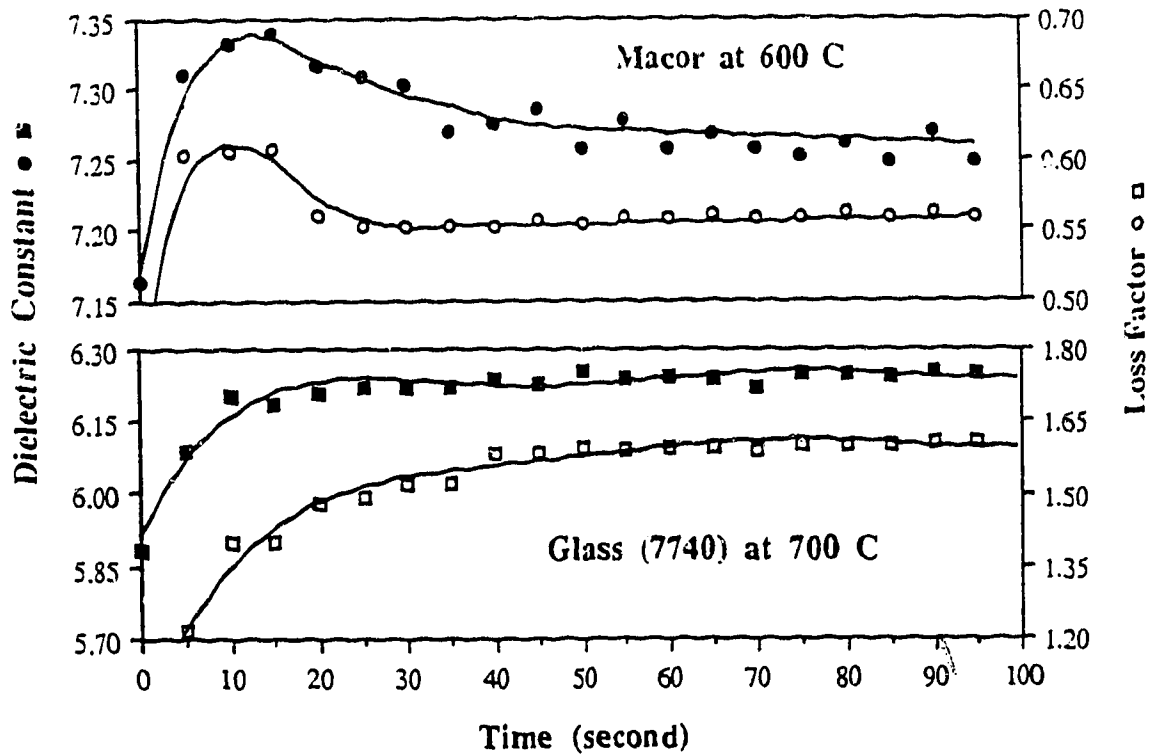


Figure A5.3 The dielectric data measured at a fixed temperature, 5 seconds for each data point.

fields. It clearly demonstrates a much flatter temperature profile than the field distribution profiles. Therefore, the uncertainty in measured dielectric data due to the temperature non-uniformity is quite minimal if the overall sample heating time is not shorter than 1 minute. Figure A5.3 shows the dielectric data of two samples measured at a fixed temperature, at 5 second intervals. We see that the data become stable after 30 seconds and the data variations can be within 3% for  $\epsilon'_r$  and 10% for  $\epsilon''_r$  after 10 seconds. In actual measurements, the sample is heated gradually from room temperature and the temperature uniformity is better than the case of Figure A5.3. Therefore, it takes less time for the measured dielectric data to reach stable values.